UNIVERSITY OF CAPETOWN

A Study Of Potential Calibrators Using The KAT-7 Radio Telescope

by

Ermias Abebe

A thesis submitted in partial fulfilment for the
Degree of Master of Science

in the
SCIENCE FACULTY
APPLIED MATHEMATICS

Supervisors:
Prof. Bruce Bassett (UCT, AIMS)
Dr. Nadeem Oozeer (SKA SA, AIMS, NWU)
Co-supervisors:
Prof. Roy Maartens (UWC)
Prof. Romeel Dave (UWC)

The financial assistance of the South African Square Kilometre Array Project towards this research is hereby acknowledged. Opinions expressed and conclusions arrived at, are those of the author and are not necessarily to be attributed to the NRF.

July 2015

Declaration of Authorship

I, Ermias A. Kassaye, know the meaning of plagiarism and declare that all of the work in the thesis, save for that which is properly acknowledged, is my own.

Signed: _____

Date: _____

Abstract

This thesis presents a study of potential calibrators observed by the Karoo Array Telescope (KAT-7). The KAT-7 is an engineering prototype for the coming sensitive array, the MeerKAT, one of the pathfinders for the Square Kilometre Array (SKA). This thesis plays a supporting role in the ongoing commissioning activities of the KAT-7, whose construction started in early 2008, and which has been undergoing engineering and science verifications since late 2010. This thesis has achieved the first steps towards identifying possible flux-density standards for short baseline interferometers such as the KAT-7. The systematic error for flux-density calibration at KAT-7 was estimated relative to 3C123, and it was found to be $\sim 5\%$ of the measured flux density. 18 ($\sim 47\%$) of the 38 sources were identified as good flux density calibrator candidates, for their Modulation Index (`MI`) and Variability Index (`VI`) values were less than 0.05 and all the sources in the field had less than 10% of the peak flux density of the calibrator candidate. One source (PKS J0837-1951), which showed low variability and hence appeared to be a good flux-density calibrator candidate (class A), was deemed to be not a good flux-density calibrator candidate because a strong confusing source was found within its primary beam. Eight sources had `MI` or `VI` values between 0.05 and 0.09 and may deserve further study as potential flux calibrator candidates. Five sources had `MI` or `VI` values greater than 0.09 suggesting significant variability while 17 sources had only one or two observations so their suitability as potential flux calibrator candidates could not be evaluated. In addition we used another measure of variability, the de-biased modulation index, for our sources comparing the observed modulation indices against Monte Carlo simulations. The result showed that the values of M_d are largely as expected and the uncertainties therefore not substantially underestimated.

Acknowledgements

First of all, I would like to thank my supervisors, Prof. Bruce Bassett and Dr. Nadeem Oozeer, for their immense and relentless contributions, guidance and inspiration throughout the research. I have learnt a lot from them about astronomy and cosmology through the invaluable discussions, workshops and presentations. These all have become assets to my future research career. I am sincerely grateful for giving me every necessary inputs for the research with their unfaltering determination. Prof. Roy Maartens and Prof. Romeel Dave co-supervised the thesis and supported me financially in the initial and final phase of this project, respectively; I owe them my deepest gratitude for their advice, encouragement and support.

I received many important and constructive comments from my colleagues in cosmology research group at AIMS: Michelle Knights, Lise du Buisson, Eli Kasai, Nima Khosarvi, Patrice Okouma, Navin Sivanandam. I thank them all not only for sharing their knowledge and experiences, but also for their huge contributions in editing my thesis. I would like to thank Rene January for facilitating all administration affairs.

My special indebtedness goes to Michelle's family: Dee Knights and Edward Kemsley, for their priceless contributions in editing my thesis carefully and curiously, in addition to pointing out and correcting some mistakenly included information in the thesis.

Amare Abebe, my good friend and a cosmology researcher at the University of Cape town, has helped me a lot from the organization of my thesis to editing and giving many important comments on the thesis; I thank him so much for being a friend in need.

The comments given by the anonymous examiners during the first submission of the thesis are invaluable. I am sure that the quality of this thesis is highly improved because of their precise and crucial feedbacks and comments. I have learnt a lot about calibration and radio astronomy from them; I sincerely thank them for their huge contribution.

I would like to thank the SKA, SA staff and researchers for their collaboration whenever I needed their help, in addition to allowing me to use the computing facilities during the data reduction and analysis. I also thank the African Institute for Mathematical sciences (AIMS) for covering my bursary at the start of this project.

Contents

List of Figures

List of Tables

Chapter 1

Introduction

1.1 Brief History Of Radio Astronomy

The ubiquitous existence of electromagnetic radiation from distant cosmic sources, such as stars, galaxies, interstellar media and others, is an essential ingredient of reliable information about the spatial distribution and composition of the sources of interest. The science of astronomy, among the oldest sciences in human history, extensively uses electromagnetic radiation to unveil the mysteries of the universe. The emphasis of this science had been limited to the observation of the visible part of the electromagnetic spectrum for many years [1, 2]. However, in the early seventeenth century, the study of astronomy was supported by the use of optical telescopes to observe objects in the universe with enhanced resolution. According to historical notes, Galileo Galilei systematically used lenses and mirrors to view objects in the solar system with better magnification than the human eye is capable of [2].

The study of cosmic sources in other frequency bands hardly received any significant attention until the 1930s. The main reasons for this were the blockage of electromagnetic spectra by the Earth's atmosphere and the absence of well designed detectors to capture radiation of various wavelengths [1]. Astronomical sources in the radio window (which extends from a wavelength of approximately 1mm to 150m) was initially detected from the Milky Way by Karl Jansky. At that time he was studying the possible transatlantic voice transmission in Bell Telephone Laboratories [3]. The main objective of his project was to identify the direction of thunderstorm static. By identifying the prominent direction, he would ultimately design antennae for transoceanic radio telephone transmission with better signal to noise ratios. During his experimental assisted observations, however, he unexpectedly received radiation from extraterrestrial sources

using a direction-sensitive antenna designed to receive radio waves at a frequency of 20.5 MHz [1, 4].

After the breakthrough discovery by Jansky, further scrutinizing of radio sources was carried out by an American radio engineer, Grote Reber, in 1937 [5]. He first constructed a parabolic reflector antenna of 9.5 m in diameter. Assuming Planck blackbody radiation could probably be an emission mechanism for radio sources, he performed his first observation at a shorter wavelength of 9.1 cm to easily detect strong radiation. However, he was unsuccessful in his attempt and detected nothing. By modifying his receiver to operate at a longer wavelength of 33 cm, he tried another observation. Unfortunately, his second attempt was also futile. By further extending his receiving wavelength to 1.87 m, he successfully detected radiation from celestial sources in 1939. His result inevitably reconfirmed the existence of radio wave emitting objects in the universe.

One of Reber's profound achievements was his systematic study of the sky at a wavelength of 1.87 m . He showed quantitatively how the radio radiation pervades in the sky [6]. Besides this, he was the pioneer in detecting the radio radiation from the sun.

Researches in radio astronomy dramatically increased after the end of World War II. The technologies developed in radios and radars for the purpose of the war were transferred to radio astronomy research after the war. However, a few researches were conducted during the war time. For example, strong radio emission from the sun was detected by James S. Hey in Britain around 1942 [4]. He and other groups in Britain, the Netherlands, and Australia pursued further researches at different wavelengths after the war. These observations played an extraordinary role in understanding the emissions from extended regions in our galaxy and other galaxy systems in the universe.

During the early stage of radio astronomy, the researches were aimed at observing limited radio bands using single radio telescopes that detect relatively strong radio emitting sources. However, rapid progresses later included all radio bands from centimetre up to sub-millimetre. Generally, the radio signal at higher centimetre wavelengths is more susceptible to ionosphere effects, whereas signals at sub-millimetre are significantly absorbed by water and nitrogen molecules. Despite these constraints, radio waves, owing to their long wavelengths, are hardly blocked by dust particles, which are the main barriers to other electromagnetic spectra [7, 8].

One of the disadvantages of longer wavelengths and single dishes is the inability of achieving a better angular resolution, $\theta_{\mathtt{res}}$. According to the Rayleigh criterion, the angular resolution of a telescope is given by

$$\theta_{\mathtt{res}} \approx \frac{\lambda}{D}, \tag{1.1}$$

where λ is the wavelength of the electromagnetic radiation being observed and D is the aperture diameter of the telescope. The diameter should be very big to obtain fine resolutions from a single radio telescope, but this is impractical and uneconomical. For example, the Green Bank radio telescope is the largest steerable single dish in the world, having an aperture diameter of 110 m [9]. It can only achieve an angular resolution of $3.4'$ at a wavelength of 11 cm. On the other hand, a 10 cm diameter optical telescope working at a wavelength of 500 nm has a resolution angle of $1.25''$.

The most efficient way of obtaining better resolution is using the interferometry technique, which was first developed by Michelson. The method requires the construction of many small telescopes, so that the signals from the telescopes can be amplified and correlated to achieve higher sensitivity and better resolution. In this case, the resolution is approximately equivalent to $\lambda/b_{\texttt{max}}$, where $b_{\texttt{max}}$ is the maximum distance between two antennae. The technique was first used for radio astronomy applications by british radio astronomer Sir Martin Ryle and his associates at the University of Cambridge [4]. Their discovery has enabled radio astronomers to view radio sources with fine angular resolution. For example, the Very Long Baseline Array (VLBA)[1], where the telescopes are located across North America, has achieved a resolution of $\sim$ 0.1 milliarcsecond (mas) because of its long baseline of 8,611 km [10]. Generally, radio astronomy aims to accomplishing better resolution, higher sensitivity and viewing the sky at various radio frequencies. For these purposes, many radio telescopes have been constructed to disclose many fundamental questions about the universe.

1.2 Interferometry Visibility

As discussed in the previous section, radio telescope detects electromagnetic radiation from various sources in the sky which can be transformed into human understandable form. Thus, the study of cosmic sources is carried out by receiving electromagnetic waves or signals at a certain point on Earth. The voltages produced in antennae, commonly known as signals, originate from a large cosmic object with many independently radiating entities at various distances from the point of observation with different frequencies [11, 12]. Such natural processes are random in that the properties of signals are inferred from their statistical manifestation.

The signal at the observer's plane is generally represented by an Electric field, $E(\vec{r})$. When the signal from a source reaches two positions $\vec{r_i}$ and $\vec{r_j}$, the outcome is defined by a spatial cross-correlation function as

[1] www.science.nrao.edu/facilities/vlba

$$V(\vec{r_i}, \vec{r_j}) = \langle E(\vec{r_i}) E^*(\vec{r_j}) \rangle. \tag{1.2}$$

The brackets in Eq.(1.2) imply ensemble averaging over time, and the asterisk denotes the complex conjugate. $V(\vec{r_i}, \vec{r_j})$ is known as visibility; it is one of the fundamental functions in radio astronomy. Practically, the spatial coherence function of an electric field is measured by an interferometer, where it multiplies and averages signals obtained from pairs of antennae.

The response of a narrowband phase-tracking interferometer to spatially incoherent radiation from the far field can be expressed by the relation between the spatial coherence function or visibility, $V(u, v, w)$, and the spectral intensity, or brightness, $I(l, m)$ [11–13]:

$$V(u, v, w) = \int \int_{\mathbf{s}} I(l, m) \frac{\exp\left(-i2\pi \left[ul + vm + wn\right]\right) dldm}{\sqrt{1 - l^2 - m^2}}, \tag{1.3}$$

where the distance in the observing plane is divided by the wavelength, λ, to give baseline coordinate or $(u, v, w) = (\vec{r_j} - \vec{r_i})/\lambda$; (l, m) are angular coordinates on the sky, or known as direction cosines.

The observation is confined to the $u - v$ plane and when $w = 0$, Equation (1.3) reduces to

$$V(u, v) = \int \int_{\mathbf{s}} I(l, m) \frac{\exp\left(-i2\pi \left[ul + vm\right]\right) dldm}{\sqrt{1 - l^2 - m^2}}. \tag{1.4}$$

The visibility $V(u, v)$ is the Fourier transform of the modified brightness distribution $I(l, m)/\sqrt{1 - l^2 - m^2}$.

The source brightness distribution is limited to the small region of sky, so that $\sqrt{1 - l^2 - m^2} \simeq 1$. Hence, Eq.(1.4) is modified to:

$$V(u, v) = \int \int_{\mathbf{s}} I(l, m) \exp\left(-i2\pi \left[ul + vm\right]\right) dldm, \tag{1.5}$$

which is a Fourier transform relation, where the spatial intensity distribution $I(l, m)$ of the source can readily be recovered from the visibility function $V(u, v)$ by applying inverse Fourier transform.

However, it is impractical to apply Eq.(1.5) without adjusting for real applications. The main reason is the impossibility of probing a point source by the elements of the interferometer; they measure only a finite size. The elements are highly direction dependent to the incoming radiation [14]. Hence, the visibility given by Eq.(1.5) must be modified by

the normalized reception pattern (primary beam) of the interferometer element, $A_\nu(s)$. Thus, the spatial coherence function has to be rewritten as

$$\hat{V}(u,v) = |\hat{V}| \exp(i\phi) = \int\int_{\mathbf{s}} A_\nu(s) I(l,m) \exp\left(-i2\pi\left[ul + vm\right]\right) dldm, \tag{1.6}$$

where $|\hat{V}|$ is the amplitude of the complex visibility and ϕ is its phase. The complex visibility $\hat{V}(u,v)$ is referenced at the phase tracking center –the point at which the field of view is centred. The Fourier inversion of Eq.(1.6) yields

$$I(l,m) = \frac{1}{A_\nu} \int\int_{\mathbf{s}} \hat{V}(u,v) \exp\left(i2\pi\left[ul + vm\right]\right) dudv. \tag{1.7}$$

The value of A_ν has to be closer to unity at the phase tracking centre to produce the intensity by direct inversion of the complex visibility. If not, the inversion will be infested with errors because A_ν rapidly goes to zero in the direction away from the center of the primary beam. Therefore, taking radiation in small regions of the sky is a critical consideration, where it has to satisfy [15]:

$$\left|\frac{\Delta\nu}{c} b.(\hat{s} - s_o)\right| = \frac{\Delta\nu}{\nu}\frac{\theta}{\theta_{res}} << 1, \tag{1.8}$$

where $\hat{s}$ is the direction towards any point on the source from the observing point; s_o is the phase tracking center; $\theta = \hat{s} - s_o$ is the field of view; θ_{res} is the synthesised beam resolution; $\Delta\nu$ and ν are the bandwidth and the central frequency, respectively; b the baseline vector; c is the speed of light.

1.3 Calibration Formalism In Radio Astronomy

Once we have the observed visibilities, the next step is how to calibrate them from various contributions. This section elaborates on the mathematical formalism behind calibration. Most of the explanations in this section are taken from a collection of lectures on synthesis imaging in radio astronomy by Taylor et.al [16].

The relation between the visibility function, $\hat{V}(u,v)$, and the intensity distribution, $I(l,m)$, in Eq.(1.5) is valid under a quintessential assumption of ignoring all intervening factors between the radio signals and the antennae. Unfortunately, the atmosphere and the instruments dominantly alter the actual visibility function of the target source.

The actual visibility function can be recovered from the measured visibility by careful consideration of subversive factors. By doing so, we can estimate the errors associated

with the measured visibility thereby determining the true visibility of the source. This method in radio astronomy is known as calibration.

Calibration deals with errors connected with instrumental and atmospheric variables. The former mainly stem from a single antenna or pairs of antennae, and the electronic devices used in the process of measurements and data acquisition. The latter are due to the interaction of radio waves with ionized atoms and molecules in the intervening medium. The net correction factors can usually be determined by transferring the parameters of known sources to the measured visibility data.

Suppose the observed visibility function generated by an interferometry array is V_{kl}^o, where the function is represented by antenna pairs (k, l) and the time of observation, t. Therefore, the basic calibration formula relating the ideal visibility, $V_{kl}^I(t)$, with the observed visibility, V_{kl}^o, can be written as:

$$V_{kl}^o(t) = G_{kl}(t)V_{kl}^I(t) + \epsilon_{kl}, \tag{1.9}$$

where G_{kl} is the antenna-based complex gain and ϵ_{kl} is a stochastic complex noise.

One method of obtaining solution to Eq.(1.9) is by using calibrator sources in the sky. The reason for observing these sources is that telescopes on the ground can only measure the phase differences rather than measuring absolute phase reference. Therefore, the reference for phase visibility to the phase tracking center or the center of the primary antenna beam can be practically accomplished by observing point-like calibrator sources. Using these sources, one can determine the phase deviation from the desired reference point. Periodic observation of these sources is very important so as to track the phase and gain changes in an array. Above all, they have the paramount advantage to estimate time dependent phase changes incurred by the atmosphere.

The abundant availability of calibrator sources in the sky with unique characteristics, such as discrete with infinitesimal diameter and high flux density, has enabled radio astronomers to use them as standard signal testers. The selection of these sources as a calibrator is based on the following essential considerations.

1. They should have invariable characteristics during the period of observation.
2. They should have known positions in the sky.
3. Their spectral properties should be known, and preferably be simple.
4. Their flux densities have to be strong enough so as to get suitable signal-to-noise ratio (SNR) for calibrating in a short time.

5. They should be available discretely in the sky without adhering to other confusing sources.

1.3.1 Baseline and Antenna-Based Complex Gain Solutions

Assume that a calibrator is a point source of known flux density S and position. In this regard, the true visibility amplitude would have the value of the flux density S, and the phase is taken as zero degree ($l = m = 0$) at phase tracking center. Therefore, the complex baseline based gain for the calibrator source is given by

$$G_{kl}(t) = \frac{V^o_{kl}(t)}{S}. \tag{1.10}$$

The stochastic term (ϵ_{kl}) that appeared in Eq.(1.9) is excluded in Eq.(1.10) because of its negligible contribution after the data is properly averaged and edited. As can be seen from Eq.(1.10), the gain solution is totally baseline dependent.

Due to the fact that most data depravities resulted from antennae or atmospheric factors that essentially occur before the correlation of signal pairs, solving for antenna based parameters (amplitude and phase) would be a plausible approach. This can be achieved by factorizing the complex gain G_{kl} as a product of the complex gain of each antenna, i.e., G_k and G_l and a residual term due to baseline based complex gain or η_{kl}. This can generally be written as

$$G_{kl}(t) = G_k(t)G^*_l(t)\eta_{kl}(t). \tag{1.11}$$

The deviation of $\eta_{kl}(t)$ from unity is commonly known as closure error. Error margins of less than 1% in amplitude and 1^o in phase are acceptable. $\eta_{kl}(t)$ is close to unity for well designed systems.

Equation (1.11) may be written in terms of amplitude and phase terms as:

$$G_{kl}(t) = G_k(t)G_l(t)\eta_{kl}(t)\exp\left(i\left[\phi_k(t) - \phi_l(t) + \phi_{kl}(t)\right]\right). \tag{1.12}$$

Suppose that the ideal visibility is $V^I_{kl} = G^I_{kl}\exp(i\psi^I_{kl})$. Observing a point source calibrator of flux density S at phase tracking center ($\psi^I_{kl} = 0$) would give $V^I_{kl} = S$. Similarly, the observed visibility in terms of its amplitude and phase is given by

$$V^o_{kl}(t) = G^o_{kl}S\exp(i(\psi^o_{kl})). \tag{1.13}$$

By taking the ratio of the observed visibility to the ideal visibility, we would find amplitude and phase calibration equations separately as:

$$G^o_{kl} = G_k(t)G_l(t)\eta_{kl}(t)S, \tag{1.14}$$

and

$$\psi^o_{kl} = \phi_k(t) - \phi_l(t) + \phi_{kl}(t). \tag{1.15}$$

A well designed system will have a residual or η_{kl} value of unity, so that it reduces the steps of finding solutions to G_k and ϕ_k for the given N antennas.

The antenna-based method has several advantages. Firstly, a configuration of N antennas has $N(N-1)/2$ baselines, which is equivalent to the number of equations to be solved. Thus, antenna based approach will reduce the number of equations to be solved to N. Therefore, antenna based method plays a crucial role in speeding up the computation time for $N > 3$. Secondly, since the antenna-based gain does not include every baseline, it will avoid problem caused by the maximum baseline, which can possibly resolve the source.

Despite of its advantages, calibration using known sources has several drawbacks. For example, the gain, G_k, may not accurately determine the corresponding gain of a target source. This is because of big time gaps between successive observations and large separations between them. Besides, it is sometimes difficult to find bright unresolved or discrete calibrator source near the target sources. Hence, these factors essentially degrade the image quality of the radio data. The next section will discuss the method of minimizing the drawbacks.

1.3.2 Self-Calibration

Both amplitude and phase will be affected while employing a calibrator source for calibration, which essentially decreases the signal to noise ratio of the resulting image. The problem can be solved by assuming an appropriate model for the source of interest. Applying the target source itself as a model so as to evaluate the complex gains is known as self-calibration.

The main intuition of self-calibration is originated from the overdetermined information accessed from the arrays. For instance, N number of antennas comprises N residual amplitude errors and $N-1$ residual phase errors provided that one antenna is selected as a reference element. The number of complex visibilities obtained from the same

number of antennas are $N(N-1)/2$. This shows that the system is overdetermined for $N > 3$, i.e., 4 antennas are required for amplitude closure.

There is no unique approach of solving the problem for having the redundant information though there are several ways of finding the solution. One way of estimating the complex gain is by applying the least square method, in which one can minimize the square of the difference between the measured and the model complex visibilities. The assumption can be translated into an expression of the form:

$$\Delta S = \sum_{m} \sum_{k,l} w_{kl}(t_m) \left| V_{kl}^{o}(t_m) - G_k(t) G_l^{*}(t) V_{kl}^{mod}(t_m) \right|^2 , \tag{1.16}$$

where $V_{kl}^{mod}(t_m)$ is the model visibilities and $w_{kl}(t_m)$ are weights applied to the various interferometer pairs for each observation at t_m. Lower weight is associated to highly noisy visibility data whereas high signal to noise ratio visibilities should receive higher weight. The derived complex gains depend on the correctness of the model. In other words, wrong model will give an incorrect image and hence parameters of the desired source.

Equation (1.16) can be rewritten in an alternative form of having the ratio of the observed visibilities to the model viabilities. Thus, a pseudo-point source is produced in the image.

$$\Delta S = \sum_{m} \sum_{k,l} w_{kl}(t_m) |V_{kl}^{mod}(t_m)|^2 \left| P_{kl} - G_k(t) G_l^{*}(t) \right|^2 , \tag{1.17}$$

where P_{kl} is the ratio of measured to model visibilities,

$$P_{kl} = \frac{V_{kl}^{o}(t_m)}{V_{kl}^{mod}(t_m)}. \tag{1.18}$$

There is no proof for the convergence of self-calibration given by Eq.(1.17) or Eq.(1.18), rather a non-linear procedure is undertaken on the data set so that asymptotic convergence is achieved iteratively. Self-calibration is, therefore, a step by step process that ultimately reduces errors degrading image quality thereby enhancing the accuracy of amplitude and phase determination.

The first step of self-calibration is the preparation of the initial model of the source. This model can be an image obtained by utilizing a calibrator source as explained in Section 1.3. The next step requires the conversion of the source into the pseudo-point source as implied in Eq.(1.18). This step leads to solving the complex gains by setting

ΔS to zero. After solving the G_k terms, we are able to find the corrected visibilities as:

$$V_{kl}^{co} = \frac{V_{kl}^{o}(t_m)}{G_k G_l^*}. \tag{1.19}$$

Based on the corrected visibility data, we can again form a new model and repeat the procedure until we reach iteratively to a minimum residual error.

1.3.3 The Need For Flux Density Calibrator Sources

The flux density (see Section 1.3.6) of a radio source may be determined if most or all parameters related to the telescopes: atmosphere, receiver, electronics, and others are known. However, absolute calibration is very challenging in practice because of the difficulty in measuring the parameters accurately. For this reason, the calibration of interferometers is commonly performed relative to standard sources, where their flux densities are measured absolutely with considerable effort [17].

Baars, et al. [18] employed sources as flux density standards. They used Cassiopeia A, Cygnus A, Taurus A, and Cyg A as primary flux density standards as they are bright radio sources. These sources were nominated as primary calibrators since their flux densities had been directly determined by single telescopes of known gains, and the observations were calibrated with suitable thermodynamic standards. As a result, their spectral flux densities were estimated with an accuracy of about 2% at frequency between 30 MHz and 30 GHz [18].

Moreover, Baars et al. calculated the flux density of 13 compact sources as secondary calibrators by taking Virgo A as a reference. Out of the 13 sources, 3C48, 3C147, 3C138, 3C286 are preferably utilized by various modern interferometers for calibration purposes, for they are discrete and compact. The remaining 9 sources (i.e. 3C123, 3C161, 3C218, 3C227, 3C249.1, 3C295, 3C348, 3C353, DR 21, and NGC 7027) have been partly resolved by most of high resolution interferometers. However, because of shortage of unresolved sources, 3C123, 3C161, 3C295, and NGC 7027 are still used as flux calibrators with considerable care.

The four sources have been studied by Very Large Array (VLA) to search for flux variability with time [17]. According to the monitoring survey performed by Perley and Butler for almost 30 years, 3C286 varies less than 1% within the duration of the study at frequencies between 1 GHz and 50 GHz. Additionally, it is the most compact and has a flat spectral index. Therefore, it is a good flux density calibrator for many interferometers. 3C286 is therefore one of the preferable flux calibrators for the VLA and most interferometers found in the northern hemisphere.

On the other hand, sources 3C48, 3C138, and 3C147 exhibit variability as much as 20% on various time spans. These sources, however, show small variability at a frequency between 1 GHz and 2 GHz, indicating that they could be good candidates as flux density calibrators for the observation performed in these frequency ranges with appropriate baseline configurations.

A reliable result for flux density scale and variability study depends on the observing strategy. Perley and Butler suggested the following methodology to accurately estimate and correct the elevation-dependent telescope characteristics [17]:

- observe for 24 hours duration to minimizing holes in the u-v coverage.
- perform five to ten individual 'snapshot' observations of each object at the desired band for the duration of 30 to 60 seconds.
- minimize short duration telescope malfunction, bad weather, and sporadic interference by multiple observation strategy.

They implemented two-dimensional Gaussian profile fitting method to estimate the flux of the selected unresolved sources. Because of its compact, flat spectral spectral index, and less variability property of 3C286, Buttler et al. [17] used it as a reference source to show the relative variability of 3C138, 3C147, and 3C48.

Since these sources are northern declination sources, they will not be very high above the KAT-7 horizon and will also be up for short duration. However, these sources can be potentially good candidates of flux density calibrators for the KAT-7 (operating at frequency of 1.83 GHz and resolution about $\sim 4'$) when they are available.

1.3.4 Active Galaxies And Their Properties

Active galaxies are known for their high luminosity, and emit large amounts of non-stellar radiation. In other words, the optical spectra of AGN show emission lines, contrary to the normal galaxies that display absorption lines because of possessing thermal behaviour [7].

Almost all active galaxies have the following prevalent properties [7, 19, 20]:

1. They have radio luminosities of greater than 10^{37} W within small emitting region, where the size ranges from a light day to a light year [21]. Moreover, excess amount of X-ray, ultraviolet, infrared and radio radiation outputs are displayed compared to the normal galaxy.

2. The nucleus is assumed to have a supermassive black hole, which serves as the central powerhouse. The emitted radiation from the nucleus is as a result of the in-falling of matter (accretion) towards the black hole so that the gravitational potential energy is converted into kinetic energy. As the kinetic energy is converted into internal energy or heat due to friction, radiation will be sent out from the region. Moreover, this region exhibits a significant variation in brightness.

3. They are known for their explosive appearances or narrow jets which radiate matter emanating from the central core with large scale clouds of radio emitting materials.

4. They have broad emission lines in their optical spectrum in some cases.

The fundamental classification of active galaxies relies on their appearance, luminosity and spectra. Galaxies fulfilling such principal criteria are radio galaxies, Quasars, Seyfert galaxies, BL Lacertae objects (BL Lacs) and Blazars.

Radio galaxies emit radiation as a consequence of the entanglement of electrons inside magnetic field, and such emission phenomenon is known as non-thermal synchrotron radiation [22, 23]. Because of the synchrotron sources, the spectrum of most radio galaxies feasibly displays smooth or slow declivity in intensity from high to low wavelengths (low to high frequencies) or showing nearly flat spectrum. The luminosity of radio galaxies stretches from 10^{33} to 10^{38} W [24].

Radio galaxies are generally classified into two categories. These are compact and extended radio galaxies [7]. Compact radio galaxies describe very small radio sources, having a diameter of a few light years.

The extended radio galaxies commonly display a double structure consisting of lobes aligned on opposite side of the nucleus, and the lobes are separated by upto a $\sim$1 Mpc. These galaxies were further classified by Fanaroff and Riley in 1974 [25]. The divisions are named as Fanaroff and Riley class I (FRI) and class II (FRII). These classifications correlate the morphologies of the source with the their total radio power. Accordingly, sources with bright jets towards their centres and having low radio luminosity are categorized as FRI. On the other hand, those sources with faint jets but possessing bright hotspot at the ends of their lobes and having higher radio powers are grouped into FRII. The critical power separating FRI and FRII is 10^{25} WHz^{-1} at 1.4 GHz [26].

Classical doubles, that have lobes aligned through center of galaxy having the bright spots at ends, refer to FRII sources. A good example in this case is Cygnus A (3C405)[2]. Its radio output is around 10^{38} W, and each lobe has a diameter of 17 kpc, approximately extending 50 kpc from the central galaxy [21].

[2] images.nrao.edu/110

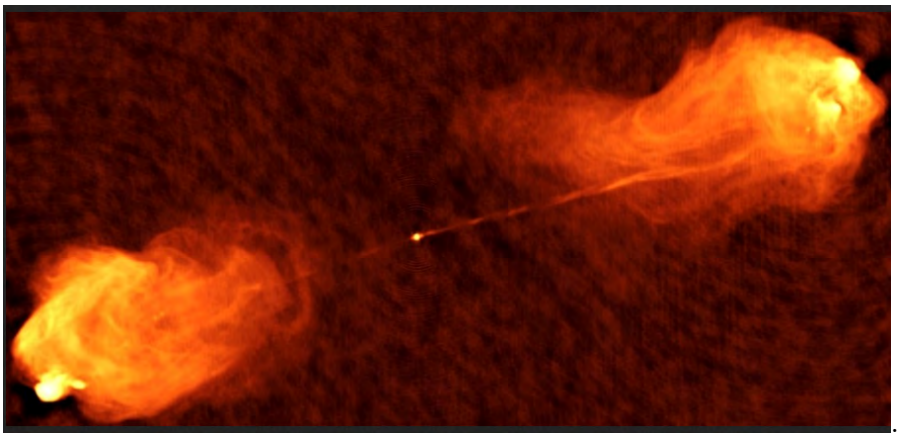

FIGURE 1.1: Radio map of Cygnus A produced by VLA telescopes in 1983 at frequency of 5 GHz with a resolution of 0.5″. The compact radio source or the core is located at the center which coincides with the galactic nuclei. The lobes in the map are oriented on the opposite side of the core. As can be seen in the map, both lobes have hot spots at their end. (R. Perley, C.Carilli and J.Dreher, NRAO)

Quasars are extragalactic objects having small angular size and high red-shift. Because of their smaller size and similar structure to stars, they were initially called quasi-stellar radio sources and later the name coined as 'Quasars'. It had been expected that almost all quasars were radio sources, but subsequent discovery showed that only 10% of such objects were radio sources or radio-loud quasars. Because of this fact, astronomers assigned a general name, known as quasi-stellar objects (QSO), to include the radio-quiet quasars [20, 24].

The emission mechanism of these objects is non-thermal radiation of continuum spectrum form. Their redshifts range from 0.06 to around 5 corresponding to the recession velocity of 6% to about 95% of the speed of light, respectively. According to Hubble's law, the distance D, where a galaxy is located from the observation point, is related to its redshift z by [27]:

$$D \approx \frac{zc}{H_0}. \tag{1.20}$$

Equation (1.20) is true for the nearby galaxies. H_0 is called the Hubble constant. According to the recent measurements by the European Space Agency Planck satellite, the value of H_0 is 67.80 ± 0.77 $\mathtt{kms}^{-1}\mathtt{Mpc}^{-1}$ [28].

The other peculiar property of these objects is their high luminosity (10^{39}-10^{41} W) on account of their distant appearance. Despite possessing high luminosity, their brightness fluctuates over periods of time as short as months or even days. The rapid variation in the brightness implies that their energy is emitted from very small regions of space, which is estimated to be the size of less than a light-day diameter.

Seyfert galaxies were the first active galaxies to be discovered in 1943 by Carl Seyfert [7, 24]. He first identified six spiral galaxies of exceptional characteristics compared with the normal galaxies. These galaxies have broad emission lines in their spectra and have nuclei which are extremely bright in the optical. The continuous spectra of Seyfert galaxies have a combination of stellar, non-thermal, and infrared (from dust) radiation. They are less powerful than quasars. They are weak radio sources, which can be categorized as 'radio quiet', with radio luminosities of $10^3 - 10^4$ times weaker than the radio loud category (i.e., radio galaxies and radio quasars) [7]. Since 1943 around 800 Seyfert galaxies have been identified with these properties.

Most of the Seyfert galaxies are morphologically spiral with the exception of around $5-10\%$ that may be elliptical. It is assumed that all spiral galaxies have passed through the Seyfert galaxies's phase in their evolution [7, 24].

BL Lacertae objects were first identified in early 1929 as optically variable objects. Due to their stellar appearance, they were presumed to be variable stars. They distinctly differ from the other active galaxies due to their frequent and erratic variation throughout the electromagnetic spectrum. More specifically, their energy variations occur without showing significant emission lines in their spectra [7].

Blazars represent the combining properties of BL Lac objects and flat spectrum radio quasars. They are different from the other AGNs in their highly oriented beams. Moreover, superluminal motion and rapid variation in all electromagnetic spectra are the common features of blazars [29]. More importantly, the ultrafast variation is specially observed at optical and high energy wavelength in time scales as short as a few minutes.

1.3.5 A Unified Model Of Active Galactic Nuclei

By comprehending the similarities and differences explained in Section 1.3.4, AGN activities can be described by a unified model that probably integrates all types of AGNs.

The basic theoretical consensus about the AGNs relies on the fact that their energy outputs are generated from the infall of gas, form an accretion disc onto a Super-Massive Black Hole (SMBH) [19]. In other words, the huge amount of gravitational potential energy is converted to photons where these photons bring about an outwardly flowing gas motion. As the result of these activities non-thermal radiation is induced closer to the accretion disk, in which the radiation can extend from the long radio wavelengths to highly energetic photons of short wavelength or X-rays [30]. Related to this fact, collimated beams form jets along the axis of the accretion disk. Additionally, as the

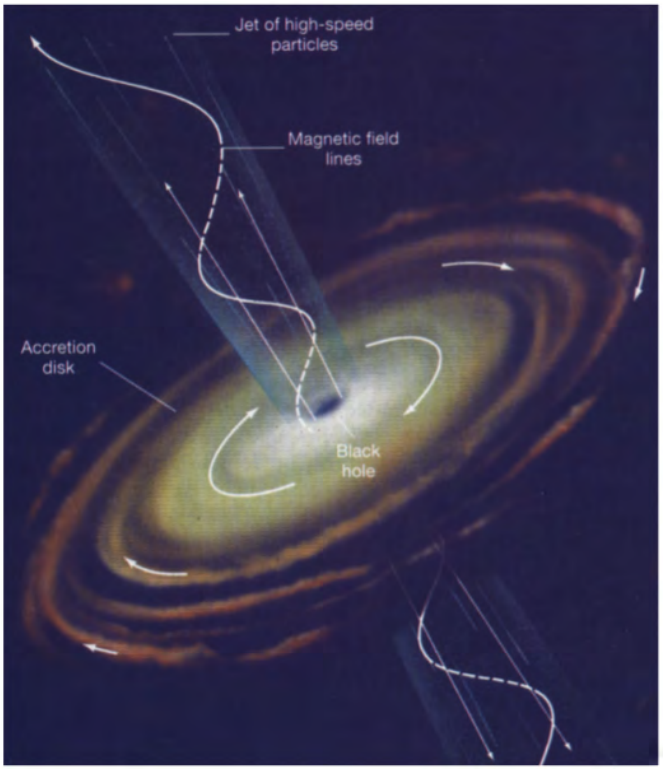

FIGURE 1.2: The widely accepted unified model of AGN. The rotating black hole assimilates dust and gas into the galactic center. As a result, powerful and rapidly non-thermal emission takes place. The image is taken from [29].

electrons recombine with gas ionized by central continuum sources, broad and narrow emission lines are produced.

As we observe the AGNs from the Earth, property of each specific type of AGNs depends on the orientation of the accretion disk to our line of sight and the amount of dust clouds and gas obscuring the nuclei. Therefore, characteristics of AGN such as accretion flow, jets and outflows, line emitting regions and obscuring materials, are of critical importance to revealing their secrets.

1.3.6 Emission Mechanisms

The emission mechanism of a radio source is studied by analysing the flux density variation along different radio frequency bands. An illustrative example is the blackbody, which ideally absorbs or emits all radiations incident upon it at all frequencies during thermal equilibrium state. The well tested theory (relating the radiation from a blackbody to frequency and temperature) is Planck's radiation law, which is given by:

$$B = \frac{2h\nu^3}{c^2}\frac{1}{\exp(\frac{h\nu}{KT}) - 1}, \tag{1.21}$$

where B is the brightness ($\mathtt{Watt\,m^{-2}\ Hz^{-1}rad^{-2}}$), h is Planck's constant ($6.63\times10^{-34}\mathtt{Js}$), ν is the frequency of the radiant object, K is Boltzmann's constant ($1.38\times10^{-23}\mathtt{J\,k^{-1}}$), and T is the temperature of the object.

For radio sources, however, the value of the photon energy ($h\nu$) is much less than KT. This assumption directs to the Rayleigh-Jeans law. According to this law, the flux density ($S = \int\int B d\Omega$) of an object at a radio wavelength, λ, follows the relation [1]:

$$S = \frac{2K}{\lambda^2}\int\int T d\Omega, \tag{1.22}$$

If we consider a constant temperature throughout the entire source, Eq.(1.22) is written in the form:

$$S = \frac{2K}{\lambda^2}T\Omega \propto \lambda^{-2}. \tag{1.23}$$

Equation (1.23) depicts the inverse relationship between the flux density and the square of the wavelength. Hence, the flux density as a function of wavelength or frequency can generally be written as:

$$S \propto \lambda^{-\alpha} \propto \nu^{\alpha}, \tag{1.24}$$

where α is a dimensionless quantity and known as a spectral index. If a radio source has a constant temperature in the entire wavelength and the flux density varies directly proportional to the square of the frequency or $\alpha = 2$, then the emission mechanism of the source is thermal radiation [1].

The other most dominant emission mechanism in a radio source is non-thermal mechanism or synchrotron radiation. The main cause of this emission is the spiralling of a high speed electron, having velocity closer to the speed of light, inside a uniform magnetic field. As an electron is entangled by the magnetic field, it accelerates in helical path by emitting radiation [1, 23].

Let us consider an electron moving at a relativistic velocity, v, inside a magnetic field, H. According to Einstein's relativity theory, the energy E of the ultra-fast particle is greater than the rest mass energy ($E_0 = m_0c^2$) by a Lorentz factor $\gamma = (1-(v/c)^2)^{-1/2}$. As a result, the relativistic energy is written as [1, 23]

$$E = \frac{m_0c^2}{\sqrt{1-(\frac{v}{c})^2}} = mc^2 = \gamma m_0c^2, \tag{1.25}$$

where m_0 is the rest mass and m is the relativistic mass.

At the moment the relativistic particle emits radiation, a cone-shaped denser pattern of radiation is produced, as shown in Figure 1.3. The cone has an apex angle θ, where its vertex is at a point of the instantaneous velocity [23]. This angle is dependent on the Lorentz factor γ and expressed as:

$$\theta = \frac{2}{\gamma} = \frac{2m_0c^2}{E}. \tag{1.26}$$

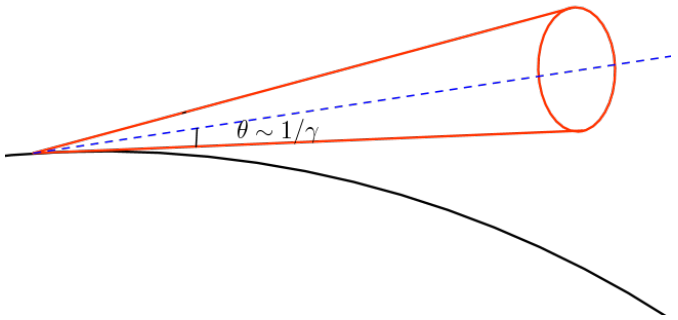

FIGURE 1.3: A cone-shaped radiation pattern (shown by red line) is formed when a highly relativistic electron radiates in a narrow beam, with width of order $\frac{1}{\gamma}$, in the direction of motion shown by black line.

As the particle orbits on a circle of radius R, it emits radiation continuously. However, the observed radiation in any particular direction is pulsed. As a result, an observer in the plane of the orbit will receive a cone of radiation once with every gyration at a time interval given by:

$$\Delta t \approx \frac{R\theta}{c}\frac{1}{\gamma^2} \approx \frac{2R}{c}\frac{1}{\gamma^3}, \tag{1.27}$$

where $R = \frac{v}{2\pi\nu}$ and ν is the frequency of emission or absorption by the particle. The radius R corresponds to the orbiting radius of the particle inside a homogeneous magnetic field in case of low speed (non-relativistic) particle. When the particle moves perpendicular to a uniform magnetic field, the centripetal force of the particle ($\frac{mv^2}{R}$) is equal to the magnetic force (evH) acting on the particle in the absence of any external forces; where e is the charge of the particle.

Combining all these factors, we obtain a monochromatic frequency of radiation in the particle's rest frame given by

$$\nu = \frac{eH}{2\pi m_0}\frac{1}{\gamma}. \tag{1.28}$$

However, strong Doppler boosting raises the low frequency of the radiation in the electron's frame into the radio regime, as well as causing the monochromatic radiation in the electrons frame to become a narrow pulse with emission over a wide range of frequency in the observer frame. In this respect, the pulse received by the observer for $v \sim c$ is

$$\Delta t \approx \frac{1}{2\pi\nu\gamma^3} \approx \frac{2m_0}{eH}\frac{1}{\gamma^2}. \tag{1.29}$$

Consequently, the frequency at which maximum power per unit band width radiated is given by:

$$\nu_{max} = \frac{1}{2\pi\Delta t} = \frac{eH}{4\pi m_0}\gamma^2. \tag{1.30}$$

If we assume a single electron, Eq.(1.30) can be rewritten in terms of the energy, E_v in electron Volts (`eV`) and magnetic field H as

$$\nu_{max} = 0.06HE_v^2, \tag{1.31}$$

where H is the magnetic flux density in Tesla = webers m^{-2}

The spectrum of a relativistic electron has a large number of closely spaced lines. The emission is spread out over a very wide range in frequency and there is a frequency at which the maximum emission occurs. The distribution generally follows a power-law of the form [31]:

$$N(E) \propto E^{-\xi}, \tag{1.32}$$

where $N(E)$ is the number of electrons as a function of energy, E is the energy of electron, and ξ is energy spectral index.

The total power emitted by a distribution of relativistic electrons with energies in the range E to $E+dE$ is therefore given by

$$P = C \times \int_0^E P(E)N(E)dE, \tag{1.33}$$

where C is a constant factor, and $P(E)$ is power radiated by a single electron.

Referring to Eq.(1.31), we observe that the power radiated by a single electron is proportional to the square of its energy. Thus, Eq.(1.33) will have the form

$$P = C \times \int_0^E E^2 E^{-\xi} dE = C \times E^{3-\xi}. \tag{1.34}$$

Moreover, Eq.(1.31) tells us that the radiation frequency of an electron is proportional to the square of its energy ($E \sim \sqrt{\nu}$). Hence, the power is written in terms of frequency as:

$$P = C \times \nu^{(3-\xi)/2}. \tag{1.35}$$

The variation of the the total power radiated by an aggregation of relativistic electrons is then described by

$$\frac{dP}{d\nu} = C \times \nu^{(1-\xi)/2} = C \times \lambda^{(\xi-1)/2}. \tag{1.36}$$

The flux density of a radio source due to such an ensemble of relativistic electrons becomes:

$$S \propto \lambda^{(\xi-1)/2} \propto \lambda^{-\alpha} \propto \nu^{\alpha}. \tag{1.37}$$

Cosmic rays (i.e., electrons, protons, and heavier nuclei with extremely high energies) have an approximate value of $\xi = 2.4$ [1]. Hence, the flux density variation with wavelength is given by

$$S \propto \lambda^{(2.4-1)/2} \propto \lambda^{0.7} \propto \nu^{-0.7}. \tag{1.38}$$

According to observations, a spectral index value of $\alpha = (\xi - 1)/2 \simeq -0.7$ is a typical indicator for the non-thermal radio sources [1].

Knowing the spectral index variation for a specific source, we can determine the flux density of the source at different frequencies once the flux density is evaluated at some frequency.

Suppose we have measured the flux density of a radio source at frequency ν_1, then the corresponding flux density at some other frequency ν_2 is given by:

$$S_{(\nu_2)} = S_{(\nu_1)} \left(\frac{\nu_2}{\nu_1}\right)^{\alpha}. \tag{1.39}$$

Based on the value of the spectral index, sources can be classified as steep spectrum when $\alpha < -0.5$; inverted spectrum when $\alpha > 0$; and flat spectrum when $-0.5 < \alpha < 0$.

The steep spectrum, which is emitted by the lobes of radio galaxies, occurs because of the relative life times of electrons with different energies. The over all curvature then happens due to the fact that electrons radiate at frequencies proportional to their energies E, and the rate at which they lose energy is proportional E^2. Thus, the highest-energy electrons radiate away their energy the most rapidly [32].

The radio spectra of compact sources are usually flat probably due to opacity effects, in contrast to the steep spectra of extended sources. The features of compact sources spectra over several orders of magnitude in frequency is thus usually attributed to either sources inhomogeneity or the presence of unresolved small discrete sources with the compact core [32]. Synchrotron self-absorption occurs usually at very low frequencies when the compact radio source becomes opaque to its own radiation. This results in a steep ($\alpha = -\frac{5}{2}$) turn down in the radio spectrum at low frequency which depends on magnetic field and angular size of the source and produces a low frequency cut off of the spectrum (Figure 1.4).

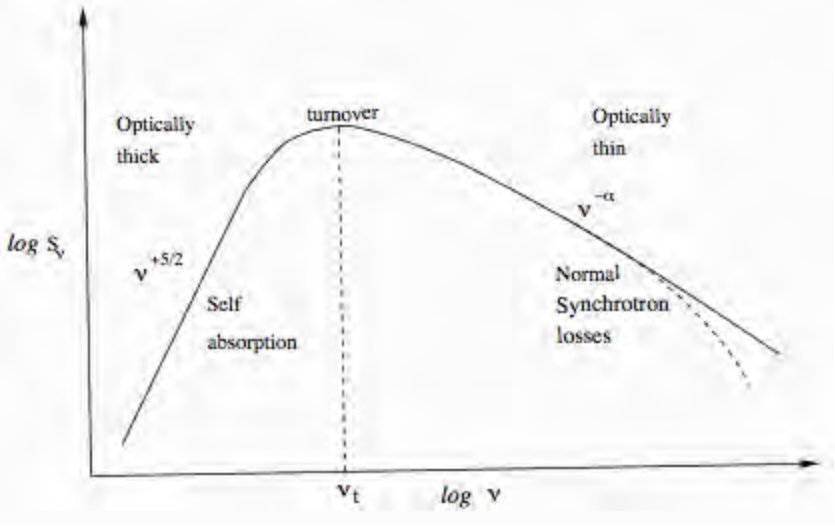

FIGURE 1.4: Illustration of synchrotron spectrum drawn without scale. At low frequencies, self-absorption occurs as a result of the source becoming optically thick. At higher frequencies, the power law shape dominates until synchrotron losses begin to dominate at still higher frequencies. The spectra of most compact sources are much flatter. As a result, there is slower fall-off frequency making compact sources more readily found in high-frequency survey [33].

In some sources, this turnover occurs at higher frequencies, up to several GHz. These are the Gigahertz-Peaked Sources (GPS). GPS sources have high luminosity of order of 10^{38} W and a steep spectrum at low frequencies, and it is believed their spectral turnover is due to synchrotron self absorption in a compact component with a large magnetic field. There are similarities between the GPS sources and another class of compact objects

called compact steep spectrum (CSS) sources in which the CSS sources are large versions of the GPS [33].

1.3.7 Variability Of AGNs

The flux density of extragalactic sources, particularly AGNs, changes remarkably in the time-scale ranging from minutes to years over the entire electromagnetic spectra. The variabilities are related to the intrinsic and extrinsic phenomenons.

The intrinsic one presumably results from the compactness of the AGNs. As the volume or the size of such sources are quite small, light takes short time to cross along the emitting volume or region. On one hand, the observed time scale of variation Δt has to satisfy the condition that $R \leq c\Delta t$, where R is the source size. On the other hand, as the galaxy recedes from the observer with redshift z, the time scale of the source, Δt_s, is related to the observer's time scale, Δt_o, by

$$\Delta t_s = \frac{\Delta t_o}{(1+z)}. \tag{1.40}$$

According to Ulrich et.al [34], the variability time scale is defined in relation to the source's flux density S and its instant change ΔS as:

$$\Delta t = \frac{S}{\Delta S} \frac{\Delta t_o}{\gamma[1 - \beta \cos\theta(1+z)]}, \tag{1.41}$$

where γ, β, and θ are as defined in Section 1.3.6.

Heeschen et al. [35] classified sources based on the time scale. According to the classification in the observer's frame, sources showing variability for $t \gg 50$ hours as long-term variable Type I, and $t < 50$ hours as short-term variable Type II sources.

The extrinsic variability is caused owing to the inhomogeneity of the Interstellar Medium (ISM) through which the radio waves are propagating. According to this assumption, a thin layer in the ISM potentially changes the phase of the incoming radio waves. Thus, there is refractive index perturbation that leads to the spatial variation of the flux density of the source. The occurrence of such a scattering phenomenon due to turbulent ionized ISM is known as Interstellar Scintillation (ISS) [36, 37].

The ISS is divided into weak and strong depending on the Fresnel scale given by

$$r_f = \sqrt{\frac{\lambda d}{2\pi}}, \tag{1.42}$$

where λ is the wavelength of the incoming wavelength and d is the distance between the thin layer (screen) to the observer. The diffraction scale depicts the transverse separation in which the phase fluctuations are coherent and constant within 1 rad. Thus, the diffraction scale is given by [37, 38]:

$$r_{dif} = \frac{\lambda d}{2\pi\theta_s}, \tag{1.43}$$

where θ_s is the angular size associated with the electron density that induces the scattering.

By comparing the Fresnel and diffraction scales given by Eq.(1.42) and Eq.(1.43), Weak Interstellar Scintillation (WISS) is designated when $r_{dif} \gg r_f$. Consequently, the timescale of WISS for the screen velocity, v_s, relative to the observer is $t_f = \frac{r_f}{v_s}$.

The Strong Interstellar Scintillation (SISS) happens when both scales are approximately the same. According to Walker [39], such a critical transition is observed in the frequency between 1 GHz and 5 GHz. As the sources considered in this thesis are observed at a frequency of 1.83 GHz, the SISS can be the possible reason for the rapid flux density variability.

The Refractive Interstellar Scintillation (RISS) is also among the causes for variability. If an element of plasma is assumed in the ISM, its refractive index of n has the form

$$n = \left[1 - \left(\frac{\nu_p}{\nu}\right)^2\right], \tag{1.44}$$

where ν is the observation frequency and ν_p is the plasma frequency. Equation (1.44) tells us that variability due to RISS becomes negligible as the observing frequency is higher. However, RISS is dominant at the observing frequency less than 1 GHz [39]. Accordingly, the sources considered in this thesis might not be highly affected by refractive interstellar scintillation as the survey carried out at a frequency greater than 1 GHz.

1.4 Motivation Of The Project

The KAT-7 telescopes are engineering precursors for the MeerKAT and ultimately for the Square Kilometre Array (SKA) projects. We have commenced the project aiming at calibrating the telescopes using well known radio sources. The properties of these sources were identified by several telescopes, such as VLA, Giant Metrewave Radio Telescope (GMRT), Australia Telescope Compact Array (ATCA), and others. Their properties were known at different operating frequencies, resolutions, baselines, and so on of the telescopes. By referring the known information about the sources by the arrays,

their properties will be studied using the KAT-7 array. The KAT-7 telescopes operate at the central frequency of about 1.83 GHz. So, by knowing the relevant parameters of the calibrator sources at this observing frequency, we can determine the complex gains (correction terms) incurred by instruments and atmospheres. In other words, we will compute the errors and then determine the actual properties of the sources at the observing frequency. As a result, we do contribute to the engineering verification. To this end, this project is of paramount importance. Moreover, the flux densities of the sources at $\nu = 1.83$ GHz are not available in the known catalogues, so this thesis will assist in filling the gap existed at this particular frequency.

The flux variability study is an indispensable criteria to identify convenient flux density calibrator candidates for the KAT-7. The less the variability of the source the more suitable it is for flux density calibration. Thus, the thesis will statistically examine the flux variabilities of the sources. Achieving this objective has an advantage in preparing flux calibrator candidates for compact interferometers with short spacings such as the KAT-7.

The work presented here does not look at the flux density stability of the instrument nor the long term stability of known radio sources. Some of these sources have already been done internally by the commissioning team of the KAT-7.

1.5 Thesis Layout

This thesis consists of five chapters. The layout of each is summarized below:

- Chapter 2: In this chapter, we present brief descriptions of the KAT-7 telescopes and their capacity as scientific instruments to explore extragalactic sources. Moreover, the properties of the target sources are discussed by reviewing different research papers and utilizing available catalogues. We study and summarize the characteristics of the sources before investigating them via the KAT-7

- Chapter 3: This chapter emphasises on the data reduction of the radio data collected from the KAT-7. We discuss in detail the step by step procedures of the data reduction processes together with the calibration formalisms to successfully extract the desired quantities. The positions measured by the KAT-7 for the selected target sources are compared with their known catalogue values. The stability and flux density accuracy of the KAT-7 is also checked in this chapter.

- Chapter 4: The statistical methods used for studying the flux variabilities of the sources are discussed in this chapter. We use different metrics to quantify the flux variability of each source. By using the metrics, we will distinguish which of the sources can be suitable calibrator candidates.

- Chapter 5: This chapter briefly presents the conclusion of this work and the recommendations for future work.

Chapter 2

The KAT-7 Array and Sample Observations

In this chapter we describe the Karoo Array Telescope (KAT-7) and present some of the specifications of the instrument. We discuss the selection process and present known parameters of each source in our sample. We also summarize the known properties of each source compiled from various catalogues and literatures.

2.1 The Karoo Array Telescope (KAT-7)

Seven radio telescopes, known as the Karoo Array Telescope (KAT-7)[1], were built in the Northern Cape province of South Africa, to serve as a precursor array. They are engineering prototypes for the next sensitive arrays, such as the MeerKAT and the Square Kilometre Array (SKA).

The geographical coordinates of the KAT-7 array are longitude $\sim 21.32°$ E and latitude $\sim 30.71°$ S. The baselines of the array span between 26 m and 185 m giving a synthesised beam of $\sim 4'$; the diameter of each telescope is 12 m giving a primary beam of $\sim 54'$ at 1.83 GHz. The main system specifications for the KAT-7 is presented in Table 2.1. More detailed information about the KAT-7 is also available at [40].

The receivers and their components for each telescope are cooled down to 70 Kelvin (-203 Celsius) so as to improve the sensitivity of the telescopes. The sensitivity describes the capability of a given radio telescope to detect the weakest (faint) radio emission; where the speed of a flux measurement is essentially associated with the sensitivity of the telescope.

[1] www.ska.ac.za/meerkat/kat7.php

Assuming the same sensitivity for all antennae involved in the observation, the minimum flux density detected in the entire system of N number of antennae is calculated as

$$\Delta S_{min} = \frac{2K_B}{\eta_a A} \frac{T_{sys}}{\sqrt{N(N-1)\Delta\nu t_{int}}}, \tag{2.1}$$

where $K_B = 1.38 \times 10^{-23}\mathtt{Jk}^{-1}$ is the Boltzmann constant, and t_{int} is the integration time. The other constants in Eq.(2.1) are listed in Table (2.1).

Substituting the required values in Eq.(2.1) from Table (2.1), the minimum flux density measured via the KAT-7 for an integration time of 100 s approximately becomes 1.5 mJy. Increasing the integration time will enhance the detection of faint sources.

TABLE 2.1: The main system specifications of the KAT-7.

Parameters	values
Dish diameter (D/m)	12
Dish Area (A/m^2)	110
Aperture efficiency (η_a)	0.66
Central frequency (ν/GHz)	1.83
Bandwidth ($\Delta\nu$/GHz)	0.25
Wavelength (λ/cm)	16.41
Minimum baseline ($b_{\mathtt{min}}$/m)	26
Maximum baseline ($b_{\mathtt{max}}$/m)	185
Polarization	Linear (H+V)
Longitude	21.321317°
Latitude	-30.706267°
System temperature (T_{sys}/K)	$\leq$ 35 across the entire frequency band ($\backsim$30 average) for all elevation angles
Synthesised resolution ($\theta_{\mathtt{res}}$)	$\sim 4'$
Primary beam (θ_{pb})	$\sim 54'$
Sky coverage (deg)	-80 to 50 (Dec) and 0 to 360 (RA)

2.2 Selection Of The Sources

Each source for this thesis was selected from various catalogues of potential calibrators that are likely to be good calibrator sources. The various known parameters characterizing each source (position, spectral index, redshift, type of source, and the flux density at 1.4 GHz) were collected from different catalogues. We used NASA Extragalactic Database (NED[2]), VizieR Service [3], Set of Identifications, Measurements, and Bibliography for Astronomical Data (SIMBAD[4]), NRAO VLA Sky Survey [41] (NVSS[5]) to

[2] ned.ipac.caltech.edu/
[3] vizier.u-strasbg.fr/viz-bin/VizieR
[4] simbad.u-strasbg.fr/simbad/
[5] www.cv.nrao.edu/nvss/NVSSPoint.shtml

extract the parameters.

The sample contains 48 sources, where the majority ($\sim$ 90%) reside over the southern sky. Classifying the sources according to their AGN group: about 46% are quasars, $\sim$ 50% are faint galaxies, and two sources are BL Lac object. About 41% of the sources showed flat spectra indices, about 43% and 8% of the sources revealed steep and inverted spectra, respectively. 4 sources ($\sim$ 8%) were found to be Giga Hertz Peak Spectrum (GPS).

Using Eq.(1.39), we extrapolated the flux density (S_{ν_2}) of the sources at the KAT-7 observing frequency (ν_2=1.83 GHz); where the reference flux density (S_{ν_1}) at ν_1 =1.4 GHz together with the spectral index α are obtained from NED, NVSS and SIMBAD catalogues. For each candidate source, we checked for other, nearby and possibly confusing sources which had flux densities $\geq$ 10% within 3° radius that of the candidate source, and rejected the candidate if any such confusing sources existed.

The spectral indices of 2 sources (i.e. PKS J0240-2309 and PKS J1924-2914) are not available in the catalogues. Thus, we used their flux densities at 1.4 GHz and 2.7 GHz recorded in the above catalogues as initial values to extrapolate their flux densities at 1.83 GHz. According to the extrapolated flux density values (Figure 2.3), $\sim$ 82% of the sources had $\leq$ 10 Jy; whereas $\sim$ 10% of the sources had flux densities between 10 Jy and 20 Jy. 3C123 is the strongest one among the sources with a flux density of about 39 Jy.

The expected flux density of a known flux-density calibrator, PKS J1939-6342 (J2000), at 1.83 GHz was in particular predicted from its polynomial relationship between flux density and frequency studied by Reynolds [42]. Thus, the polynomial relation based on measurements between 408 MHz and 8640 MHz is given by

$$\log_{10}(S) = -30.7667 + 26.4908x - 7.0977x^2 + 0.605334x^3, \tag{2.2}$$

where $x = \log_{10}(\nu)$ and ν is in MHz. The polynomial fitted with the data within 1 $\sim$ 2% error over the range 1-10 GHz [42, 43]. Hence, S = 13.59 Jy (i.e. possible error within 0.14 Jy (1%) $\sim$ 0.27 Jy (2%)) at our central frequency ν=1827 MHz.

The histograms [Figure (2.1, 2.2, 2.3)] illustrate the quantitative description of the sample in terms of their position in the sky, spectral index, flux density and redshift. The key results are summarized in Table 2.4 and 2.5.

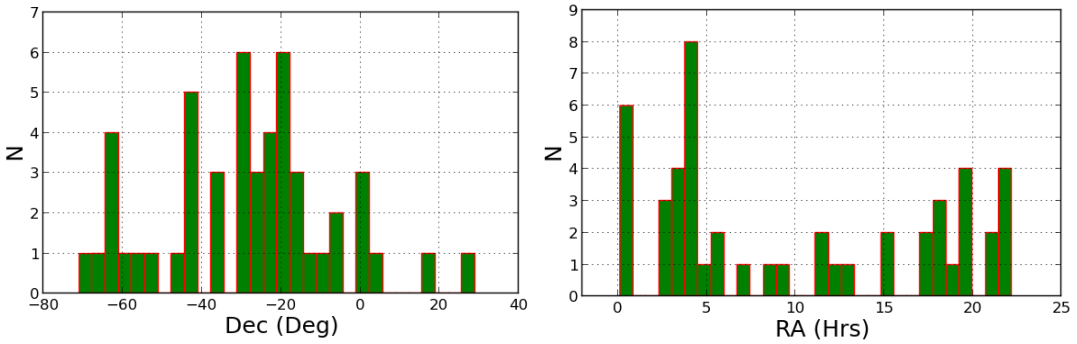

FIGURE 2.1: The number of sources (N) as a function of declination (`Dec`) and right ascension (`RA`). As can be seen from the left plot, majority of the sources are located in the southern sky ($0 < \texttt{Dec} < -80°$)

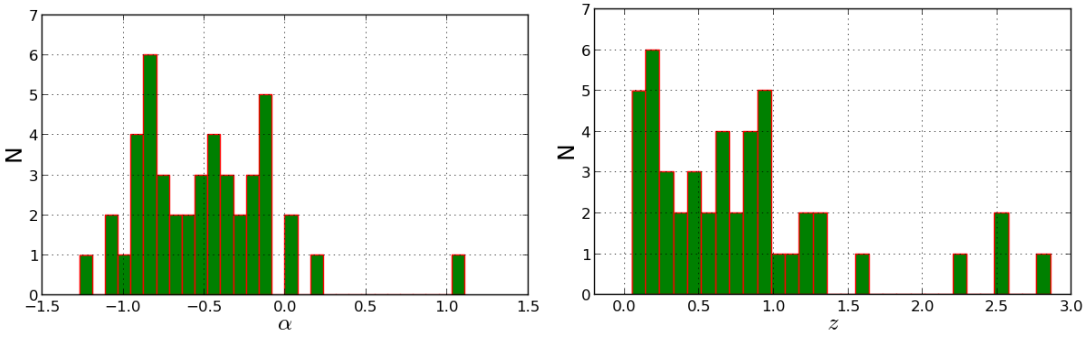

FIGURE 2.2: The left and right side histograms show the number of sources as a function of spectral index and redshift, respectively. The sample sources comprise of flat spectrum ($-0.5 < \alpha < 0$), steep spectrum $\alpha < -0.5$, and inverted spectrum $\alpha > 0$. Majority ($\sim 76\%$) of the selected sources are located at redshift $0 < z \leq 1$.

2.3 Observations Of The Sample Sources

The potential calibrator sources studied in this thesis were observed between Oct 13, 2012 and February 23, 2013 during the commissioning phase of the KAT-7 . All observations were performed in the continuum mode with two linear polarizations over a 0.25 GHz bandwidth centred at 1.83 GHz. Initially, 3 minutes and 5 minutes scans were made on each flux-density and phase calibrator, respectively; the process was repeated every one hour. The summary about the observations are presented in Table 2.2.

We only consider the datasets that contain flux-density calibrator, PKS J1939-6342, in order to flux calibrate the sources using a single calibrator for consistency. As we discussed in Section 1.3.3, 3C286, 3C138, 3C147, and 3C48 are potential flux-density calibrators. We did not utilize any of them as flux-density calibrators due to the fact that they were rarely observed, unlike PKS J1939-6342, in the selected observation runs

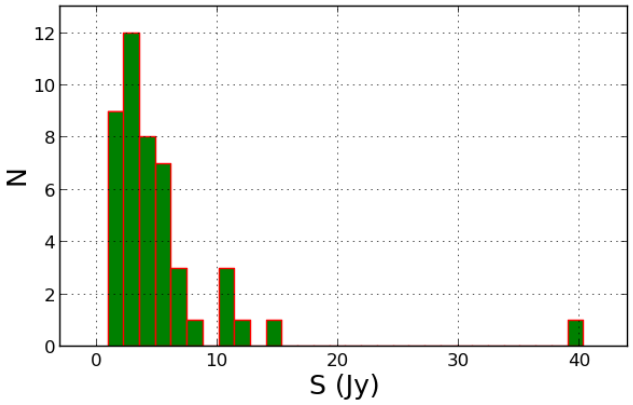

FIGURE 2.3: The number of sources as a function of expected flux density at 1.83 GHz, where $\sim 82\%$ of the sources have flux densities between 1 Jy and 10 Jy.

(datasets). However, we used 3C286, 3C147, and 3C48 to check the stability and flux-density accuracy of the KAT-7 by flux calibrating them with respect to PKS J1939-6342; for more explanation, refer Section 3.8.

Though the sources in our sample are known potential phase calibrators, we selected specific sources that would be utilized to phase calibrate target sources depending on coherently assessed requirements. The requirements are presented in Chapter 3 under Section 3.2. The sources that will be employed as phase calibrators in each dataset are listed in Table 2.2. The selected phase calibrators with their corresponding target sources are also presented in Table 2.3. The flux densities of the selected phase calibrators and their respective target sources will be estimated relative to PKS J1939-6342. However, the positions of the target sources will be derived with respect to the phase calibrators for reliability check.

The observations were carried out on the antennas that were functioning in full mode. On average 6 out of the 7 antennae were available in 8 of the observations, and only one observation was carried out with 5 antennae.

TABLE 2.2: The table illustrates observation dates (i.e. the equivalent Julian dates are calculated by taking the average of the starting to the final observation times in each observation), and the total number of observed sources, the number of sources used as target sources in our analysis, the total observation time, the flux calibrator, the selected phase calibrators to calibrate the target sources, and the number of well functioned antennas during observation.

Observation Date (dd/mm/yy)	Equivalent Julian Dates (JD)	Number of Observed Sources	Total Integration time (sec)	Flux Calibrator	Selected Phase Calibrators	Number of antennas
13-14/10/12	2456214.391	13	10765.5	PKS J1934-6342	PKS J0022+0014, PKS J0025-2602, PKS J0240-2309, PKS J0252-7104	7
14-15/10/12	2456215.435	36	31225.4	PKS J1939-6342	PKS J0025-2602, PKS J0022+0014, PKS J0240-2309, PKS J0252-7104, PKS J0318+1628, PKS J0440-4333, 3C123, PKS J0744-0629	7
15/10/12	2456216.127	28	25855.9	PKS J1939-6342	PKS J0025-2602, PKS J0252-7104, PKS J1833-2103, PKS J1941-1524	7
27/10/12	2456228.540	40	36935.9	PKS J1939-6342; 3C147 and 3C48 for checking purpose	PKS J0022+0014, PKS J0025-2602, PKS J0240-2309, PKS J0252-7104, PKS J0318+1628, PKS J0440-4333, PKS J0744-0629, PKS J1154-3505	6
7-8/11/12	2456238.429	65	45600.6	PKS J1939-6342; 3C147 and 3C48 for checking purpose	PKS J0022+0014, PKS J0025-2602, PKS J0240-2309, PKS J0252-7104, PKS J0318+1628, PKS J0440-4333, PKS J0744-0629, PKS J1154-3505, PKS J1833-2103, PKS J1941-1524, PKS J2206-1835	5
14-15/11/12	2456246.260	38	36143.9	PKS J1939-6342	PKS J0022+0014, PKS J0025-2602, PKS J0240-2309,PKS J0252-7104, PKS J0318+1628, PKS J0440-4333, 3C123, PKS J0744-0629, PKS J1154-3505	6
05/02/13	2456329.366	11	9919.9	PKS J1939-6342; 3C147 and 3C48 for checking purpose	PKSJ0252-7104	6
11/02/13	2456334.700	20	18715.3	PKS J1939-6342; 3C286 for checking purpose	PKS J0252-7104, PKS J1154-3505, PKS J1510-0543	6
16/02/13	2456339.868	31	28730.4	PKS J1939-6342	PKS J0025-2602, PKS J0022+0014, PKS J0240-2309, PKS J0252-7104, PKS J0318+1628, PKS J0440-4333, 3C123, PKS J0744-0629	6
23/02/13	2456347.126	23	21750.3	PKS J1934-6342	PKS J0022-2602, PKS J0025-2602, PKS J0240-2309, PKS J0252-7104, PKS J318+1628, 3C123	7

TABLE 2.3: The selected phase calibrators (sources that would be employed to phase calibrate the target sources) and the respective target sources in the data reduction process are shown in the table.

Group Number	Phase Calibrators	Target Sources
1	PKS J0022+0014	PKS J0059+006
2	PKS J0025-2602	PKS J0010-4153 PKS J0042-4414 PKS J0044-3530
3	PKS J0240-2309	PKS J0351-2744 PKS J0405-1308 PKS J0409-1757
4	PKS J0252-7104	PKS J0303-6211 PKS J0309-6058 PKS J0408-6544 PKS J0420-6223
5	PKS J0318+1628	PKS J0442-0017 PKS J0323+0534
6	3C123 (J0437+2940)	PKS J0318+1628
7	PKS J0440-4333	PKS J0444-2809 PKS J0453-2807 PKS J0538-4405
8	PKS J0744-0629	PKS J0837-1951 PKS J0943-0819
9	PKS J1154-3505	PKS J1130-1449 PKS J1248-1959 PKS J1311-2216
10	PKS J1510-0543	PKS J1517-2422
11	PKS J1833-2103	PMN J1712-2809 PKS J1830-3602
12	PKS J1941-1524	PKS J1924-2914
13	PKS J1819-6345	PKS J1744-5144 PKS J1935-4620
14	PKS J2206-1835	PKS J2129-1821 PKS J2131-2036 PKS J2151-3027 PKS J2152-2828 PKS J2219-2756

2.4 Known Properties Of The Sources

This section summarizes what is already known about the sources from various published literatures. The summary assists the selection process to decide which of the sources should be used as phase calibrators and target sources during the data reduction routine. Moreover, it plays a crucial role when we compare the flux variability of each source obtained from this thesis against the previously published results. All flux density time series plots shown below have directly been copied from the ATCA calibrator database website [44] except for 3C123.

- **3C286** - is a compact steep-spectrum quasar at redshift z=0.846. According to its VLA image, a small emission structure is revealed at a resolution of about 2.5″ [45]. It has been used as a flux density calibrator in most interferometers because of showing less than 1% variability at various frequencies studied over 30 years by Perley et al. [17].

- **3C48** - is a compact steep-spectrum quasar at redshift z=0.367. It has compact structure, where it shows small components at a resolution of about 1.2″. The flux variability of this source has been conducted over 30 years, where the result indicated its flux density variability. For instance, the flux variabilities at frequencies of [1.465, 4.885, and 43.340] GHz are approximately 1.5%, 2.3%, and 11%, respectively [17].

- **3C147** - is a compact steep-spectrum quasar at redshift z=0.545. Observations made on this source at [1.6, 5, 8.4, 15, 22.5] GHz with a resolution $\sim$ 0.1″ [46]

showed that it has a weak, extended component to the north and a stronger and more compact structure to the south. The variability study performed by Perley et al. [17] asserted that it has varied approximately by 1.2%, 1.9%, and 13.6% at frequencies [1.465, 4.885, and 43.340] GHz, respectively. This source has been used by VLA collaboration as a flux density scale calibrator because of its small angular size and high spectral flux density.

- **PKS J1939-6342** - is identified as a radio source at redshift z=0.185. It has been used as a flux calibrator by ATCA because of its stable flux density and compact structure [47]. The data available by Australia Telescope National Facility (ATNF[6]) show that the flux density of PKS J1939-6342 has varied by less than $\sim 2\%$ and $\sim 0.4\%$ within 10 years (2000-2010) at frequencies 1384 MHz and 1757 MHz, respectively. In addition to this, Figure 2.4 reveals the source's constant flux density with time. For example, the thirteen flux densities measured between 2006 and 2014 at 2100 MHz had almost equal magnitudes of $\sim$ 12.6 Jy. Similarly, more than 40 flux density measurements taken between 2007 and 2014 at 5500 MHz exhibited almost the same magnitudes of $\sim$ 5.0 Jy. Therefore, utilizing PKS J1939-6342 as a flux density calibrator (standard) to determine the flux density of other sources is justifiable.

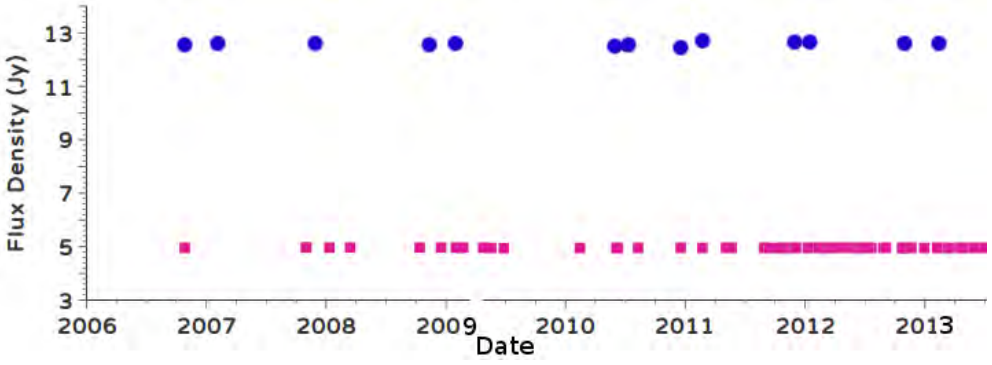

FIGURE 2.4: The flux density versus time plot PKS J1939-6342 from ATCA database [44] at frequencies of 2100 MHz (blue points) and 5500 MHz (light magenta points).

- **PKS J0010-4153** - is a compact steep-spectrum radio galaxy at redshift z=1.120 [48]. According to VLBI observation, it is resolved at 0.2″. Moreover, the optical spectrum of this source is so faint and very noisy that it is difficult to distinguish emission lines from noise [49]. The flux density data by ATNF showed that its flux density changed by $\sim 2\%$ within 4 years and $\sim 6\%$ within 9 years at 1384 MHz and 2368 MHz, respectively. Additionally, Figure 2.5 tells us that its flux density decreased from $\sim$ 3.8 Jy in 2009 to $\sim$ 3.2 Jy in 2011 at 2100 MHz; however, the

[6] www.atnf.csiro.au/

five flux density measurements taken at 5500 MHz between 2009 and 2012 had equal magnitudes of $\sim$ 1.1 Jy.

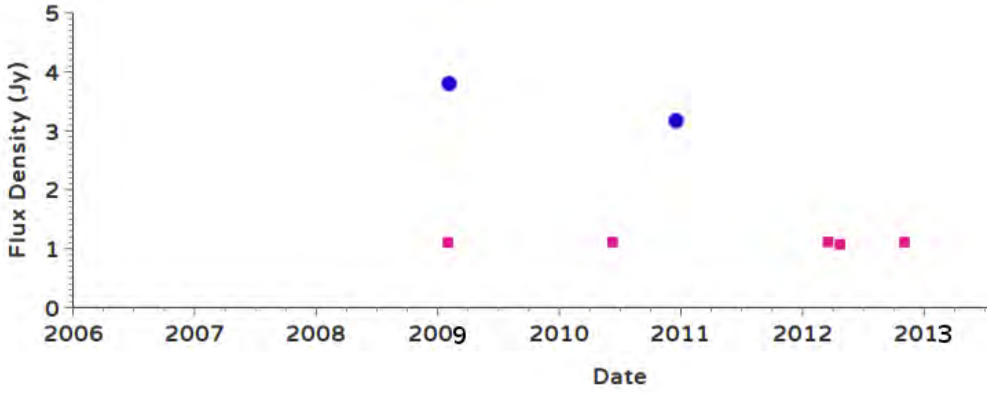

FIGURE 2.5: The flux density versus time plot PKS J0010-4153 from ATCA database [44] at frequencies of 2100 MHz (blue points) and 5500 MHz (light magenta points).

- **PKS J0022+0014** - is a compact flat-spectrum radio quasar at redshift z=0.305 [50]. At a frequency of 2100 MHz, only one flux density measurement (i.e. $\sim$ 2.2 Jy) was made at the end of 2010; the four flux density measurements taken between 2011 and 2013 were nearly equal to $\sim$ 1.1 Jy at 5500 MHz; see Figure 2.6.

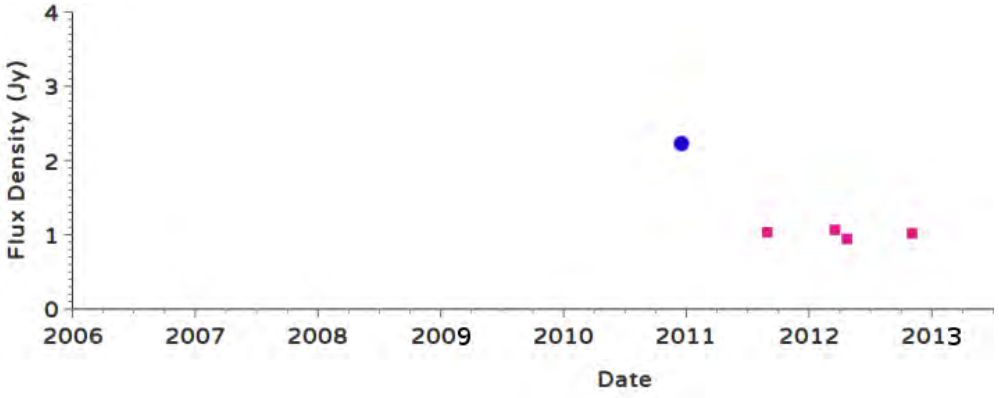

FIGURE 2.6: The flux density versus time plot PKS J0022+0014 from ATCA database [44] at frequencies of 2100 MHz (blue points) and 5500 MHz (light magenta points).

- **PKS J0025-2602** - is a flat-spectrum radio source at redshift z=0.332. It is also known as a Compact Steep Spectrum (CSS) as its radio spectrum peaks at a frequency lower than 500 MHz [51]. As noted from Figure 2.7, the three flux densities measured in 2009, 2011, and 2013 at 2100 MHz had almost the same magnitudes of $\sim$ 6.8 Jy. Similarly, the five flux density measurements taken between 2009 and 2014 at 5500 MHz were nearly the same, and each one had a magnitude of $\sim$ 3.3 Jy; however, one flux density measurement in 2010 was slightly smaller than the others, having $\sim$ 3.0 Jy.

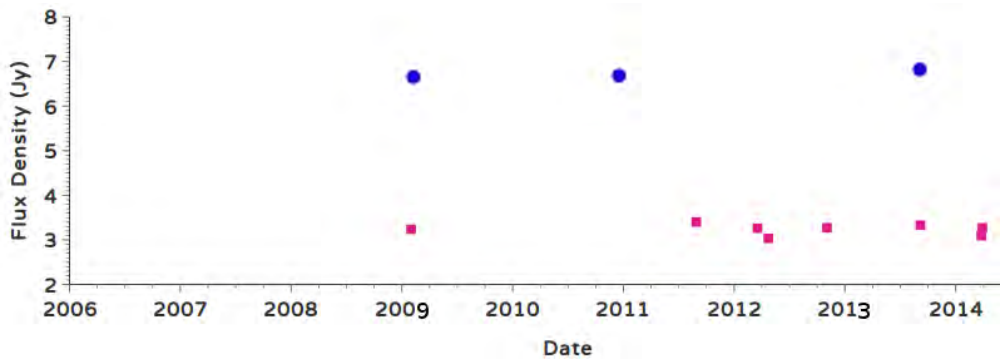

FIGURE 2.7: The flux density versus time plot PKS J0025-2602 from ATCA database [44] at frequencies of 2100 MHz (blue points) and 5500 MHz (light magenta points).

- **PKS J0042-4414** - is a small steep-spectrum radio source at redshift z=0.346. It has two lobes dominating its emission. However, core or jets have not been detected in the images. Both Lobes are polarized with the eastern side showing higher fractional polarization compared to the western side [52]. Its flux density measured at 2100 MHz decreased from $\sim$ 1.6 Jy in 2009 to $\sim$ 1.2 Jy at the end of 2010. The two flux densities measured at 5500 MHz between 2009 and 2012 had nearly equal magnitudes of $\sim$ 0.4 Jy; the three flux density measurements between 2012 and 2013 had almost equal magnitudes of $\sim$ 0.3 Jy, which showed decrement from the former values.

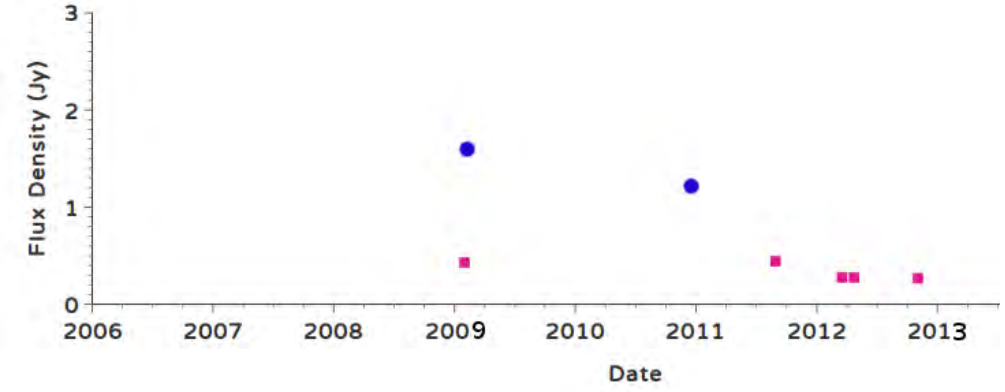

FIGURE 2.8: The flux density versus time plot PKS J0042-4414 from ATCA database [44] at frequencies of 2100 MHz (blue points) and 5500 MHz (light magenta points).

- **PKS J0044-3530** - is identified as a radio galaxy having steep-spectrum at redshift z=0.980. The two flux densities at 2100 MHz of this source (see Figure 2.9) showed slight difference, increasing from $\sim$ 1.6 Jy in 2009 to $\sim$ 1.9 Jy in 2011. However, its flux densities measured between 2009 and 2013 at 5500 MHz were nearly uniform, each having a magnitude of $\sim$ 0.85 Jy.

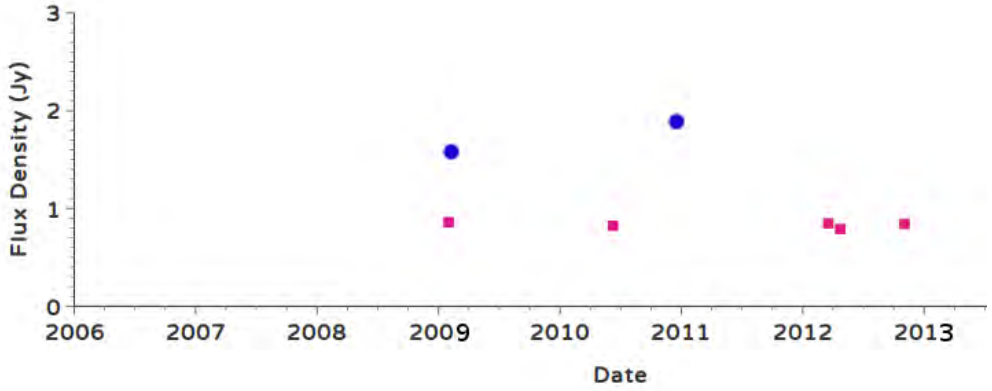

FIGURE 2.9: The flux density versus time plot PKS J0044-3530 from ATCA database [44] at frequencies of 2100 MHz (blue points) and 5500 MHz (light magenta points).

- **PKS J0059+006** - is categorized as a flat-spectrum quasar at redshift z=0.719. According to the VLBA observation at 4.8GHz [53], the source displayed a compact core with jet emission extending beyond 20 mas from the core. According to the ATCA Monitoring Observations of 202 Compact Radio Sources at 16 epochs between 1996 October and 2000 February by Tingay et al. [54], the variability indices [7] of this source at 1.4 GHz, 2.5 GHz, 4.8 GHz, and 8.6 GHz are 2.0%, 4.0%, 8.0%, and 12 %, respectively. Figure 2.10 indicated that its flux density slightly decreased from $\sim$ 2.2 Jy in 2009 to $\sim$ 2.1 Jy in 2011 at 2100 MHz. The five flux densities measured at 5500 MHz between 2009 and 2013 were nearly the same, each equivalent to $\sim$ 1.5 Jy.

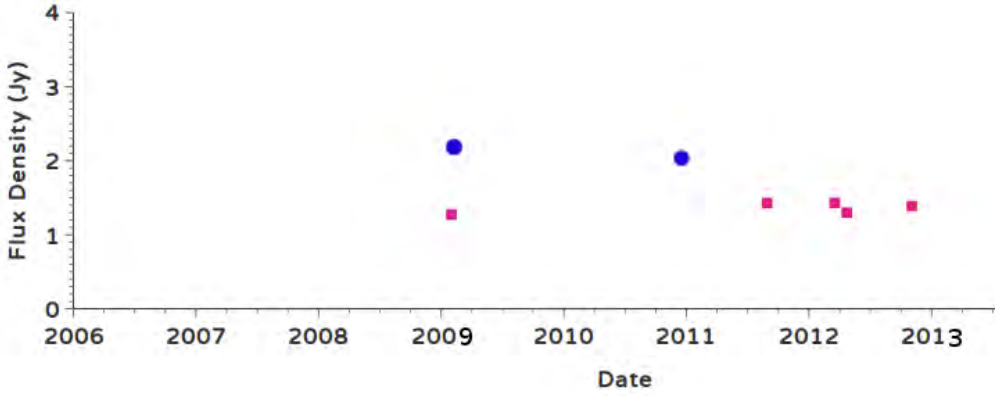

FIGURE 2.10: The flux density versus time plot PKS J0059+006 from ATCA database [44] at frequencies of 2100 MHz (blue points) and 5500 MHz (light magenta points).

- **PKS J0240-2309** - is identified as a quasar at redshift z= 2.223. It is a GPS with a peak around 1.4 GHz. According to VLBI imaging, it exhibits a core-jet

[7] The variability index in the Tingay et al. [54] paper is defined as the Root Mean Square (RMS) variation from the mean flux density, divided by the mean flux density. We also define the same quantity with different name (i.e. we call it modulation index) in Chapter 4 of this thesis.

structure with a compact core dominated at 2 and 5 GHz [53]. According to the ATCA Monitoring Observations of 202 Compact Radio Sources at 16 epochs between 1996 October and 2000 February by Tingay et al. [54], the variability indices of this source at 1.4 GHz, 2.5 GHz, 4.8 GHz, and 8.6 GHz are 1.0%, 2.0%, 3.0%, and 5.0%, respectively. As noted from Figure 2.11, the three flux density measurements at 2100 MHz between 2009 and 2013 had nearly equal magnitudes of $\sim$ 5.1 Jy. The five flux densities measured at 5500 MHz between 2009 and 2013 showed very small fluctuations, having a minimum of $\sim$ 2.1 Jy in 2009 and a maximum of $\sim$ 2.6 Jy in 2011.

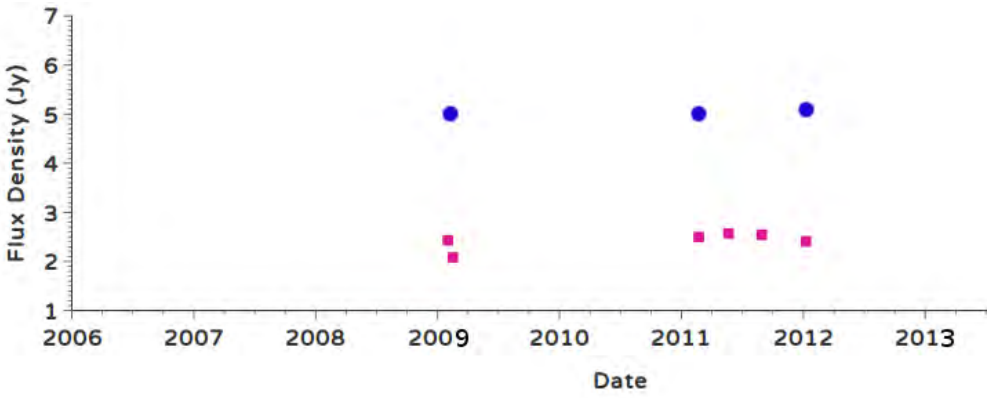

FIGURE 2.11: The flux density versus time plot PKS J0240-2309 from ATCA database [44] at frequencies of 2100 MHz (blue points) and 5500 MHz (light magenta points).

- **PKS J0252-7104** - is a compact steep-spectrum radio source at redshift z=0.563 [55]. As shown in Figure 2.11, two flux density measurements at 2100 MHz in 2009 and 2011 were found to be almost equal with a magnitude of $\sim$ 4.0 Jy. Similarly, the five flux densities measured at 5500 MHz between 2009 and 2012 had almost equal magnitudes of $\sim$ 1.5 Jy.

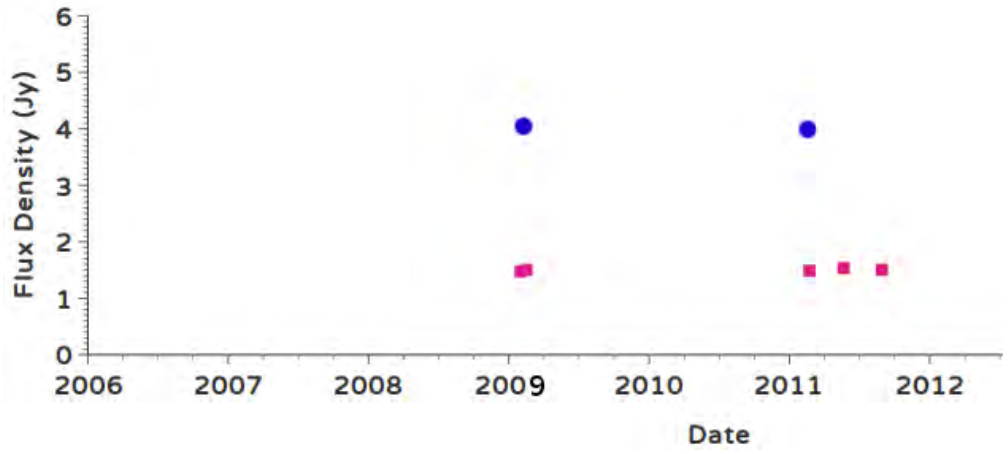

FIGURE 2.12: The flux density versus time plot PKS J0252-7104 from ATCA database [44] at frequencies of 2100 MHz (blue points) and 5500 MHz (light magenta points).

- **PKS J0303-6211** - is a flat-spectra quasar at redshift z= 1.351. According to the ATCA Monitoring Observations of 202 Compact Radio Sources by Tingay et al. [54], the variability indices of this source at 1.4 GHz, 2.5 GHz, 4.8 GHz, and 8.6 GHz are 4.0%, 4.0 %, 2.0 %, and 2.0%, respectively. As noted from Figure 2.13, the flux density of the source increased from $\sim$ 2.8 Jy in 2009 to $\sim$ 3.5 Jy in 2011 at 2100 MHz. Twenty two flux densities were measured between 2009 and 2014 at 5500 MHz, where maximum and minimum flux densities of $\sim$ 2.4 Jy and $\sim$ 1.8 Jy were recorded in 2009 and 2013, respectively.

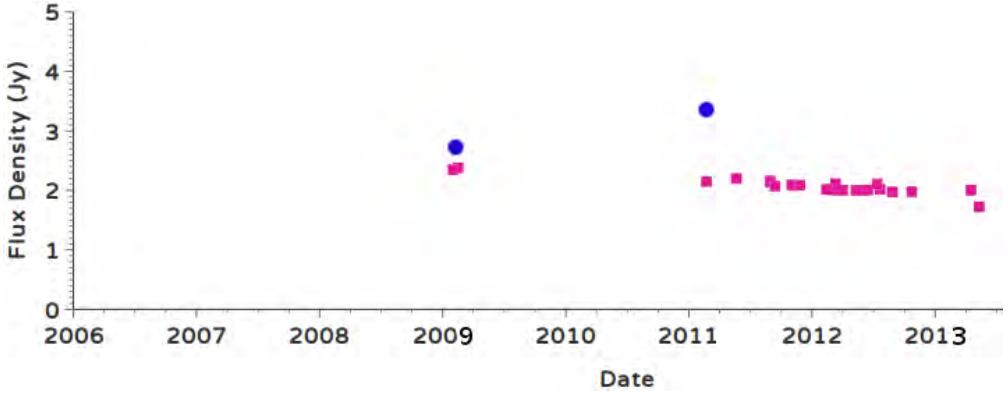

FIGURE 2.13: The flux density versus time plot PKS J0303-6211 from ATCA database [44] at frequencies of 2100 MHz (blue points) and 5500 MHz (light magenta points).

PKS J0309-6059- is a flat-spectra quasar at redshift z= 0.480. According to the ATCA Monitoring Observations of 202 Compact Radio Sources at 16 epochs between 1996 October and 2000 February by Tingay et al. [54], the variability indices of this source at 1.4 GHz, 2.5 GHz, 4.8 GHz, and 8.6 GHz are 6.0%, 9.0%, 8.0%, and 5.0%, respectively. As can be seen from the ATCA database plot shown

in Figure 2.14, two flux density measurements at 2100 MHz in 2009 and 2011 were nearly equal with a magnitude of $\sim$ 1.1 Jy. Nineteen flux densities were measured between 2009 and 2014 at 5500 MHz, where maximum and minimum flux densities of $\sim$ 1.6 Jy and $\sim$ 1.4 Jy were recorded in 2009 and 2013, respectively.

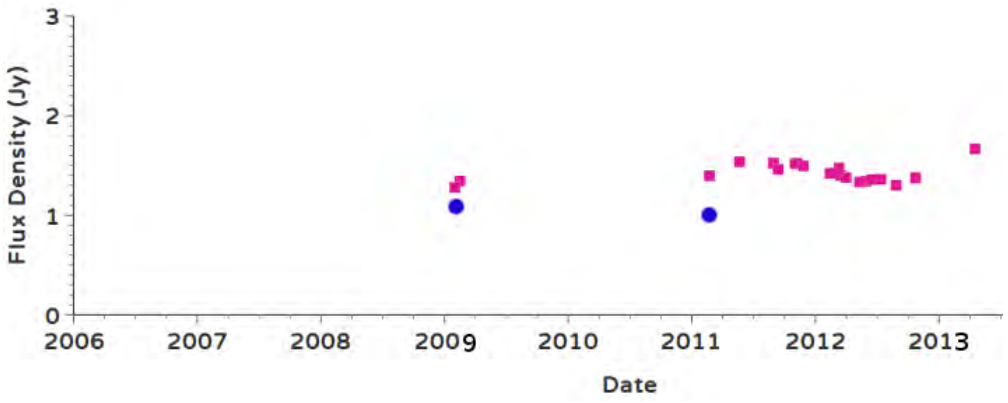

FIGURE 2.14: The flux density versus time plot PKS J0309-6059 from ATCA database [44] at frequencies of 2100 MHz (blue points) and 5500 MHz (light magenta points).

- **PKS J0318+1628** - identified as a quasar at redshift z=0.907. It exhibits either flat or inverted spectrum at low frequency and steep spectrum at frequencies greater than 1 GHz [56].
- **PKS J0323+0534** - is classified as a radio galaxy under the category of GPS at redshift z=0.178. According to VBLA's observation at 1.6 GHz [57], the source shows a strong diffusive component and a weak extended component in the South. Four flux density measurements between 2011 and 2014 were nearly identical, each having $\sim$ 0.8 Jy at 5500 MHz.

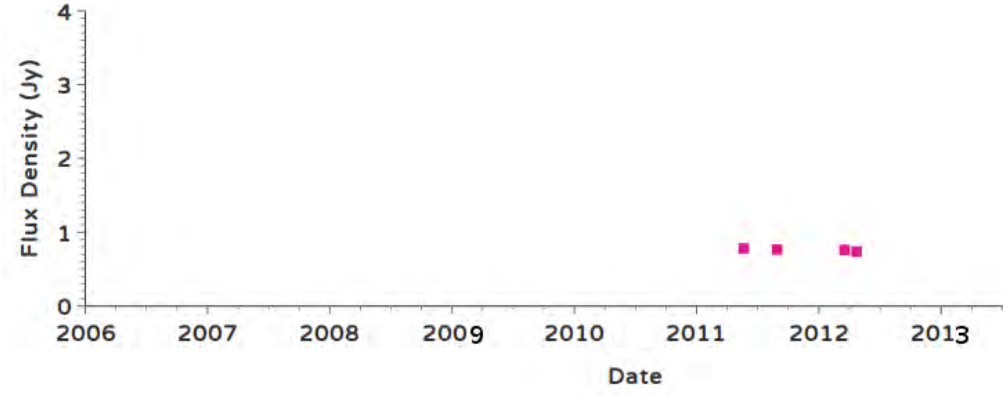

FIGURE 2.15: The flux density versus time plot PKS J0323+0534 from ATCA database [44] at frequency of 5500 MHz (light magenta points).

- **PKS J0351-2744** - is a FR II radio galaxy with steep-spectrum at redshift z=0.065. It is also known for its brightness in a dense region with an elongated structure [58]. Its elongated structure is also seen in the 1.4 GHz NVSS image. Refer figure 3.6 to look at its NVSS image.

- **PKS J0405-1308**: It is a quasar with steep-spectrum at redshift z= 0.570 and has a very compact core. It exhibits a faint jet emission stretching to the south-east [53]. According to the ATCA Monitoring Observations of 202 Compact Radio Sources at 16 epochs between 1996 October and 2000 February by Tingay et al. [54], the variability indices of this source at 1.4 GHz, 2.5 GHz, 4.8 GHz, and 8.6 GHz are 1.0%, 3.0%, 5.0%, and 15%, respectively. As can be seen from Figure 2.16, its flux density of $\sim$ 3.6 Jy in 2009 decreased to $\sim$ 3.3 Jy in 2011 at 2100 MHz. At 5500 MHz, three flux densities were measured between 2009 and 2012; of which two of them had almost the same magnitudes of $\sim$ 2.7 Jy, whereas the third one was slenderly lower than the two having a magnitude of $\sim$ 2.5 Jy.

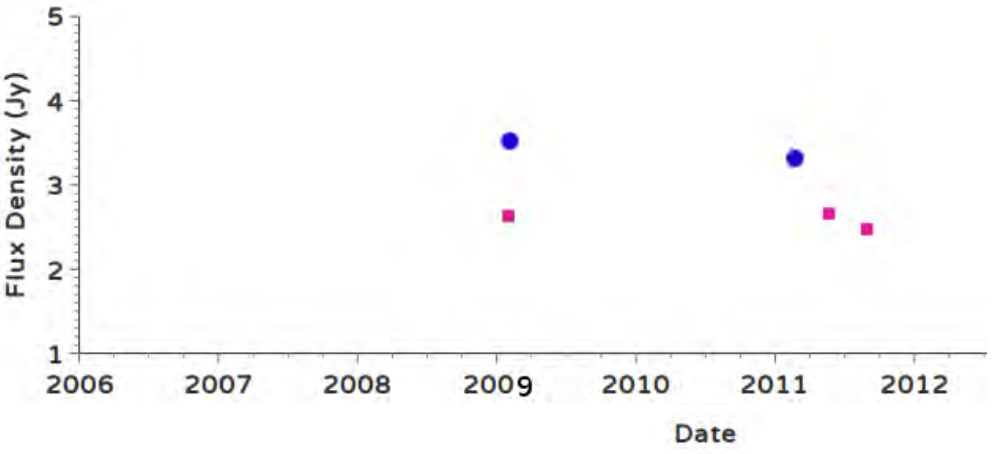

FIGURE 2.16: The flux density versus time plot PKS J0405-1308 from ATCA database [44] at frequencies of 2100 MHz (blue points) and 5500 MHz (light magenta points).

- **PKS J0409-1757** - is a steep-spectrum quasar at redshift z=0.722. According to the ATCA calibrator database (Figure 2.17), its flux densities in 2009 and 2011 were identical, each having $\sim$ 1.6 Jy at 2100 MHz. Besides, its flux densities displayed nearly equal magnitudes of 0.7 Jy in 2009, 2011, and 2012 at 5500 MHz.

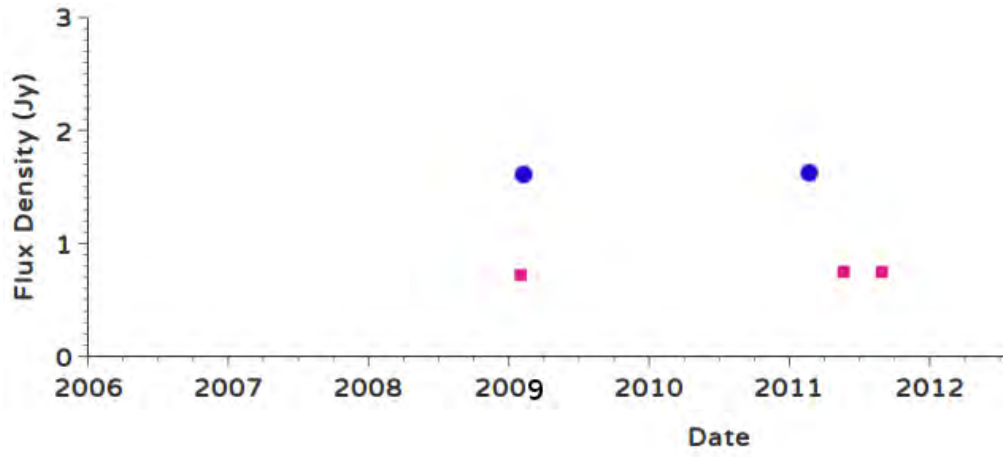

FIGURE 2.17: The flux density versus time plot PKS J0409-1757 from ATCA database [44] at frequencies of 2100 MHz (blue points) and 5500 MHz (light magenta points).

- **PKS J0408-6544** - is a steep-spectrum quasar at redshift z=0.962. According to the ATCA database plot shown in Figure 2.18, the three flux densities measured at 2100 MHz between 2007 and 2012 were nearly the same, each having a magnitude of $\sim$ 9.6 Jy. Additionally, the three flux densities measured at 5500 MHz between 2009 and 2012 were almost equal with a magnitude of $\sim$ 2.7 Jy.

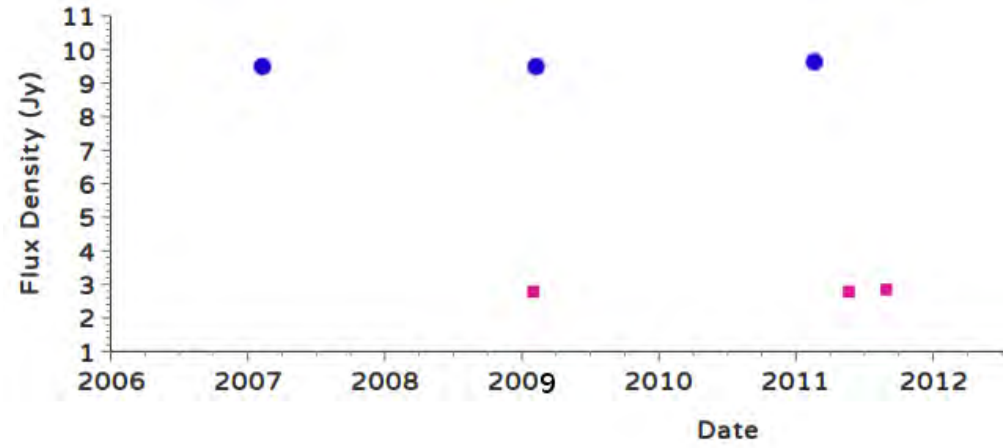

FIGURE 2.18: The flux density versus time plot PKS J0408-6544 from ATCA database [44] at frequencies of 2100 MHz (blue points) and 5500 MHz (light magenta points).

- **PKS J0420-6223** - is a steep-spectrum radio galaxy at redshift z=0.81. The three flux densities measured at 2100 MHz between 2007 and 2012 had almost the same magnitudes of $\sim$ 2.2 Jy as shown in Figure 2.19. Likewise, the three flux densities measured at 5500 MHz between 2009 and 2012 were almost invariable, each having $\sim$ 1.9 Jy.

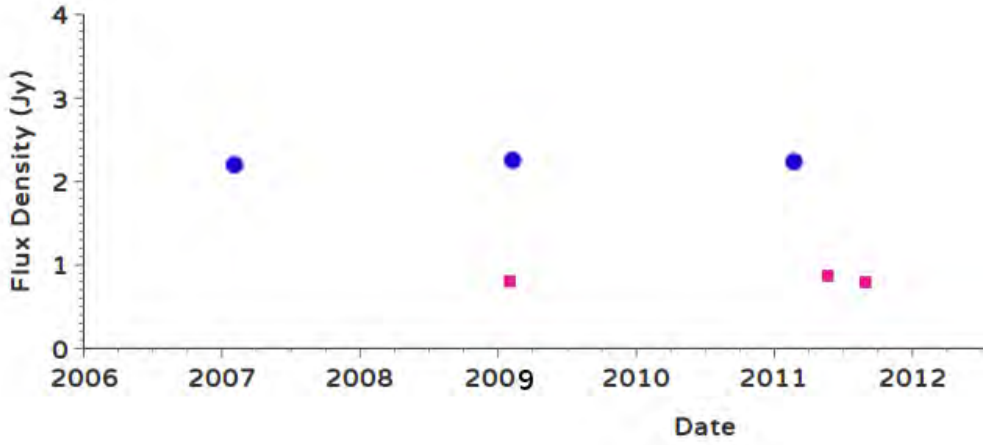

FIGURE 2.19: The flux density versus time plot PKS J0420-6223 from ATCA database [44] at frequencies of 2100 MHz (blue points) and 5500 MHz (light magenta points).

- **PKS J0440-4333** - is an extremely luminous quasar at redshift z= 2.863. Its radio spectrum is complex in that it has a flat-spectrum at low frequency while very steep-spectrum above 5GHz. VLBI observations of the source at 2.3 GHz have revealed a core-jet structure. According to the ATCA Monitoring Observations of 202 Compact Radio Sources at 16 epochs between 1996 October and 2000 February by Tingay et al. [54], the variability indices of this source at 1.4 GHz, 2.5 GHz, 4.8 GHz, and 8.6 GHz are 2.0%, 5.0%, 10.0%, and 10.0%, respectively. As shown in Figure 2.20, its flux density of $\sim$ 3.9 Jy in 2009 slightly decreased to $\sim$ 3.3 Jy in 2012 at 2100 MHz. The five flux densities measured at 5500 MHz between 2011 and 2013 had nearly equal magnitudes of $\sim$ 1.9 Jy; but the flux measured in 2009 had $\sim$ 2.5 Jy, which was slightly higher.

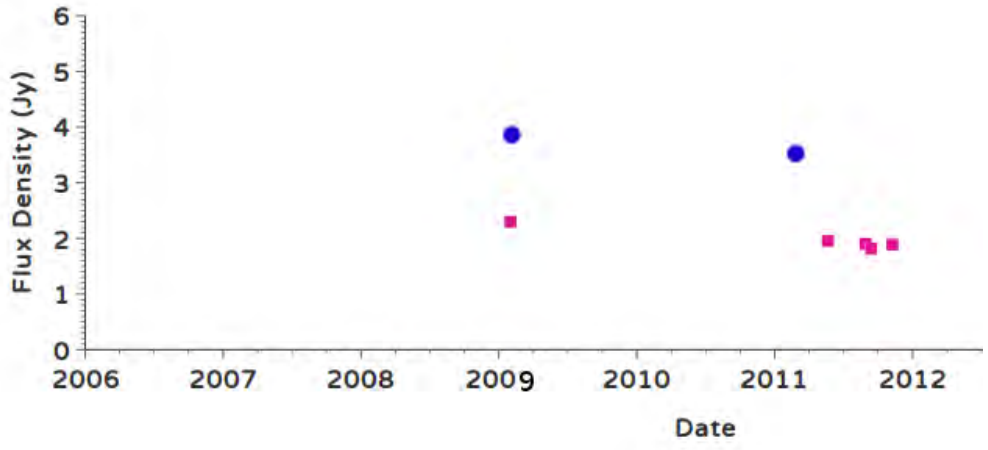

FIGURE 2.20: The flux density versus time plot PKS J0440-4333 from ATCA database [44] at frequencies of 2100 MHz (blue points) and 5500 MHz (light magenta points).

- **PKS J0442-0017** - is a flat-spectrum quasar at redshift z= 0.844, and its spectrum peaks at 2 GHz [59]. According to the ATCA Monitoring Observations of 202 Compact Radio Sources at 16 epochs between 1996 October and 2000 February by Tingay et al. [54], the variability indices of this source at 1.4 GHz, 2.5 GHz, 4.8 GHz, and 8.6 GHz are 9.0%, 11.0%, 10.0%, and 11.0%, respectively. As shown in Figure 2.21, its flux density $\sim$ 2.7 Jy in 2009 slightly decreased to $\sim$ 2.4 Jy in 2011 at 2100 MHz. The three flux densities measured at 5500 MHz fluctuated between $\sim$ 2.4 Jy in 2009 and $\sim$ 2.9 Jy in 2011.

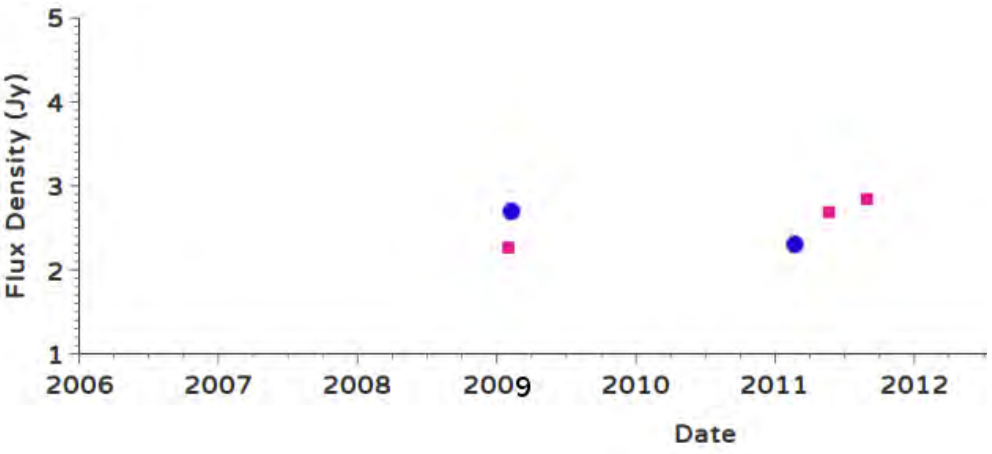

FIGURE 2.21: The flux density versus time plot PKS J0442-0017 from ATCA database [44] at frequencies of 2100 MHz (blue points) and 5500 MHz (light magenta points).

- **PKS J0444-2809** - is a steep-spectrum FRII radio source at redshift z=0.147. Its radio lobes have complex morphology. Moreover, it has a core without having radio jets [60].

- **3C123** - is a radio galaxy at redshift z=0.218. It has an extended structure on arcsecond scale, and it is not preferable to use it as a calibrator for high-resolution interferometry. This structure is revealed in wide frequency intervals that range from 25 MHz to 98 GHz [61]. It is mostly used as a calibrator at low frequencies. The variability study on this source (see Figure 2.22) by Perley et al. [17] over 30 showed that it has approximately varied by less than 1.0 % at frequencies 1.465 GHz and 4.885 GHz.

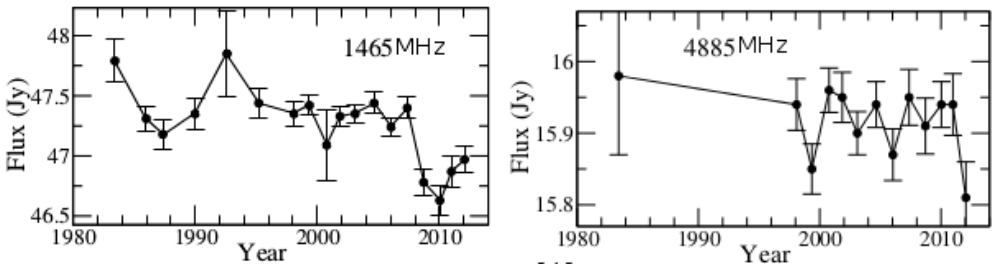

FIGURE 2.22: The flux density versus time plot for 3C123 at frequencies 1465 MHz (left) and 4885 MHz (right). Taken from [17].

- **PKS J0453-2807** - is a flat-spectrum quasar at redshift z=2.559. It has a jet structure [62]. According to the ATCA Monitoring Observations of 202 Compact Radio Sources at 16 epochs between 1996 October and 2000 February by Tingay et al. [54], the variability indices of this source at 1.4 GHz, 2.5 GHz, 4.8 GHz, and 8.6 GHz are 2.0%, 3.0%, 5.0%, and 9.0%, respectively. As shown in Figure 2.23, its flux density of $\sim$ 2.3 Jy in 2009 slightly decreased to $\sim$ 2.1 Jy in 2011 at 2100 MHz. The two flux densities measured at 5500 MHz in 2011 had almost equal magnitudes of $\sim$ 1.9 Jy.

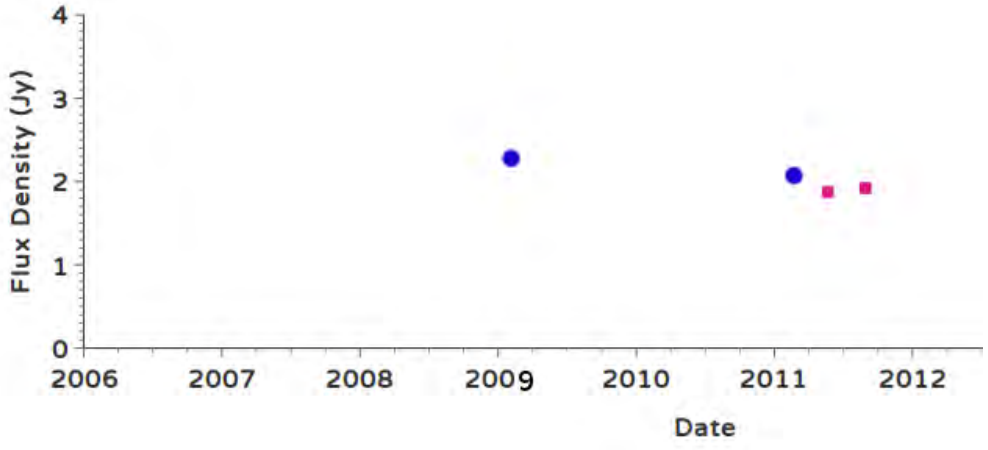

FIGURE 2.23: The flux density versus time plot PKS J0453-2807 from ATCA database [44] at frequencies of 2100 MHz (blue points) and 5500 MHz (light magenta points).

- **PKS J0538-4405** - is a flat spectrum quasar at redshift z= 0.894. It showed a significant variability in almost all electromagnetic spectra that had been detected. According to the ATCA Monitoring Observations of 202 Compact Radio Sources at 16 epochs between 1996 October and 2000 February by Tingay et al. [54], the variability indices of this source at 1.4 GHz, 2.5 GHz, 4.8 GHz, and 8.6 GHz are 22.0%, 24.0%, 30.0%, and 35.0%, respectively. The 5 GHz VLBI image showed that it has an asymmetric core-jet structure [63]. Figure 2.24 reveals that the source is highly variable. For instance, its flux density changed significantly from

$\sim$ 4.0 Jy in 2006 to $\sim$ 7.8 Jy in 2011 at 2100 MHz. The flux densities measured at 5500 MHz between 2007 and 2013 clearly revealed its strong variability; where its flux densities fluctuated between its peak value of $\sim$ 10.9 Jy in 2011 and its minimum value of $\sim$ 4.9 Jy in 2013.

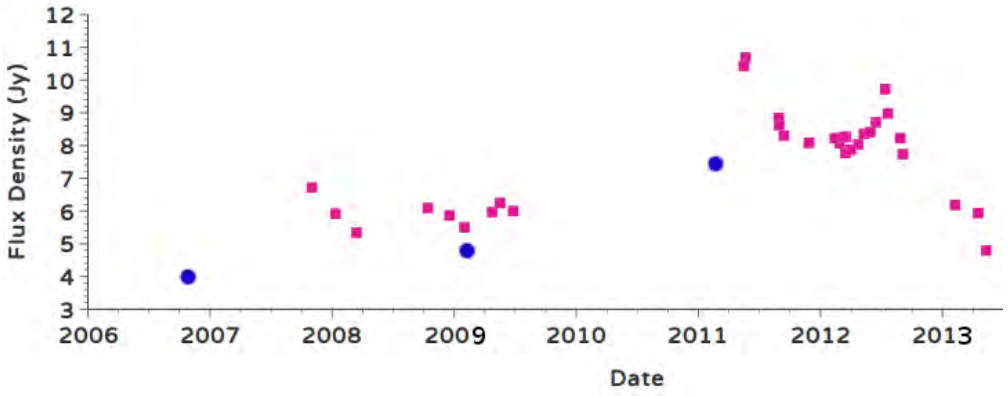

FIGURE 2.24: The flux density versus time plot PKS J0538-4405 from ATCA database [44] at frequencies of 2100 MHz (blue points) and 5500 MHz (light magenta points).

- **PKS J0534+1927** - is a steep-spectrum radio galaxy. No redshift information is given about this source in the NED catalogue.
- **PKS J0744-0629** - is flat-spectrum radio galaxy. No redshift information is given about the source in the NED catalogue. It is categorized as GPS for showing change in its spectrum around 1 GHz. As shown in Figure 2.25, the flux densities of this source in 2009 and 2012 at 2100 MHz were identical and equal to$\sim$ 6.07 Jy; Similarly, the five flux densities measured at 5500 MHz between 2009 and 2013 were nearly uniform, each having $\sim$ 2.7 Jy.

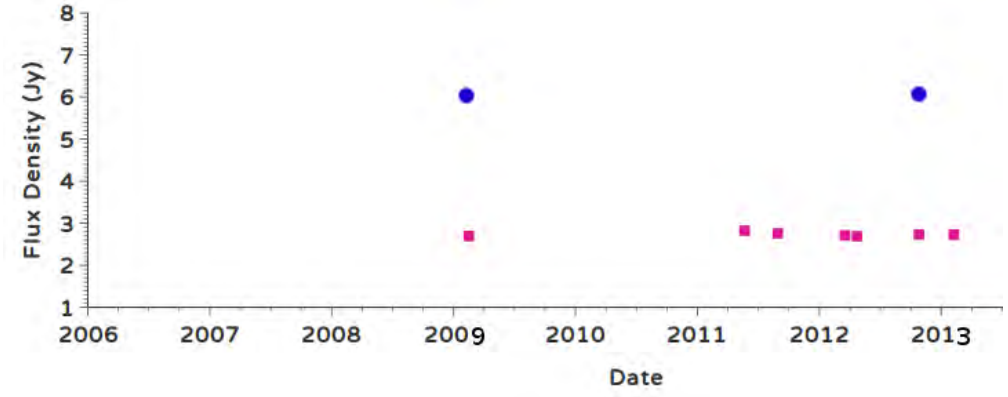

FIGURE 2.25: The flux density versus time plot PKS J0744-0629 from ATCA database [44] at frequencies of 2100 MHz (blue points) and 5500 MHz (light magenta points).

- **PKS J0837-1951** - is a compact steep-spectrum radio galaxy at redshift z= 1.032. The two flux densities measured at 2100 MHz between 2007 and 2009 had nearly equal magnitudes of $\sim$ 3.5 Jy. Similarly, the nine flux density measurements between 2009 and 2014 at 5500 MHz (Figure 2.26) had almost the same magnitudes of $\sim$ 1.4 Jy.

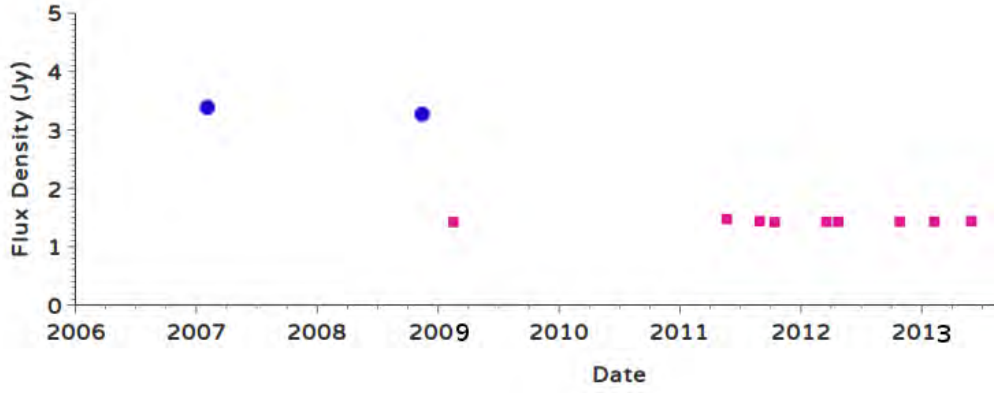

FIGURE 2.26: The flux density versus time plot PKS J0837-1951 from ATCA database [44] at frequencies of 2100 MHz (blue points) and 5500 MHz (light magenta points).

- **PKS J0943-0819** - is a flat-spectrum radio source at redshift z=0.228. It is identified as a GPS, which attains its peak around 0.5 GHz. Observations by VLBA revealed that PKS J0943-0819 has a compact double structure [64]. The two flux density measurements at 2100 MHz between 2007 and 2009 had nearly equal magnitudes of $\sim$ 2.2 Jy. Similarly, the nine flux density measurements recorded by the ATCA database at 5500 MHz between 2009 and 2014 (Figure 2.27) showed that they had almost identical magnitudes of $\sim$ 1.1 Jy.

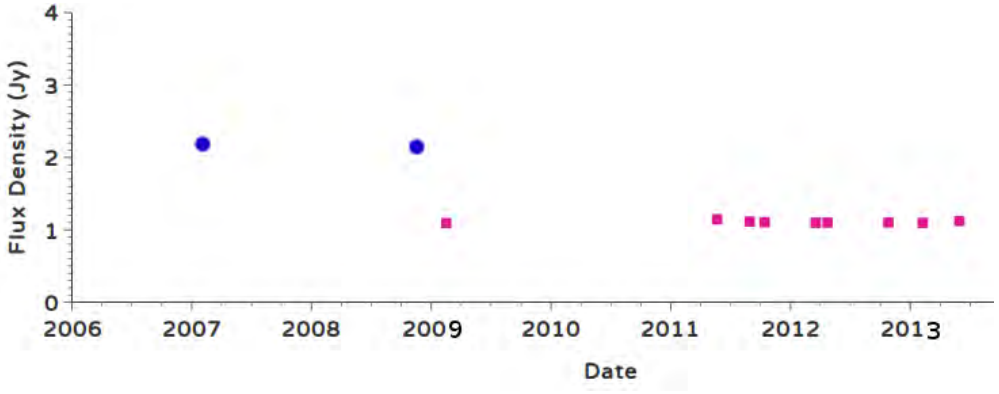

FIGURE 2.27: The flux density versus time plot PKS J0943-0819 from ATCA database [44] at frequencies of 2100 MHz (blue points) and 5500 MHz (light magenta points).

- **PKS J1130-1449** - is a flat-spectrum quasar at redshift z= 1.184. It is strong and compact and shows steep spectrum at higher frequencies. It exhibits continuous variability between low to high frequencies. According to the image obtained from VLBA, the source displays jets that originate from the core and bend at a distance about 3 mas into a direction of kilo parsec-scale radio structure [65]. As shown in Figure 2.28, its flux density $\sim$ 4.8 Jy in 2009 decreased to $\sim$ 4.3 Jy in 2010 at 2100 MHz. It displayed a peak flux density of $\sim$ 3.9 Jy in 2009 and attained nearly uniform values of $\sim$ 3.0 Jy between 2011 and 2014 at 5500 MHz.

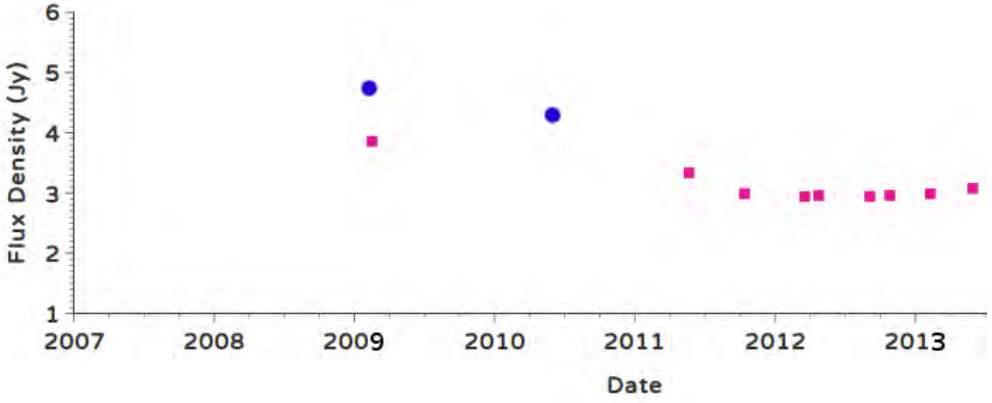

FIGURE 2.28: The flux density versus time plot PKS J1130-1449 from ATCA database [44] at frequencies of 2100 MHz (blue points) and 5500 MHz (light magenta points).

- **PKS J1154-3505** - is a compact steep spectrum quasar at redshift z=0.258. Only one flux density was measured in 2013 having a magnitude of $\sim$ 7.0 Jy at 2100 MHz; see Figure 2.29.The ten flux density measurements recorded in the ATCA calibrator database between 2009 and 2014 did not exhibit any significant change, as shown in Figure 2.29; almost all flux densities between these years had $\sim$ 2.8 Jy at 5500 MHz.

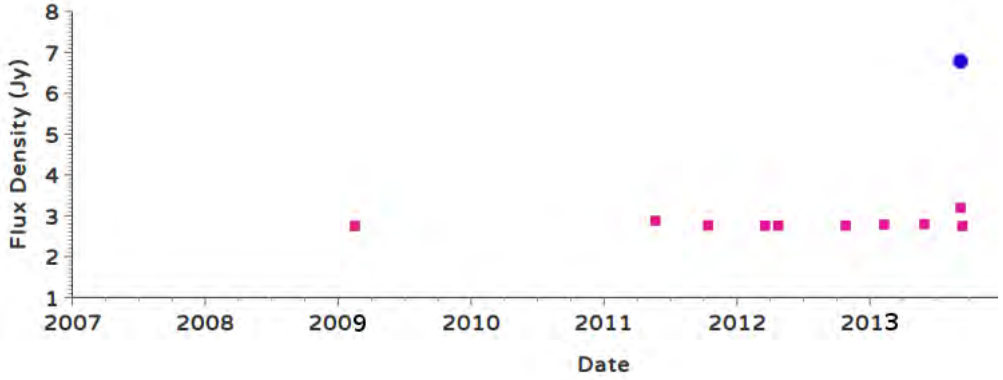

FIGURE 2.29: The flux density versus time plot PKS J1154-3505 from ATCA database [44] at frequencies of 2100 MHz (blue point) and 5500 MHz (light magenta points).

- **PKS J1248-1959** - is identified as a CSS under the class of quasar with a redshift z=1.275. It showed variability at low frequencies [66]. Only one flux density was measured between 2009 and 2014 in the ATCA calibrator database with a magnitude of $\sim$ 4.1 Jy at 2100 MHz; see Figure 2.30. The nine flux density measurements at 5500 MHz between 2009 and 2014 did not show any significant variability; each of the flux densities had nearly equal magnitude of $\sim$ 2.2 Jy.

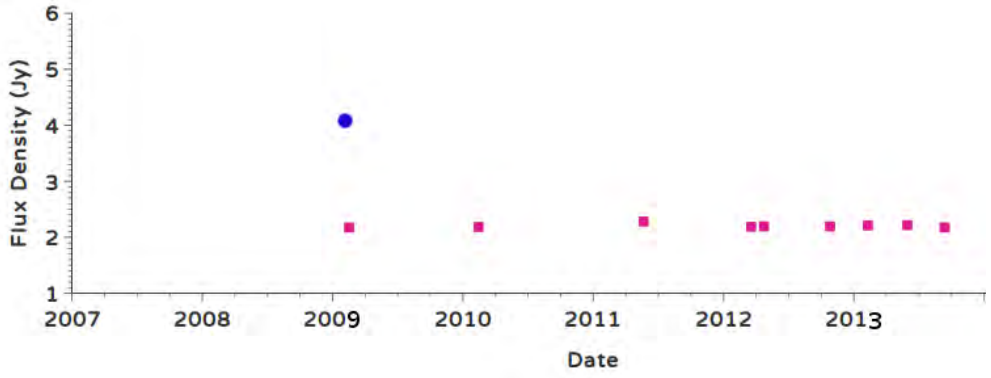

FIGURE 2.30: The flux density versus time plot PKS J1248-1959 from ATCA database [44] at frequencies of 2100 MHz (blue point) and 5500 MHz (light magenta points).

- **PKS J1311-2216** - is a steep spectrum radio galaxy at redshift z=0.800. According to the ATCA 6 km baselines observations at a frequency of 4.8 GHz, the unresolved component holds 95% of the flux density [53]. Only one flux density was measured between 2009 and 2014 in the ATCA calibrator database having a magnitude of $\sim$ 3.4 Jy at 2100 MHz; see Figure 2.31. The ten flux density measurements at 5500 MHz between 2009 and 2014 did not show any significant variability; each of them had nearly equal magnitude of $\sim$ 1.0 Jy.

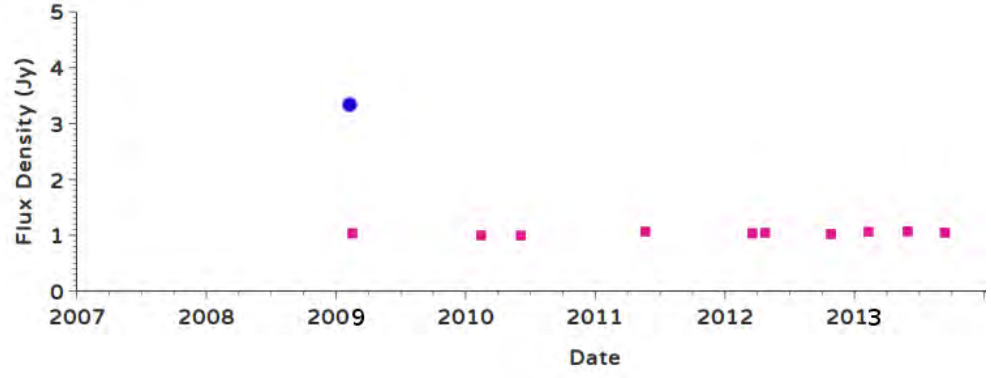

FIGURE 2.31: The flux density versus time plot PKS J1311-2216 from ATCA database [44] at frequencies of 2100 MHz (blue point) and 5500 MHz (light magenta points).

- **PKS J1510-0543** - is a flat-spectrum quasar at redshift z=1.185. The three flux densities measured at 2100 MHz between 2007 and 2013 had nearly equal magnitudes of $\sim$ 2.8 Jy. The three flux density measurements in 2009, 2012, and 2013 at 5500 MHz were almost identical and equal to $\sim$ 1.8 Jy, except its slightly higher flux density ($\sim$ 2.9 Jy) in 2011.

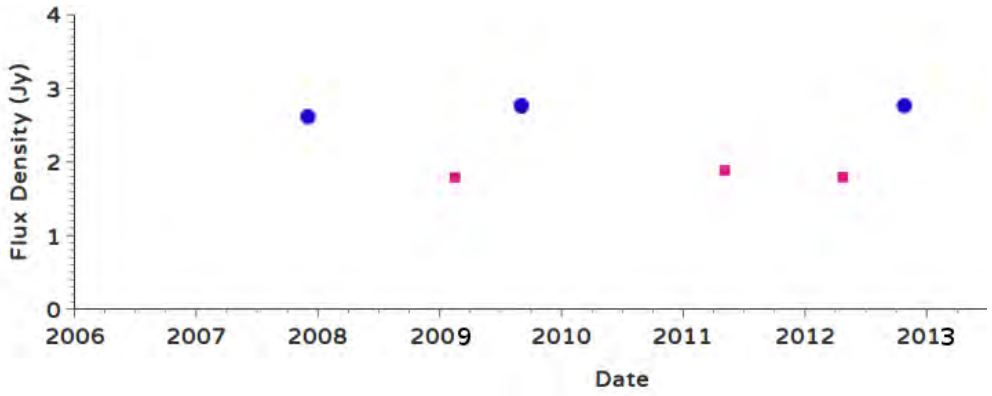

FIGURE 2.32: The flux density versus time plot PKS J1510-0543 from ATCA database [44] at frequencies of 2100 MHz (blue points) and 5500 MHz (light magenta points).

- **PKS J1517-2422** - is classified as BL Lac object having a flat spectrum at redshift z=0.049. It exhibits a core jet on arcsec scales. It shows a significant variability in optical ranges [67]. However, the two flux densities measured at 2100 MHz between 2007 and 2013 had nearly equal magnitudes of $\sim$ 2.3 Jy. Similarly, the four flux densities measured at 5500 MHz between 2011 and 2014 were nearly identical with each having a magnitude $\sim$ 2.5 Jy.

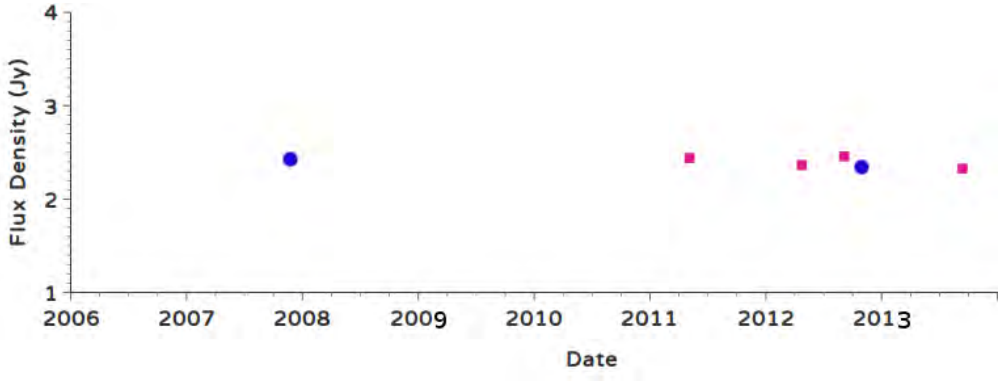

FIGURE 2.33: The flux density versus time plot PKS J1517-2422 from ATCA database [44] at frequencies of 2100 MHz (blue points) and 5500 MHz (light magenta points).

- **PMN J1712-2809** - is a radio source having steep spectrum with an extended morphology. Its flux density increased from $\sim$ 1.3 Jy in 2011 to $\sim$ 2.1 Jy in 2013

at 2100 MHz, as shown in Figure 2.34. However, the three flux densities measured at 5500 MHz did not show significant change between 2011 and 2014; each of them had nearly equal magnitude of ~ 0.5 Jy.

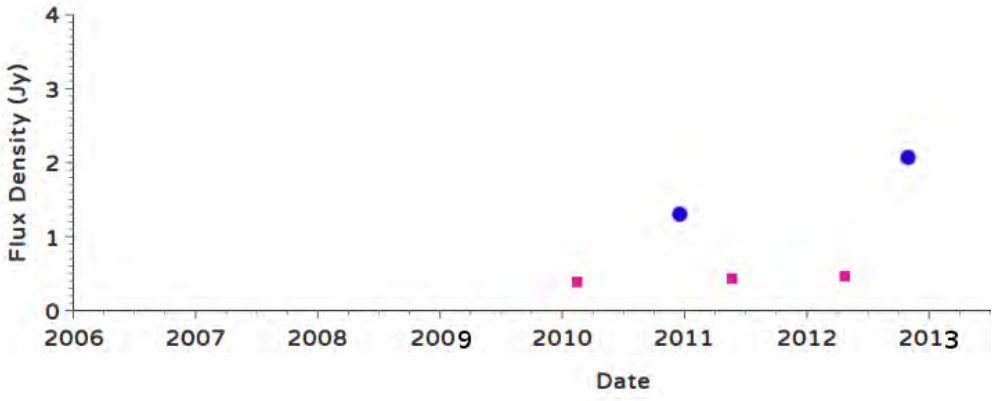

FIGURE 2.34: The flux density versus time plot PKS J1712-2809 from ATCA database [44] at frequencies of 2100 MHz (blue points) and 5500 MHz (light magenta points).

- **PKS J1819-6345** - is a radio source at redshift $z = 0.064$ having a CSS spectrum with a basic double-lobed structure [68]. As can be seen from Figure 2.35, the two flux density measurements taken at 2100 MHz between 2011 and 2013 had almost equal magnitudes of $\sim$ 9.7 Jy. Similarly, the seven flux density measurements taken at 5500 MHz between 2010 and 2013 had nearly equal magnitude of $\sim$ 4.2 Jy, except a slight decline to $\sim$ 3.9 Jy in 2011.

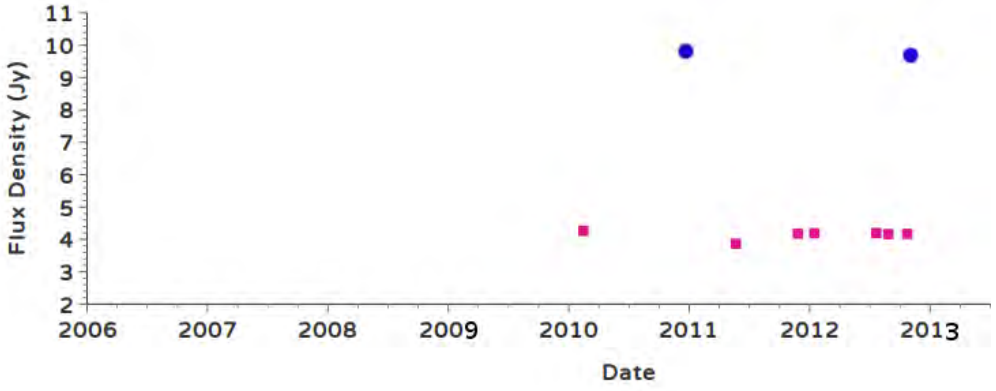

FIGURE 2.35: The flux density versus time plot PKS J1819-6345 from ATCA database [44] at frequencies of 2100 MHz (blue points) and 5500 MHz (light magenta points).

- **PKS J1830-3602** - is a radio source at redshift $z = 0.0120$ having a steep spectrum. Its flux density significantly increased from ~ 0.03 Jy at the end of 2010 to ~ 4.3 Jy at the end of 2012 at 2100 MHz, as shown in Figure 2.36. However, the four flux densities measured at 5500 MHz did not show significant change between

2011 and 2013; each of them had nearly equal magnitude of $\sim$ 1.0 Jy.

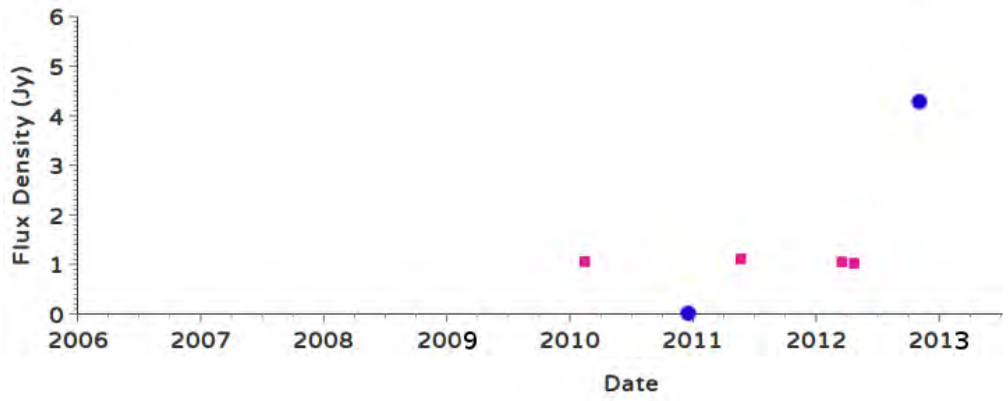

FIGURE 2.36: The flux density versus time plot PKS J1830-3602 from ATCA database [44] at frequencies of 2100 MHz (blue points) and 5500 MHz (light magenta points).

- **PKS J1833-2103** - is identified as a BL Lac object with flat radio spectrum at redshift z=2.507. According to the ATCA Monitoring Observations of 202 Compact Radio Sources at 16 epochs between 1996 October and 2000 February by Tingay et al. [54], the variability indices of this source at 1.4 GHz, 2.5 GHz, 4.8 GHz, and 8.6 GHz are 6.0%, 13.0%, 24.0%, and 39.0%, respectively. As shown in Figure 2.37, its flux density of $\sim$ 11.9 Jy at the end of 2010 increased to $\sim$ 13.3 Jy at the end of 2012 at 2100 MHz. Moreover, the three flux densities measured between 2011 and 2013 at 5500 MHz varied between $\sim$ 11.2 Jy and $\sim$ 9.7 Jy.

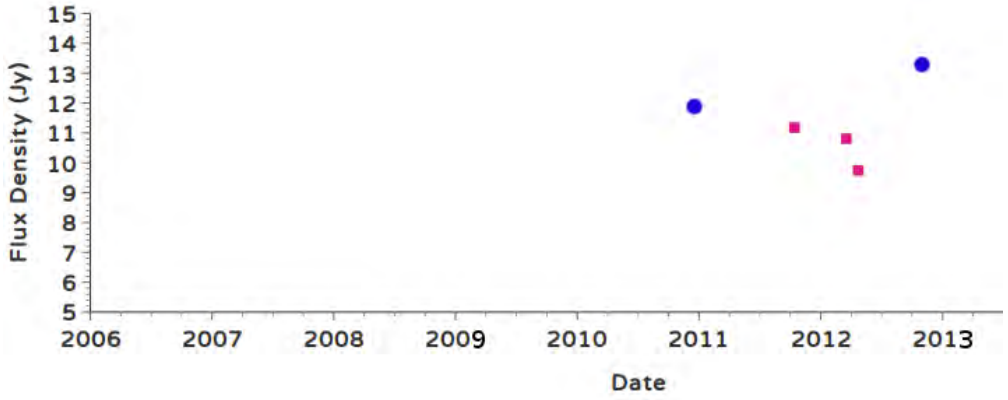

FIGURE 2.37: The flux density versus time plot PKS J1833-2103 from ATCA database [44] at frequencies of 2100 MHz (blue points) and 5500 MHz (light magenta points).

- **PKS J1924-2914** - is a quasar at redshift z=2.507. According to the ATCA Monitoring Observations of 202 Compact Radio Sources at 16 epochs between 1996 October and 2000 February by Tingay et al. [54], the variability indices of this source at 1.4 GHz, 2.5 GHz, 4.8 GHz, and 8.6 GHz are 5.0%, 9.0%, 16.0%,

and 19.0%, respectively. As evident from Figure 2.38, the flux densities of the source changed significantly at 5500 MHz between 2007 and 2014. For instance, the source had minimum flux densities ($\sim$ 9.0 Jy) between 2007 and 2009, and reached maximum ($\sim$ 17.4 Jy) in 2010; then it declined to $\sim$ 10.6 Jy in 2013. Moreover, the two flux density measurements at 2100 MHz also exhibited variation from $\sim$ 11.6 Jy in 2011 to $\sim$ 12.8 Jy in 2013.

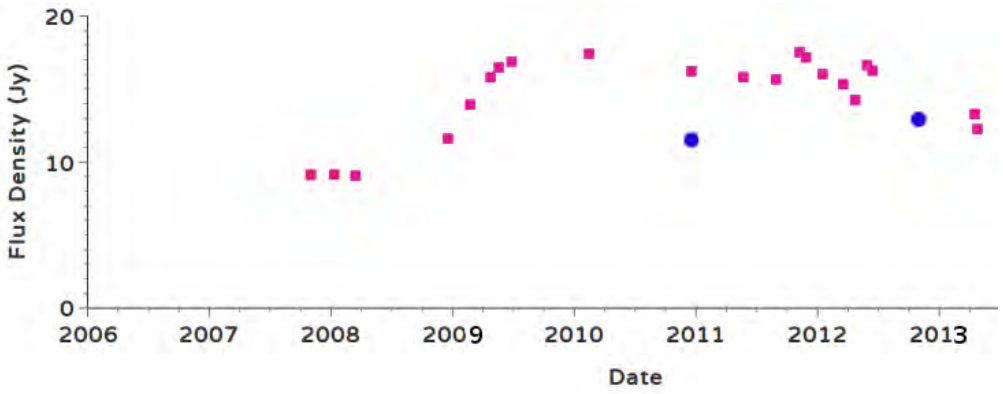

FIGURE 2.38: The flux density versus time plot PKS J1924-2914 from ATCA database [44] at frequencies of 2100 MHz (blue points) and 5500 MHz (light magenta points).

- **PKS J1941-1524** - is a quasar with a steep-spectrum property at redshift z=0.452. It is a small source with two lobes. However, it has not been observed as having any core or jets [60]. As can be observed from Figure 2.39, its flux density slightly changed from $\sim$ 2.4 Jy in 2011 to $\sim$ 2.5 Jy 2012 at 2100 MHz. Regarding the five flux densities measured at 5500 MHz between 2010 and 2013, there was a significant flux density change from $\sim$ 0.8 Jy in 2010 to $\sim$ 1.6 Jy in 2012.

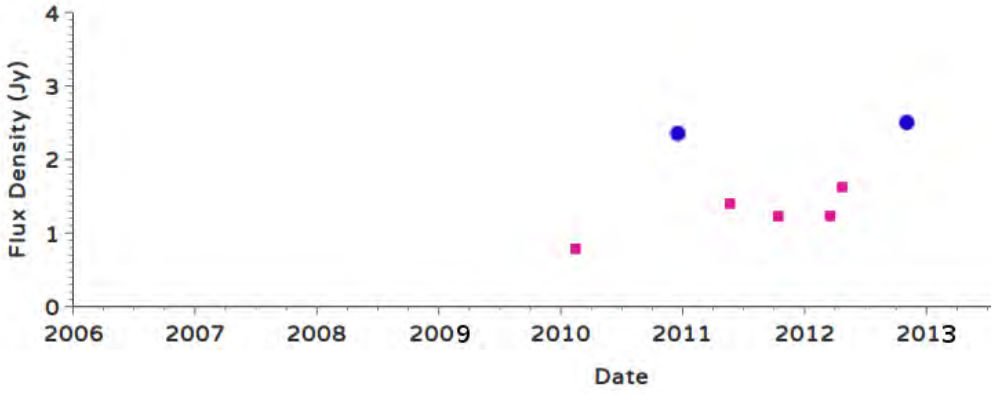

FIGURE 2.39: The flux density versus time plot PKS J1941-1524 from ATCA database [44] at frequencies of 2100 MHz (blue points) and 5500 MHz (light magenta points).

- **PKS J2129-1821** - is a flat-spectrum quasar at redhift z= 0.680. As shown in Figure 2.40, the two flux densities measured at 2100 MHz between 2010 and 2012 had nearly equal magnitudes of $\sim$ 1.3 Jy. Similarly, the four flux densities measured at 5500 MHz between 2010 and 2013 were almost equal to $\sim$ 0.9 Jy.

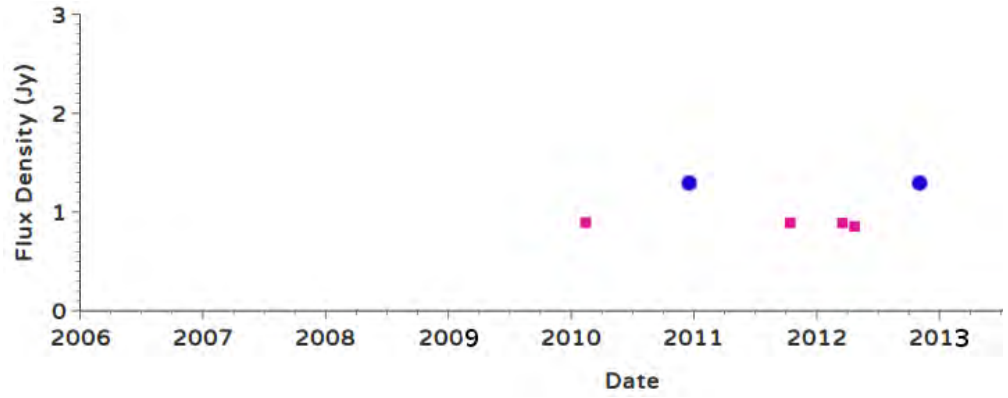

FIGURE 2.40: The flux density versus time plot PKS J2129-1821 from ATCA database [44] at frequencies of 2100 MHz (blue points) and 5500 MHz (light magenta points).

- **PKS J2131-2036** - is a quasar at redshift z=1.615. As shown in Figure 2.41, the two flux densities measured at 2100 MHz between the end of 2010 and 2012 had almost equal magnitudes of $\sim$ 1.3 Jy. Similarly, the four flux densities measured at 5500 MHz between 2010 and 2013 had nearly similar magnitudes of $\sim$ 0.5 Jy.

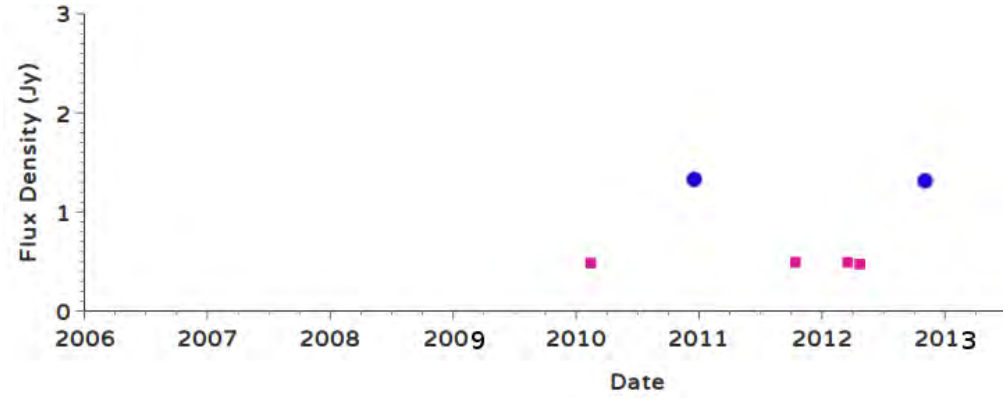

FIGURE 2.41: The flux density versus time plot PKS J2131-2036 from ATCA database [44] at frequencies of 2100 MHz (blue points) and 5500 MHz (light magenta points).

- **PKS J2151-3027** - is a flat-spectrum quasar at redshift z=2.345. According to the ATCA Monitoring Observations of 202 Compact Radio Sources at 16 epochs between 1996 October and 2000 February by Tingay et al. [54], the variability indices of this source at 1.4 GHz, 2.5 GHz, 4.8 GHz, and 8.6 GHz are 4.0%, 4.0%, 5.0%, and 8.0%, respectively. The fifteen flux density measurements observed at

5500 MHz between 2010 and 2014 fluctuated between maximum and minimum flux densities of $\sim$ 1.7 Jy in 2013 and $\sim$ 1.1 Jy in 2012; see Figure 2.42.

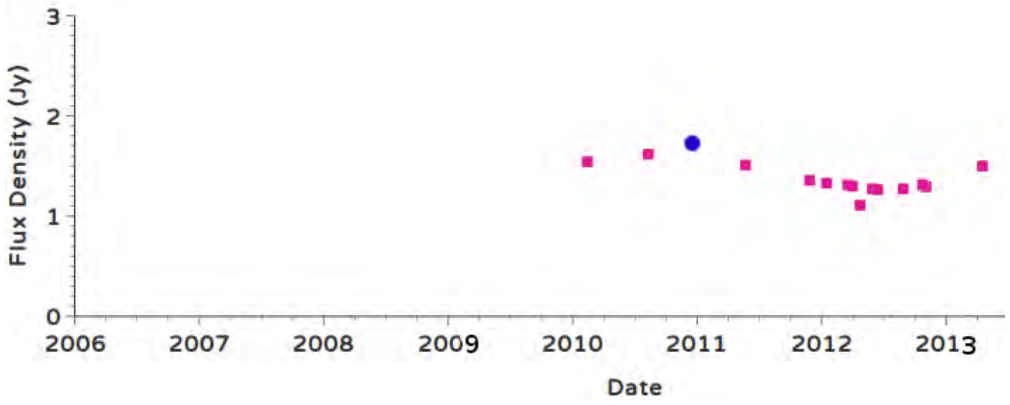

FIGURE 2.42: The flux density versus time plot PKS J2151-3027 from ATCA database [44] at frequencies of 2100 MHz (blue point) and 5500 MHz (light magenta points).

- **PKS J2152-2828** - is a steep-spectrum radio galaxy at redshift z=0.479. As shown in Figure 2.40, one flux density measurement (i.e. $\sim$ 2.1 Jy) at 2100 MHz was made at the end of 2010. The four flux densities measured at 5500 MHz between 2010 and 2013 had almost similar magnitudes of $\sim$ 1.1 Jy.

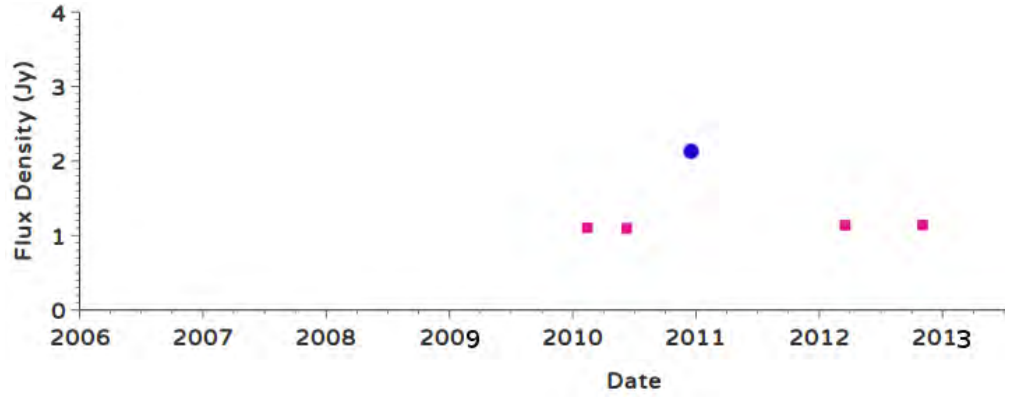

FIGURE 2.43: The flux density versus time plot PKS J2152-2828 from ATCA database [44] at frequencies of 2100 MHz (blue point) and 5500 MHz (light magenta points).

- **PKS J2206-1835** - is identified as a quasar with a flat spectrum at redshift z=0.618. According to the ATCA Monitoring Observations of 202 Compact Radio Sources at 16 epochs between 1996 October and 2000 February by Tingay et al. [54], the variability indices of this source at 1.4 GHz, 2.5 GHz, 4.8 GHz, and 8.6 GHz are 2.0%, 3.0%, 2.0%, and 2.0%, respectively. The source is resolved and extended in VLBI observations. However, it was found to be unresolved sources as observed by the ATCA at 2.3GHz [61]. The two flux densities (see Figure 2.44)

measured at 5500 MHz on Aug 29, 2011 and Oct 13, 2011 were found to be $\sim$ 4.1 Jy and $\sim$ 4.0 Jy, respectively.

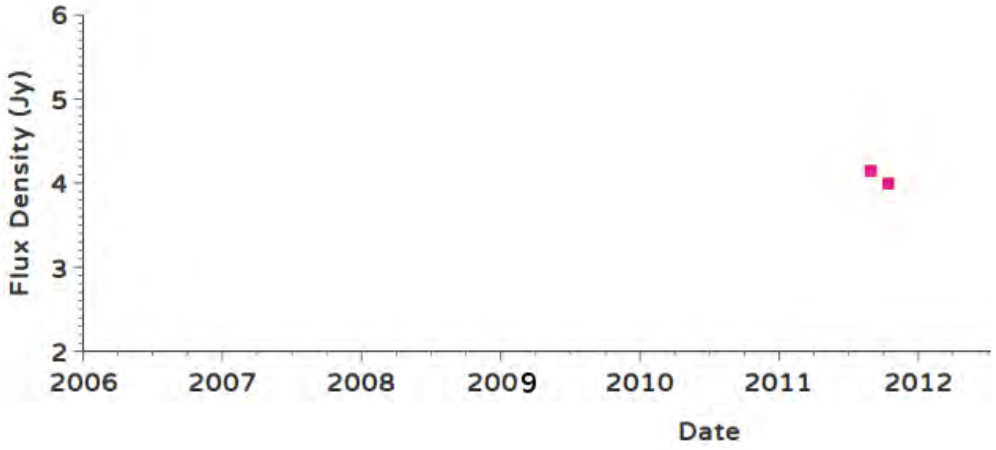

FIGURE 2.44: The flux density versus time plot PKS J2206-1835 from ATCA database [44] at frequency of 5500 MHz (light magenta points).

- **PKS J2219-2756** - It is an inverted-spectrum radio galaxy at redshift z=0.657. As shown in Figure 2.45, the source's flux densities showed discernible change at 5500 MHz between 2012 and 2013, having a maximum and minimum values of $\sim$ 0.41 Jy on April 22, 2012 and $\sim$ 0.04 Jy on Feb 19, 2012.

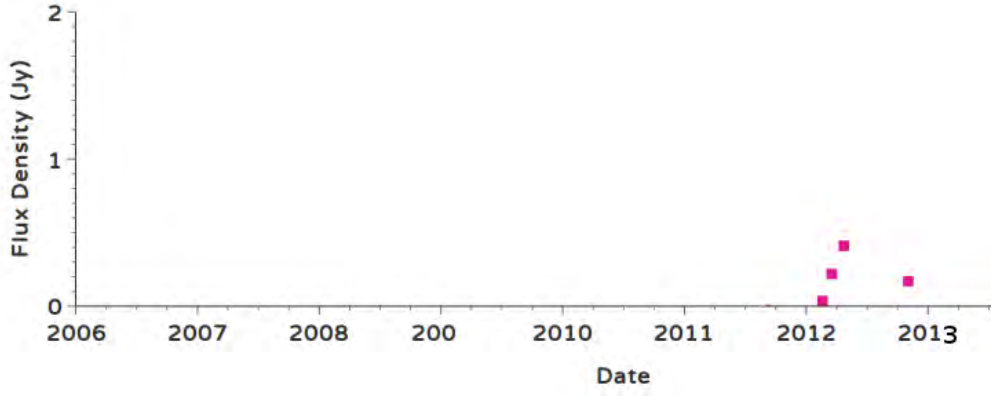

FIGURE 2.45: The flux density versus time plot PKS J2219-2756 from ATCA database [44] at frequency of 5500 MHz (light magenta points).

TABLE 2.4: The known parameters and properties of the the sources from the catalogues (NVSS, NED and SIMBAD). The columns are: Source name; Right Ascension (J2000) (HH:mm:ss); Declination (J2000) (deg:arcmin:arcsec); Spectral index (α) from the catalogues; Flux density at 1.4 GHz; Expected flux density at 1.83 GHz (KAT-7 observing frequency); redshift z; Spectral Identification (SID) based on the α, where F is flat, S is steep and I is inverted. Sources which show peak between 0.5 GHz to 10 GHz are assigned as GHz Peaked Spectrum (GPS) ; Type Identification (TID); where QSO, RS and BL Lac are quasar, Radio Source, and BL Lacertae, respectively.

Source Name	RA	Dec	α	$S_{1.4}$	$S_{1.83}$	z	SID	TID
PKS J1939-6342	19:39:25.42	-63:42:43.70	***	14.98	13.59	0.185	GPS	RS
PKS J0010-4153	00:10:52.45	-41:53:10.80	-0.91	4.44	3.53	1.120	S	RS
PKS J0022+0014	00:22:25.42	00:14:56.20	-0.43	3.01	2.70	0.940	F	RS
PKS J0025-2602	00:25:49.17	-26:02:12.80	-0.56	8.75	7.60	0.332	S	QSO
PKS J0042-4414	00:42:08.99	-44:14:00.50	-0.84	3.40	2.75	0.350	S	RS
PKS J0044-3530	00:44:41.01	-35:30:33.70	-0.65	2.56	2.18	0.980	S	QSO
PKS J0059+006	00:59:05.53	00:06:51.50	-0.45	2.50	2.24	0.710	F	QSO
PKS J0240-2309	02:40:08.14	-23:09:16.00	***	6.26	4.99	2.220	GPS	QSO
PKS J0252-7104	02:52:46.31	-71:04:36.20	-0.81	5.90	4.83	0.563	S	RS
PKS J0303-6211	03:03:50.81	-62:11:25.40	0.20	2.43	2.56	1.351	I	QSO
PKS J0309-6058	03:09:56.07	-60:58:39.90	-0.15	0.98	0.94	0.480	F	QSO
PKS J0318+1628	03:18:57.77	16:28:33.10	-0.32	7.96	7.10	0.907	F	QSO
PKS J0323+0534	03:23:20.31	05:34:11.90	-0.81	2.79	2.28	0.178	S	RS
PKS J0351-2744	03:51:39.45	-27:44:04.40	-0.91	6.11	4.87	0.065	S	RS
PKS J0405-1308	04:05:33.94	-13:08:14.40	-0.48	4.22	3.74	0.570	F	QSO
PKS J0409-1757	04:09:06.68	-17:57:09.40	-0.72	2.36	1.97	0.722	S	RS
3C123	04:37:04.57	29:40:14.20	-0.89	49.21	38.77	0.218	S	RS
PKS J0408-6544	04:08:20.28	-65:45:08.50	-1.09	16.02	12.16	0.962	S	QSO
PKS J0420-6223	04:20:56.19	-62:23:37.90	-1.02	3.01	2.32	0.810	S	Rs
PKS J0440-4333	04:40:17.07	-43:33:09.00	-0.24	4.53	4.27	2.860	F	QSO
PKS J0442-0017	04:42:38.62	-00:17:42.80	-0.18	3.38	3.23	0.844	F	QSO
PKS J0444-2809	04:44:36.57	-28:10:12.80	-0.85	7.23	5.84	0.147	S	RS
PKS J0453-2807	04:53:14.67	-28:07:36.60	-0.13	2.51	2.43	2.559	F	QSO
PKS J0534+1927	05:34:44.51	19:27:21.70	-0.63	6.99	5.98	****	S	RS
PKS J0538-4405	05:38:50.18	-44:05:10.30	0.05	2.89	2.93	0.894	I	QSO
PKS J0744-0629	07:44:21.65	-06:29:35.30	-0.32	8.08	7.46	****	F	RS
PKS J0837-1951	08:37:11.23	-19:51:55.90	-0.84	4.74	3.84	1.032	S	RS

TABLE 2.5: The known parameters and properties of the the sources from the catalogues (NVSS, NED and SIMBAD). The columns are: Source name; Right Ascension (J2000) (hour:minute:second); Declination (J2000) (deg:arcminute:arcsecond); Spectral index (α) from the catalogues; Flux density at 1.4 GHz; Expected flux density at 1.83 GHz (KAT-7 observing frequency); redshift z; Spectral Identification (SID) based on the α, where F is flat, S is steep and I is inverted. Sources which show peak between 0.5 GHz to 10 GHz are assigned as GHz Peaked Spectrum (GPS); Type Identification (TID); where QSO, RS and BL Lac are quasar, Radio Source, and BL Lacertae, respectively.

Source Name	RA	Dec	α	$S_{1.4}$	$S_{1.83}$	z	SID	TID
PKS J0943-0891	09:43:36.86	-08:19:32.00	-0.50	2.51	2.43	0.228	F	RS
PKS J1130-1449	11:30:07.05	-14:49:27.20	-0.16	5.62	5.40	1.184	F	QSO
PKS J1154-3505	11:54:21.76	-35:05:29.40	-0.47	6.20	5.50	0.258	F	QSO
PKS J1248-1959	12:48:23.98	-19:59:18.60	-0.50	5.14	4.53	1.275	F	QSO
PKS J1311-2216	13:11:39.29	-22:16:41.20	-1.07	5.20	3.97	0.800	S	RS
PKS J1510-0543	15:10:53.55	-05:43:07.10	-0.47	3.57	3.17	1.185	F	QSO
PKS J1517-2422	15:17:41.85	-24:22:20.00	0.07	2.04	2.08	0.049	I	BL Lac
PMN J1712-2809	17:12:57.30	-28:09:35.80	-0.71	5.18	4.29	**	S	RS
PKS J1744-5144	17:44:25.47	-51:44:43.10	-0.15	6.95	6.68	0.630	F	RS
PKS J1819-6345	18:19:35.04	-63:45:48.60	-0.89	13.38	10.80	0.065	S	RS
PKS J1830-3602	18:30:58.77	-36:02:30.00	-1.27	7.24	5.26	0.120	S	RS
PKS J1833-2103	18:33:39.98	-21:03:39.90	-0.12	10.89	10.57	2.507	F	BL Lac
PKS J1924-2914	19:24:51.44	-29:14:31.00	***	13.39	12.98	0.353	**	QSO
PKS J1935-4602	19:35:57.15	-46:20:43.10	-0.94	13.07	10.31	0.231	S	RS
PKS J1941-1524	19:41:14.97	-15:24:31.30	-0.73	6.72	5.60	0.452	S	QSO
PKS J2129-1821	21:29:21.41	-18:21:22.90	-0.33	1.41	0.97	0.680	F	QSO
PKS J2131-2036	21:31:01.51	-20:36:56.10	-0.86	2.07	1.67	1.615	S	QSO
PKS J2151-3027	21:51:55.54	-30:27:53.60	-0.16	1.24	1.19	****	F	RS
PKS J2152-2828	21:52:03.78	-28:28:29.00	-0.15	2.87	2.50	0.479	F	RS
PKS J2206-1835	22:06:10.33	-18:35:39.00	-0.31	6.40	5.90	0.618	F	QSO
PKS J2219-2756	22:19:42.57	-27:56:26.00	1.11	2.02	1.58	0.657	I	RS

2.5 Summary

This chapter dealt with the processes undertaken for the sample selections and observations. Given the key system specifications of the KAT-7, we could readily observe the sources. We considered 10 observations that were carried out between Oct 13, 2012 and February 23, 2013 as part of the KAT-7 commissioning phase. We selected those observations that included the flux density calibrator, PKS J1939-6342, so as to be consistent while flux calibrating the sources.

Of the 48 sources, $\sim$ 90 % of them lie in the southern sky. The estimated flux densities of the sources at 1.83 GHz indicated that $\sim$ 82% of the sources had flux densities between 1 Jy and 10 Jy. About 10% of the sources had flux densities between 10 Jy and 20 Jy. 3C123 is the strongest source where its extrapolated flux density at 1.83 GHz is about 39 Jy. The sample consists of $\sim$ 46% quasars, $\sim$ 50% radio galaxies, and two BL Lac object (PKS J1517-2422 and PKS J1833-2103). According to their spectral indices, $\sim$ 41%, $\sim$ 43%, and $\sim$ 8% of the sources showed flat, steep, and inverted spectra, respectively. 4 sources ($\sim$ 8%) were found to be Giga Hertz Peak Spectrum (GPS). Majority ($\sim$ 76%) of the selected sources located at redshifts $z \leq 1$.

This chapter also rendered essential information about the characteristic of each source on the basis of previous studies and different catalogues. The discussion mainly emphasised on the variability feature of each source's flux density with time.

Chapter 3

Radio Data Reduction

The correlation of the electric field between each pair of antennas through the observation course gives a set of measurements, which are known as raw radio data. Data reduction is the process of analysing these measurements to eventually obtain the actual sky brightness along with its parameters. Data reduction is a very tedious process and one needs to be very meticulous at each and every stage. The entire data reduction in this thesis was exclusively carried out using Common Astronomy Software Applications (CASA)[1] – a package prepared by National Radio Astronomy Observatory (NRAO) for the purpose of reducing radio data.

The following sections will present the data reduction procedures in CASA together with the calibration formalism. A collection of lectures on synthesis imaging in radio astronomy by Taylor et.al [16] is intensively used in the discussions.

3.1 The KAT-7 Radio Data Reduction

The raw data from the KAT-7 are initially stored and tabulated in Hierarchical Data Format (HDF5) by an in-house software. The in-house conversion software applies some flaggings, such as satellites as well as edge truncation due to the bandpass. Furthermore, an elevation cut-off is also implemented to take all the scans located above 20° elevation. This avoids some blockages due to the surrounding mountains. However, any elevation cut-off would exclude some visibilities, which would make the beam slightly worse. The HDF5 is then converted to Measurement Set (MS), which holds the necessary information about antennas, sources, polarization, spectral or frequency, sets of observation intervals, and others.

[1] casa.nrao.edu

3.1.1 Flagging

We started the data reduction procedure by editing the visibility data. The editing or flagging process mainly focuses on the identification and removal of extremely corrupted data. Some of the main causes for the severe corruption are interference from terrestrial sources, radio frequency interference (RFI), an unexpected fluctuation in the measuring instruments, bad weather, malfunctioning receivers, antenna tracking inaccuracies, incorrect observing parameters, data recording errors and others. These errors can be identified in the preliminary stage of data reduction because of their highly scattered appearance in the sampled data and their feasible contribution in unexpected phase variation.

The flagging of data in CASA can be done by plotting the visibility data using the task name '*plotms*'. The amplitude and phase can be plotted against several x-axis options such as channel, antenna, baseline, frequency, time, and etc. The discrepant points can easily be identified from the plot, so that we can remove them by selecting the '*flagging*' icon of the interactive window for both polarisations (Stokes XX and YY) and cross-polarisations (XY and YX). By using this procedure, we properly flagged the data collected from the KAT-7. It should be noted that unedited data in the visibility domain will induce significant errors when Fourier transformed into the image plane.

3.1.2 Delay calibration

Geometric and instrumental differential time delays are common in radio astronomy. The first one arises from the configuration of antennas, in which radio signals from the same source will arrive at different times at the antenna pairs. This can be usually adjusted by inserting an equivalent delay time in the system. The delay can be determined by knowing the position of antennas, but there will be errors due to miscalculation and miscalibration of the geometric delay when we insert it in the system. This consequently induces instrumental delay.

In order to adjust the errors due to the delays, we need to analyse the signals in terms of instantaneous bandwidths ($\Delta\nu$) as it is difficult to receive a monochromatic frequency in practice.

Noting that the frequency response should be coherent over the desired bandwidth, the integrated visibility function over a continuum observation or finite bandwidth is given by:

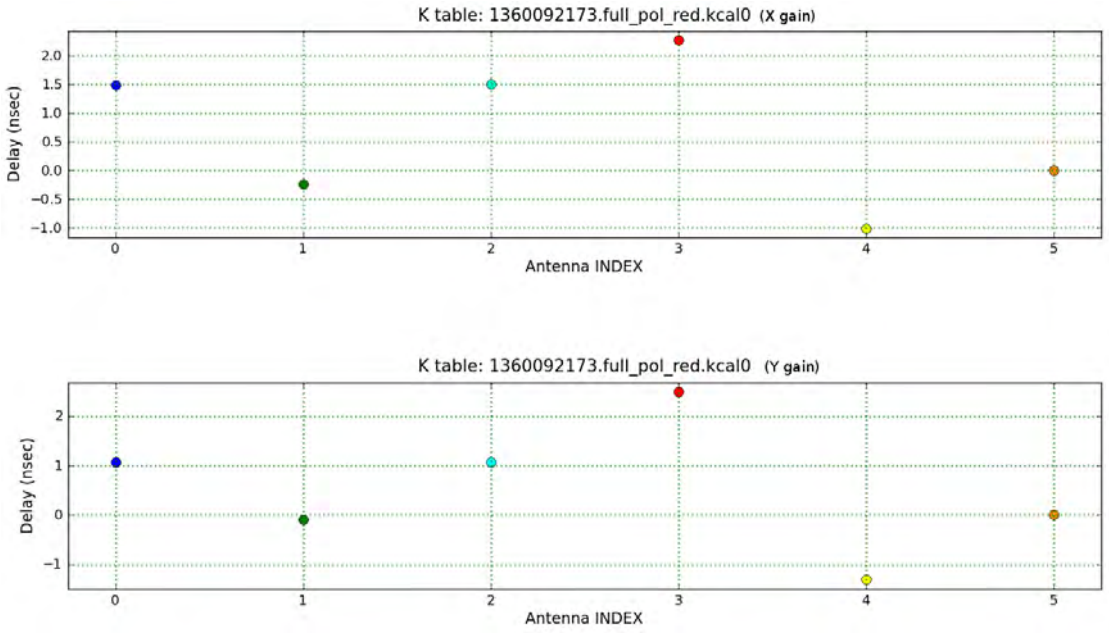

FIGURE 3.1: The time delay calibration taken from one of the data reductions. The horizontal axis represents antenna index, where antenna number corresponds to antenna index + 1. For example, Antenna INDEX = 0 is equivalent to antenna 1, and so on. In all the data reduction processes, we used antenna 6 (Antenna INDEX= 5) as a reference antenna. The point colors are arbitrary. The top and bottom plot describe the X and Y gains of the antennas. The maximum ($\sim$ 2.3 ns) and minimum ($\sim$ 0.2 ns) delays occurred for antenna 4 and antenna 2, they were both relative to antenna 6 (i.e. the reference antenna).

$$V_{kl}^{o}(t) = \int_{0}^{\infty} \left[\int_{-\infty}^{\infty} A_{\nu}(l,m) I_{\nu}(l,m) e^{-2i\pi\nu\Delta\tau_g} dl dm \right] e^{-2i\pi\nu\Delta\tau_r} B_{kl}(\nu) d\nu. \tag{3.1}$$

The term enclosed by the square brackets represents the geometric delay, where $\Delta\tau_g$ describes the geometric delay time for $k-l$ baseline. $B_{kl}(\nu)$ is the complex gain as a function of frequency, and $\Delta\tau_r$ is the residual instrumental delay for the $k-l$ baseline.

The phase difference $\Delta\Phi$ between the ends of the band, that results from a net residual delay $\Delta\tau_g - \Delta\tau_r$, is given by

$$\Delta\Phi = 2\pi\Delta\nu(\Delta\tau_g - \Delta\tau_r), \tag{3.2}$$

where $\Delta\nu$ the spanned bandwidth of the observations. If the phase difference between the ends of the band is greater than about one radian, it will produce a recognizable loss of coherence across the band. Therefore, the delay between signals must be less than about $(\frac{160}{\Delta\nu})$ nanoseconds, where $\Delta\nu$ is given in MHz. For the KAT-7, the delay between signals should be less than about 5.12 ns between the ends of the band. We checked the delays in all data reductions were less than $\sim$ 5 ns.

The delay calibration in CASA can be performed by selecting the strong and discrete source among the observed sources. In the data reduction process, we utilized the flux calibrator, PKS J1939-6342, for delay calibration.

3.1.3 Bandpass Calibration

The purpose of bandpass calibration is to find out the relative gain of an antenna or baseline as a function of frequency. It is dependent on the electronic devices used in an individual antenna and the transmission systems connecting antenna to correlators. This results in the slow change of gain with time while varying significantly with frequency. Hence, once the bandpass gain is estimated at a certain time, it will be implemented for all channels. Bandpass gain can be determined by observing a strong calibrator source with flat spectrum over the span of the desired frequency band.

Theoretically, an ideal system is assumed to have a unit response between $(\nu_0 - \Delta\nu)$ and $(\nu_0 + \Delta\nu)$ and otherwise zero. However, this assumption is not valid when we apply it in real situations. The main reason is the impracticality of finding a system that rapidly changes from 0 to 1 at the edges. In other words, there is an inevitable response around the boundaries. Besides, it is difficult to produce a unit response along the desired bandpass. So, bandpass gain solution is an important part of calibration when we deal with real radio data.

Equation (1.9) in Section 1.3 is implemented for the purpose of bandpass calibration by rewriting in the form:

$$V^o_{kl}(\nu, t) = G_{kl}(\nu, t)V^I_{kl}(t), \tag{3.3}$$

where $G_{kl}(\nu, t)$ is the baseline-based complex gain as a function of time and frequency.

The gain term can be separated into time dependent, $A_{kl}(t)$, and frequency dependent, $B_{kl}(\nu)$, complex gains. This would make Eq.(3.3) to be written in the form:

$$V^o_{kl}(\nu, t) = A_{kl}(t)B_{kl}(\nu)V^I_{kl}(t). \tag{3.4}$$

The time-dependent gain mainly comes from atmospheric factors, where they strongly affect the phase term. Comparing the two terms, the frequency-dependent gain varies quiescently over the baselines.

For bandpass calibration, the calibrator reference source should approximately be flat spectrum over the required frequency band. In other words, the V^I_{kl} has to be independent of frequency.

The bandpass calibration is determined so that one can average the data in frequency [69]. Averaging the data not only reduces the size of the data but it enhances the sensitivity for the determination of time-dependent gains. For the purpose of averaging, we need to sum up the frequency-dependent terms in Eq.(3.4) over the frequency:

$$\sum_{\nu} V^{o}_{kl}(\nu, t) = A_{kl}(t) V^{I}_{kl}(t) \sum_{\nu} B_{kl}(\nu). \tag{3.5}$$

The time-dependent terms (i.e., $A_{kl}(t)$ and $V^{I}_{kl}(t)$) in Eq.(3.4) and (3.5) are eliminated when we divide Eq.(3.4) by Eq.(3.5):

$$\frac{B_{kl}(\nu)}{\sum_{\nu} B_{kl}(\nu)} = \frac{V^{o}_{kl}(\nu, t)}{\sum_{\nu} V^{o}_{kl}(\nu, t)}. \tag{3.6}$$

Equation (3.6) essentially avoids time-dependent gain due to atmospheric effects and minimizes extra source structure. Moreover, it removes the spectral variable region, where we are able to achieve flat spectrum portion for the bandpass solution. The observed visibility summed over the frequency is usually assigned as the initial channel (i.e., $\sum_{\nu} V^{o}_{kl}(\nu, t)$=channel-0).

The bandpass gain is strongly dependent on the antenna. Thus, the frequency-dependent gain can approximately be written as a product of the gain term of each pair of antennas.

$$B_{kl}(\nu) \approx B_{k}(\nu) B^{*}_{l}(\nu). \tag{3.7}$$

Therefore, by combining the continuum-chopped visibilities from Eq.(3.6) with the antenna-dependent bandpass gains from Eq.(3.7), we readily solve for the bandpass gain of the observed radio data.

The averaging of the radio data over frequency [i.e., Eq.(3.6)] in CASA is performed by using the task name '*split*'. We need to provide the necessary inputs for the task so as to obtain the averaged data. Some of the main parameters necessary for the splitting are the channel width, the number of channels, the time interval that the data needs to be averaged. All these are calculated from the '*Spectral Window*' file under the measurement file (MS).

According to Figure 3.2, the gain amplitude of each antenna varies less than 10% across the channels, and such variation is acceptable. In all our data reduction runs, we properly checked the fulfilment of this condition. The red and blue colors in Figure 3.2 represent the X and Y gains, respectively.

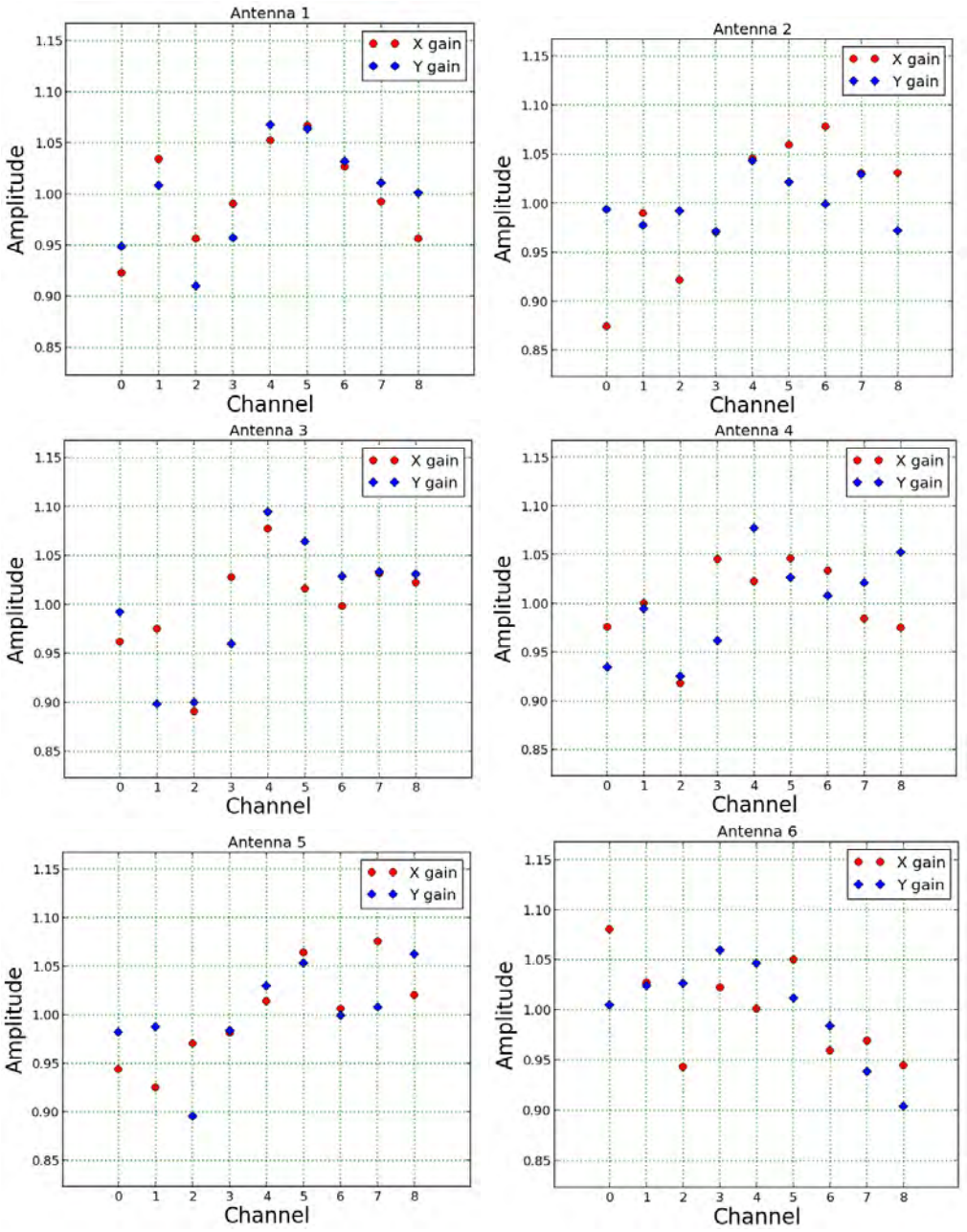

FIGURE 3.2: Each plot shows the bandpass amplitude variation along each channel iterated in terms of antenna, where the antenna number is written on the top of each plot. The colors show the X gain (red) and Y gain (blue). The plots are excerpted from one of the datasets reduced for this thesis.

The estimation of the calibration gain (G_{kl}) in CASA passes through certain procedures. Initially, we need to set the proper flux density of the known calibrator source using the task '*setjy*'. In our case, we considered the datasets or observations that contained PKS J1939-6342 as our standard flux calibrator throughout the data reduction run. This source was observed frequently in the observation runs compared to other known flux calibrators, because it is southern declination source. Using only this source as

flux-density calibrator has an advantage of reducing biases that may occur if we utilize various flux-density calibrators. In addition to this benefit, elevation-dependent effects causing errors in flux density determination would be minimized for using PKS J1939-6342. Moreover, the study by Reynolds [70] via ATCA on this source over the frequencies 1.4 GHz to 8.6 GHz revealed that the source is a good flux density calibrator for the southern observatories. Additionally, its variability in the given frequencies was found to be less than 0.5% [70].

The task '*setjy*' recognizes most of the standard flux-density (amplitude) calibrators, and thus it sets the expected flux density of the source at the observing frequency. The parameter '*field*' should correctly contain the source name. In our data reduction, we also set other parameters: '*fluxdensity=-1*' to search through flux calibrator and put the standard value; '*scalechan=True*' to scale the flux density on a per channel basis; '*standard= Perley-Bulter 2012'* to set the flux density determined by Perley and Butler in 2010.

After properly setting the amplitude of the flux-density calibrator, we proceeded to solve for the bandpass using the task '*bandpass*'. To calculate the bandpass response, we implemented temporary phase calibration along the selected channels. In our case, we made the calibration using a subset of the central channels (3 to 5) out of the 9 available channels. It is preferable to select these channels as they are relatively free from interference effects. As most of phase variations originate from the atmosphere, all channels are affected equally. Hence, the calibration on the specific channels can be implemented for the entire channels.

The flux-density calibrator (PKS J1939-6342) was used for the purpose of bandpass calibration because of its high signal to noise ratio and its point-like property. Consequently, the bandpass solution in CASA is processed by assigning the averaged file name under the task '*vis*', the field id of the flux-density calibrator under '*field*', the reference antenna (i.e. we used antenna 6 in all the data reduction processes) under '*refant=ant6*'. The minimum baselines per antenna set to be 4 under '*minblperant*', and the minimum SNR was adjusted to be 3 under '*minsnr*'. The SNR below 3 would be rejected. Moreover, a complex gain in each channel would be solved by specifying '*bandtype=B*'. Under the parameters '*caltable*' and '*gaintable*', we put the appropriate table name for the purpose of the output gain and the antenna dependent phase calibration solutions, respectively.

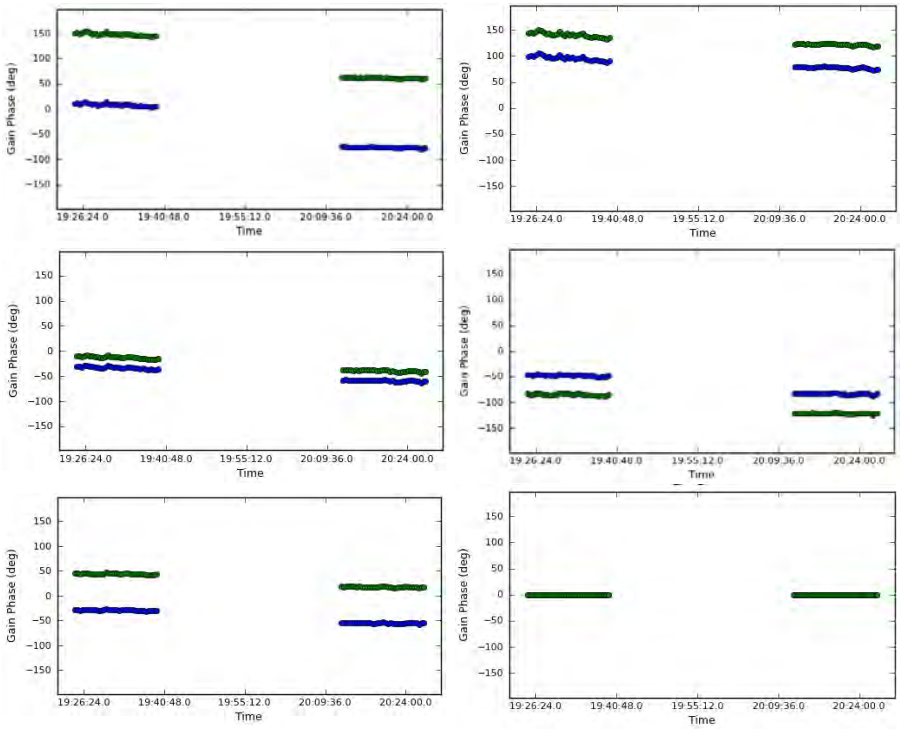

FIGURE 3.3: Each plot shows the gain phase solution on each antenna as a function of time. The left panels from the top to the bottom represent the gain phase solution on antenna 1, antenna 2 and antenna 3, respectively. The right panels from the top plot to the bottom show the phase gain solution on antenna 2, antenna 4, and antenna 6, respectively. X and Y gains of each antenna are plotted in blue and green, respectively. The plots reveal that the phase gains in each antenna are almost constant in time. This shows that the antennas are stable in phase. The gain phase on antenna 6 is a smooth horizontal line along zero because antenna 6 is used as a reference antenna.

The next step is to determine the flux density of the sources using the flux-density calibrator. This method is known as flux-density bootstrapping. Initially, we set the source to have a flux density of 1 Jy. After solving for the time dependent complex gain ($Gkl(t)$) as given by Eq.(1.10), then we derive the flux density of the source by comparing with the flux-density calibrator (PKS J1939-6342), where its flux density set by CASA at 1.83 GHz is I=13.249 Jy.

The flux densities of the sources in this thesis have been determined in the above way. This assumption is justifiable because the flux-density calibrator we used, PKS J1939-6342, has a known, stable flux density, and has no linear or circular polarization. However, the flux-density bootstrapping process causes residual calibration errors, where the bootstrapping accuracy is not well known. We will determine the bootstrapping accuracy for the KAT-7 later in chapter 4.

The gain solution in CASA was carried out using the task '*gaincal*'. In this case, we used

the bandpass calibration table as an input to the '*gaintable*' parameter under the '*gaincal*'. The parameter '*field*' would take the phase calibrator field name. Other important parameters under the '*gaincal*' are '*solint=inf*', describing the solution interval from arbitrary value up to the scan boundary; '*gaintype=G*', describing time-dependent gain; '*calmode=ap*', indicating the solution for amplitude and phase; '*refant=ant6*', describing the reference antenna.

The gain calibration was followed by flux scale bootstrapping using the task '*fluxscale*'. The essential inputs are the averaged MS file under '*vis*', the calibration table under '*caltable*', the name of the output table under '*fluxtable*', the field name that would be bootstrapped under '*transfer*', the flux calibrator under '*reference*'.

3.2 Selection Of Phase Calibrators And Target Sources

According to Perley et al. [71], the phase calibrator needs to be close to the target source. The reason is that when the gap between the phase calibrator and the target source is small (preferably within the range of 10° to 15°), the phase perturbation caused by atmosphere will be minimized significantly. We set out some criteria to categorize the sources as phase calibrators and target groups. Thus, we implemented the following standards in the data reduction run.

1. We initially separated the sources based on their cross-proximity along the Right Ascension (RA) and Declination (Dec) (i.e. both are converted into degrees) using their catalogued positions. After doing this, we calculated the mean position of RA and Dec representing the sources' center in a group. By taking the mean position as a centre, we constructed a circle of radius 16° to identify which of the sources would be inside the circle as phase versus target pairs. In this way, we identified a cluster of sources confined in a particular group as shown in Figure 3.4.

2. The phase calibrator needs to be bright, should have an accurately determined position, and shows a simple (preferably compact) radio structure [72]. In our case, the brightest source among the sources in each group was identified by comparing their extrapolated flux densities (refer Section 2.2 as well as Table 2.4 and 2.5) at 1.83 GHz using Eq.(1.39). After selecting the brightest source in the group, we further probed the source's structure and flux variability from different literatures and catalogues. For this purpose, we had already studied the properties of the sources (see Section 2.4) before starting the data reduction. If the source were bright but had complex structure and significantly variable, we would select the second brightest source with compact structure in the group. For example, we

used this requirement for choosing PKS J0440-4333 and PKS J1941-1524 as phase calibrators. By doing so, we identified 14 phase calibrators and 33 target sources as presented in Table 3.1.

3. After selecting the phase calibrator, we calculated the angular distance (AD) between the phase and the target source using:

$$\mathtt{AD} = \arccos(A + B) \tag{3.8}$$

where $A = \cos(\mathtt{Dec}_1) \times \cos(\mathtt{Dec}_2) \times \cos(\mathtt{RA}_1 - \mathtt{RA}_2)$ and $B = \sin(\mathtt{Dec}_1) \times \sin(\mathtt{Dec}_2)$. $\mathtt{Dec}_1$ and $\mathtt{Dec}_2$ are the declinations of the phase and target source, respectively; $\mathtt{RA}_1$ and $\mathtt{RA}_2$ are the right ascensions of the phase and the target source, respectively.

The AD would tell us whether the phase calibrator sources are far beyond the desirable distance (10° to 15°) from the target source. In our case, 16 of the target sources ($\sim$ 49%) are at angular distance of $\sim$ 9° to $\sim$ 15° from their respective phase calibrators. Whereas the remaining target sources ($\sim$ 51%) are separated from their phase calibrators between $\sim$ 16° and $\sim$ 29°, as shown in Table 3.1. Since the atmospheric effect is quite stable at 1.83 GHz in small array configuration such as the KAT-7, the relatively high AD value may not significantly affect the phase calibration of the target sources [71].

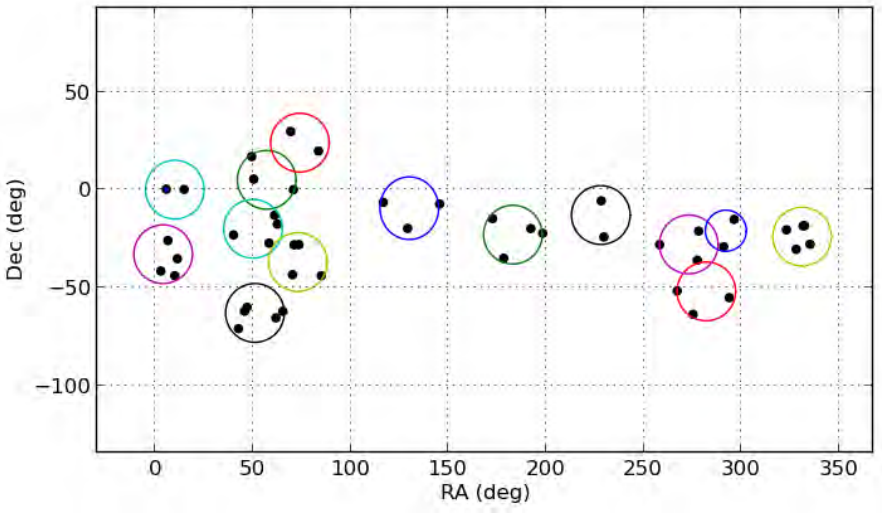

FIGURE 3.4: Each circle represents a group that contains sources according to their proximity. A maximum of 16° radius is drawn to inscribe all sources around the vicinity. After putting together the sources according to their proximity, the one with highest flux density and compact structure was selected as a phase calibrator. The last circle in the right side inscribes 6 sources though two sources are invisible because of covering one over the other due to their cross-proximity due to the scale of our plot.

TABLE 3.1: The table comprises the phase calibrators and the corresponding target sources. AD refers to the Angular Distance between the phase calibrator and the science source. It is advisable AD to be in the range of 15° so as to minimize atmospheric effects. In our case, some of the target sources are far from this limit. However, atmospheric effects are known to be less erratic at a frequency of 1.83 GHz, so that the derived positions of the target sources would not be highly affected if AD is larger than the recommended limit.

Phase calibrators versus science targets and the angular separation.		
Phase calibrators	Target sources	AD (deg)
PKS J0022+0014	PKS J0059+006	8.9
PKS J0025-2602	PKS J0010-4153	14.9
	PKS J0042-4414	17.9
	PKS J0044-3530	9.7
PKS J0240-2309	PKS J0351-2744	16.8
	PKS J0405-1308	22.3
	PKS J0409-1757	21.6
PKS J0252-7104	PKS J0303-6211	9.4
	PKS J0309-6058	11.9
	PKS J0408-1757	9.7
	PKS J0420-6223	12.9
PKS J0318+1628	PKS J0323+0534	11.6
	PKS J0442+0534	26.6
3C123 (0437+2940)	PKS J0534+1927	16.3
PKS J0440-4333	PKS J0538-4405	10.7
	PKSJ0444-2809	18.6
	PKS J0453-2807	17.5
PKS J0744-0629	PKS J0837-1951	19.0
	PKS J0943-0819	28.8
PKS J1154-3505	PKS J1130-1449	22.3
	PKS J1248-1959	20.5
	PKS J1311-2216	21.8
PKS J1510-0543	PKS J1517-2422	19.9
PKS J1819-6345	PKS J1935-5509	20.5
	PKS J1744-5144	16.4
PKS J1833-2103	PMN J1712-2809	19.3
	PKS J1830-3602	14.6
PKS J1941-1524	PKS J1924-2914	14.4
PKS J2206-1835	PKS J2129-1821	8.8
	PKS J2131-2036	8.3
	PKS J2151-3027	12.4
	PKS J2152-2828	10.3
	PKS J2219-2756	9.9

After setting out the above standards, we applied the calibration using the CASA task '*applycal*'. In this final stage of the calibration, we included all the calibration tables (i.e., delay, flux, bandpass) under the parameter '*gaintable*'. For properly calibrated sources, the flux density (amplitude) should lie around the phase center, as shown in Figure (3.5); otherwise, there may be calibration error during the steps, and the whole process of flagging and calibration needs to be rerun.

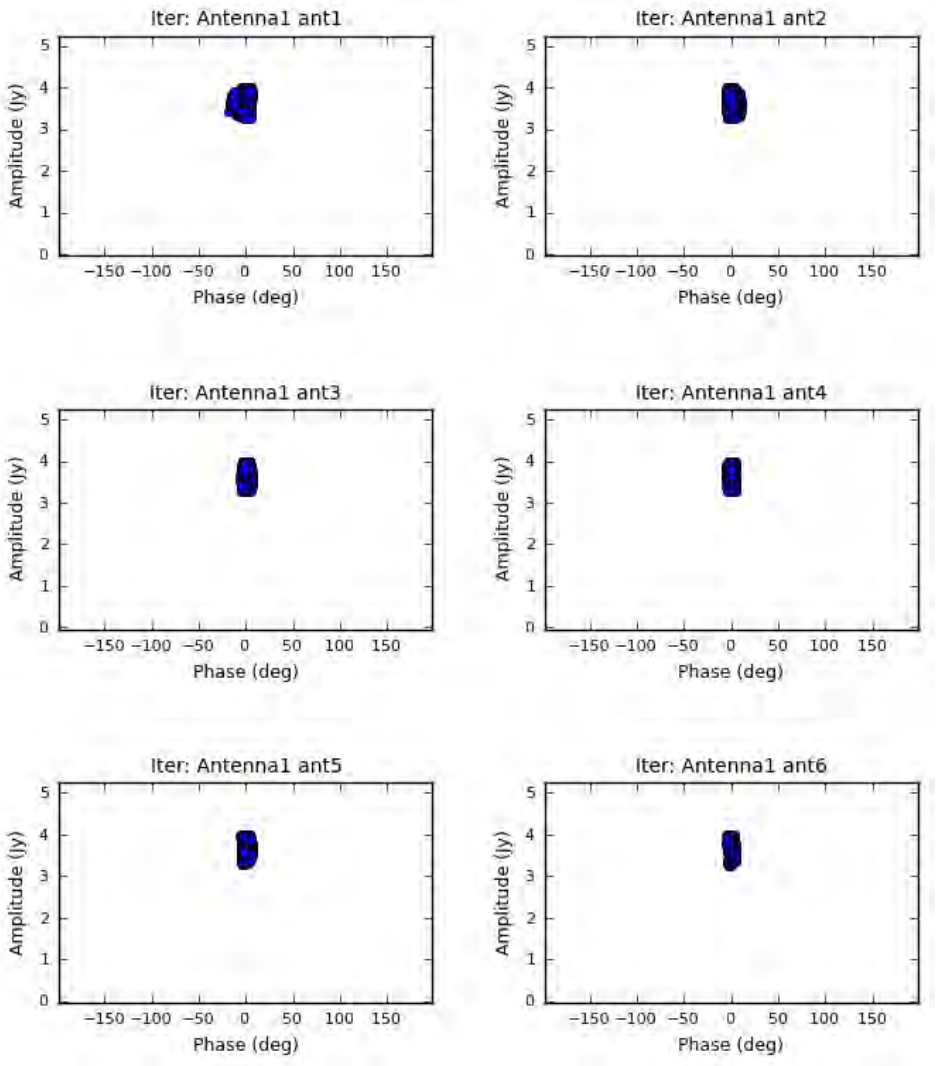

FIGURE 3.5: The plots explain that the visibility amplitudes are consistent across baselines and times; the visibility phases are near 0, which are expected values for a point source located at the phase center. They tell us whether the calibration procedures have been done properly. The phase center is the point on the sky at which the interferometer is pointed (phase tracking center). Note that ant1, ant2, and etc refer to antenna 2, antenna 3, and etc respectively according to the CASA convention. The plots are taken from one of the reduced datasets of PKS J0010-4153 observed by the 7 antennas for XX polarization. We also checked for YY polarization in the same way and found no discrepant results.

The next step after finalizing the calibration is splitting of the entire data to analyse each source individually. This is done by a task name '*split*' by providing the correct field name as initially given in the MS file, and assigning appropriate file name under '*outputvis*'.

After successfully splitting the data, the next step will be producing an image of each source. The following section will discuss the basic idea and algorithm used in the imaging of the sources.

3.3 Imaging and Deconvolution: CLEAN Algorithm

Equation (1.5) of Section 1.2 should be modified to correctly handle the actual radio data. In actual situation, the observed visibilities are recorded at discrete points or (u_j, v_j), where $j = 1, 2, ..., N$. In the case of KAT-7 configuration, N may reach thousands while scanning the desired sources. Having this in mind, we additionally put the practical consideration of the inaccessibility of $V(u, v)$ everywhere. For this reason, we need to sample in a particular place in the $u - v$ plane, so the sampling function $S(u, v)$ has to be combined with $V(u, v)$ [16]. Such assumption would prompt us to write Eq.(1.5) in the form:

$$I_D(l, m) = \int\int_{\mathbf{s}} \hat{V}(u, v) S(u, v) \exp\left(i2\pi \left[ul + vm\right]\right) dudv. \tag{3.9}$$

The intensity distribution $I_D(l, m)$ in Eq.(3.9) is called dirty image. The relation between the dirty image and the desired image or $I(l, m)$ is alternatively written by convolution theorem as:

$$I_D = I \otimes B, \tag{3.10}$$

where the symbol $\otimes$ refers to convolution operation and B is given by

$$B(l, m) = \int\int S(u, v) \exp\left(i2\pi \left[ul + vm\right]\right) dudv. \tag{3.11}$$

B is called the synthesised beam. Its alternative name is point spread function or dirty beam, which arises as a result of the sampling function $S(u, v)$. The point spread function can be perceived the way a point source of light spreads in the spatial dimension while passing through an aperture. An approximation to the true image is produced by deconvolution (i.e., find solution to I in Eq.(3.10)) based on some added information and assumptions.

With regard to a discrete set of baselines (u_j, v_j), the dirty image is defined as

$$I_D(l, m) = \sum_j c_j V(u_j, v_j) \exp(2i\pi(ul + vm), \tag{3.12}$$

where c_j is an arbitrary coefficient modifying the sampling. Substituting the expression of visibility function $V(u_i, v_j)$ given in Eq.(1.5) into Eq.(3.12) yields

$$I_D = \int\int I(l', m') \left[\sum_j c_j \exp(2i\pi(u(l - l') + v(m - m')) \right] dl'dm' \tag{3.13}$$

The simplified form of 3.13 is written as

$$I_D = \int\int I(l', m') B_0(l - l', m - m')dl'dm' \tag{3.14}$$

Equation 3.14 can be rewritten as a convolution of the true intensity I with the synthesised beam B_0:

$$I_D = I * B_0 \qquad \text{and} \qquad B_0(l, m) = \sum_j c_j \exp(2i\pi(u_j l + v_j m)) \tag{3.15}$$

Where B_0 is the dirty beam centred at the origin. From the dirty image I_D and the known dirty beam B_0, one can generate the real image by the deconvolution process.

In this thesis, we used a modified 'CLEAN' algorithm initially developed by Högbom [73]. It is a non-linear, iterative mechanism that removes artefacts due to insufficient (u, v) coverage. The algorithm generally breaks down the intensity distribution into point source responses, and then replaces each one with the corresponding response to a clean 'beam'.

We went through the following basic steps of the 'CLEAN' algorithm so as to obtain the desired image of the source.

1. We determined the strength and location of the brightest pixel, $I(l_i, m_i)$, in the entire dirty image. The peak is assumed to be a result of a real signal, whereas the contribution of sidelobe responses is minor to the real emission.

2. By translating the dirty beam, $B(l, m) = F(S(u, v))$, we made the central pixel to be at the same location as $I(l_i, m_i)$. Then, we scaled it with a factor C to get $I(l_i, m_i) = CB(l_i + \Delta l, m_i + \Delta m)$

3. we subtracted from each pixel in the dirty image the corresponding value in the dirty beam. In this case, we defined a loop gain value $\Upsilon \ll 1$ to multiply the dirty beam. Thus, the residual is calculated as $R(l, m) = I(l_i, m_i) - C\Upsilon B(l_i + \Delta l, m_i + \Delta m)$.

4. We repeated step 2 iteratively until we ensure the removal of all significant source structure from the map.

5. We convolved the delta function in the cleaned model with the clean beam response. In other word, we replaced each delta function with a clean beam function of the corresponding amplitude.

6. Finally, we obtained the output by adding the residuals intensity from step 3 into the clean beam map.

The algorithm is implemented in CASA using the task name '*clean*'. The CLEAN image is expected to express a smooth version of the true image, though unavoidable noise and distortion can exist in the cleaned image.

The two of the important inputs of '*clean*' are image size ('*imsize*') in pixels of the map and cell size ('*cell*') in arcseconds of a pixel. These two quantities calculated by using the known values of the KAT-7 antenna. The primary beam (θ_{pb}), that depicts the area of the sky observed with the telescope, is a pivotal parameter in determining both parameters. Thus, the Full Width Half Maximum (FWHM) of primary beam of a uniformly illuminated antenna is given by [74]:

$$\theta_{pb} = \frac{1.22c}{\nu D} \times \frac{180}{\pi}, \tag{3.16}$$

where $\nu = 1827$ MHz and D= 12 m are the central frequency and diameter of the KAT-7, respectively. Hence, the primary beam (θ_{pb}) of the KAT-7 is about 0.8°.

On the other hand, the FWHM of the synthesized beam (θ_{sy}) of KAT-7 determines the interferometers resolution, where it is calculated from the maximum baseline B_{max} in number of wavelength. For KAT-7, $B_{max} \approx 200$ m, and hence the synthesised is calculated using

$$\theta_{sy} = \frac{\lambda}{B_{max}}, \tag{3.17}$$

where $\lambda = 16.4$ cm is the wavelength corresponding to the central frequency. The central lobe of the dirty beam has to be resolved not to be limited by the pixel size. In this case, we need to choose the cell size to be about a quarter of the FWHM synthesized beam. Therefore, the cell size (C_z) can be given by

$$C_z = \frac{\lambda}{4B_{max}} \tag{3.18}$$

Substituting the corresponding value of B_{max} in Eq.(3.18), the cell size approximately becomes 0.68 arcmin. We set the dimension of the images to be six times larger than the primary beam ($\sim 0.8^{\circ}$), and hence it is equal to 4.8°. Therefore, the associated image size (IS) is

$$\text{IS} = \frac{6 \times 60}{0.68} = 529 \text{ pixels} \tag{3.19}$$

For convenience, we have reduced the image size to 512, and the images obtained from KAT-7 are drawn in the square size of 512 × 512 as well as 0.5 arcmin × 0.5 arcmin of cell size. Furthermore, we used a threshold of 1.5 mJy[2], 2500 iteration cycles, natural weighting and robust of 0.5 as parameters to create the image.

It should be noted that the CLEAN algorithm works well when the true brightness distribution constitutes a few unresolved sources. Besides this constraint, the algorithm requires narrow emission region and small field of view for its successful implementation. In dealing with point sources, specially for AGNs as in this thesis, the algorithm is the favoured one to find the necessary scientific output from the images.

3.4 Examining Confusing Sources

During the CLEANing process, we examined for confusing sources located inside the KAT-7 FWHM of primary beam ($\sim 0.8^{\circ}$). Since the KAT-7 field of view is larger than either ATCA or VLA, there are inevitable confusing emission surrounding the source. Hence, reproducing and examining these sources in the image plane have to be performed properly so that confusing emission towards the source will be minimized appreciably. For this purpose, we extracted the whole lists of confusing sources located within 1° of a given source from NVSS (includes sources with `Dec` $\geq -30^{\circ}$) and SUMSS [75] [3] (includes sources with `Dec` $< -30^{\circ}$) catalogues. In this way, we identified the confusing sources surrounding our sample source properly.

After identifying confusing sources surrounding a given sample source, we generated masks around them in the image plane. By repeated iteration, we CLEANed the confusing sources until we obtained a residual image of noise-like distribution. In addition to this, we checked for over CLEANing (i.e. whether negative flux density around the field of view was produced) through the CASA's interactive display ('*viewer*').

[2] Using the KAT-7 parameters, the expected point source rms is given by $\Delta I = \frac{K}{\sqrt{N(N-1)(N_{IF})T_{int}\delta\nu}}$, where $K = \frac{0.12T_{sys}}{\eta_a}$, N is the number of antennas, T_{int} is the total on source integration time in hours, $\delta\nu$ is the effective continuum band width, N_{IF} is the number of spectral channels, T_{sys} is the system temperature , and η_a is antenna efficiency

[3] www.physics.usyd.edu.au/sifa/Main/SUMSS

3.4.1 Self-Calibration In Phase

We have so far discussed about calibration of the visibilities when the gains from a phase calibrator source are transferred to the target source. Observations for the calibrator and the target source are made in different direction and time. As a result of this, the gains for the calibrator may not be correct for the target source because the atmosphere may change in time and has varying spatial structure. Thus, we implemented self-calibration – which uses a model of the target source itself reconstructed from the data – to solve for improved values of the complex antenna gains. The reader can also refer Section 1.3.2 for detailed discussions on the principles of self-calibration.

We carried out self-calibration in CASA by using the task '*gaincal*'. The calibrated MS of each source was utilized as a model and put under the parameter '*vis*'. The gain solutions were written in a table assigned under '*caltable*'. We set the solution interval to be 5 minutes under '*solint*'. The minimum baseline per antenna ('*minblperant*') and minimum SNR ('*minsnr*') were set to be 4 and 3, respectively. We also implemented time dependent gain ('*gaintype=G*').

In the previous calibration procedures (Section 3.2), residual errors in phase calibration (i.e. causing coherence losses) induce significant errors (biases) in the measured flux densities. So, self-calibration in phase is vital so as to improve the accuracy in measuring the flux densities of the sources. This step is implemented by the CASA command '*calmode=p*', which stands for self-calibration in phase. No amplitude self-calibration was done.

We do not measure the absolute phase of a given source. Hence, self-calibration should be carried out by setting a zero phase on reference antenna, where we used the same antenna ('*refant=6*') as the initial calibration (3.1.3). This procedure of self-calibration in phase is causing the loss of all positional information about the source. As a result, uncertainty in the position measurement will occur. This suggests that the position measurement of each target source has to be derived from an image produced before any phase calibration. It is important to note that the positions of the phase calibrators are not measured independently, since it is assumed that their positions taken from the catalogues are their actual positions. So, measuring their positions do not provide any additional information, for they should be equivalent to their catalogue positions except for small coherence errors. Generally, self-calibration is stopped when the root mean square (rms) noise in the image stabilises. The flux density of each source was derived from the self-calibrated image using the procedure discussed in the next section.

3.5 Model Fitting To The 'CLEAN' Image

After successfully generating the 'CLEAN' image, we need to extract necessary parameters from each image. To do this, we implement a model that appropriately represents the intensity distribution of the final image. Since the sources in this thesis are expected to be unresolved, we have utilized two dimensional elliptical Gaussian function to estimate the desired parameters from the final 'CLEAN' images. In our case, the elliptical Gaussian is essentially specified by six parameters; where S is the total flux density; (l_0, m_0) are the cosine directions along the right ascension and declination with the phase tracking center; (a, b) are the Full Width Half Maxima (FWHM) along the major and minor axis; $\phi_{\mathtt{maj}}$ is the position angle of the major axis. By putting all these parameters in the elliptical Gaussian function, the intensity distribution model, $I_{\mathtt{md}}(l, m)$, is given by

$$I_{\mathtt{md}}(l,m) = S \exp\left(-\frac{1}{2}\left[\left(\frac{\sqrt{8\ln 2}\; l^{'}}{a}\right)^2 + \left(\frac{\sqrt{8\ln 2}\; m^{'}}{b}\right)^2\right]\right), \tag{3.20}$$

where $(l^{'}, m^{'})$ are cosine directions along the major and minor with respect to the center of the ellipse which is given by

$$\begin{pmatrix} l^{'} \\ m^{'} \end{pmatrix} = \begin{pmatrix} -\sin\phi_{\mathtt{maj}} & \cos\phi_{\mathtt{maj}} \\ \cos\phi_{\mathtt{maj}} & \sin\phi_{\mathtt{maj}} \end{pmatrix} \begin{pmatrix} l - l_0 \\ m - m_0 \end{pmatrix}. \tag{3.21}$$

If the actual image intensity distribution at each pixel is $I(l_i, m_j)$, then the parameters and error estimates in the target region are calculated from the method of maximum likelihood. By supposing the noise to be Gaussian in image plane $((l, m))$, the likelihood of the model is expressed as a product of Gaussian terms. This is given by

$$L \backsim \prod_{i=1}^{M_p}\prod_{j=1}^{M_p} \exp\left[-\frac{1}{2}\left(\frac{I(l_i,m_j) - I_{\mathtt{md}}(l_i,m_j;p_0,p_1,...,p_k)}{\sigma}\right)^2\right], \tag{3.22}$$

where M_p is the number of independent pixels in the image, $p_1, ..., p_n$ are parameters corresponding to the model image, and σ is the standard deviation of the image assuming that the errors are normally distributed. Multiplying Eq.(3.22) by negative logarithm will give the residual between the 'CLEAN' and model image:

$$\chi^2 = \sum_{i=1}^{M_p}\sum_{j=1}^{M_p}\left(\frac{I(l_i,m_i) - I_{\mathtt{md}}(l_i,m_j;p_1,...,p_n)}{\sigma}\right)^2. \tag{3.23}$$

The best fit parameters are obtained at the minimum point of χ^2. This is equivalent to taking the partial derivative of χ^2 with respect to the parameters and set to zero.

$$\frac{\partial \chi^2}{\partial p_k} = 0, \tag{3.24}$$

where $k = 1, ..., 6n$ and p_k are the parameters to be determined from the above condition.

By employing the above equations, the CASA task name *'imfit'* estimates the parameters of a given CLEANed image. In other words, the *'imfit'* fits a 2-dimensional Gaussian to the source of interest in the image plane to solve for the six parameters. The estimation is done by drawing a rectangular box around the CLEANed image and choosing the coordinates of the diagonal line (i.e., the bottom left and top right coordinates in terms of pixel values) for the parameter *'box'*. Then, the *'imfit'* output would give us the required quantities along with the uncertainties for a given source. In this way, the position, intensity and the source's emission size were estimated from the image. Nonetheless, the fitting does not necessarily give the exact values of the parameters owing to the ideal assumption that the noise related to the pixel has to be random and Gaussian. The model is only useful for point-like sources, if the source has a more complex structure, the model will not be appropriate.

3.6 Reliability Of The Parameters Determined By The Model Fitting

After estimating the position and integrated flux density of each source using *'imfit'*, we further rechecked the reliability of the values by comparing with SUMSS [4], and NVSS [5] catalogues. By considering the flux density of each source at 1.4 GHz from the catalogues, we extrapolated the respective flux density at the KAT-7 observing frequency (1.83 GHz), as explained in Section 1.3.6.

The reliability check has several advantages. For instance, we were able to redo the data reduction procedures when we encountered large offsets. This helped us to recognize errors resulting from calibration procedures. When the offsets remained the same after the redoing of the reduction, we compared the catalogue and derived images to check the presence of blended sources and extended structures. The next section therefore delivers a quantitative comparison between the catalogued and the KAT-7 positions.

[4] vizier.u-strasbg.fr/viz-bin/VizieR
[5] www.cv.nrao.edu/nvss/NVSSPoint.shtml

3.7 Positional Accuracy

As shown in Table 3.1, 14 sources were utilized to phase calibrate 33 sources. The position of each target source was derived relative to its phase calibrator, assuming that the chosen phase calibrator has accurately determined position. In this case, the catalogued positions of the selected phase calibrators are regarded as their true values. As we mentioned in Section 3.4.1, self-calibration in phase makes the position measurement uncertain. Hence, the positions of the target sources measured before self-calibration in phase were used for the cross-check between the catalogued and the derived positions .

For the purpose of the reliability check, the concatenated MS was considered for those sources which were observed more than once during the observation sessions. This improves the accuracy of measuring the positions of the target sources due to increasing the u-v coverage. Since the accuracies achieved for sources with concatenated MS and sources with a single MS should not be the same, we performed the reliability check for each category separately for consistency.

The Right Ascension (RA) and Declination (Dec) of each target source were derived from the image produced before self-calibration in phase using *'imfit'*. The catalogue positions were collected from online catalogues as discussed in Section 2.2 and summarized in Tables 3.2. Finally, we estimated the offset for each target source (i.e. the difference between the catalogue and derived position). The offsets along RA and Dec are presented in Table 3.2.

The derived positions contain errors in RA and Dec due to the unavoidable existence of noise in the images. These uncertainties (ϵ_R and ϵ_D) are given in Table 3.2 with respect to their the derived positions. The uncertainties given in the catalogued positions for the target sources are identical, despite different values are presented in NVSS and SUMSS[6] catalogues [75]. For example, for sources taken from NVSS (Dec $> -30°$), their uncertainties in RA and Dec are $0.45''$ and $0.6''$, respectively; whereas for sources taken from SUMSS (Dec $< -30''$), their uncertainties in RA and Dec are $1.5''$ and $1.7''$, respectively. Hence, the RA uncertainties for the catalogued positions lie between $0.45''$ and $1.5''$, whereas the corresponding Dec are between $0.6''$ and $1.7''$. Comparing these values with the position uncertainties of the KAT-7 images, $\sim 61\%$ of our sources' uncertainties in their RA scattered between $0.45''$ and $1.5''$; whereas $\sim 30\%$ of the sources' uncertainties scattered below $0.45''$. The remaining $\sim 9\%$ displayed uncertainties in their images above $1.5''$. Similar comparison in Dec showed that $\sim 46\%$ of our sources had uncertainties in their images between $0.6''$ and $1.7''$. The remaining $\sim 42\%$ and $\sim 12\%$ of the sources were found to have uncertainties below $0.6''$ and above $1.7''$, respectively.

[6] www.physics.usyd.edu.au/sifa/Main/SUMSS

TABLE 3.2: The catalogued and the measured positions of the selected target sources are presented in the table; the difference between the catalogue and measured position or offset is calculated. The table also contains the measurement errors as well as the offsets. The catalogued (RA (cat) and Dec(Cat))are taken from NVSS and SUMSS. The columns from left to right are: Source name; Right Ascension (J2000) (hour:minute:second) of the catalogued positions = RA (cat); Declination (J2000) (deg:arcminute:arcsecond) of the catalogued positions = Dec (cat); RA (KAT-7)$\pm\epsilon''_R$ and Dec (KAT-7) $\pm\epsilon''_D$ are measured positions by the KAT-7 along with their respective noises in the image. N is number of observations; $\Delta RA''$ and $\Delta Dec''$ are offsets in RA and Dec, respectively.

Source Name	RA(Cat)	Dec (Cat)	RA$\pm\epsilon''_R$ (KAT-7)	Dec $\pm\epsilon''_D$ (KAT-7)	N	$\Delta RA''$	$\Delta Dec''$
PKS J0010-4153	00:10:52.45	-41:53:10.80	00:10:52.49±0.60	-41:53:11.17±0.59	7	-0.60	0.37
PKS J0042-4414	00:42:12.36	-44:14:20.00	00:42:12.80±0.13	-44:14:34.61±0.14	7	-6.60	14.61
PKS J0044-3530	00:44:41.01	-35:30:33.70	00:44:41.54±0.50	-35:30:42.37±0.50	7	-7.95	8.67
PKS J0059+006	00:59:05.53	00:06:51.50	00:59:05.54±0.90	00:06:49.74±1.21	5	-0.15	2.03
PKS J0303-6211	03:03:50.81	-62:11:25.40	03:03:50.81±0.40	-62:11:25.99±0.38	8	-0.01	1.59
PKS J0309-6058	03:09:56.07	-60:58:39.90	03:09:56.04±0.81	-60:58:39.74±0.71	6	0.45	-0.16
PKS J0323+0534	03:23:20.31	05:34:11.90	03:23:20.30±0.45	05:34:10.59±0.59	6	0.15	1.31
PKS J0351-2744	03:51:39.45	-27:44:04.40	03:51:38.17±5.15	-27:44:09.08±6.03	6	19.20	4.68
PKS J0405-1308	04:05:33.94	-13:08:14.40	04:05:33.99±0.20	-13:08:12.99±0.25	6	-0.75	-1.41
PKS J0409-1757	04:09:06.68	-17:57:09.40	04:09:06.70±0.36	-17:57:08.06±0.44	6	-0.30	-1.33
PKS J0408-6544	04:08:20.28	-65:45:08.50	04:08:20.34±0.67	-65:45:09.52±0.67	6	-0.90	1.01
PKS J0420-6223	04:20:56.19	-62:23:37.90	04:20:55.44±0.36	-62:23:39.15±0.28	5	11.25	1.25
PKS J0442-0017	04:42:38.62	-00:17:42.80	04:42:38.54±1.45	-00:17:42.83±1.82	5	-1.20	0.03
PKS J0444-2809	04:44:36.25	-28:09:22.30	04:44:36.66±1.21	-28:09:44.39±1.52	5	-6.15	22.09
PKS J0453-2807	04:53:14.67	-28:07:36.60	04:53:14.72±0.54	-28:07:37.25±0.63	5	-0.75	0.65
PKS J0534+1927	05:34:44.51	19:27:21.70	05:34:44.49±0.28	19:27:20.97±0.51	4	0.30	0.73
PKS J0538-4405	05:38:50.18	-44:05:10.30	05:38:50.40±0.10	-44:05:09.20±0.17	5	-3.30	-1.10
PKS J0837-7003	08:37:11.23	-19:51:55.90	08:37:11.08±0.83	-19:51:58.24±0.99	5	2.25	2.34
PKS J0943-0891	09:43:36.86	-08:19:32.00	09:43:36.86±0.37	-08:19:31.53±0.47	4	0.01	-0.47
PKS J1130-1449	11:30:07.05	-14:49:27.20	11:30:07.06±0.25	-14:49:28.27±0.28	2	-0.15	1.07
PKS J1248-1959	12:48:23.98	-19:59:18.60	12:48:24.07±0.92	-19:59:18.15±0.89	4	-1.35	-0.45
PKS J1311-2216	13:11:39.29	-22:16:41.20	13:11:39.80±1.54	-22:16:41.47±1.80	3	-7.65	0.29
PKS J1517-2422	15:17:41.85	-24:22:20.00	15:17:41.17±0.91	-24:22:14.58±1.23	1	10.20	-5.42
PMN J1712-2809	17:12:57.30	-28:09:35.80	17:12:56.92±1.03	-28:09:34.61±1.22	2	5.10	-1.19
PKS J1744-5144	17:44:25.47	-51:44:43.10	17:44:25.55±1.18	-51:44:46.14±0.98	1	3.45	3.17
PKS J1830-3602	18:30:58.77	-36:02:30.00	18:30:58.86±0.50	-36:02:30.16±0.29	1	1.64	0.05
PKS J1935-4602	19:35:57.15	-46:20:43.10	19:35:56.83±0.86	-46:20:42.48±0.86	2	1.80	3.40
PKS J1924-2914	19:24:51.44	-29:14:31.00	19:24:51.11±0.11	-29:14:31.18±0.19	2	4.95	0.18
PKS J2129-1821	21:29:21.41	-18:21:22.90	21:29:21.45±1.00	-18:21:17.43±1.50	1	-0.60	-2.71
PKS J2131-2036	21:31:01.51	-20:36:56.10	21:31:01.47±0.36	-20:36:55.66±0.55	1	0.60	0.45
PKS J2151-3027	21:51:55.54	-30:27:53.60	21:51:55.55±0.78	-30:27:54.09±1.17	1	0.45	0.87
PKS J2152-2828	21:52:03.78	-28:28:29.00	21:52:03.69±1.18	-28:28:31.41±1.25	1	1.35	2.41
PKS J2219-2756	22:19:42.57	-27:56:26.00	22:19:42.79±1.98	-27:56:21.30±2.96	1	-3.44	-4.70

We analysed the offsets of the 33 target sources (see Table 3.2) by grouping them into two depending on the number of observations. The first group consists of 11 sources, representing only one observation. The second group comprises 22 sources, representing more than one observations. The reliability analysis for the second group was carried out based on the concatenated MS.

For the first group (the left panel of Figure 3.7), the offsets of 9 sources ($\sim 82\%$) rested within a radius $5''$. The remaining two sources, PKS J2219-2756 and PKS J1517-2422, showed deviations about $\sim 6''$ and $\sim 12''$, respectively. For the second group (the right panel of Figure 3.7), 16 sources ($\sim 73\%$) deviated by $\sim 5''$. The offsets of 4 sources ($\sim 18\%$) were estimated between $10''$ and $20''$. The remaining two sources, PKS J1311-2216 and PKS J0444-2809, showed deviations $\sim 8''$ and $\sim 23''$, respectively.

By combining the two groups, we analysed the overall deviation along the RA and Dec (see Figure 3.8). Accordingly, we found that the standard deviation along RA and Dec are $\sim 5.1''$ and $\sim 5.0''$, respectively. This indicates that the KAT-7 array can approximately measure position to the accuracy of $\sim 5''$. This result is acceptable taking into account the low resolution ($\sim 4'$) of the KAT-7.

Two sources, PKS J0444-2809 ($\Delta\texttt{RA} \approx -6.2''$, $\Delta\texttt{Dec} \approx 22.1''$) and PKS J0351-2744 ($\Delta\texttt{RA} \approx 19.2''$, $\Delta\texttt{Dec} \approx 4.68''$), showed exceptionally high positional offsets. We assume that such positional offsets could be due to the structure of the sources. In order to check the validity of our assumption, we compared the image of the KAT-7 with that of the NVSS for each source (see Figure 3.6). For example, the concatenated KAT-7 CLEAN image (i.e. the image before self-calibrated in phase) of PKS J0351-2744 has a synthesised beam $3.10'$, $2.64'$, and position angle (p.a)= $5.5°$. By extracting the FITS image of the same source from the NVSS catalogue, we convolved it with the given KAT-7 parameters for this source by using the CASA task name '*imsmooth*'. The position of the convolved NVSS image are: RA= 03:51:38.31 $\pm 5.92''$ and Dec= -0.27:44:13.85 $\pm 6.87''$. As a result, the offsets in RA and Dec of the convolved image reduced to $2.10''$ and $4.78''$, respectively.

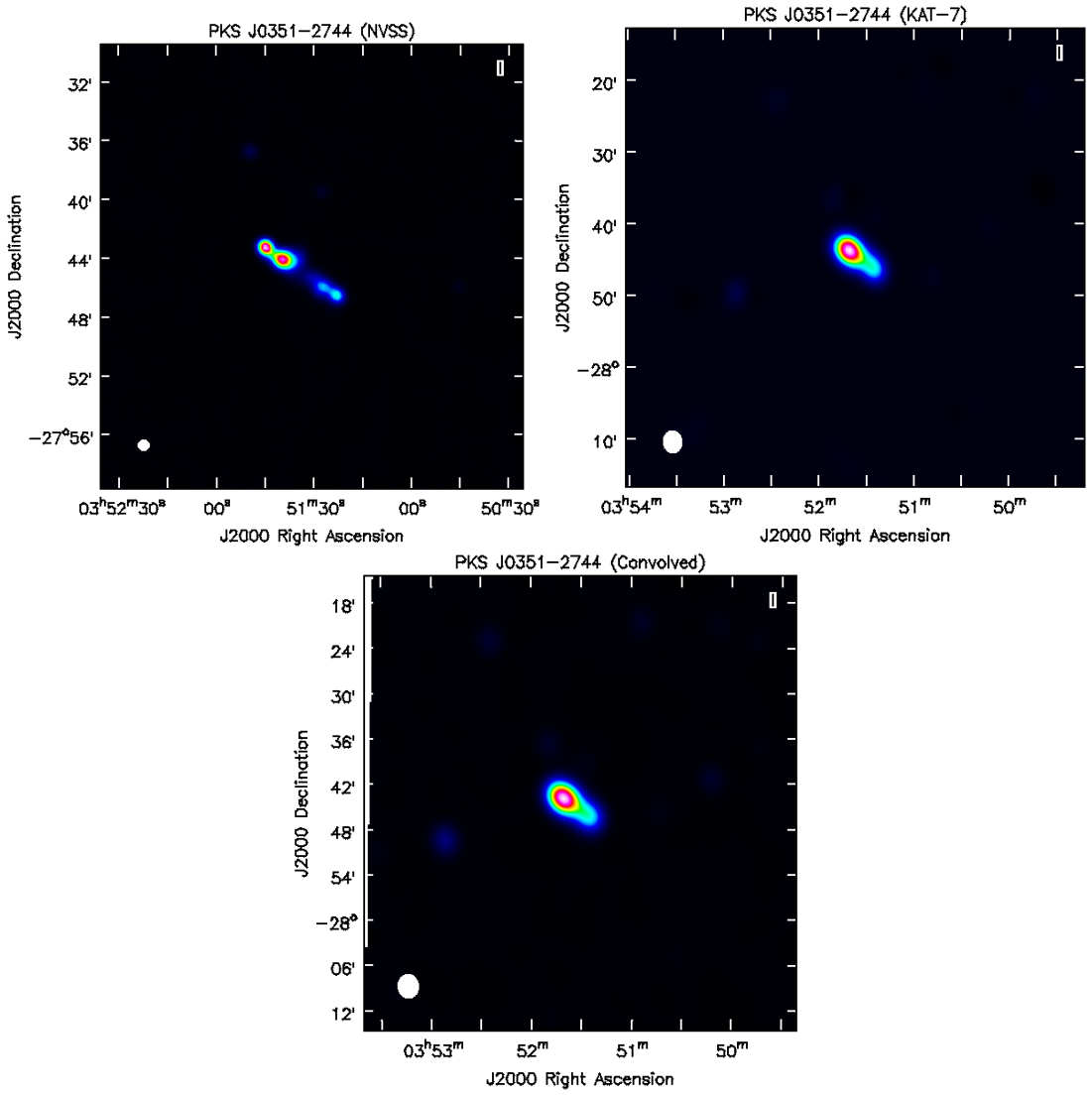

FIGURE 3.6: The top left side is the original NVSS image of PKS J0351-2744, the top right side is the same image from the KAT-7, and the bottom image is the convolution of NVSS beam with the KAT-7 clean beam.

We performed the same procedure for PKS J0444-2809 using its synthesised beam 4.68′, 2.90′, and p.a= 151°. The position of the convolved NVSS image was found to be: RA= 04:44:37.33 ±0.41″ and Dec= -28:09:46.071 ±0.52″. The offsets in RA and Dec changed to −10.05″ and 1.6″, respectively. So, this analysis showed that the relatively high offsets displayed in these two sources are not basically instrumental origin. Rather, it reveals how the resolution can specifically affect the determination of positions for extended sources.

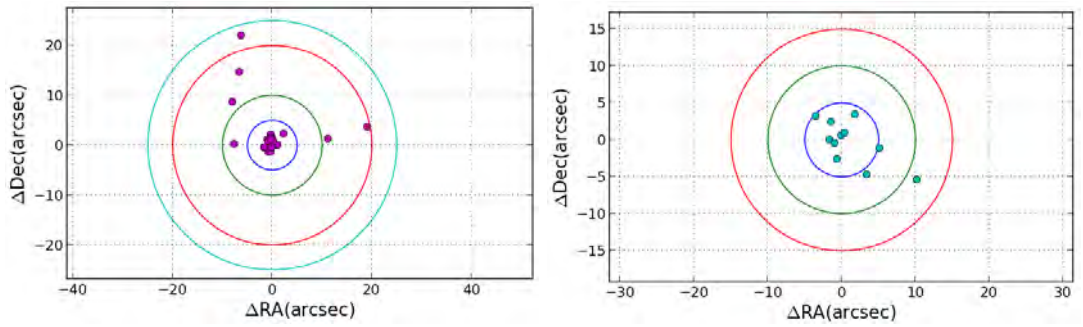

FIGURE 3.7: The left and right plots show the offsets of our target sources between the catalogued and the KAT-7 positions. In the left plot, each source was observed for more than one sessions and thus the offsets were evaluated for the concatenated visibilities. The sources' offsets on the left plot are represented by the points within radii of 5″, 10″, 20″ and 25″. The right panel depicts the offsets of the target sources that were analysed by one observation. The points on the right plot located within radii of 5″, 10″, and 15″ represent the sources' offsets.

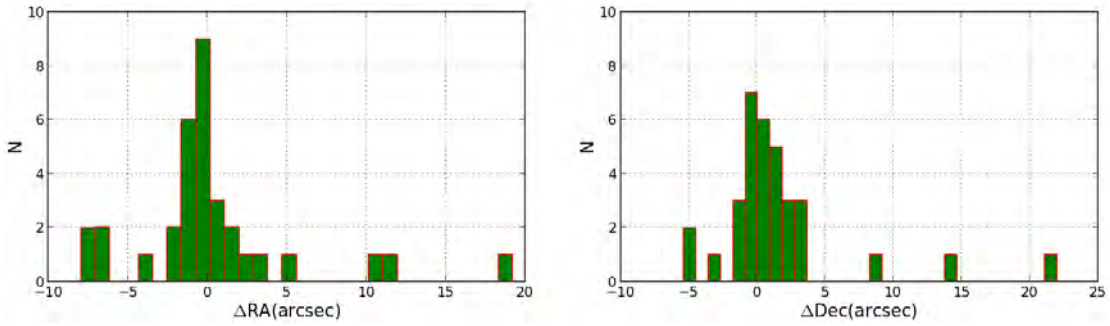

FIGURE 3.8: The bar charts depict how many of the sources exhibit small or large positional offsets along the RA (left) and Dec (right). The standard deviation along RA and Dec are $\sim 5''.1$ and $\sim 5''.0$

3.8 Flux Density Accuracy

We initially checked the suitability and flux density accuracy of KAT-7 using the well known flux standard sources, namely 3C147 and 3C48. These sources were observed on Oct 27, 2012, Nov 7, 2012, and Feb 5, 2013 along with the flux density calibrator, PKS J1939-6342. After performing proper flagging and calibration as mentioned in Section 3.1, we determined their flux densities by bootstrapping with PKS J1939-6342 using the task '*fluxscale*'. We assumed their catalogued positions to be the true positions of the sources. The calibrated images were self-calibrated in phase and then the flux densities of the sources were calculated on the specified dates; where the results are given in Table 3.3.

In order to check whether their flux densities obtained from the KAT-7 were consistent with other radio data, we compared their measured fluxes with the analytic expressions

determined by the VLA between 500 MHz and 50 GHz. The analytic expressions for 3C147 and 3C48 as given by [71] are:

$$\log(S_E) = 1.318 - 0.741\log(\nu) - 0.167\log(\nu)^2 + 0.015\log(\nu)^3, \tag{3.25}$$

and

$$\log(S_E) = 1.448 - 0.673\log(\nu) - 0.211\log(\nu)^2 - 0.041\log(\nu)^3, \tag{3.26}$$

where S_E is the expected flux density in Jy and ν is the frequency in GHz. Thus, the expected flux densities for 3C147 and 3C48 at the KAT-7 frequency, $\nu = 1.83$ GHz become 18.03 Jy and 12.95 Jy, respectively.

In addition to the above two sources, we also checked the suitability and accuracy of 3C286 as measured by the KAT-7. This source was observed only once (i.e on Feb 11, 2013) along with PKS J1939-6342. Using the method described above, we derived the flux density of 3C286 with respect to PKS J1939-6342. The measured flux density was found to be 13.195 ± 0.025 Jy. The spectral flux density of 3C286 as determined by Perley et al [17] between 1 GHz and 50 GHz is given by:

$$\log(S_E) = 1.252 - 0.461\log(\nu) - 0.172\log(\nu)^2 + 0.034\log(\nu)^3, \tag{3.27}$$

Thus, the expected flux density of 3C286 at 1.83 GHz is 13.176 Jy.

The comparison between their expected (S_E) and measured ($\langle S_{ms} \rangle$) flux densities is calculated using a fractional difference equation:

$$\Delta S/S_E = \frac{\langle S_{ms} \rangle - S_E}{S_E}. \tag{3.28}$$

TABLE 3.3: The table illustrates the flux densities of 3C147 and 3C48 (observed on the same day) measured after self-calibration in phase by bootstrapping with PKS J1939-6342. The flux fractional difference ($\Delta S/S_E\%$) is calculated by taking into account the measured flux density, S_{ms} and the expected flux density, S_E.

Source	S_E Jy	S_{ms}± err (Jy) (Oct 27 2012)	S_{ms}± err (Jy) (Nov 7 2012)	S_{ms}±err (Jy) (Feb 5 2013)	$\Delta S/S_E\%$ (Oct 27 2012)	$\Delta S/S_E\%$ (Nov 7 2012)	$\Delta S/S_E\%$ (Feb 5 2013)
3C147	18.03	18.24 ± 0.03	18.23 ± 0.09	17.78 ± 0.01	1.16	1.09	-1.41
3C48	12.95	13.22 ± 0.04	13.13 ± 0.01	13.15 ± 0.01	2.04	1.39	1.52

The flux fractional deviations for 3C147 and 3C48 at each session were found to be less than 2% as observed in Table 3.3. Whereas, the fractional deviation for 3C286 was

found to be 0.15%. These results can be considered as initial proofs whereby the KAT-7 data is almost on the same flux scale as other radio data.

Similarly, we analysed the fractional flux density of the 47 sources. For these sources, however, we used their expected flux densities estimated at the KAT-7 observing frequency, as mentioned in Section 2.2. $\langle S_{ms} \rangle$ in Eq (3.28) for these sources represents the average flux density $\langle S \rangle$ of a source taken at different times during the KAT-7 observations.

The fractional flux density differences calculated for these sources (as shown in Figure 3.9) indicated that 33 sources ($\sim$ 71%) deviated from the expected flux densities by less than 10%. 9 sources ($\sim$ 19%) showed 10% up to 20% variation from the expected flux densities, and 3 sources ($\sim$ 6%) strayed between 20% to 50% from the expected flux densities. The remaining two sources, that showed more than 50% fractional deviation from their predicted flux densities, are PKS J2151-3027 ($\sim$ 86.5%) and PKS J0538-4405 ($\sim$ 150%). The high deviations seem to be due to the flux variability characteristics of these sources, and the literature reviews presented for these sources in Section 2.4 also asserted the claim.

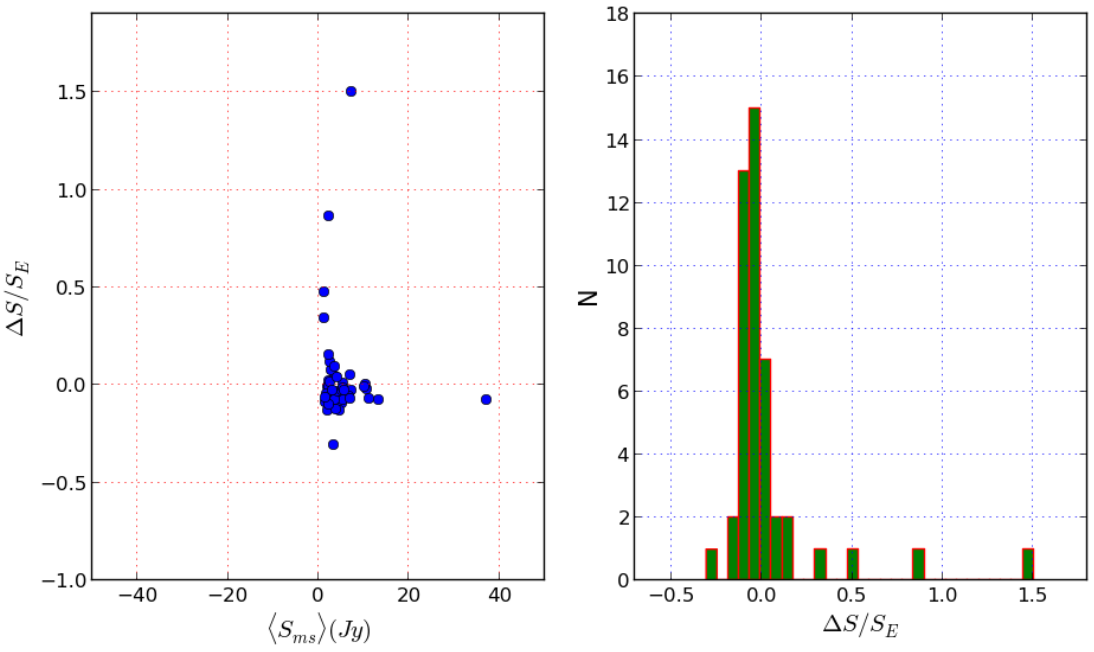

FIGURE 3.9: The left panel shows the fractional difference of the expected flux density as a function of the measured flux densities. The number of sources against their fractional difference is represented by the bar chart as shown on the right panel. The flux density of the majority of the sources ($\sim$ 71%) deviated from the expected flux densities by less than 10%.

3.9 Spectra Of The Sample Sources

This section focuses on the spectral energy density (SED) properties of the sources by considering the flux densities of the sources at different frequencies. As emphasised in Section 1.3.6, the spectral index of the source comprises a crucial information about the emission mechanism. In our case, the sources are assumed to follow the relation $S \propto \nu^{\alpha}$ because of their non-thermal emission mechanism. In order to prove whether the sources are abided by the assumed power law relation, we excerpted the flux densities and frequencies measured by various telescopes.

As the sources in this thesis were observed at a frequency of 1827 MHz, we included frequencies that range from 843 MHz up to a maximum of 4885 MHz. Accordingly, we collected the flux densities measured by:

- the Molongo Observatory Synthesis (MOST) at 843 MHz
- the NRAO VLA Sky Survey (NVSS) at 1400 MHz
- Parkes Radio Sources Catalogue (PKS) 2700 and 4850 MHz

The compiled values are found in SUMSS catalogues under the specific entry SPECFIND [7] for all our sources. Additionally, the flux at 1827 MHz obtained from the KAT-7 in this thesis is included to complement the analysis.

After excerpting the multi-frequency data, we implemented the flux density versus frequency relationship to fit the data. For convenience, we multiplied the relation $S \propto \nu^{\alpha}$ by logarithm to convert into a linear form:

$$\log(S) = C + \alpha \log(\nu), \tag{3.29}$$

where C is an arbitrary constant which is determined along with the spectral index (α) by using the least square method. The method provides a best fit for the given data with a minimum uncertainty while estimating the spectral index of each source. As can be seen from Figure 3.10 through Figure 3.13, the relation given in Eq.(3.29) holds true for most of the sources with a minimum deviation from the real data points.

[7] vizier.u-strasbg.fr/viz-bin/VizieR

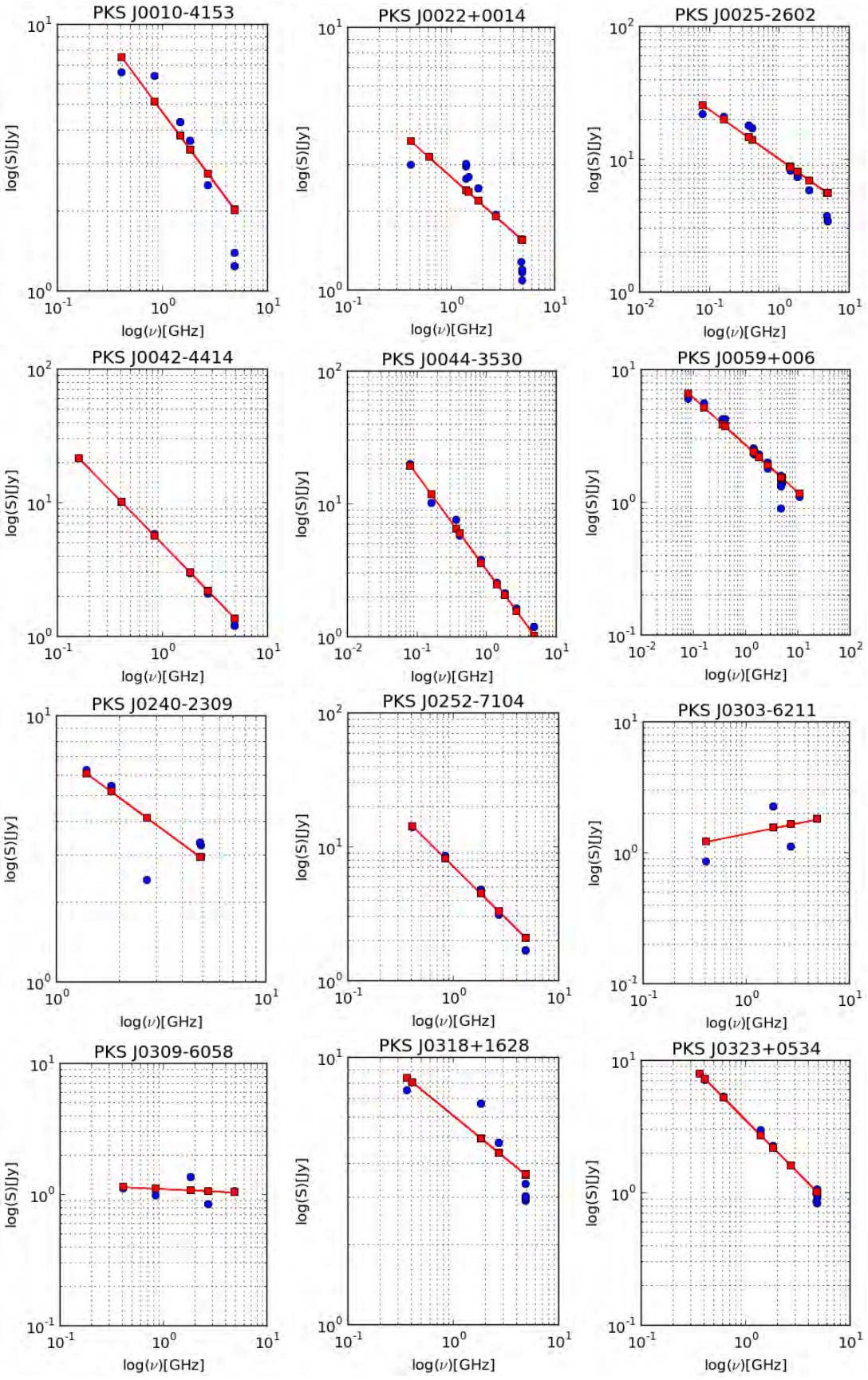

FIGURE 3.10: The flux density versus frequency relation of the sources. The source's name is written on the top of each plot. We used the relation $S \propto v^{\alpha}$ to fit the flux densities and frequencies extracted from the catalogues and the KAT-7 for each source. The best fit to the data points using least square method is shown by red lines, and the blue points are the actual data points measured by different interferometers, including the KAT-7 at 1.83 GHz.

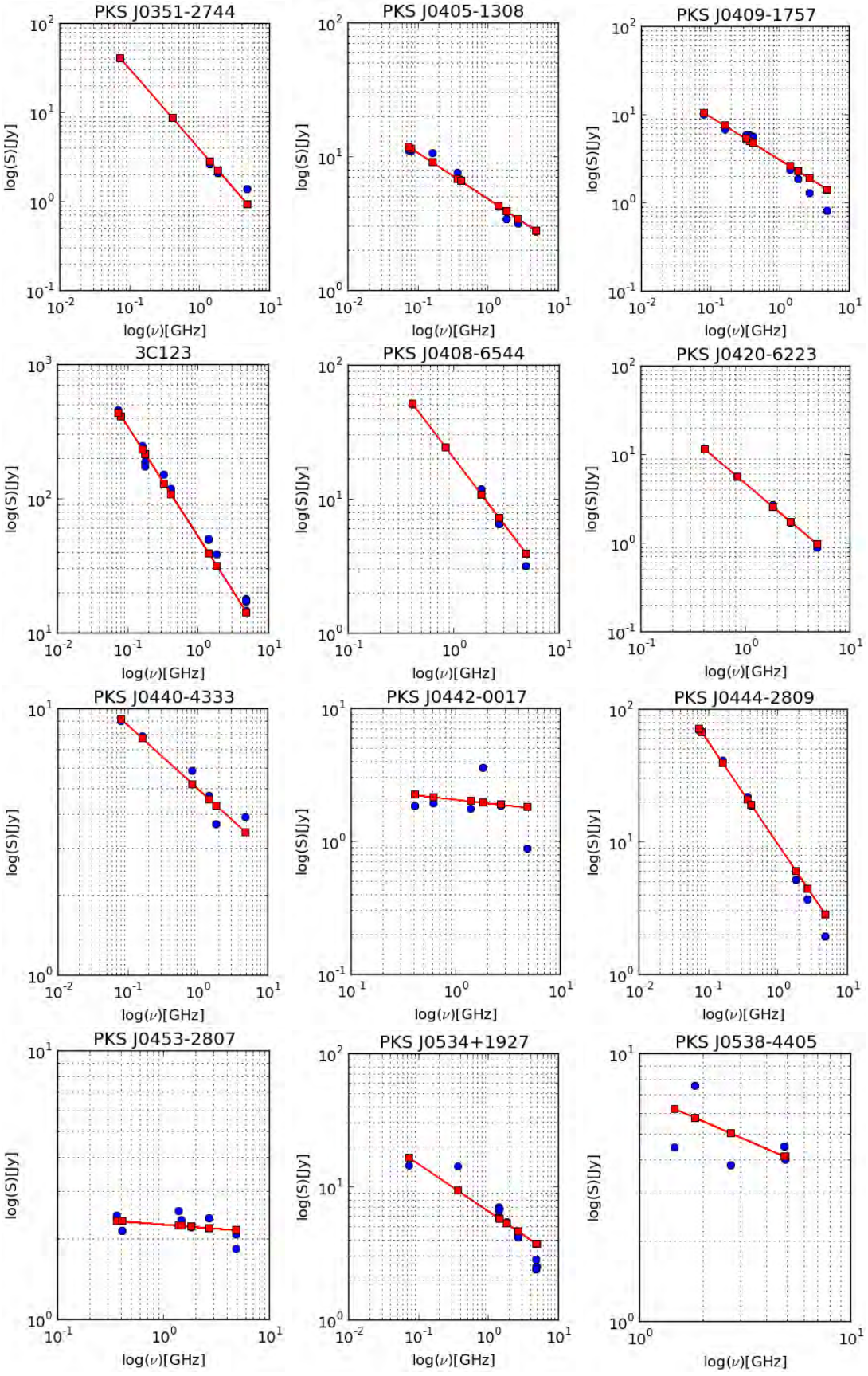

FIGURE 3.11: The flux density versus frequency relation of the sources. The source's name is written on the top of each plot. We used the relation $S \propto v^{\alpha}$ to fit the flux densities and frequencies extracted from the catalogues and the KAT-7 for each source. The best fit to the data points using least square method is shown by red lines, and the blue points are the actual data points measured by different interferometers, including the KAT-7 at 1.83 GHz.

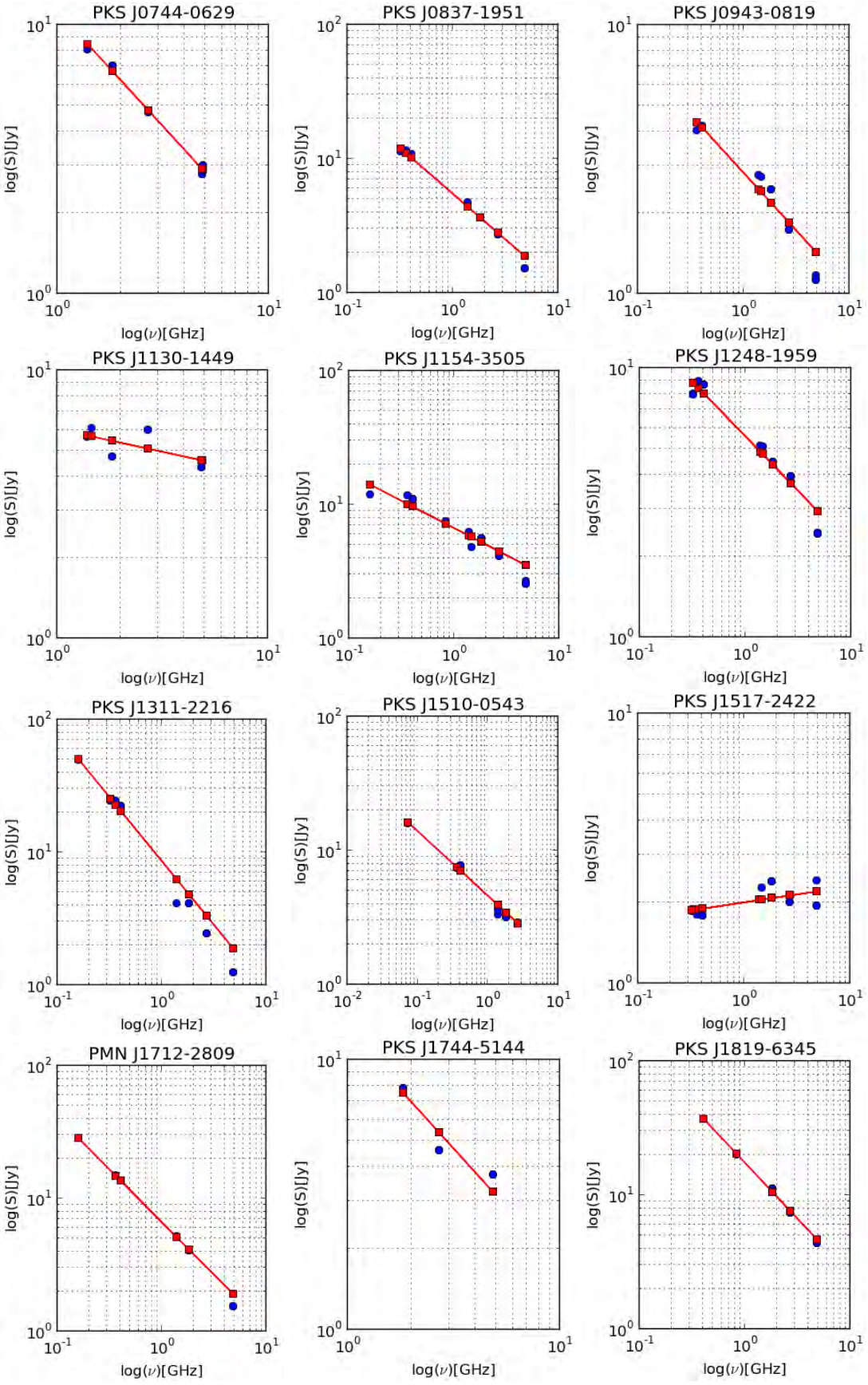

FIGURE 3.12: The flux density versus frequency relation of the sources. The source's name is written on the top of each plot. We used the relation $S \propto v^{\alpha}$ to fit the flux densities and frequencies extracted from the catalogues and the KAT-7 for each source. The best fit to the data points using least square method is shown by red lines, and the blue points are the actual data points measured by different interferometers, including the KAT-7 at 1.83 GHz.

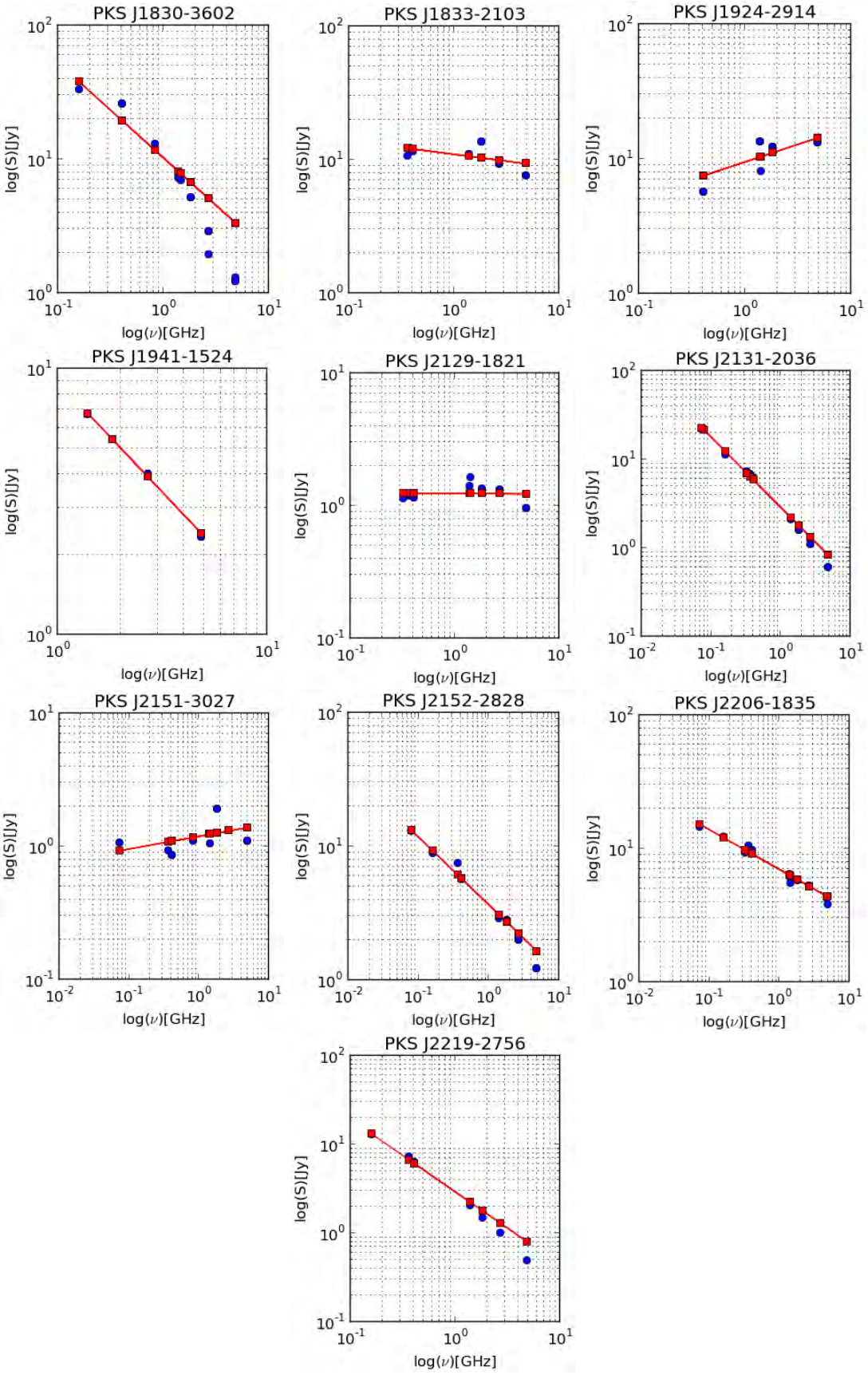

FIGURE 3.13: The flux density versus frequency relation of the sources. The source's name is written on the top of each plot. We used the relation $S \propto v^{\alpha}$ to fit the flux densities and frequencies extracted from the catalogues and the KAT-7 for each source. The best fit to the data points using least square method is shown by red lines, and the blue points are the actual data points measured by different interferometers, including the KAT-7 at 1.83 GHz.

3.10 Summary

The main points presented in this chapter are:

- We discussed a step by step data reduction procedures for the radio data observed by the KAT-7 for this thesis. We explained how the flux densities of the phase and target sources were estimated using the flux-density calibrator (PKS J1939-6342). Similarly, the criteria for selecting phase calibrators and target sources were discussed in detail. Based on the criteria, we identified 14 phase calibrators and 33 target sources.

- Confusing sources around a field of view of 1° were examined for the phase calibrators and target sources. We extracted the confusing sources surrounding a particular source from the NVSS and SUMSS catalogues. The flux densities of the phase and target sources were derived after examining for confusing sources and self-calibration in phase. However, the positions of all the target sources were determined before self-calibration in phase.

- The reliability check for position of each target source was carried out by comparing with the catalogued value. The flux density of each source obtained from the KAT-7 was also compared with the extrapolated flux density at 1.83 GHz.

- We examined whether the spectral energy density of each source follows the expected power law relation ($S \propto \nu^{\alpha}$). The flux density of each source measured at 1.83 GHz for this thesis is included in the analysis along with the flux density measured in other frequencies from different arrays.

Chapter 4

Results and Discussion

This section discusses the statistical methods applied to quantitatively determine the flux density variability of the sources. After the statistical analysis, we will identify which of the sources can be potential flux-density calibrator candidates.

4.1 Systematic Error Estimation

In order to study the flux density variability of our source, we initially extract the flux density of each source (i.e. measured at a specific time) from the self-calibrated CLEANed image using Gaussian fitting, as discussed in Section 3.5. In this regard, the specific source at a certain time, t_1, has a flux density along with its corresponding measurement uncertainty. The uncertainty in this case is related to a random error due to estimating a flux density of a source from its CLEANed image. The total error, however, comes as a result of random error as well as systematic error during data processing procedures. The estimation of the latter has no formal procedure, but we apply the following flexible assumption.

Our assumption relies on the fact that the systematic error increases or decreases the flux of a source by some percent of its measured flux taken at a specific time. The systematic error is mainly caused by flux transfer (bootstrapping) from the flux calibrator to the target source. The VLA calibrator manual prepared by Perley et. al [1] noted that there would be a systematic error of 3 to 5% of the measured flux due to bootstrapping.

To determine the systematic error in our case, we selected 3C123 because it has been particularly well-studied and has been shown to have a very constant flux density over time, as confirmed by Perley et. al [17] over 30 years of observations of 3C123. Hence,

[1] https://science.nrao.edu/facilities/vla/docs/manuals

we use 3C123 as our reference source to predict the systematic error, assuming that any apparent flux variability of this source is due to systematic error.

To estimate the systematic error we set the reduced χ^2 to unity for our observations. Perley et. al [17] found a relation between the spectral flux density (S in Jy) of 3C123 and its frequency (ν_G in GHz):

$$\log(S) = 1.8077 - 0.8018\log(\nu_G) - 0.1157\left[\log(\nu_G)\right]^2 . \tag{4.1}$$

Substituting ν_G= 1.83 GHz into Eq.(4.1) would give the expected flux density or S = 38.84 Jy. Nonetheless, the derived flux densities via the KAT-7 for this source were found to be variable with time as shown in Table 4.1 which attribute to systematic error in our observations.

TABLE 4.1: The table illustrates the flux densities of 3C123 measured at different times along with the corresponding random errors by the KAT-7.

Date	Oct 14 2012	Nov 6 2012	Nov 14 2012	Feb 16 2013	Feb 23 2013
Flux S_i in Jy	37.31	39.07	38.13	34.22	38.13
Random error σ_i in Jy	0.47	0.24	0.19	0.23	0.28

The reduced Chi-square (χ^2_r) is:

$$\chi^2_r = \frac{1}{N-1}\sum_{i}^{N}\left[\frac{(S_i - S_{1.83})^2}{\sigma_i^2 + \sigma_s^2}\right], \tag{4.2}$$

where N is the number of observations, S_i is the measured flux at specific time, $S_{1.83}$ is the expected flux at 1.83 GHz, σ_i is the random error while deriving a flux at a particular time, and σ_s is the systematic error.

By setting this equation to one and solving for σ_s we find σ_s= 1.98 Jy. This is equivalent to 5.1 % of 38.84 Jy, which is the expected flux density of 3C123 at 1.83 GHz, slightly larger than the systematic errors in the literature. Based on this result, we assign a 5% systematic error of the measured flux density to all sources under consideration and add this in quadrature with the statistical errors for all sources.

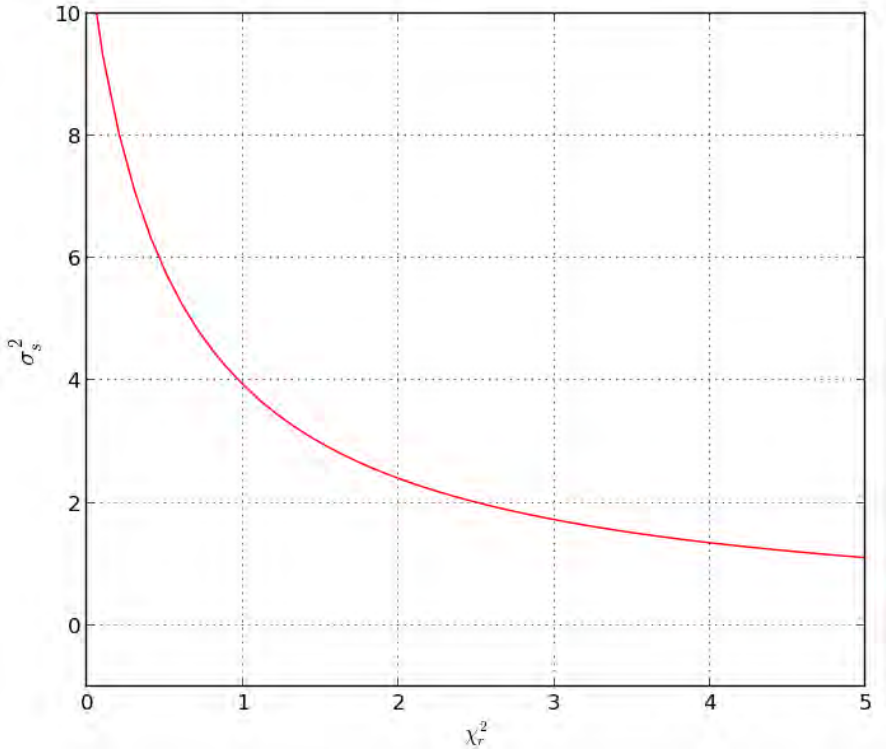

FIGURE 4.1: Reduced Chi-square (χ_r^2) against systematic error square (σ_s^2). The systematic error square given in Eq. 4.2 is estimated by numerical iteration. σ_s^2 converges to 3.92 ($\sigma_s = 1.98$) at χ_r^2 =1. This means the systematic error is about 5% of 38.84 Jy – the assumed flux density of 3C123 at 1.83 GHz as calculated by Eq. (4.1).

4.2 Weighted Flux Density, Mean Flux Density And Total Error

Our flux density measurement for each source has the form $S_i(t_i) \pm \delta_{ci}$; where $S_i(t_i)$ for $i = 1, 2, ..., N$ is the flux measurement of a particular source at a certain time t_i; δ_{ci} is the total error resulting from the five percent flux transfer (bootstrapping) uncertainty and the random error. We estimate the total error by adding in quadrature the systematic error ($0.05S_i$) and random error, σ_i, as

$$\delta_{ci} = \sqrt{(0.05S_i)^2 + \sigma_i^2}. \tag{4.3}$$

The weighted average flux density of a source for the N individual measurements is, therefore, given by [76]:

$$\langle S \rangle_w = \frac{\sum_i^N S_i \frac{1}{\delta_{ci}^2}}{\sum_i^N \frac{1}{\delta_{ci}^2}}. \tag{4.4}$$

The inverse weighted average error corresponding to the weighted average flux density for N individual measurements is given by [76]:

$$\langle\sigma\rangle_w = \sqrt{\frac{N}{\sum_i^N \frac{1}{\delta_{ci}^2}}}. \tag{4.5}$$

Hence, the flux density measurement for an individual source in this thesis is reported as $\langle S\rangle_w \pm \langle\sigma\rangle_w$.

The mean flux density of a source is defined by:

$$\langle S\rangle = \frac{\sum_i^N S_i}{N}. \tag{4.6}$$

Additionally, the spread of a flux density in each source about the mean $\langle S\rangle$ is defined by a standard deviation:

$$\sigma = \sqrt{\frac{\sum_i^N (S_i - \langle S\rangle)^2}{N}}. \tag{4.7}$$

4.3 Flux Variability Measures

The flux density variability of a source has been studied by applying a number of metrics to quantify variability. In this thesis, we adopt three different metrics.

The first is the variability index [77] which is defined as:

$$\mathtt{VI} = \frac{S_{\mathtt{max}} - S_{\mathtt{min}}}{S_{\mathtt{max}} + S_{\mathtt{min}}}, \tag{4.8}$$

where $S_{\mathtt{max}}$ and $S_{\mathtt{min}}$ represent the maximum and minimum flux densities of a source in the entire observations, respectively. The variability index `VI` provides a measure of the maximum observed fractional variation of a source. However, this quantity cannot capture all aspects of variability since it depends on only two flux values and ignores the remaining measurements and is sensitive to outliers. However, we use `VI` in this thesis as one summary of variability.

The second metric is the modulation index defined by [78, 79] and given by:

$$\mathtt{MI} = \frac{\sigma}{\langle S\rangle}, \tag{4.9}$$

where σ and $\langle S \rangle$ are given by Eq (4.6) and Eq (4.7), respectively. The modulation index quantifies the fractional variation of the peak flux density relative to the mean. It is a good indicator of the strength of variability because it uses all the flux density measurements of a source taken at different times. When we have only two flux densities measured at two different times, then the source's `MI` is equal to `VI`.

The third metric is the de-biased modulation index. It takes into account the random and systematic uncertainties of a flux density measurement derived at a particular time. According to Chen et al. [76], the de-biased modulation index, $\mathtt{M}_d$, is defined as:

$$\mathtt{M}_d = \frac{\langle \sigma \rangle_w}{\langle S \rangle_w} \sqrt{\frac{\chi^2}{N-1} - 1}, \tag{4.10}$$

where $\langle \sigma \rangle_w$ and $\langle S \rangle_w$ are given by Eq 4.4 and Eq 4.5, respectively. The Chi-square χ^2 is defined as

$$\chi^2 = \sum_i^N \frac{(S_i - \langle S \rangle_w)^2}{\delta_{ci}^2}, \tag{4.11}$$

$\mathtt{M}_d$ yields an imaginary value for χ^2 when $\frac{\chi^2}{N-1} < 1$. This happens about 50% of the time even when the error bars are correct (since if the model and errors are correct, the expected value of the reduced χ^2 should be unity). However, an imaginary $\mathtt{M}_d$ may also signal that the errors have been overestimated. We will see that many of our sources have imaginary $\mathtt{M}_d$, as discussed below.

4.4 `MI` And `VI` Variability Metrics Result

We follow [79] in referring to an `MI` value of 0.05 as a flux variation of 5%. The analysis based on `MI` (left panel of Figure 4.2) indicated that 30 out of 38 sources ($\sim$ 79%) showed flux variation of less than 5%; 6 out of 38 sources ($\sim$ 16%) revealed 5% to 10% flux variation. The remaining two sources, PKS J0538-4405 and PKS J0351-2744, displayed 11.67 % and 28.59% flux variation from their average value, respectively.

The `VI`s of 23 out of 38 sources ($\sim$ 61%) were found to be less than 5% (right panel of Figure 4.2); whereas the `VI`s of 12 sources ($\sim$ 32%) extended from 5% to 10%. The remaining three sources, PKS J0442-0017, PKS J0538-4405, and PKS J0351-2744, revealed 12.83%, 17.82%, and 41.76% variation between their maximum and minimum fluxes, respectively.

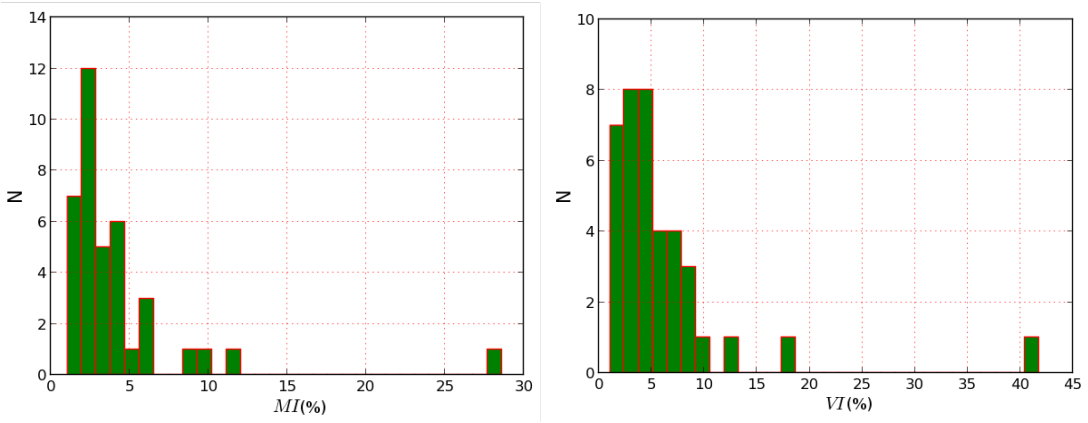

FIGURE 4.2: The histogram describing the modulation index (MI) [left panel] and variability index (VI) [right panel] of the sources. Majority of the sources ($93-95\%$) have MI and VI values $\leq 10\%$.

4.5 $\mathtt{M}_d$ Variability Metric Result

As stated by Chen et al. [76], the variability analysis based on $\mathtt{M}_d$ corrects for the obvious bias in MI in the case of noisy measurements. The measurement uncertainties are the most decisive parameters to find out a plausible $\mathtt{M}_d$. As we can see from Eq.(4.10), $\mathtt{M}_d$ is real when $\chi^2 \geq N-1$ and imaginary when $\chi^2 < N-1$.

We estimated the systematic error, which is presumably the dominant error, by assuming 3C123 has constant flux densities over time (see Section 4.1). Then, we applied an estimation of 5 % (of measured flux density) systematic error to all sources. In this regard, the $\mathtt{M}_d$ of 3C123 has to be small because of the assumption that it is invariable source or its $\chi^2 \rightsquigarrow N-1$ at 5% systematic error. However, calculating the $\mathtt{M}_d$s of the other sources with 5% systematic error yielded imaginary values for most of the sources.

From the unbiased variability metric ($\mathtt{M}_d$) obtained at 5% systematic error, we can summarize the following points.

- Out of the 38 sources analysed using $\mathtt{M}_d$ only 11 sources ($\sim 29\%$) had real $\mathtt{M}_d$s (see Table 4.2 and 4.2).
- Four among the 11 sources were distinguished for having high magnitudes of variabilities according to the three metrics. These sources are: PKS J0351-2744 ($\mathtt{M}_d = 32.8\%$, $\mathtt{MI} = 28.9\%$, $\mathtt{VI} = 41.8\%$), PKS J0442-0017 ($\mathtt{M}_d = 9.5\%$, $\mathtt{MI} = 8.7\%$, $\mathtt{VI} = 12.8\%$), PKS J0538-4405 ($\mathtt{M}_d = 14.6\%$, $\mathtt{MI} = 11.6\%$, $\mathtt{VI} = 17.82\%$), and PKS J1833-2103 ($\mathtt{M}_d = 12.4\%$, $\mathtt{MI} = 9.5\%$, $\mathtt{VI} = 9.5\%$). More specially, PKS J0351-2744 is a highly variable source according to the three metrics.

- The metrics of 8 ($\sim$ 21%) out of 38 sources were calculated relying on only two data points (see Table 4.3). Hence, their metrics may not sufficiently ensure their flux variabilities. Hence, we need to incorporate more data so as to confidently justify their variabilities.

4.6 Simulation Of Debiased Modulation Index, $\mathtt{M}_d$

To determine whether the observed imaginary $\mathtt{M}_d$ values were unexpected for each of our sources, we simulate each source's observations with Monte Carlo methods. Assuming that each source truly is constant, and taking the dates and measured errors for our observations, we simulate for each source 30,000 Gaussian realizations of the flux densities appropriate for each source, and hence this gives 30,000 measurements of $\mathtt{M}_d$ for each source.

Thus, the simulated flux density, S_{sm}, for a given observation of a given source is given by:

$$S_{sm} = \langle S \rangle_w + N(0, \delta_{ci}), \tag{4.12}$$

where $N(0, \delta_{ci})$ describes a standard mean-zero normal distribution with standard deviation δ_{ci}. For each source and observation we apply this 30,000 times and compute the resulting $\mathtt{M}_d$ values that would result from these simulated observations in the obvious way by computing the χ^2 in each case.

The simulated Chi-square is:

$$\chi^2_s = \sum_i^N \frac{(S_{sm} - \langle S \rangle_w)^2}{\delta^2_{ci}}. \tag{4.13}$$

Hence, the simulated de-biased modulation index $\mathtt{M}_{sd}$ would be:

$$\mathtt{M}_{sd} = \frac{\langle \sigma \rangle_w}{\langle S \rangle_w} \sqrt{\frac{\chi^2_s}{N-1} - 1}, \tag{4.14}$$

In our simulation we made an assumption that the flux density of a source has a constant flux density. Hence, the Gaussian distribution of $\mathtt{M}_{sd}$ describes the possible values of $\mathtt{M}_{sd}$ if the source's flux density is constant. According to this, if the source's $\mathtt{M}_d$ is less than the majority of the $\mathtt{M}_{sd}$ in the distribution, then it is compatibly with no flux variability

since all the M_{sd} were simulated from a non-variable model. To quantify this, we compute the fraction, f, of simulations with $M_{sd} \geq M_d$ for each source. Only if $f < 0.05$ is there reasonable evidence of variability since in this case there is only a 5% probability of seeing such a large value of M_d due to statistical fluctuations given that the source really is constant and the errors are Gaussian.

4.7 Modulation Index Analysis: M_d Versus M_{sd}

In this section, we will focus on the comparison between the actual de-biased modulation index, M_d, and the simulated set of indices, M_{sd}.

Of the 11 sources with real M_d, three sources (PKS J0351-2744, PKS J0442-0017 and PKS J0538-4405) show statistically significant evidence for variability with less than 0.6% of the 30,000 Gaussian simulations in each case having M_{sd} values as large as the observed M_d values.

All other sources were statistically compatible with being constant other than PKS J1833-2103 which showed some evidence of variability with only $\sim 5.3\%$ of the simulations having a large value of M_{sd} than the observed M_d.

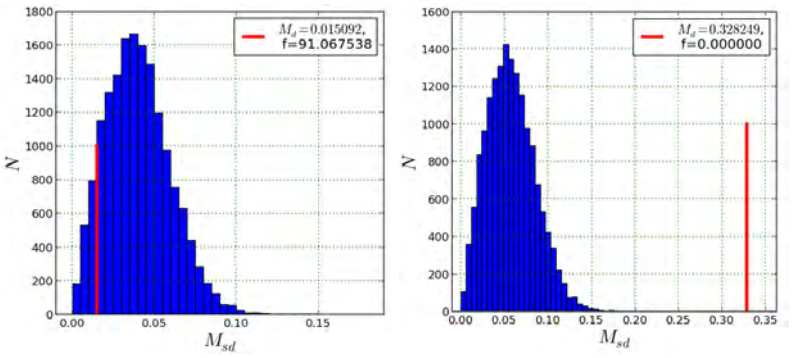

FIGURE 4.3: The histogram of the real simulated de-biased modulation indices along with our observed value (shown by the vertical red line) for 3C123 (left) and PKS J0351-2744 (right). The fraction of simulated modulation indices, f, larger than the observed value, along with the observed value is shown at the top of the figure. A value of $f < 0.1$ (0.05) suggest that the source is variable since they correspond approximately to probabilities of 10% (5%) that the source is actually constant but has a large M_d due to Gaussian error fluctuations. From this it is clear that PKS J0351-2744 is a highly variable source according to this test.

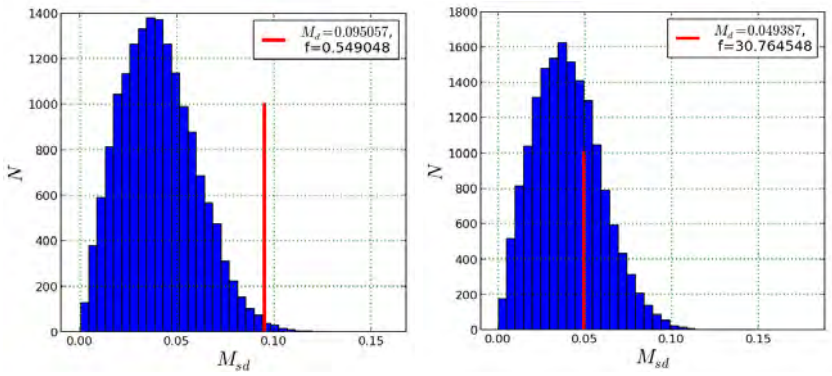

FIGURE 4.4: The histogram of the real simulated de-biased modulation indices along with our observed value (shown by the vertical red line) for PKS J0442-0017 (left) and PKS J0444-2809 (right). The fraction of simulated modulation indices, f, larger than the observed value, along with the observed value is shown at the top of the figure.

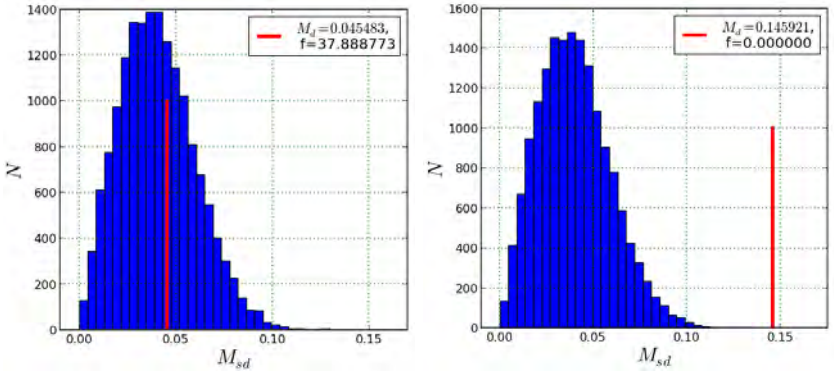

FIGURE 4.5: The histogram of the real simulated de-biased modulation indices along with our observed value (shown by the vertical red line) for PKS J0453-2807 (left) and PKS J0538-4405 (right). The fraction of simulated modulation indices, f, larger than the observed value, along with the observed value is shown at the top of the figure.

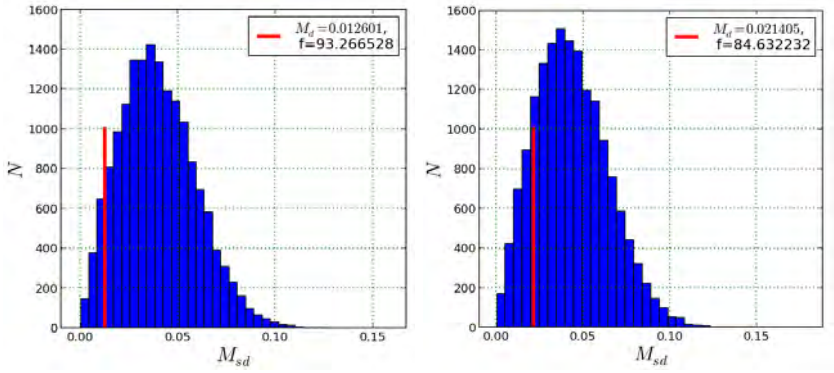

FIGURE 4.6: The histogram of the real simulated de-biased modulation indices along with our observed value (shown by the vertical red line) for PKS J0744-0629 (left) and PKS J0837-1951 (right). The fraction of simulated modulation indices, f, larger than the observed value, along with the observed value is shown at the top of the figure.

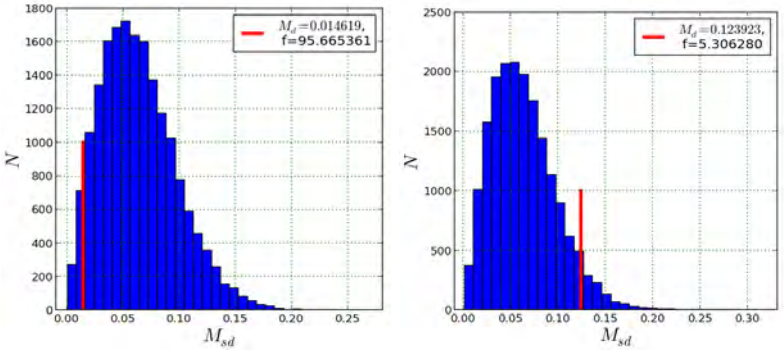

FIGURE 4.7: The histogram of the real simulated de-biased modulation indices along with our observed value (shown by the vertical red line) for PMN J1712-2809 (left) and PKS J1833-2103 (right). The fraction of simulated modulation indices, f, larger than the observed value, along with the observed value is shown at the top of the figure.

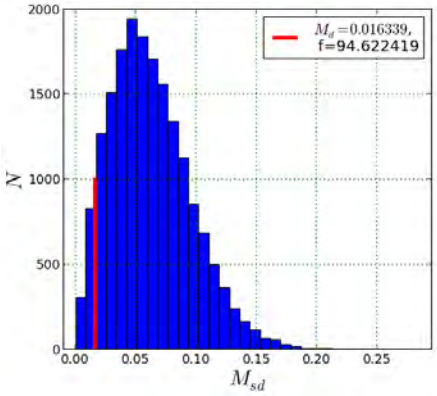

FIGURE 4.8: The histogram of the real simulated de-biased modulation indices along with our observed value (shown by the vertical red line) for PKS J1941-1524. The fraction of simulated modulation indices, f, larger than the observed value, along with the observed value is shown at the top of the figure.

We wind up our discussion by summarizing the result of our simulation for the eleven sources as follow.

1. **3C123**: We employed this source as a reference to determine the systematic error, as explained in Section (4.1) so by construction it has a small modulation index, $\mathtt{M}_d$.

2. **PKS J0351-2744**: Referring to Table 4.2, we observe that the source's `VI`, `MI`, and $\mathtt{M}_d$ are remarkably high. These metrics undoubtedly tell us that the source is highly variable. None of our 30,000 Monte Carlo simulations had a debiased modulation index as high as the observed $\mathtt{M}_d$; see the right side of Figure 4.3. So the source is certainly variable, and hence we do not recommend the source to be used as a flux-density calibrator.

3. **PKS J0442-0017**: Only 0.5% of our Monte Carlo simulations had a large value of $\mathtt{M}_{sd}$ than the observed one, as shown on the left side of Figure 4.4. This strongly suggests variability of the source flux. The other two variability metrics of the source (i.e. `MI` = 8.71% and `VI` = 12.83%) are relatively high, supporting this conclusion. In addition to this, the literature review presented in Section 2.4 about this source confirmed its flux instability at various frequencies. The stated reasons suggest that the source is not a good flux density calibrator candidate.

4. **PKS J0444-2809**: Approximately 31% our simulations for this source had large debiased modulation indices than the observed value and hence the source is compatible with being constant in time. However, the summary given in Section 2.4 and the position analysis conducted in this research (Section 3.7) have indicated the source's complex morphology – which has also an impact on its flux behaviour. Hence, we recommend further work to determine if this is a good flux-density calibrator candidate.

5. **PKS J0453-2807**: This source is consistent with having a constant flux since approximately 38% of its Monte Carlo simulations had larger debiased modulation indices than the observed value; see the left side of Figure 4.5. We recommend further work so as to convincingly state its suitability as a flux-density calibrator candidate.

6. **PKS J0538-4405**: The probability that the source to have a constant flux density is zero; see the right side of Figure 4.5. The summary given in Section 2.4 also stressed that the source is strongly variable. Thus, we do not recommend this source to be used as a flux-density calibrator.

7. **PKS J0744-0629**: This source is a good flux density calibrator candidate since $\sim$ 93% of the simulations had larger debiased modulation index values. This is supported by the summary presented in Section 2.4.

8. **PKS J0837-1951**: The source seems a good flux-density calibrator candidate since $\sim$ 86% of the simulations had larger debiased modulation indices, as shown on the right side of Figure 4.6. However, there is a confusing source about 30′, having a flux density 33 % of that of PKS J0837-1951; see Figure 4.44 . Hence, the source is unsuitable to be a good flux-density calibrator candidate.

9. **PMN J1712-2809**: The $\mathtt{M}_d$ of the source is calculated from just two flux density measurements that can make the result uncertainly reliable. The left side of Figure 4.7 shows the resulting $\mathtt{M}_d$ value was low compared to most of the Monte Carlo simulations. We therefore classify this as a potential future calibrator to be checked with more data.

10. **PKS J1833-2103**: This source has `MI` and `VI` values (refer Table 4.3) that are high enough to point to strong variability. Only about $\sim$ 5.0% of the simulations had larger debiased modulation indices which also supports the variability hypothesis; as shown on the right side of Figure 4.7 Furthermore, a survey conducted by Tingay et al. [54] (see the summary given in Section 2.4) showed that the source's modulation indices at various frequencies are high. Therefore, PKS J1833-2103 is not a suitable flux density calibrator candidate.

11. **PKS J1941-1524**: The $\mathtt{M}_d$ of this source is calculated from just two flux density measurements that can make the result uncertainly reliable. The resulting $\mathtt{M}_d$ value was low compared to most of the Monte Carlo simulations. We therefore classify this as a potential future calibrator to be checked with more data.

As we mentioned earlier, the $\mathtt{M}_d$ values of 27 sources were found to be imaginary. For these sources, we decide their suitability as flux density calibrator candidates based on the `MI` and `VI` metrics into four categories. Accordingly, we set the following benchmarks (classifying the sources A through D) for reasonable justification.

A. If both `MI` and `VI` of a source are between 0 and 0.05, then the source is highly probable to be a good flux density calibrator candidate.

B. If either `MI` or `VI` of a source is between 0.05 and 0.09, then we need to carry out further study on the source before deciding its suitability as a flux density calibrator candidate (unconfirmed candidate).

C. If a source is analysed based on only two observations or insufficient information about the source is available in the literatures and catalogues about its flux characteristic, then it is unpersuasive to justify its suitability from the limited data and evidence (undecided candidate).

D. If either `MI` or `VI` of a source is greater than 0.09, then the source has high chance of becoming a bad flux density calibrator candidate.

Based on the above criteria, we have identified the sources' categories. In addition to the 27 sources, we include the 11 sources, whose M_d are real numbers, into one of the aforementioned categories looking at the explanation given under each source (see Section 4.7). The summarized results about each source are presented in Tables 4.2 and 4.3.

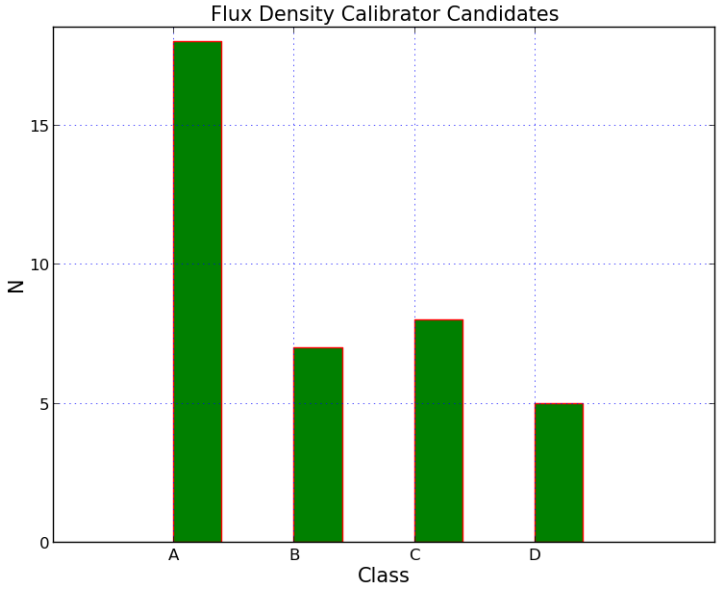

FIGURE 4.9: The histogram demonstrate the number of sources (N) against flux calibrator candidates. According to the requirement we set, 18 sources out of 38 ($\sim$ 47%) were identified as good flux density calibrator candidates (class A); whereas 5 sources out of 38 ($\sim$ 13%) showed significant flux variabilities, and hence they are bad calibrator candidates (class D). The combination of unconfirmed flux density calibrator candidates (class B) and undecided (class C) consist of 16 sources ($\sim$ 40%).

TABLE 4.2: The table presents the final results obtained from the KAT-7. The columns are: Source name; Right Ascension (J2000) (hh:mm:ss); Declination (J2000) (deg:arcmin:arcsec); The number of observation, N; The weighted average calculated with 5% systematic uncertainty, $\langle S\rangle_w \pm \langle\sigma\rangle_w$; The mean flux density, $\langle S\rangle$; The Chi-square value calculated at 5% systematic uncertainty of the source, χ^2; The debiased variability index calculated at 5% systematic uncertainty, $\mathtt{M}_d$; The modulation index, MI; The variability index, VI; The Spectral index (α) obtained after including the result obtained from KAT-7; Class designation based on the suitability of the sources as flux calibrator candidates (good flux density calibrator candidate (class A), unconfirmed flux density calibrator candidate (class B), Undecided (class C), and bad flux density calibrator candidate (class D). The blank values (shown by dots) under $\mathtt{M}_d$ are imaginary, meaning that the variability was consistent with being zero.

Source Name	RA	Dec	N	$\langle S\rangle_w \pm \langle\sigma\rangle_w$(Jy) (at 5%)	$\langle S\rangle$	χ^2 (at 5% S_i)	M_d (at 5% S_i)	MI %	VI %	α	Class
PKS J0010-4153	00:10:52.49	-41:53:11.17	7	3.654±0.186	3.657	1.481	.....	2.37	4.05	-0.53	A
PKS J0022+0014	00:22:25.42	00:14:56.20	5	2.447±0.133	2.445	0.499	.....	1.71	2.78	-0.35	A
PKS J0025-2602	00:25:49.17	-26:02:12.80	7	7.350±0.370	7.357	1.430	.....	2.33	4.01	-0.37	A
PKS J0042-4414	00:42:12.80	-44:14:34.61	7	2.959±0.154	2.953	3.624	.....	4.12	7.31	-0.81	B
PKS J0044-3530	00:44:41.54	-35:30:42.37	7	2.154±0.109	2.157	1.936	.....	2.71	4.52	-0.72	A
PKS J0059+006	00:59:05.54	00:06:49.74	5	2.286±0.114	2.287	0.500	.....	1.60	1.88	-0.35	A
PKS J0240-2309	02:40:08.14	-23:09:16.00	6	5.504±0.280	5.512	2.348	.....	2.79	4.18	-0.58	A
PKS J0252-7104	02:52:46.31	-71:04:36.20	8	4.639±0.232	4.646	2.236	.....	2.70	3.74	-0.78	A
PKS J0303-6211	03:03:50.81	-62:11:25.99	8	2.276±0.114	2.285	6.209	.....	4.40	7.17	0.15	B
PKS J0309-6058	03:09:56.04	-60:58:39.74	6	1.385±0.069	1.389	3.230	.....	3.62	5.62	-0.04	B
PKS J0318+1628	03:18:57.77	16:28:33.10	6	6.646±0.332	6.655	1.628	.....	2.57	4.24	-0.32	A
PKS J0323+0534	03:23:20.30	05:34:10.59	6	2.263±0.128	2.258	0.948	.....	2.33	2.96	-0.79	A
PKS J0351-2744	03:51:38.17	-27:44:09.08	6	2.776±0.217	3.372	93.230	0.328	28.59	41.76	-0.90	D
PKS J0405-1308	04:05:33.99	-13:08:12.99	6	3.503±0.176	3.511	2.409	.....	3.19	4.43	-0.35	A
PKS J0409-1757	04:09:06.70	-17:57:08.06	6	1.881±0.095	1.884	1.325	.....	4.72	3.83	-0.49	A
3C123 [a]	04:37:04.57	29:40:14.20	5	37.202±1.879	37.372	4.399	~ 0	4.47	6.62	-0.79	A
PKS J0408-6544	04:08:20.34	-65:45:09.52	6	11.263±0.564	11.287	2.717	.....	3.25	5.26	-1.04	B
PKS J0420-6223	04:20:55.44	-62:23:39.15	5	2.755±0.144	2.755	0.103	.....	2.28	1.59	-0.99	A
PKS J0440-4333	04:40:17.07	-43:33:09.00	5	3.751±0.189	3.766	3.196	.....	4.24	5.95	-0.24	B
PKS J0442-0017	04:42:38.54	-00:17:42.83	5	3.479±0.177	3.353	17.902	0.095	8.71	12.83	-0.12	D
PKS J0444-2809	04:44:36.66	-28:09:44.39	5	5.235±0.264	5.278	7.839	0.049	6.38	8.75	-0.77	B
PKS J0453-2807	04:53:14.72	-28:07:37.25	5	2.133±0.109	2.150	7.180	0.045	5.79	8.68	-0.03	B
PKS J0534+1927	05:34:44.49	19:27:20.97	4	5.516±0.279	5.520	0.453	.....	1.71	2.31	-0.35	A
PKS J0538-4405	05:38:50.40	-44:05:09.20	5	7.081±0.357	7.332	37.400	0.146	11.67	17.82	-0.34	D

[a] We use the source to determine the systematic error for KAT-7; see Section 4.1 .

TABLE 4.3: The table presents the final results obtained from the KAT-7. Continued from table 4.2.

Source Name	RA	Dec	N	$\langle S\rangle_w \pm \langle\sigma\rangle_w$(Jy) (at 5%)	$\langle S\rangle$	χ^2 (at 5% S_i)	M_d (at 5% S_i)	MI %	VI %	α	Class
PKS J0744-0629	07:44:21.65	-06:29:35.30	5	6.928±0.347	6.957	4.253	0.013	4.51	7.12	-0.86	A [a]
PKS J0837-1951	08:37:11.08	-19:51:58.24	5	3.535±0.194	3.586	4.607	0.021	5.85	8.91	-0.68	D [b]
PKS J0943-0891	09:43:36.86	-08:19:31.53	4	2.456±0.124	2.460	1.191	.....	2.84	3.58	-0.43	A
PKS J1130-1449	11:30:07.06	-14:49:28.27	2	4.673±0.243	4.670	0.174	.....	1.53	1.53	-0.17	C
PKS J1154-3505	11:54:21.76	-35:05:29.40	4	5.538±0.281	5.553	2.214	.....	3.85	4.84	-0.41	A
PKS J1248-1959	12:48:24.07	-19:59:18.15	4	4.373±0.225	4.373	0.903	.....	2.48	3.48	-0.41	A
PKS J1311-2216	13:11:39.80	-22:16:41.47	3	4.170±0.238	4.234	1.779	.....	5.01	5.71	-0.96	C
PKS J1510-0543	15:10:53.55	-05:43:07.10	1	3.111±0.154	—-	—-	—-	—-	—-	-0.48	—-
PKS J1517-2422	15:17:41.17	-24:22:14.58	1	2.366±0.115	—-	—-	—-	—-	—-	0.06	—-
PMN J1712-2809	17:12:56.92	-28:09:34.61	2	3.899±0.196	3.909	1.089	0.014	3.71	3.71	-0.88	C
PKS J1744-5144	17:44:25.55	-51:44:46.14	2	6.876±0.345	6.882	0.299	.....	1.94	1.94	-0.86	C
PKS J1819-6345	18:19:35.04	-63:45:48.60	2	10.697±0.537	10.699	0.085	.....	1.03	1.03	-0.84	C
PKS J1830-3602	18:30:58.86	-36:02:30.16	1	5.073±0.254	—-	—-	—-	—-	—-	-0.71	—-
PKS J1833-2103	18:33:39.98	-21:03:39.90	2	11.467±0.588	11.677	7.006	0.124	9.47	9.47	-0.12	D [c]
PKS J1924-2914	19:24:50.70	-29:14:29.46	2	12.292±0.615	12.292	0.167	.....	1.45	1.45	0.26	C
PKS J1935-4602	19:35:56.83	-46:20:42.48	2	9.871±0.494	9.871	0.635	.....	2.79	2.79	-0.84	C
PKS J1941-1524	19:41:14.97	-15:24:31.30	2	5.302±0.266	5.318	1.106	0.016	3.73	3.73	-0.83	C
PKS J2129-1821	21:29:21.45	-18:21:17.43	1	1.328±0.066	—-	—-	—-	—-	—-	-0.01	—-
PKS J2131-2036	21:31:01.47	-20:36:55.66	1	1.526±0.076	—-	—-	—-	—-	—-	-0.80	—-
PKS J2151-3027	21:51:55.55	-30:27:54.09	1	1.627±0.082	—-	—-	—-	—-	—-	-0.10	—-
PKS J2152-2828	21:52:03.69	-28:28:31.41	1	2.451±0.122	—-	—-	—-	—-	—-	-0.51	—-
PKS J2206-1835	22:06:10.33	-18:35:39.00	1	5.775±0.289	—-	—-	—-	—-	—-	-0.31	—-
PKS J2219-2756	22:19:42.79	-27:56:21.30	1	1.522±0.078	—-	—-	—-	—-	—-	-0.82	—-

[a] We assigned this source as class A based on its M_d value.

[b] This source nominated as bad flux-density calibrator candidate (class D) because there is a confusing source (NVSS J083639-201658) at about $30'$, which has a flux density 33 % of that of PKS J0837-1951.

[c] We nominated this source as class D based on its M_d value.

4.8 The Radio Light Curve Plots

Each plot shown below depicts the flux density variation of a source with time (radio light curve). The standard name of each source is written on top of each plot. The metrics describing variability measures of the sources are presented in Tables 4.2 and 4.3.

The time parameter in each plot is represented by Modified Julian Day (MJD); where MJD = JD-2400000.5. The Julian Days (JD) corresponding to each dataset are shown in Table 2.2. Note that the JDs listed in Table 2.2 describe the mean of the starting and final observation times.

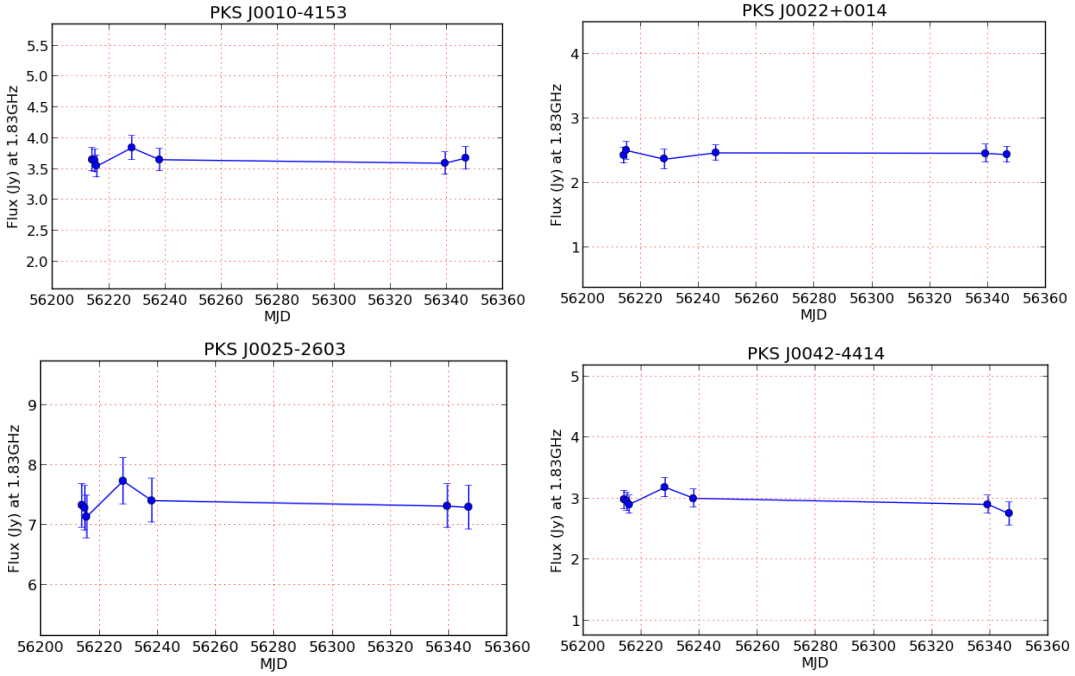

FIGURE 4.10: Each plot shows the flux variability of the source with time. The standard name of the source is written on the top each plot. Each error bar incorporates a random error and 5% (of the measured flux) as the systematic error.

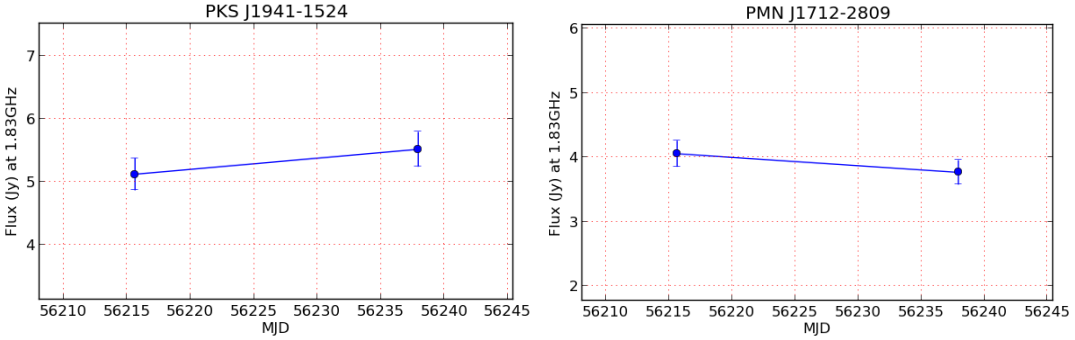

FIGURE 4.15: Each plot shows the flux variability of the source with time. The standard name of the source is written on the top each plot. Each error bar incorporates a random error and 5% (of the measured flux) as the systematic error.

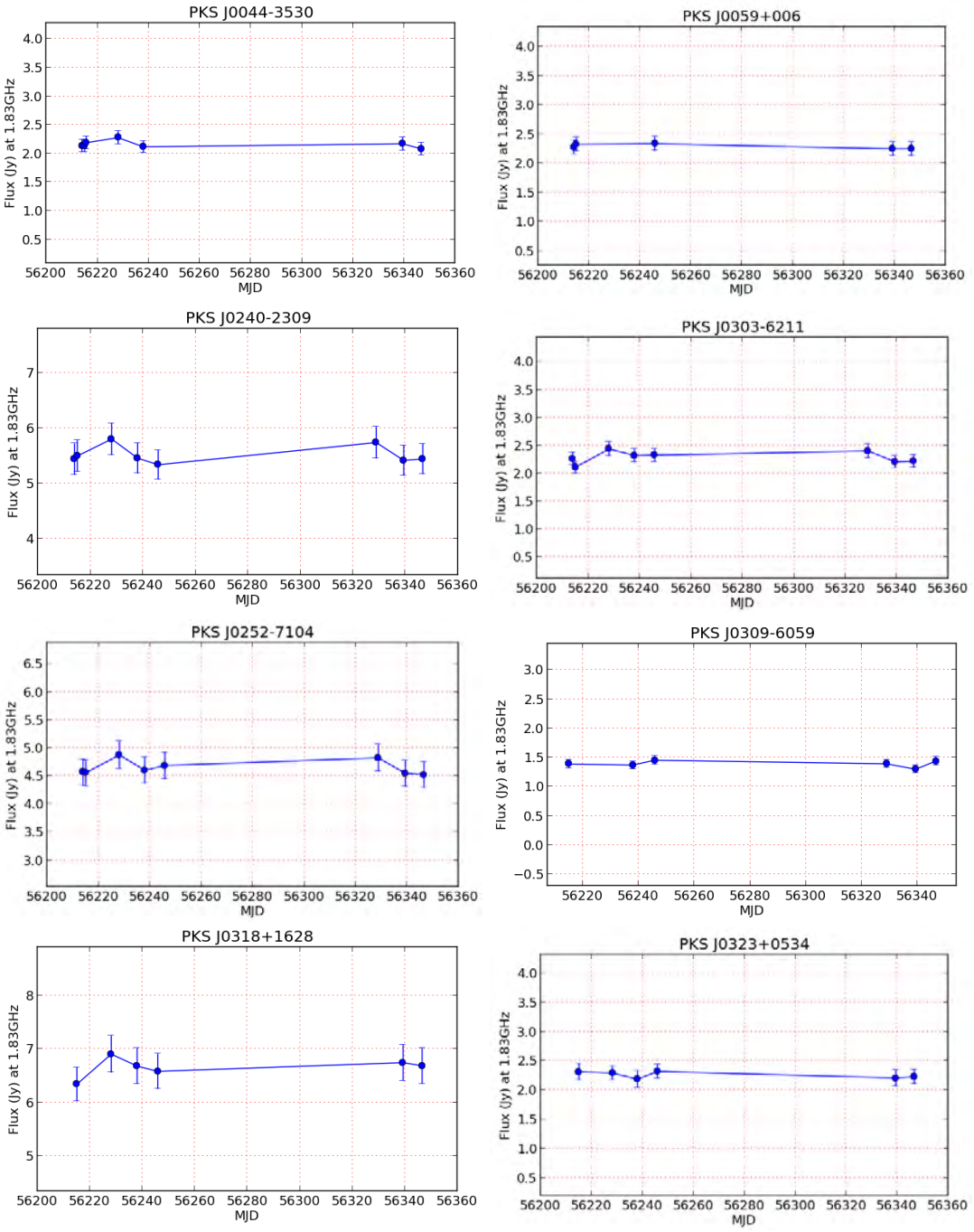

FIGURE 4.11: Each plot shows the flux variability of the source with time. The standard name of the source is written on the top each plot. Each error bar incorporates a random error and 5% (of the measured flux) as the systematic error.

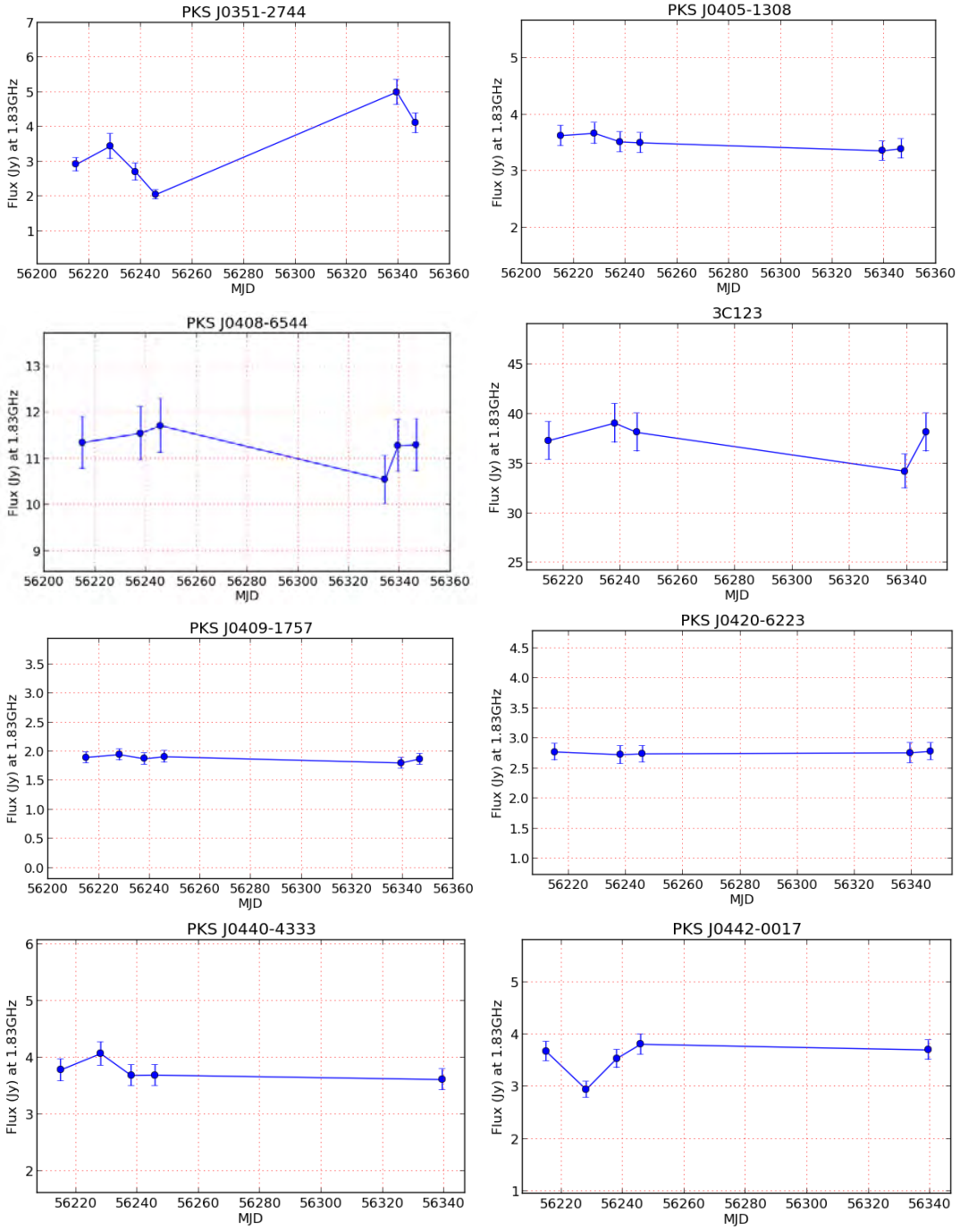

FIGURE 4.12: Each plot shows the flux variability of the source with time. The standard name of the source is written on the top each plot. Each error bar incorporates a random error and 5% (of the measured flux) as the systematic error.

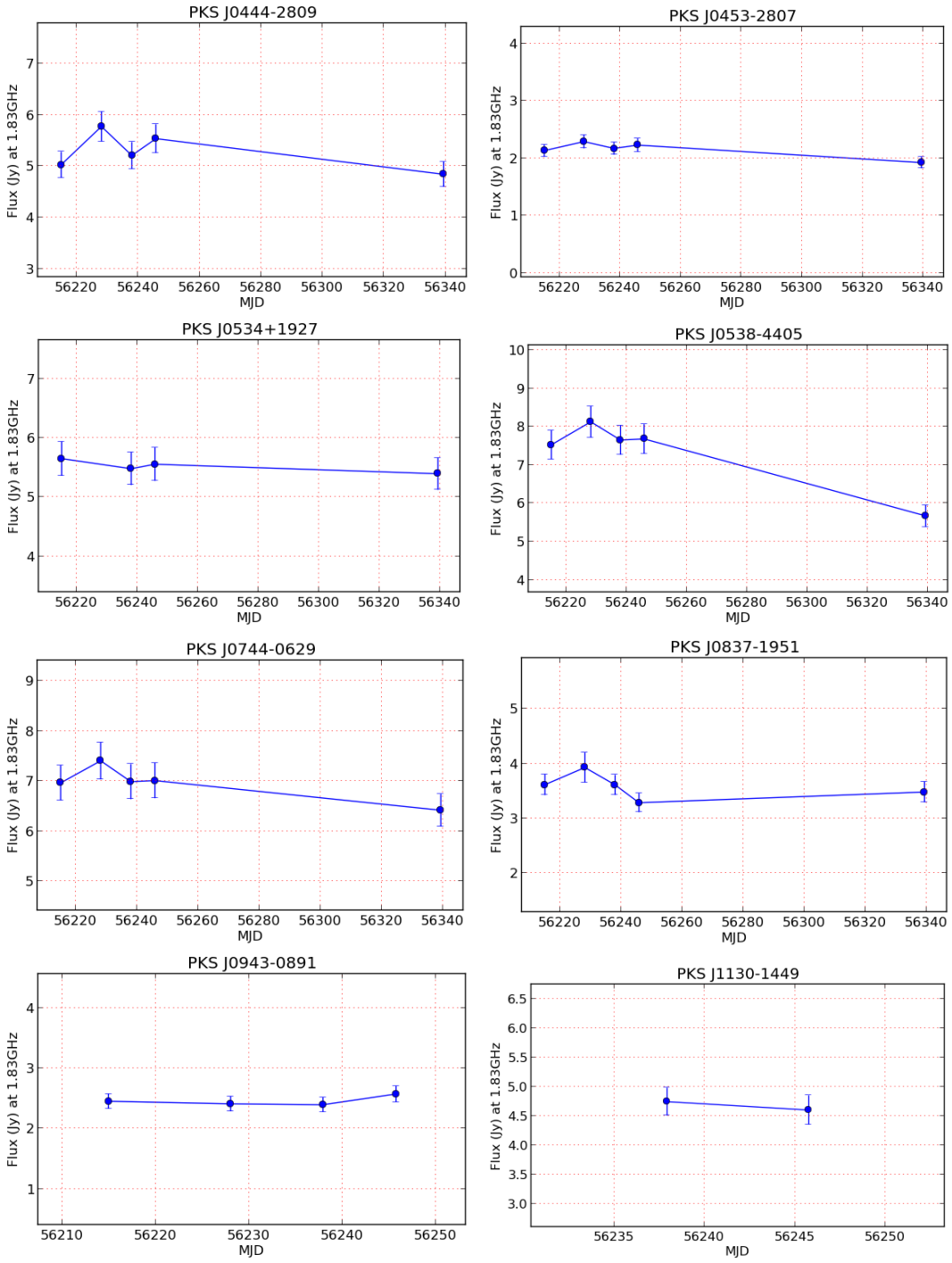

FIGURE 4.13: Each plot shows the flux variability of the source with time. The standard name of the source is written on the top each plot. Each error bar incorporates a random error and 5% (of the measured flux) as the systematic error.

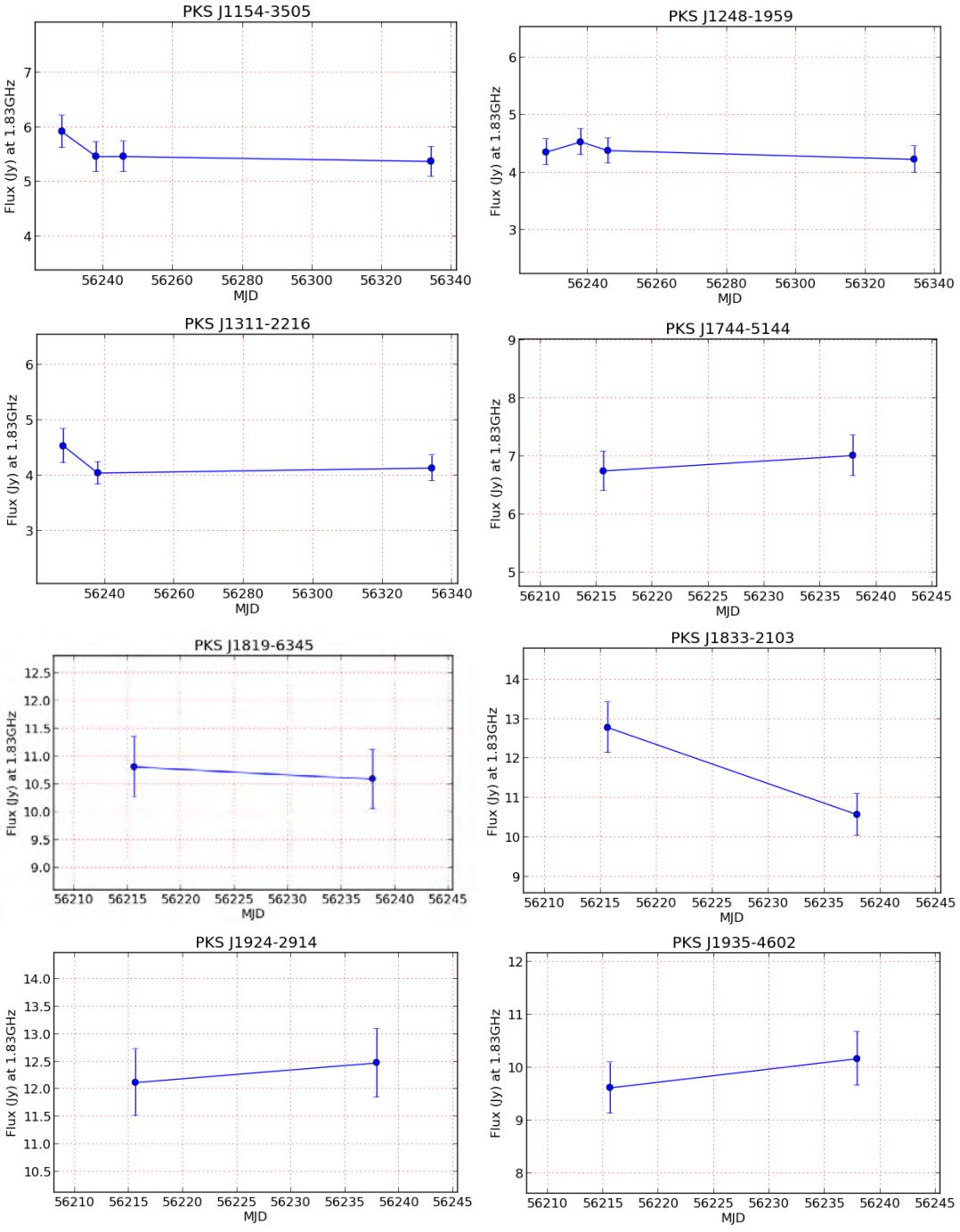

FIGURE 4.14: Each plot shows the flux variability of the source with time. The standard name of the source is written on the top each plot. Each error bar incorporates a random error and 5% (of the measured flux) as the systematic error.

4.9 Image Morphology

We imaged the sources by combining all the visibilities if observed more than once. We do not apply any weights on the visibilities while concatenating the MS files but redo some flagging if required. We run a standard clark clean with 2500 iterations and natural weighting (as discussed in Section 3.3) and stopping at a threshold flux of around 1 mJy. The root mean square (rms) in each image was calculated in a region free of sources; where the rms and peak brightness of each image are written in the caption. Accordingly, the contours are drawn considering the $\pm$ 3$\times$ rms as the initial value and increasing until 32 times of 3$\times$ rms. The negative contours are represented by dash lines.

We fixed the dimensions of each image to be about $2^\circ \times 2^\circ$ in order to show the confusing sources scattered within the KAT-7 primary beam ($\sim 0.8^\circ$). We used pyBDSM [2] to examine all sources within the image of each candidate. We set the threshold for the source boundary to be 3 $\times\sigma$, and the source detection threshold to be 5 $\times\sigma$, where σ is the rms noise in the image. We found 36 ($\sim$ 95%) out of the 38 sources with a flux density of not more than 10 % of the flux of the potential flux-density calibrator. The two sources having confusing sources in the primary beam are PKS J0351-2744 and PKS J0837-1951. We nominated the former one as a poor flux-density calibrator candidate (class D) source based on its variability metrics (Section 4.7). Though the latter seems to be a good flux-density calibrator candidate (class A) according to its variability metrics, there is a strong confusing source or NVSS J083639-201658 (i.e. having a flux density 33 % of the candidate source about 30$'$ to the south; see Figure 4.44) that makes it a confusing flux-density calibrator candidate.

The following figures show the images of the candidates observed using the KAT-7. The synthesised beam is shown as the filled red ellipse in the left bottom corner.

[2] www.lofar.org/wiki/doku/pybdsm

- **3C48 (J0137+3309)**

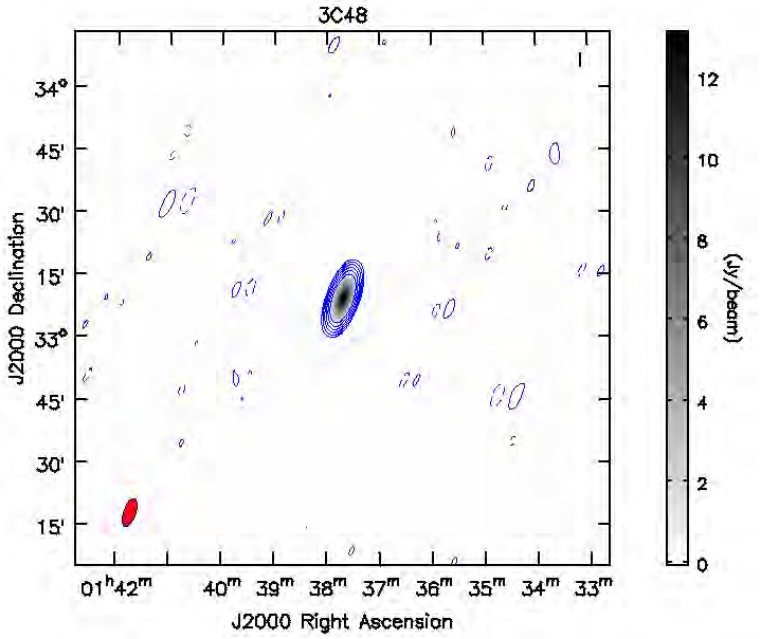

FIGURE 4.16: KAT-7 1.83 GHz radio image of 3C48. Contours are drawn at [-1, 1, 2, 4, 8, 16, 32]× 48.60 mJy/beam; where the image has a noise of 16.20 mJy/beam and peak brightness of 13.20 Jy/beam. The synthesised beam is $6.95' \times 2.87'$ and is shown in the left bottom with a red filled ellipse.

- **3C147 (J0542+4951)**

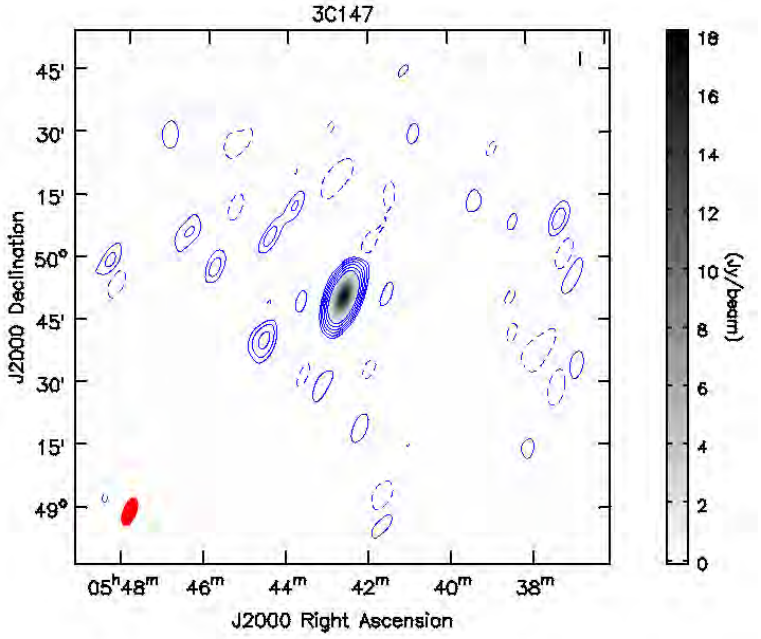

FIGURE 4.17: KAT-7 1.83 GHz radio image of 3C147. Contours are drawn at [-1, 1, 2, 4, 8, 16, 32]× 42.90 mJy/beam; where the image has a noise of 14.30 mJy/beam and peak brightness of 18.19 Jy/beam. The synthesised beam is $6.94' \times 3.17'$ and is shown in the left bottom with a red filled ellipse.

- **3C286 (J1331+3030)**

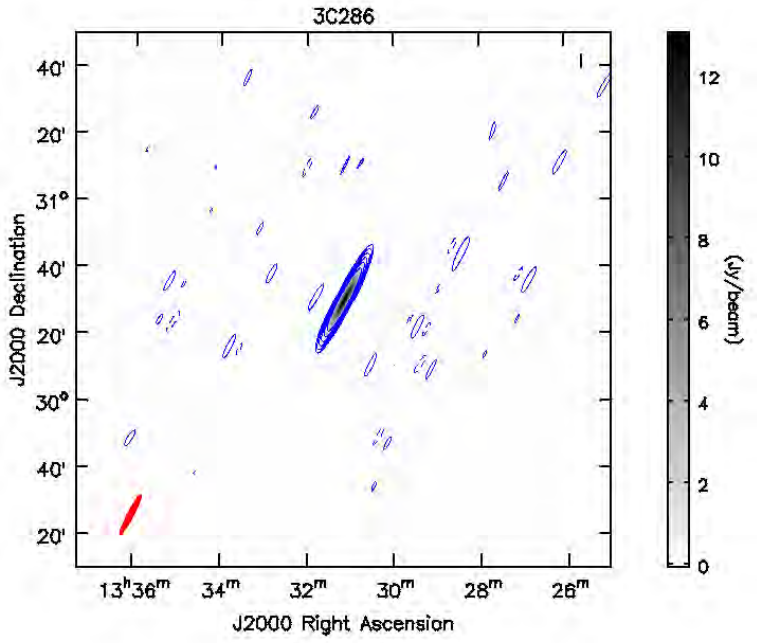

FIGURE 4.18: KAT-7 1.83 GHz radio image of 3C286. Contours are drawn at [-1, 1, 2, 4, 8, 16, 32]× 66.90 mJy/beam; where the image has a noise of 22.30 mJy/beam and peak brightness of 13.07 Jy/beam. The synthesised beam is $13.9' \times 1.8'$ and shown in the left bottom with a red filled ellipse.

- **PKS J0010-4153**

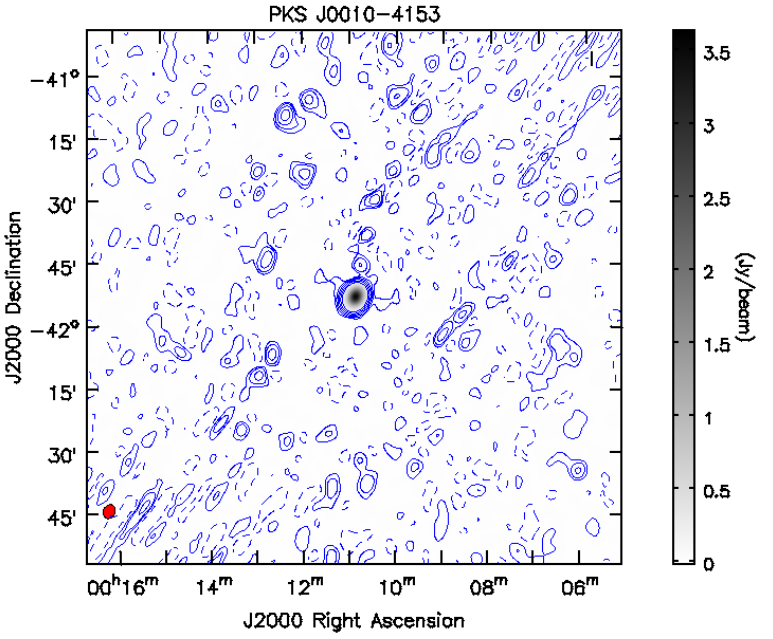

FIGURE 4.19: KAT-7 1.83 GHz radio image of PKS J0010-4153. Contours are drawn at [-1, 1, 2, 4, 8, 16, 32]× 5.4 mJy/beam; where the image has a noise of 1.83 mJy/beam and peak brightness of 3.64 Jy/beam. The synthesised beam is $2.65' \times 2.41'$ and shown in the left bottom with a red filled ellipse.

- **PKS J0022+0014**

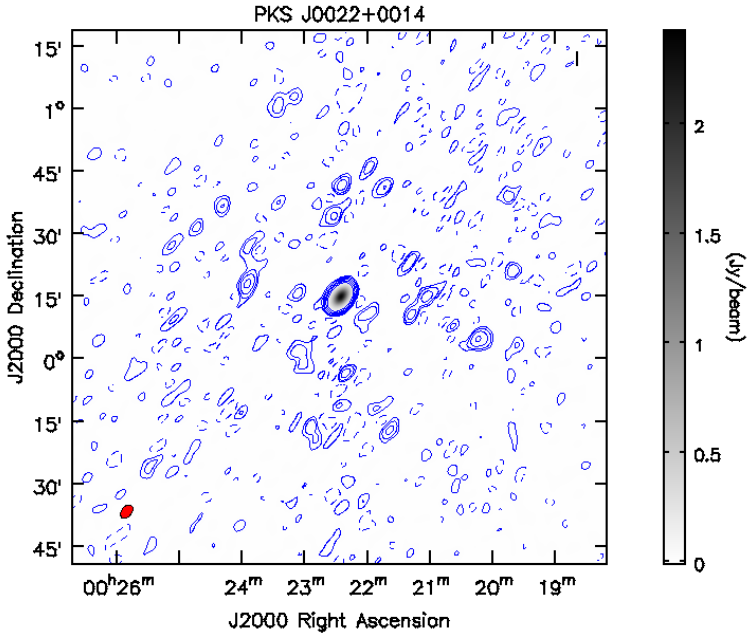

FIGURE 4.20: KAT-7 1.83 GHz radio image of PKS J0020+0014. Contours are drawn at [-1, 1, 2, 4, 8, 16, 32]× 3.24 mJy/beam; where the image has a noise of 1.08 mJy/beam and peak brightness of 2.43 Jy/beam. The synthesised beam is $3.65' \times 2.37'$ and shown in the left bottom with a red filled ellipse.

- **PKS J0025-2602**

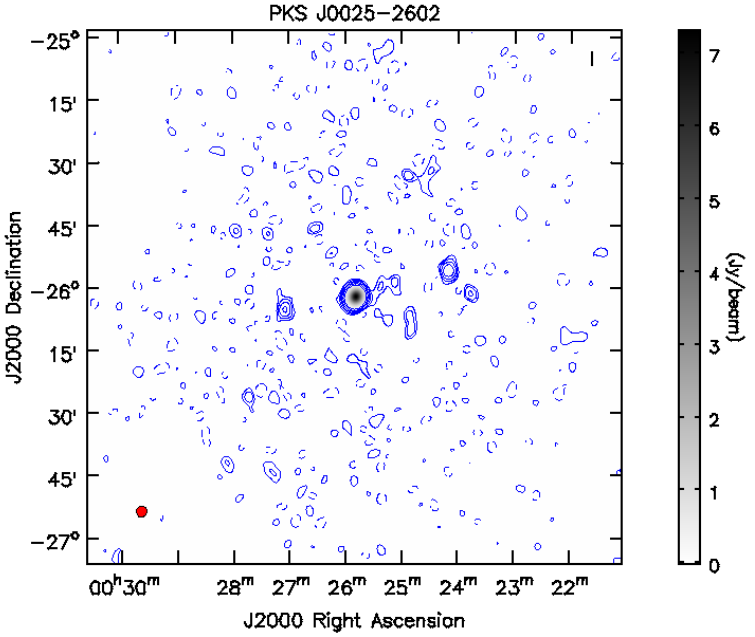

FIGURE 4.21: KAT-7 1.83 GHz radio image of PKS J0025-2602. Contours are drawn at [-1, 1, 2, 4, 8, 16, 32]× 10.1 mJy/beam; where the image has a noise of 3.71 mJy/beam and peak brightness of 7.32 Jy/beam. The synthesised beam is $2.73' \times 2.65'$ and shown in the left bottom with a red filled ellipse.

- **PKS J0042-4414**

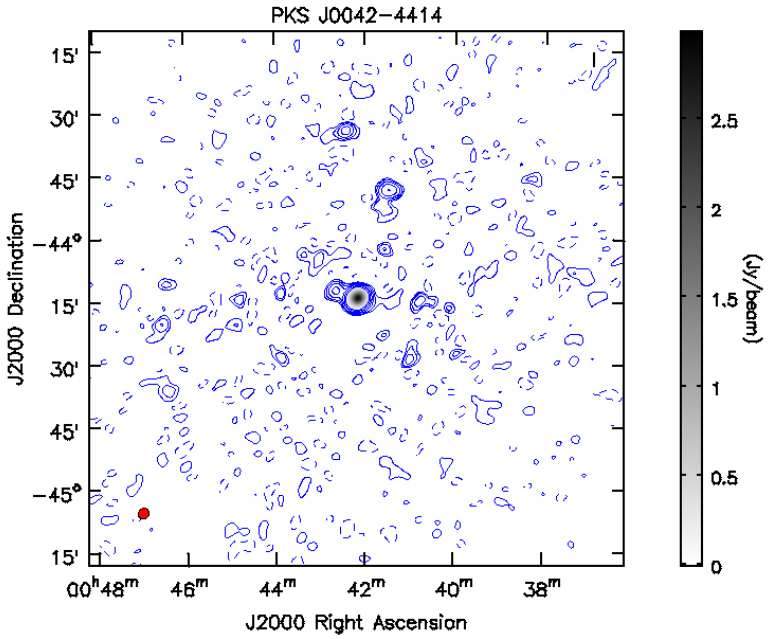

FIGURE 4.22: KAT-7 1.83 GHz radio image of PKS J0042-4414. Contours are drawn at [-1, 1, 2, 4, 8, 16, 32]× 4.35 mJy/beam; where the image has a noise of 1.45 mJy/beam and peak brightness of 2.99 Jy/beam. The synthesised beam is $2.73' \times 2.48'$ and shown in the left bottom with a red filled ellipse.

- **PKS J0044-3530**

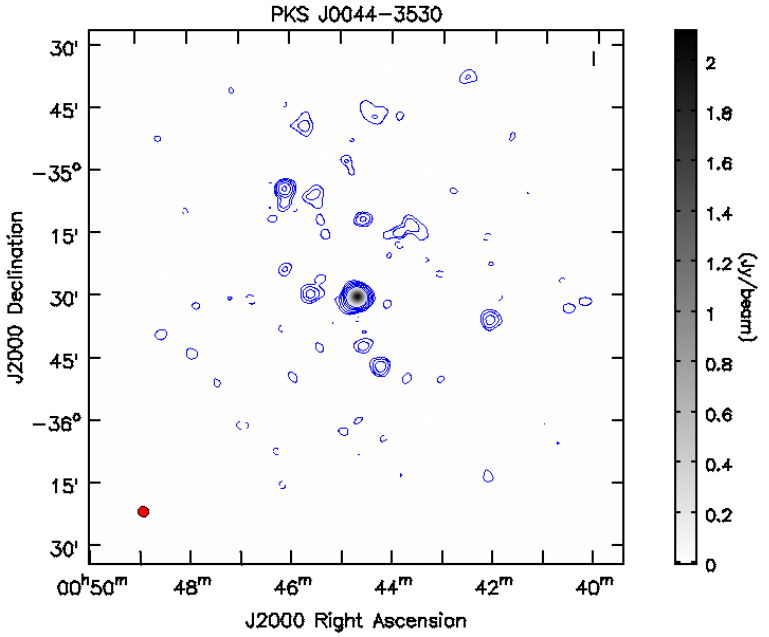

FIGURE 4.23: KAT-7 1.83 GHz radio image of PKS J0044-3530. Contours are drawn at [-1, 1, 2, 4, 8, 16, 32]× 4.89 mJy/beam; where the image has a noise of 1.63 mJy/beam and peak brightness of 2.12 Jy/beam. The synthesised beam is $2.64' \times 2.50'$ and shown in the left bottom with a red filled ellipse.

- **PKS J0059+006**

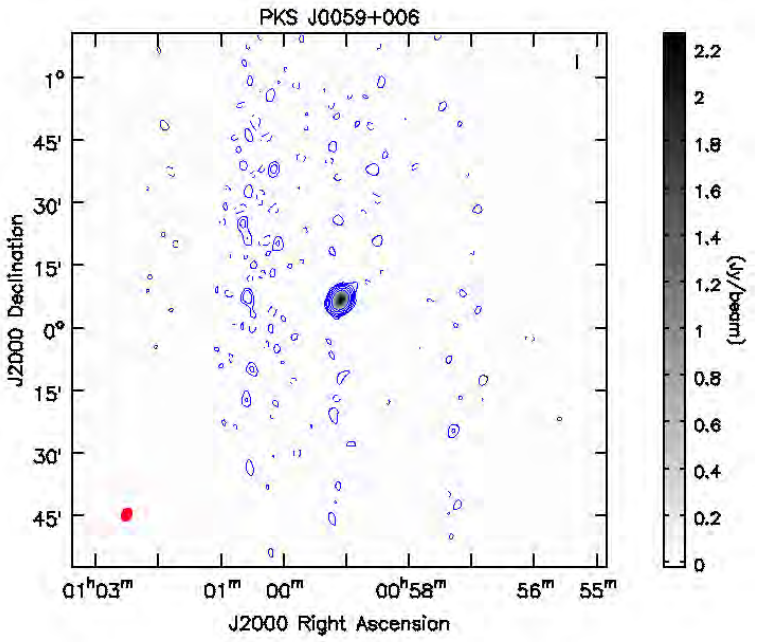

FIGURE 4.24: KAT-7 1.83 GHz radio image of PKS J0059+006. Contours are drawn at [-1, 1, 2, 4, 8, 16, 32]× 12.51 mJy/beam; where the image has a noise of 4.17 mJy/beam and peak brightness of 2.26 Jy/beam. The synthesised beam is 3.24′ × 2.53′ and shown in the left bottom with a red filled ellipse.

- **PKS J0240-2309**

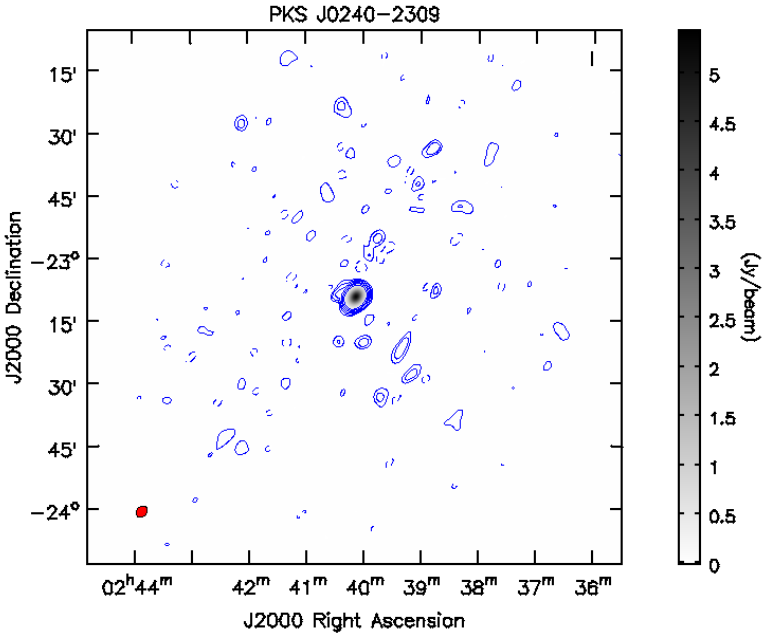

FIGURE 4.25: KAT-7 1.83 GHz radio image of PKS J0240-2309. Contours are drawn at [-1, 1, 2, 4, 8, 16, 32]× 8.49 mJy/beam; where the image has a noise of 2.83 mJy/beam and peak brightness of 5.44 Jy/beam. The synthesised beam is 2.99′ × 2.35′ and is shown in the left bottom with a red filled ellipse.

- **PKS J0252-7104**

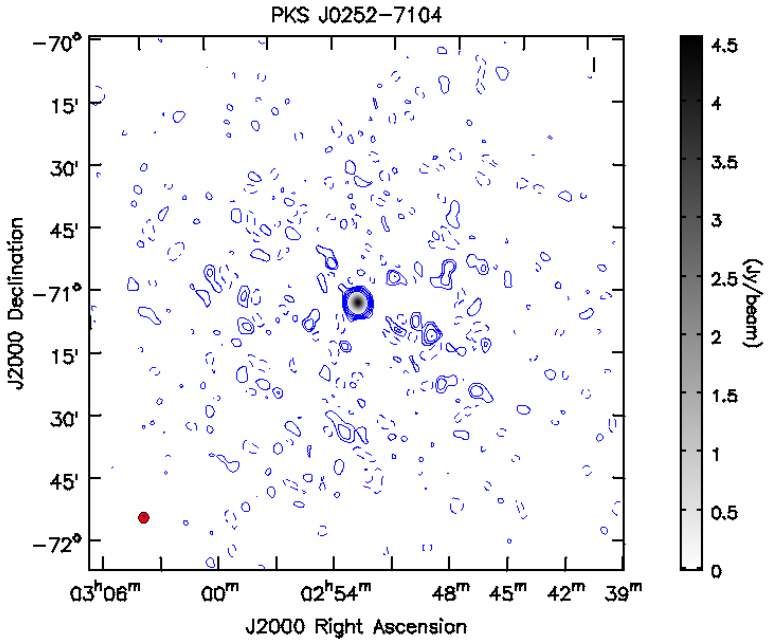

FIGURE 4.26: KAT-7 1.83 GHz radio image of PKS J0252-7104. Contours are drawn at [-1, 1, 2, 4, 8, 16, 32]× 7.00 mJy/beam; where the image has a noise of 2.33 mJy/beam and peak brightness of 4.56 Jy/beam. The synthesised beam is $2.67' \times 2.40'$ and shown in the left bottom with a red filled ellipse.

- **PKS J0303-6211**

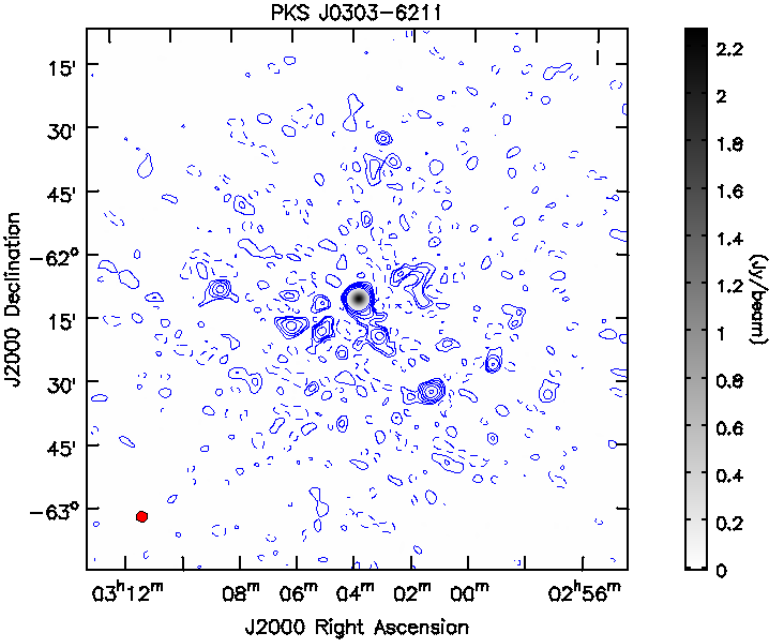

FIGURE 4.27: KAT-7 1.83 GHz radio image of PKS J0303-6211. Contours are drawn at [-1, 1, 2, 4, 8, 16, 32]× 3.00 mJy/beam; where the image has a noise of 1.00 mJy/beam and peak brightness of 2.28 Jy/beam. The synthesised beam is $2.67' \times 2.49'$ and shown in the left bottom with a red filled ellipse.

- **PKS J0309-6058**

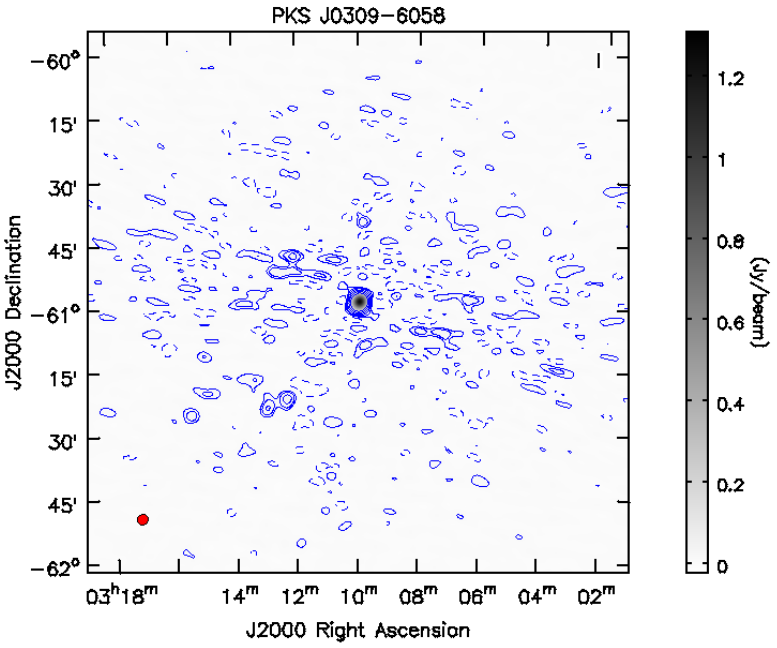

FIGURE 4.28: KAT-7 1.83 GHz radio image of PKS J0309-6058. Contours are drawn at [-1, 1, 2, 4, 8, 16, 32]× 7.00 mJy/beam; where the image has a noise of 2.33 mJy/beam and peak brightness of 1.31 Jy/beam. The synthesised beam is $3.70' \times 3.13'$ and shown in the left bottom with a red filled ellipse.

- **PKS J0318+1628**

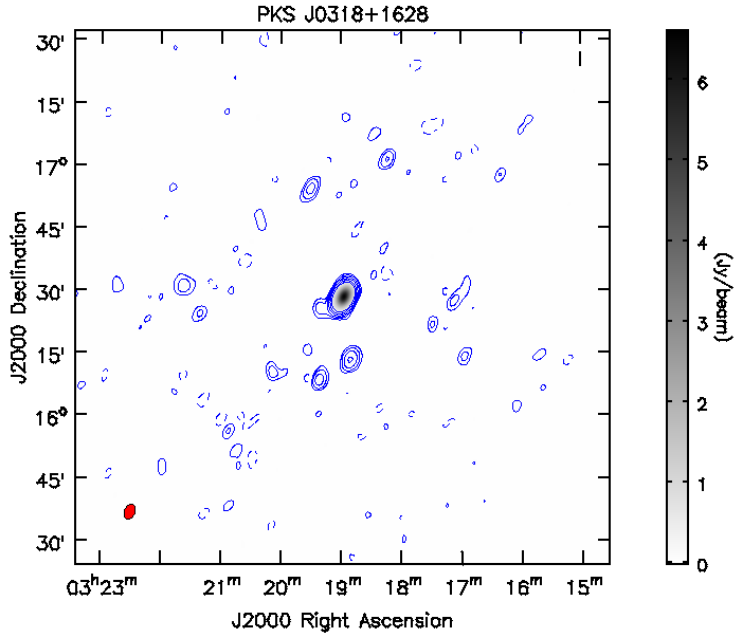

FIGURE 4.29: KAT-7 1.83 GHz radio image of PKS J0318+1628. Contours are drawn at [-1, 1, 2, 4, 8, 16, 32]× 13.00 mJy/beam; where the image has a noise of 4.33 mJy/beam and peak brightness of 6.62 Jy/beam. The synthesised beam is $3.80' \times 2.51'$ and shown in the left bottom with a red filled ellipse.

- **PKS J0323+0534**

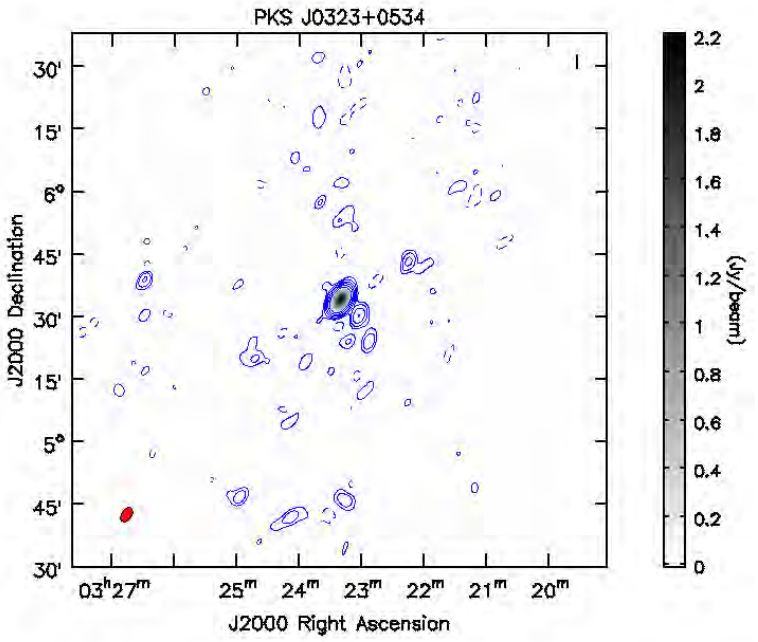

FIGURE 4.30: KAT-7 1.83 GHz radio image of PKS J0323+0534. Contours are drawn at [-1, 1, 2, 4, 8, 16, 32]× 7.00 mJy/beam; where the image has a noise of 2.33 mJy/beam and peak brightness of 2.21 Jy/beam. The synthesised beam is 3.73′ × 2.43′ and shown in the left bottom with a red filled ellipse.

- **PKS J0351-2744**

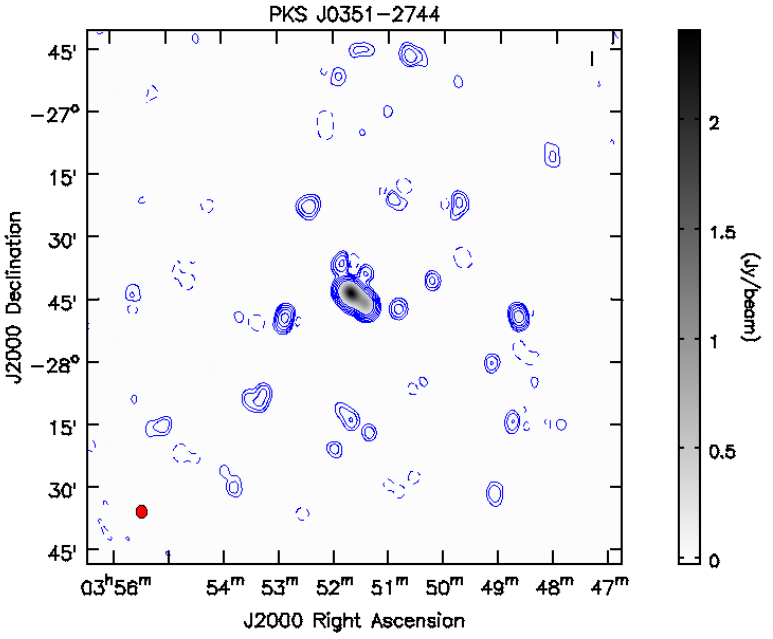

FIGURE 4.31: KAT-7 1.83 GHz radio image of PKS J0351-2744. Contours are drawn at [-1, 1, 2, 4, 8, 16, 32]× 6.10 mJy/beam; where the image has a noise of 2.10 mJy/beam and peak brightness of 2.41 Jy/beam. The synthesised beam is 3.10′, 2.64′ and shown in the left bottom with a red filled ellipse.

- **PKS J0405-1308**

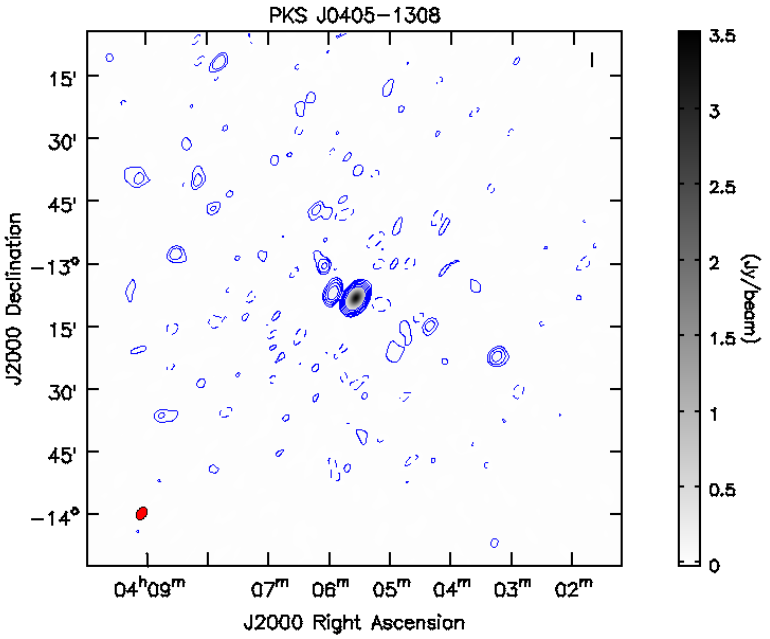

FIGURE 4.32: KAT-7 1.83 GHz radio image of PKS J0405-1308. Contours are drawn at [-1, 1, 2, 4, 8, 16, 32]× 9.80 mJy/beam; where the image has a noise of 3.27 mJy/beam and peak brightness of 3.51 Jy/beam. The synthesised beam is $3.31' \times 2.32'$ and shown in the left bottom with a red filled ellipse.

- **PKS J0408-6544**

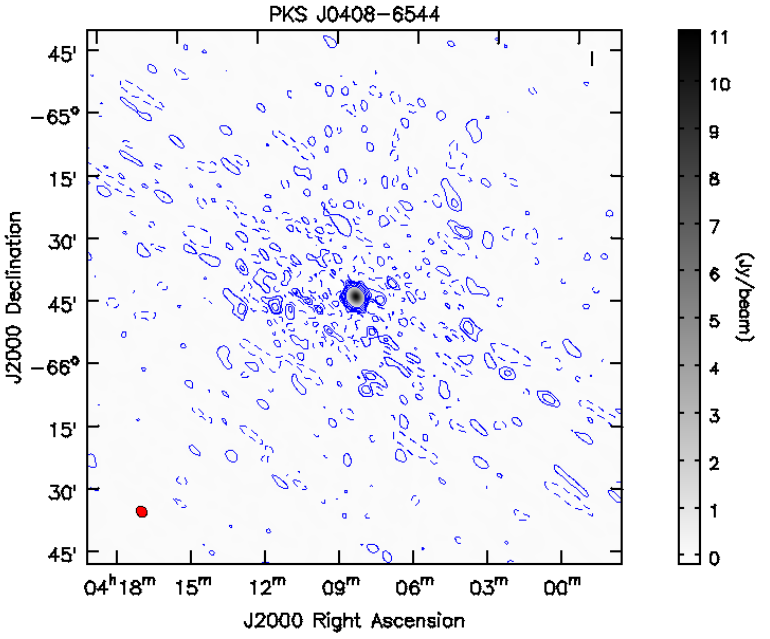

FIGURE 4.33: KAT-7 1.83 GHz radio image of PKS J0408-6544. Contours are drawn at [-1, 1, 2, 4, 8, 16, 32]× 36.00 mJy/beam; where the image has a noise of 12.00 mJy/beam and peak brightness of 11.10 Jy/beam. The synthesised beam is $2.87' \times 2.39'$ and is shown in the left bottom with a red filled ellipse.

- **PKS J0409-1757**

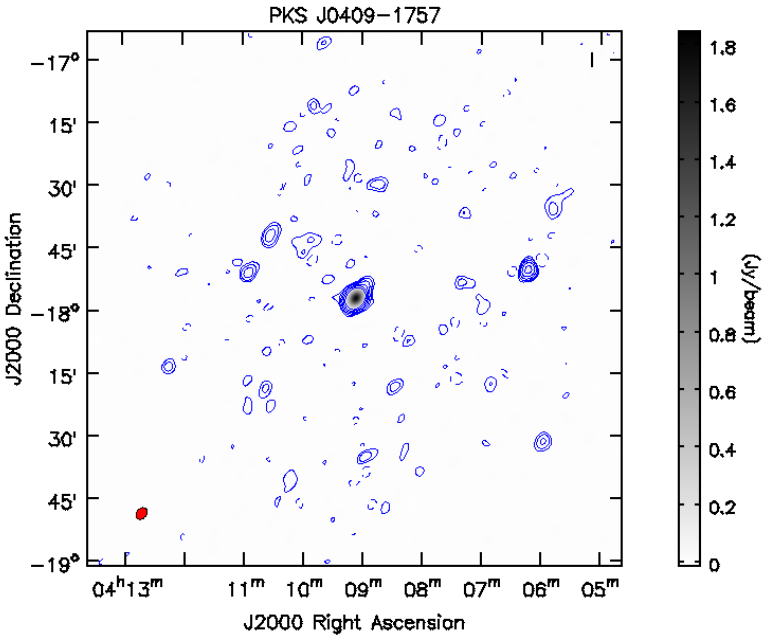

FIGURE 4.34: KAT-7 1.83 GHz radio image of PKS J0409-1757. Contours are drawn at [-1, 1, 2, 4, 8, 16, 32]× 5.00 mJy/beam; where the image has a noise of 1.67 mJy/beam and peak brightness of 1.835 Jy/beam. The synthesised beam is $3.06' \times 2.38'$ and shown in the left bottom with a red filled ellipse.

- **PKS J0420-6223**

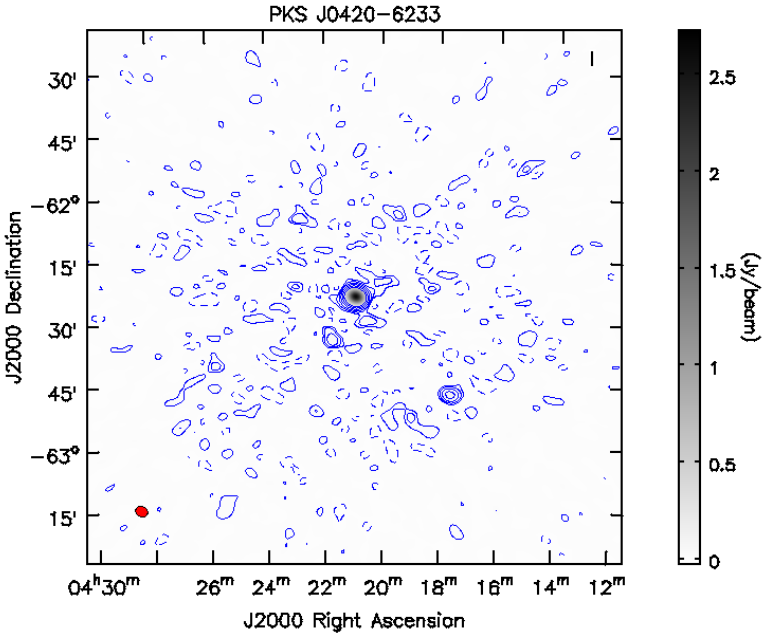

FIGURE 4.35: KAT-7 1.83 GHz radio image of PKS J0420-6223. Contours are drawn at [-1, 1, 2, 4, 8, 16, 32]× 9.10 mJy/beam; where the image has a noise of 3.00 mJy/beam and peak brightness of 2.73 Jy/beam. The synthesised beam is $3.02' \times 2.43'$ and shown in the left bottom with a red filled ellipse.

- **3C123 (J0437+2940)**

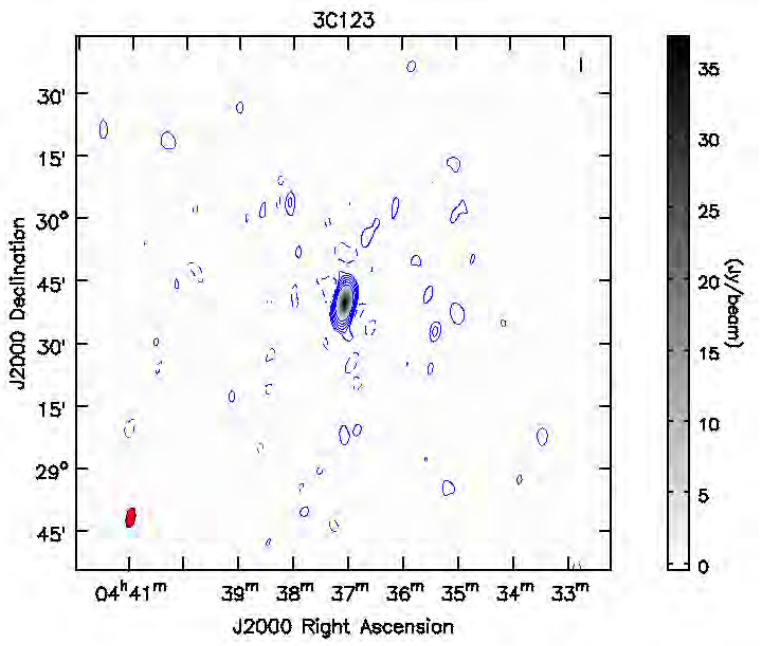

FIGURE 4.36: KAT-7 1.83 GHz radio image of 3C123. Contours are drawn at [-1, 1, 2, 4, 8, 16, 32]× 0.11 Jy/beam; where the image has a noise of 0.037 Jy/beam and peak brightness of 37.1 Jy/beam. The synthesised beam is $6.21' \times 2.56'$ and shown in the left bottom with a red filled ellipse.

- **PKS J0440-4333**

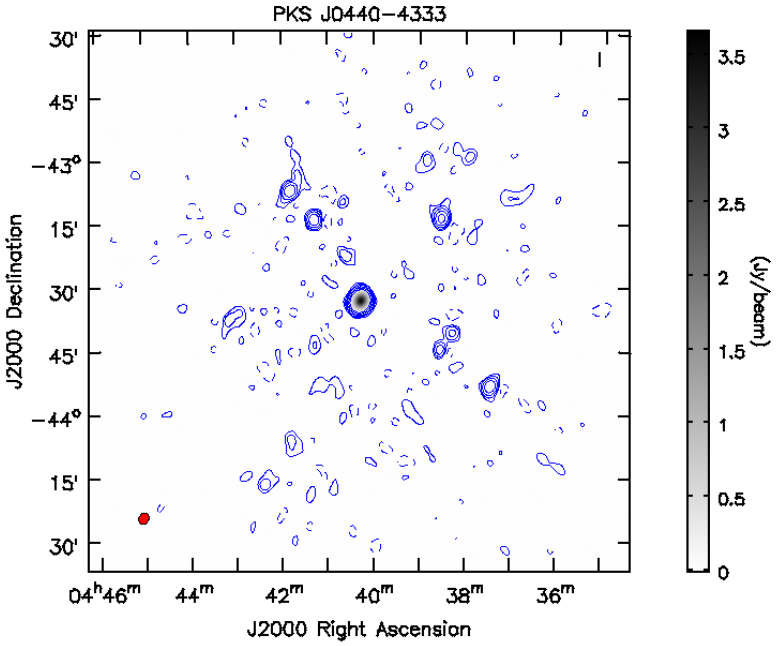

FIGURE 4.37: KAT-7 1.83 GHz radio image of PKS J0440-4333. Contours are drawn at [-1, 1, 2, 4, 8, 16, 32]× 8.01 mJy/beam; where the image has a noise of 3.27 mJy/beam and peak brightness of 3.66 Jy/beam. The synthesised beam is $2.79' \times 2.36'$ and shown in the left bottom with a red filled ellipse.

- **PKS J0442-0017**

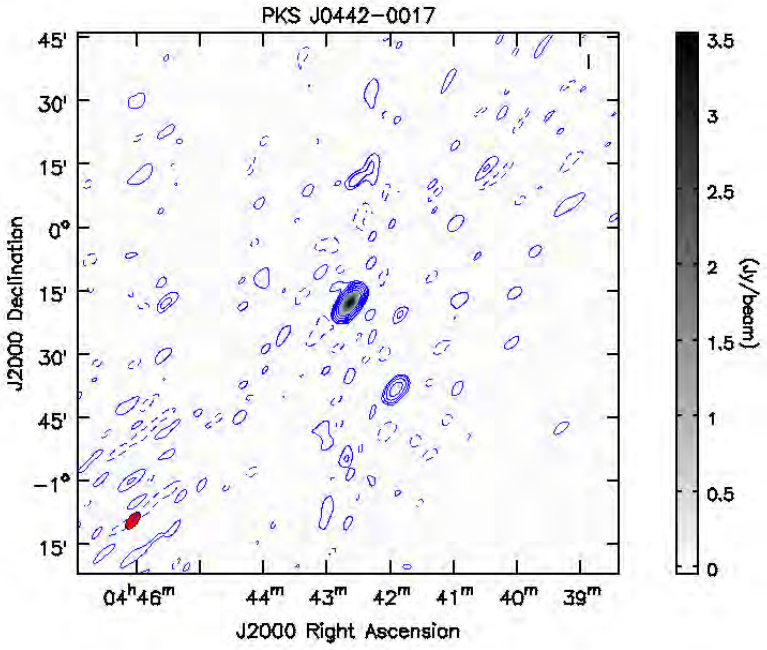

FIGURE 4.38: KAT-7 1.83 GHz radio image of PKS J0442-0017. Contours are drawn at [-1, 1, 2, 4, 8, 16, 32]× 21.60 mJy/beam; where the image has a noise of 7.20 mJy/beam and peak brightness of 3.54 Jy/beam. The synthesised beam is $3.31' \times 2.32'$ and shown in the left bottom with a red filled ellipse.

- **PKS J0444-2809**

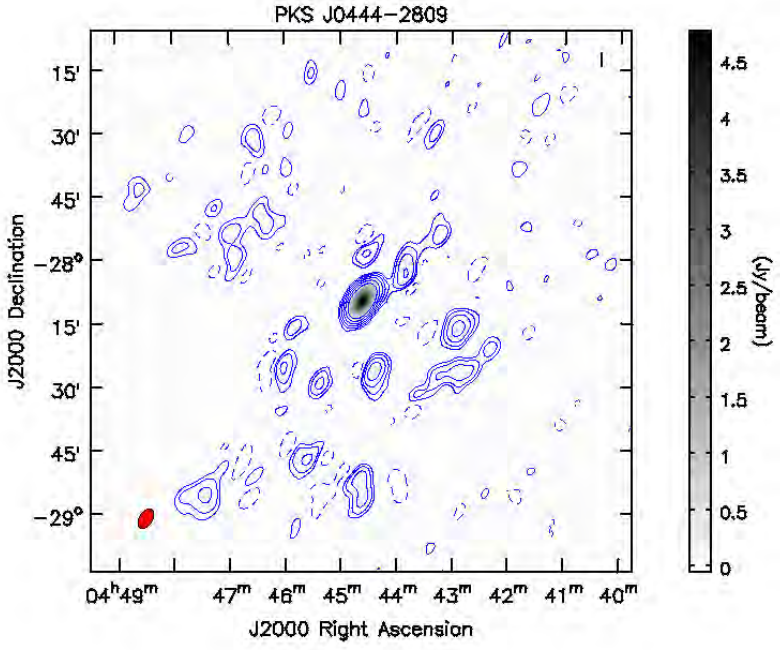

FIGURE 4.39: KAT-7 1.83 GHz radio image of PKS J0444-2809. Contours are drawn at [-1, 1, 2, 4, 8, 16, 32]× 19.10 mJy/beam; where the image has a noise of 6.37 mJy/beam and peak brightness of 4.77 Jy/beam. The synthesised beam is $4.68' \times 2.90'$ and shown in the left bottom with a red filled ellipse.

- **PKS J0453-2807**

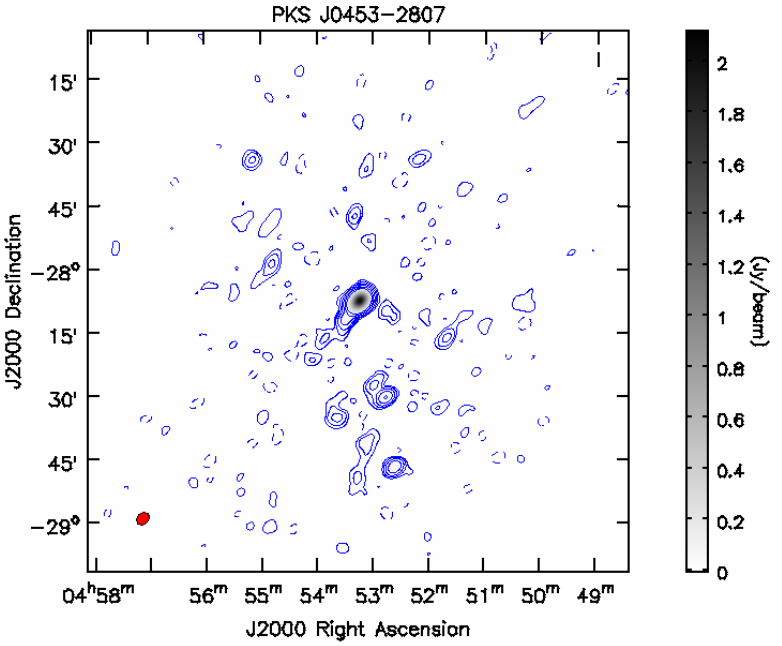

FIGURE 4.40: KAT-7 1.83 GHz radio image of PKS J0453-2807. Contours are drawn at [-1, 1, 2, 4, 8, 16, 32]× 4.10 mJy/beam; where the image has a noise of 1.37 mJy/beam and peak brightness of 2.12 Jy/beam. The synthesised beam is $3.28' \times 2.51'$ and shown in the left bottom with a red filled ellipse.

- **PKS J0534+1927**

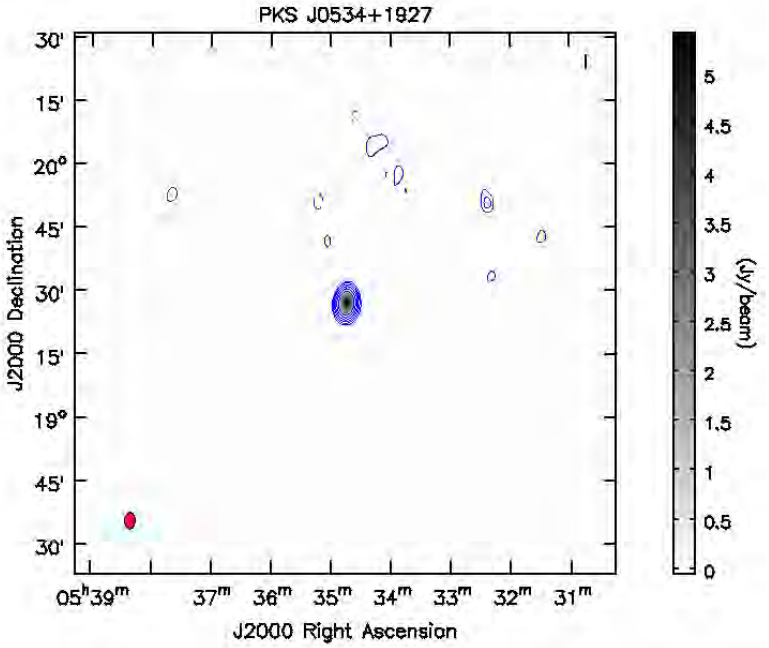

FIGURE 4.41: KAT-7 1.83 GHz radio image of PKS J0534+1927. Contours are drawn at [-1, 1, 2, 4, 8, 16, 32]× 38.40 mJy/beam; where the image has a noise of 12.80 mJy/beam and peak brightness of 5.42 Jy/beam. The synthesised beam is $3.88' \times 2.49'$ and shown in the left bottom with a red filled ellipse.

- **PKS J0538-4405**

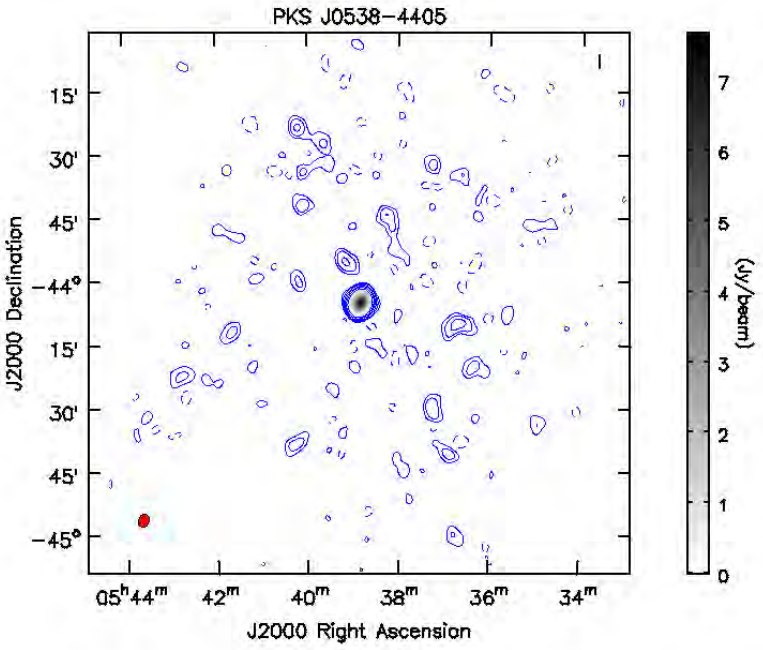

FIGURE 4.42: KAT-7 1.83 GHz radio image of PKS J0538-4405. Contours are drawn at [-1, 1, 2, 4, 8, 16, 32]× 8.10 mJy/beam; where the image has a noise of 2.80 mJy/beam and peak brightness of 7.68 Jy/beam. The synthesised beam is $3.31' \times 2.32'$ and shown in the left bottom with a red filled ellipse.

- **PKS J0744-0629**

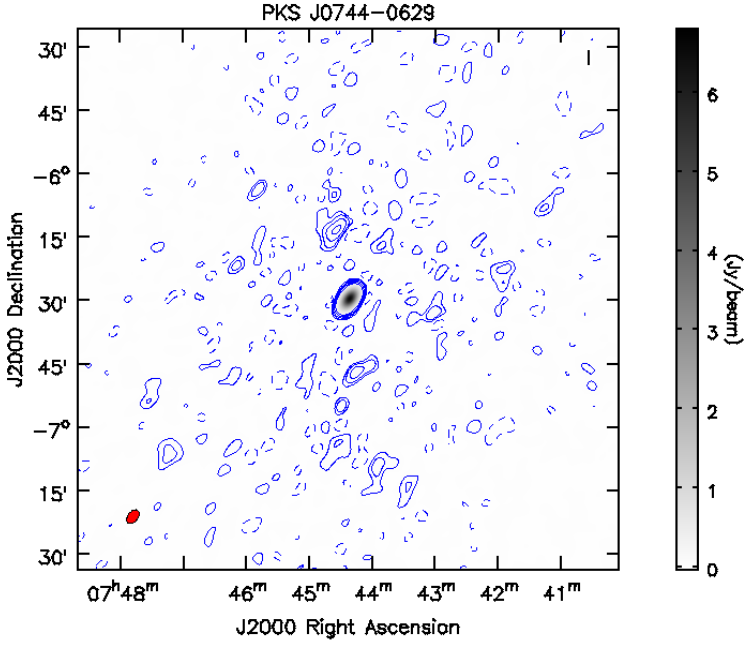

FIGURE 4.43: KAT-7 1.83 GHz radio image of PKS J0744-0629. Contours are drawn at [-1, 1, 2, 4, 8, 16, 32]× 14.10 mJy/beam; where the image has a noise of 4.65 mJy/beam and peak brightness of 6.85 Jy/beam. The synthesised beam is $3.31' \times 2.32'$ and shown in the left bottom with a red filled ellipse.

- **PKS J0837-1951**

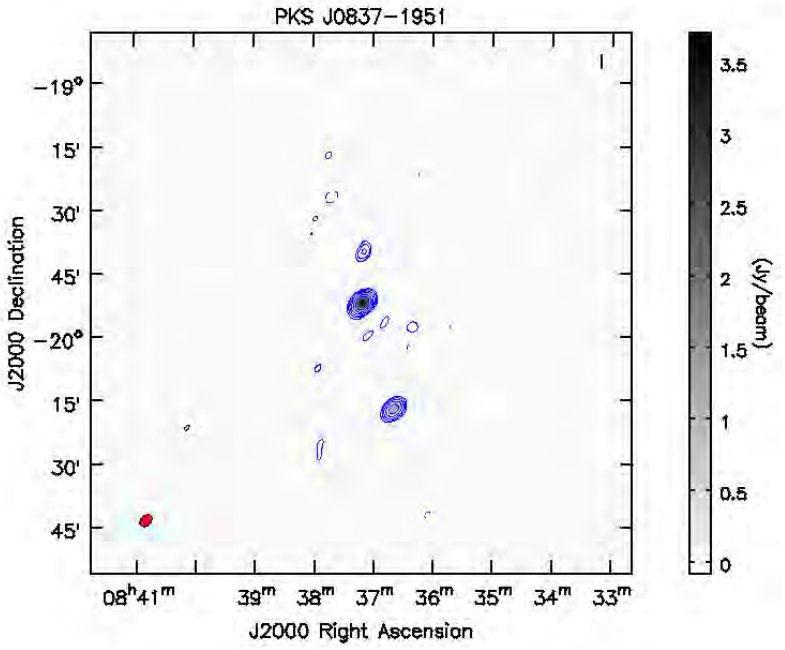

FIGURE 4.44: KAT-7 1.83 GHz radio image of PKS J0837-1951. Contours are drawn at [-1, 1, 2, 4, 8, 16, 32]× 49.20 mJy/beam; where the image has a noise of 16.40 mJy/beam and peak brightness of 3.71 Jy/beam. The synthesised beam is $3.31' \times 2.38'$ and shown in the left bottom with a red filled ellipse.

- **PKS J0943-0891**

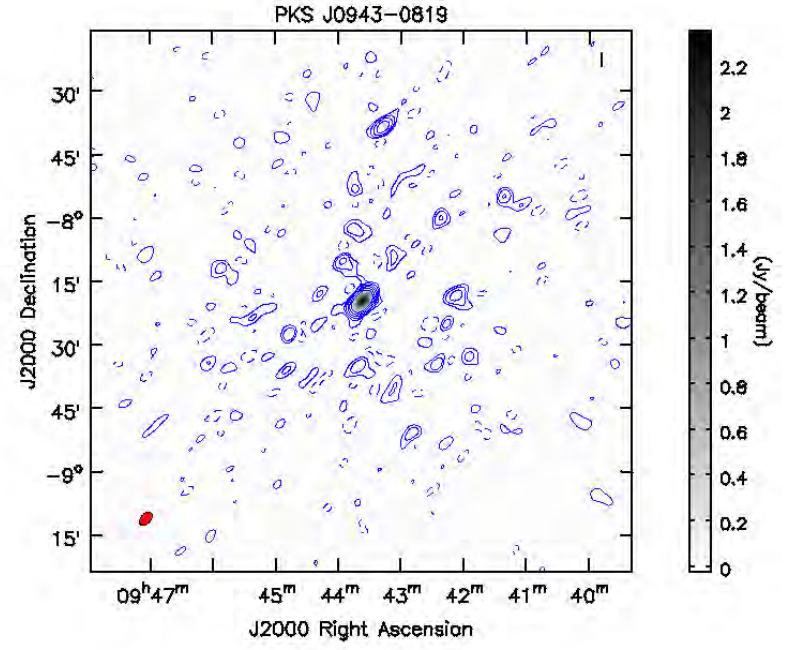

FIGURE 4.45: KAT-7 1.83 GHz radio image of PKS J0943-0891. Contours are drawn at [-1, 1, 2, 4, 8, 16, 32]× 11.10 mJy/beam; where the image has a noise of 3.70 mJy/beam and peak brightness of 2.35 Jy/beam. The synthesised beam is $3.74' \times 2.39'$ and shown in the left bottom with a red filled ellipse.

- **PKS J1130-1449**

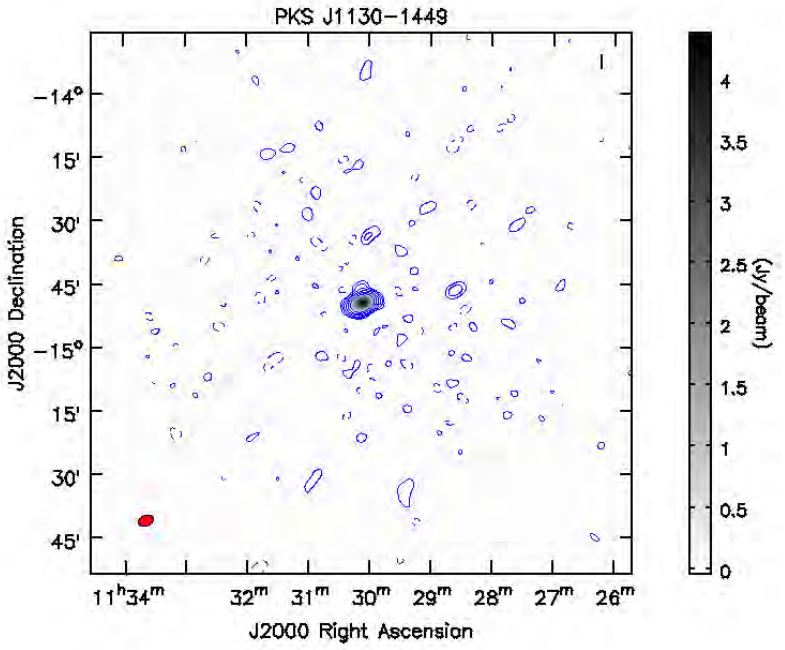

FIGURE 4.46: KAT-7 1.83 GHz radio image of PKS J1130-1449. Contours are drawn at [-1, 1, 2, 4, 8, 16, 32]× 22.09 mJy/beam; where the image has a noise of 7.36 mJy/beam and peak brightness of 4.38 Jy/beam. The synthesised beam is $3.64' \times 2.47'$ and shown in the left bottom with a red filled ellipse.

- **PKS J1154-3505**

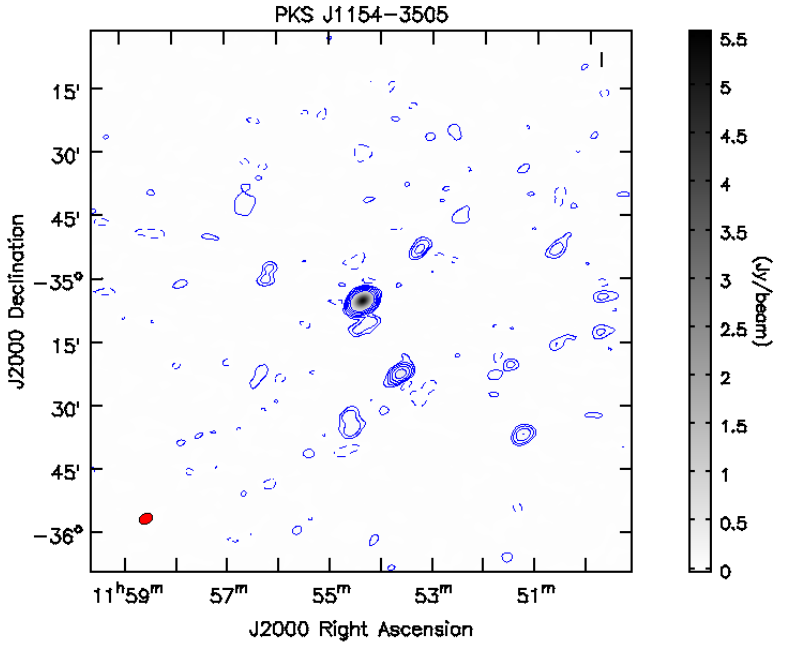

FIGURE 4.47: KAT-7 1.83 GHz radio image of PKS J1154-3505. Contours are drawn at [-1, 1, 2, 4, 8, 16, 32]× 15.00 mJy/beam; where the image has a noise of 3.00 mJy/beam and peak brightness of 5.55 Jy/beam. The synthesised beam is $3.28' \times 2.40'$ and shown in the left bottom with a red filled ellipse.

- **PKS J1248-1959**

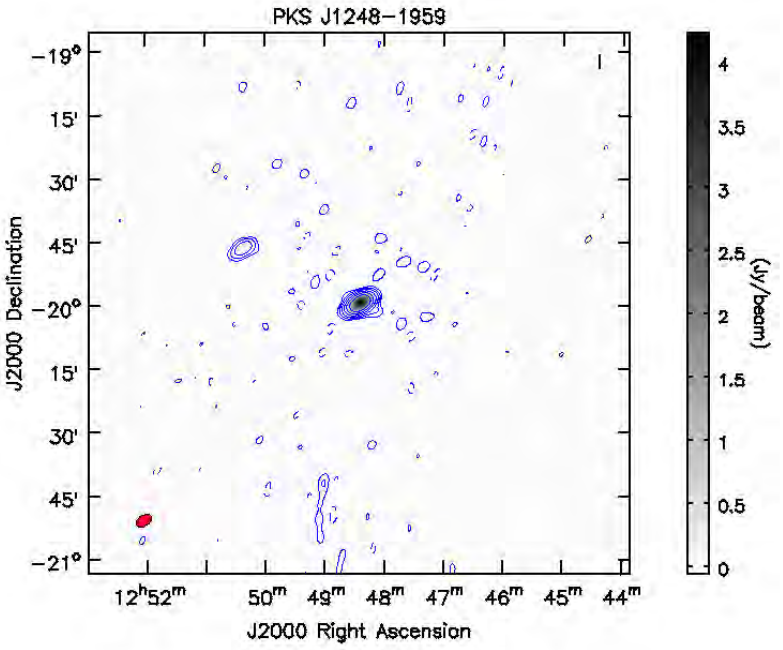

FIGURE 4.48: KAT-7 1.83 GHz radio image of PKS J1248-1959. Contours are drawn at [-1, 1, 2, 4, 8, 16, 32]× 40.01 mJy/beam; where the image has a noise of 13.33 mJy/beam and peak brightness of 4.23 Jy/beam. The synthesised beam is $4.05' \times 2.53'$ and shown in the left bottom with a red filled ellipse.

- **PKS J1311-2216**

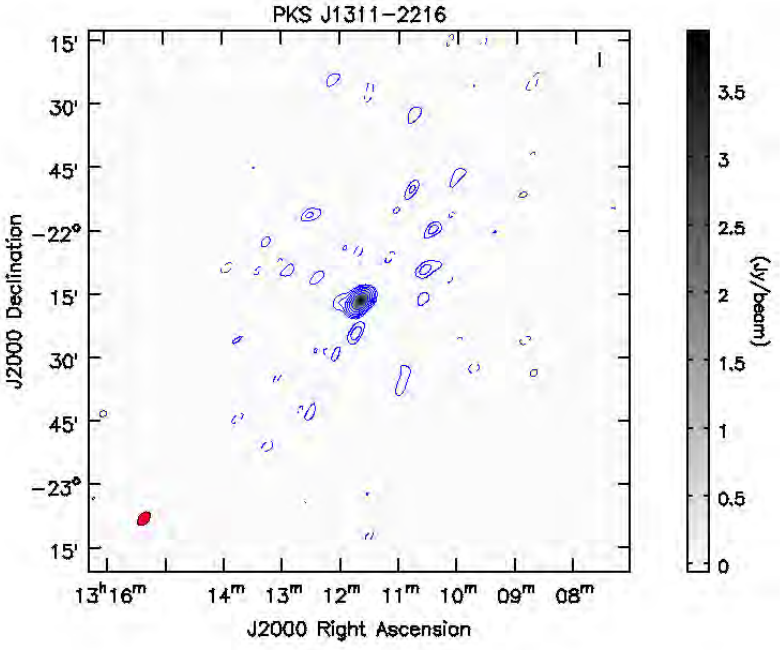

FIGURE 4.49: KAT-7 1.83 GHz radio image of PKS J1311-2216. Contours are drawn at [-1, 1, 2, 4, 8, 16, 32]× 11.10 mJy/beam; where the image has a noise of 3.70 mJy/beam and peak brightness of 3.94 Jy/beam. The synthesised beam is $3.81' \times 2.43'$ and shown in the left bottom with a red filled ellipse.

- **PKS J1510-0534**

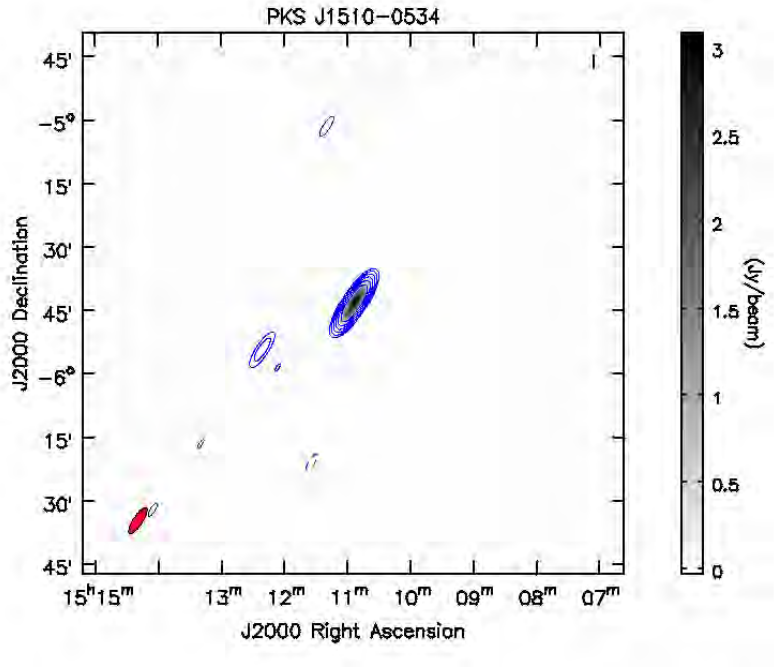

FIGURE 4.50: KAT-7 1.83 GHz radio image of PKS J1510-0534. Contours are drawn at [-1, 1, 2, 4, 8, 16, 32]× 24.00 mJy/beam; where the image has a noise of 8.00 mJy/beam and peak brightness of 3.11 Jy/beam. The synthesised beam is $7.17' \times 2.19'$ and shown in the left bottom with a red filled ellipse.

- **PKS J1517-2422**

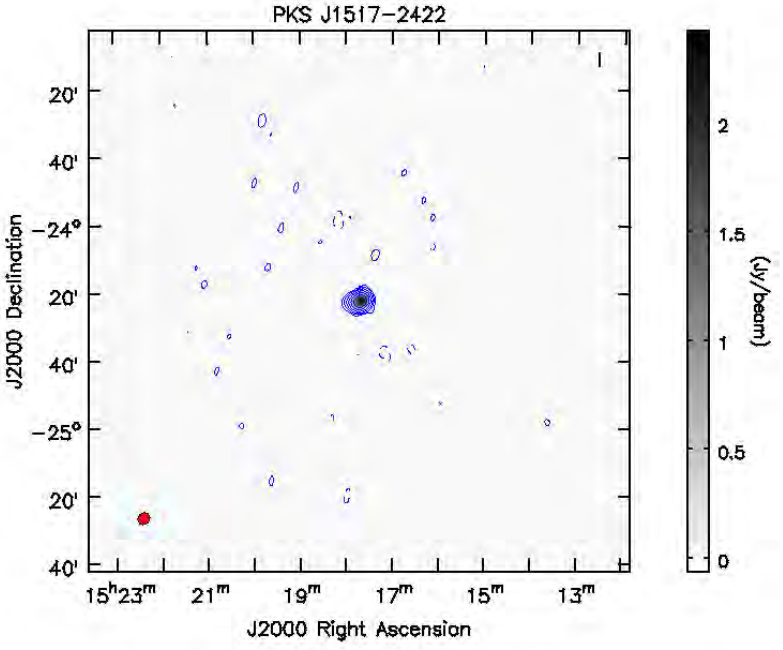

FIGURE 4.51: KAT-7 1.83 GHz radio image of PKS J1517-2422. Contours are drawn at [-1, 1, 2, 4, 8, 16, 32]× 35.60 mJy/beam; where the image has a noise of 11.87 mJy/beam and peak brightness of 2.33 Jy/beam. The synthesised beam is $5.17' \times 2.62'$ and shown in the left bottom with a red filled ellipse.

- **PKS J1744-5144**

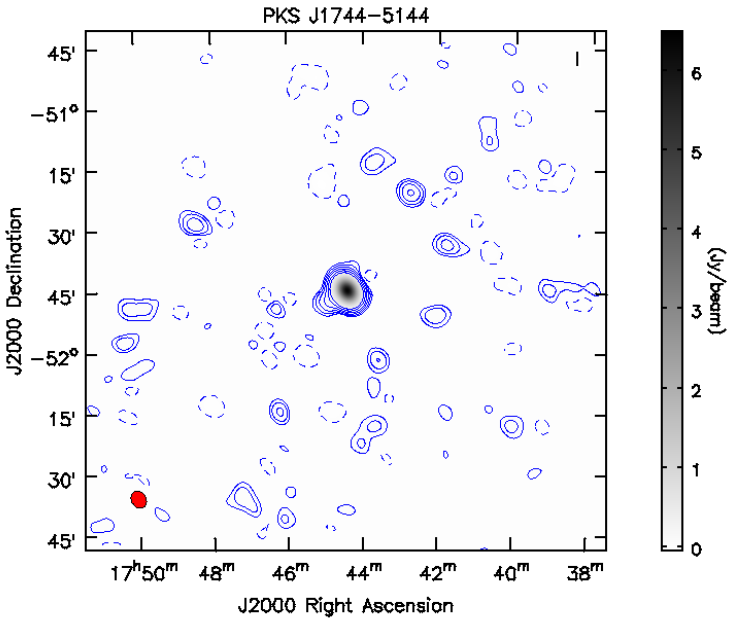

FIGURE 4.52: KAT-7 1.83 GHz radio image of PKS J1744-5144. Contours are drawn at [-1, 1, 2, 4, 8, 16, 32]× 8.58 mJy/beam; where the image has a noise of 2.86 mJy/beam and peak brightness of 7.38 Jy/beam. The synthesised beam is $3.80' \times 3.26'$ and shown in the left bottom with a red filled ellipse.

- **PMN J1712-2809**

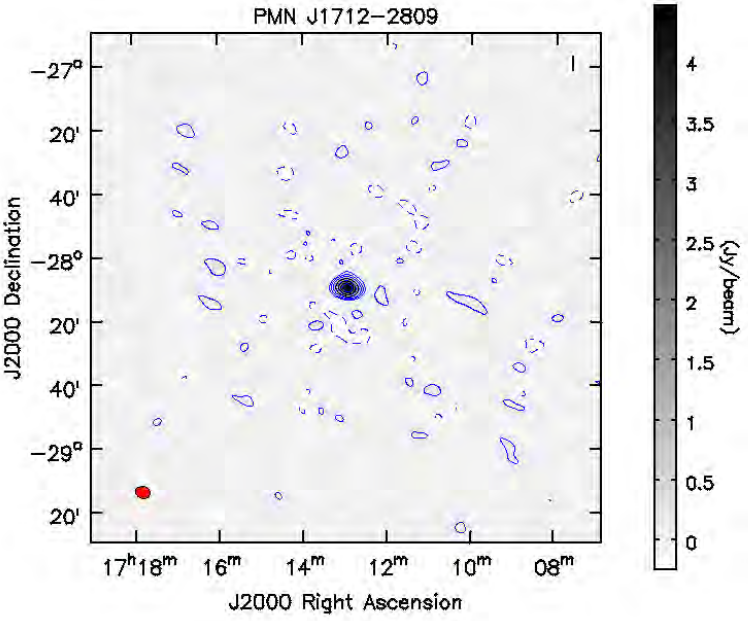

FIGURE 4.53: KAT-7 1.83 GHz radio image of PMN J1712-2809. Contours are drawn at [-1, 1, 2, 4, 8, 16, 32]× 98.89 mJy/beam; where the image has a noise of 33.33 mJy/beam and peak brightness of 4.47 Jy/beam. The synthesised beam is $6.93' \times 3.34'$ and shown in the left bottom with a red filled ellipse.

- **PKS J1819-6345**

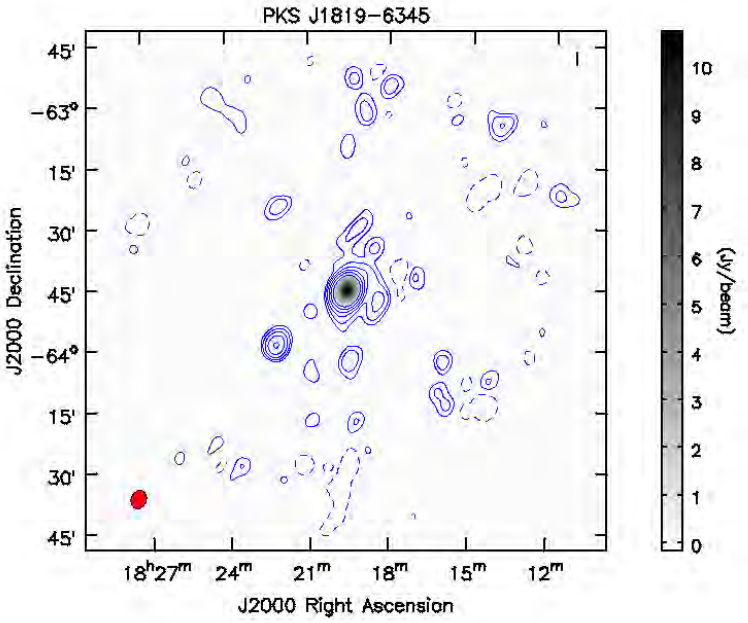

FIGURE 4.54: KAT-7 1.83 GHz radio image of PKS J1819-6345. Contours are drawn at [-1, 1, 2, 4, 8, 16, 32]× 43.01 mJy/beam; where the image has a noise of 13.33 mJy/beam and peak brightness of 10.68 Jy/beam. The synthesised beam is $3.80' \times 3.26'$ and shown in the left bottom with a red filled ellipse.

- **PKS J1830-3602**

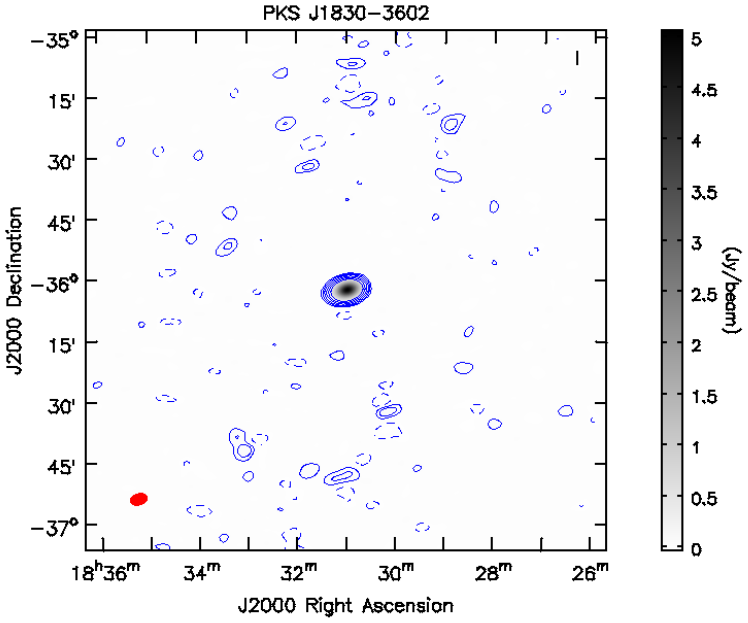

FIGURE 4.55: KAT-7 1.83 GHz radio image of PKS J1830-3602. Contours are drawn at [-1, 1, 2, 4, 8, 16, 32]× 14.16 mJy/beam; where the image has a noise of 4.72 mJy/beam and peak brightness of 5.07 Jy/beam. The synthesised beam is $4.28' \times 2.81'$ and shown in the left bottom with a red filled ellipse.

- **PKS J1833-2103**

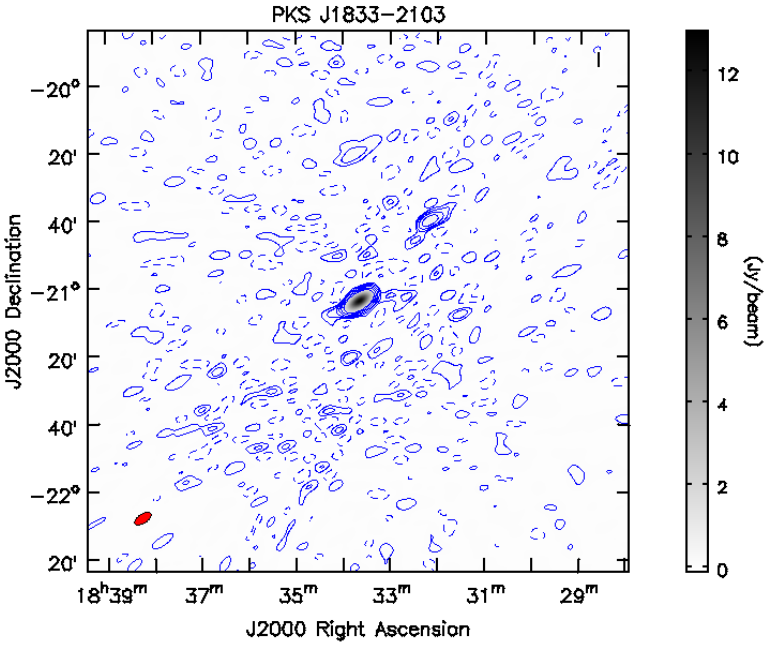

FIGURE 4.56: KAT-7 1.83 GHz radio image of PKS J1833-2103. Contours are drawn at [-1, 1, 2, 4, 8, 16, 32]× 38.10 mJy/beam; where the image has a noise of 7.20 mJy/beam and peak brightness of 12.91 Jy/beam. The synthesised beam is $5.71' \times 2.69'$ and shown in the left bottom with a red filled ellipse.

- **PKS J1924-2914**

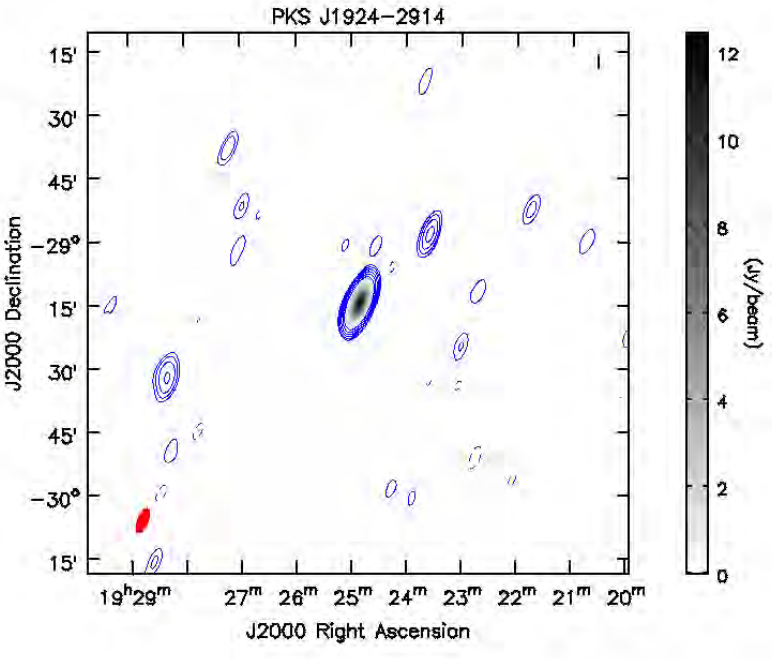

FIGURE 4.57: KAT-7 1.83 GHz radio image of PKS J1924-2914. Contours are drawn at [-1, 1, 2, 4, 8, 16, 32]× 15.27 mJy/beam; where the image has a noise of 5.09 mJy/beam and peak brightness of 12.44 Jy/beam. The synthesised beam is $6.15' \times 2.58'$ and shown in the left bottom with a red filled ellipse.

- **PKS J1935-4620**

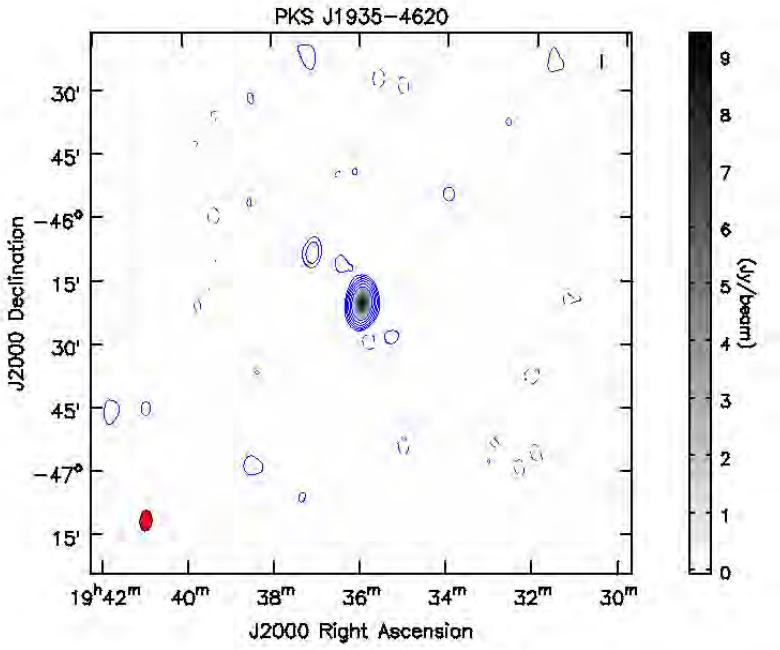

FIGURE 4.58: KAT-7 1.83 GHz radio image of PKS J1935-4620. Contours are drawn at [-1, 1, 2, 4, 8, 16, 32]× 15.6 mJy/beam; where the image has a noise of 5.20 mJy/beam and peak brightness of 9.42 Jy/beam. The synthesised beam is $4.86' \times 2.83'$ and shown in the left bottom with a red filled ellipse.

- **PKS J1941-1524**

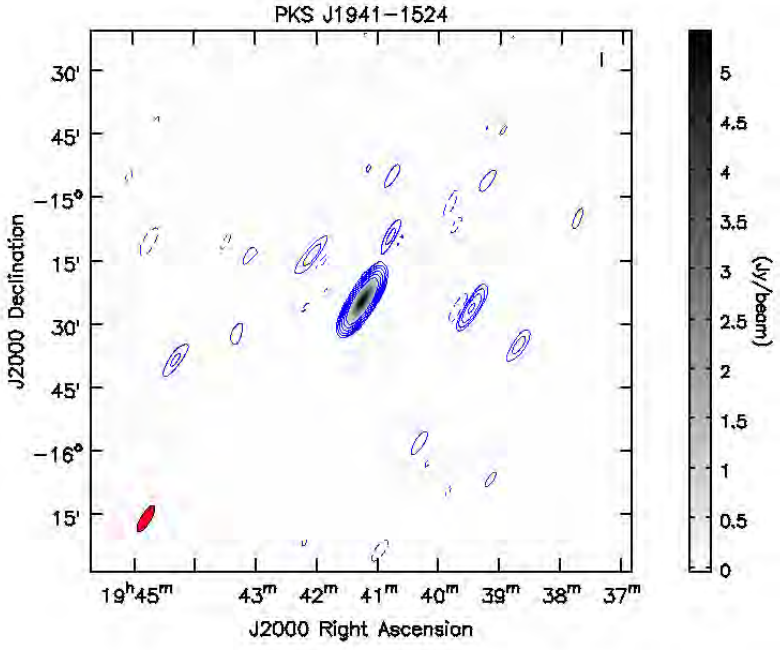

FIGURE 4.59: KAT-7 1.83 GHz radio image of PKS J1941-1524. Contours are drawn at [-1, 1, 2, 4, 8, 16, 32]× 20.40 mJy/beam; where the image has a noise of 6.80 mJy/beam and peak brightness of 5.29 Jy/beam. The synthesised beam is $7.29' \times 2.31'$ and shown in the left bottom with a red filled ellipse.

- **PKS J2129-1821**

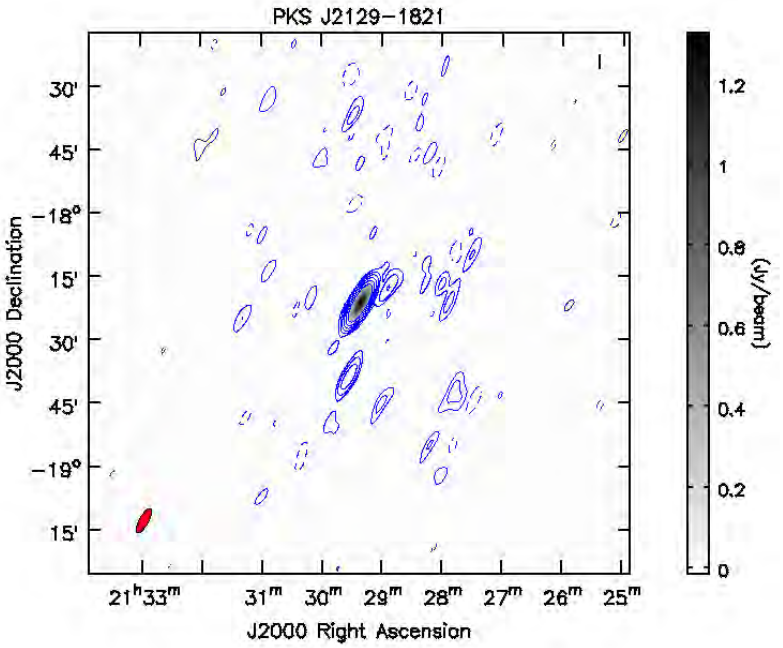

FIGURE 4.60: KAT-7 1.83 GHz radio image of PKS J2129-1821. Contours are drawn at [-1, 1, 2, 4, 8, 16, 32]× 7.50 mJy/beam; where the image has a noise of 2.50 mJy/beam and peak brightness of 1.33 Jy/beam. The synthesised beam is $6.65' \times 2.11'$ and shown in the left bottom with a red filled ellipse.

- **PKS J2131-2036**

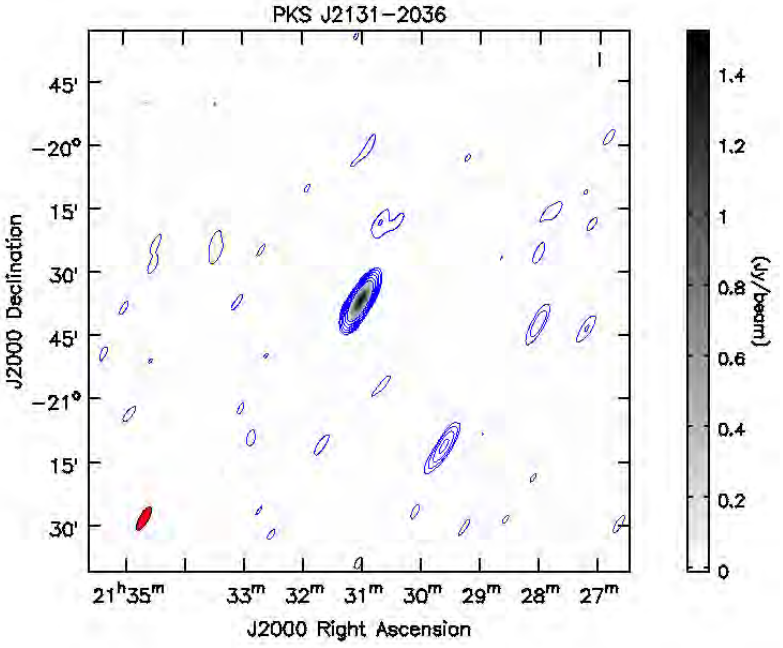

FIGURE 4.61: KAT-7 1.83 GHz radio image of PKS J2131-2036. Contours are drawn at [-1, 1, 2, 4, 8, 16, 32]× 6.00 mJy/beam; where the image has a noise of 2.00 mJy/beam and peak brightness of 1.52 Jy/beam. The synthesised beam is $6.34' \times 2.10'$ and shown in the left bottom with a red filled ellipse.

- **PKS J2151-3027**

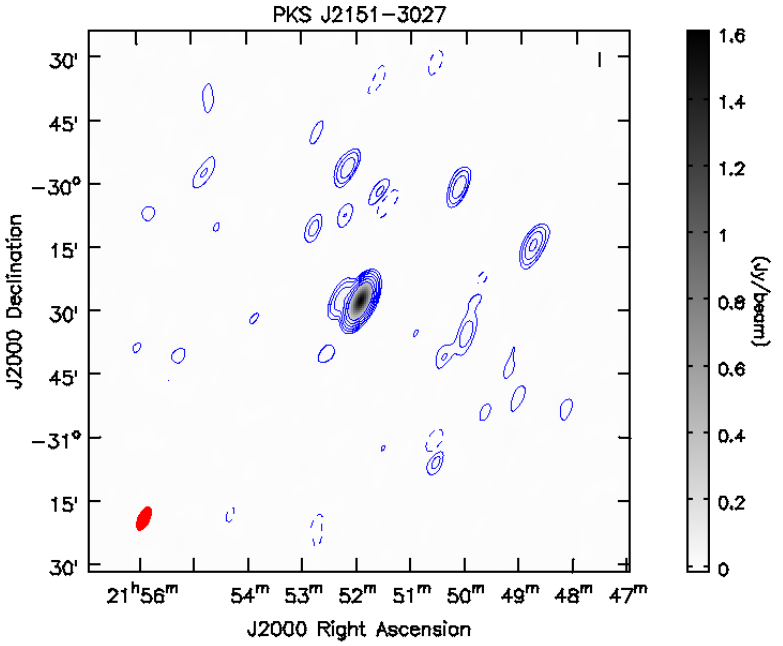

FIGURE 4.62: KAT-7 1.83 GHz radio image of PKS J2151-3027. Contours are drawn at [-1, 1, 2, 4, 8, 16, 32]× 7.53 mJy/beam; where the image has a noise of 2.51 mJy/beam and peak brightness of 1.61 Jy/beam. The synthesised beam is $5.93' \times 2.74'$ and shown in the left bottom with a red filled ellipse.

- **PKS J2152-2828**

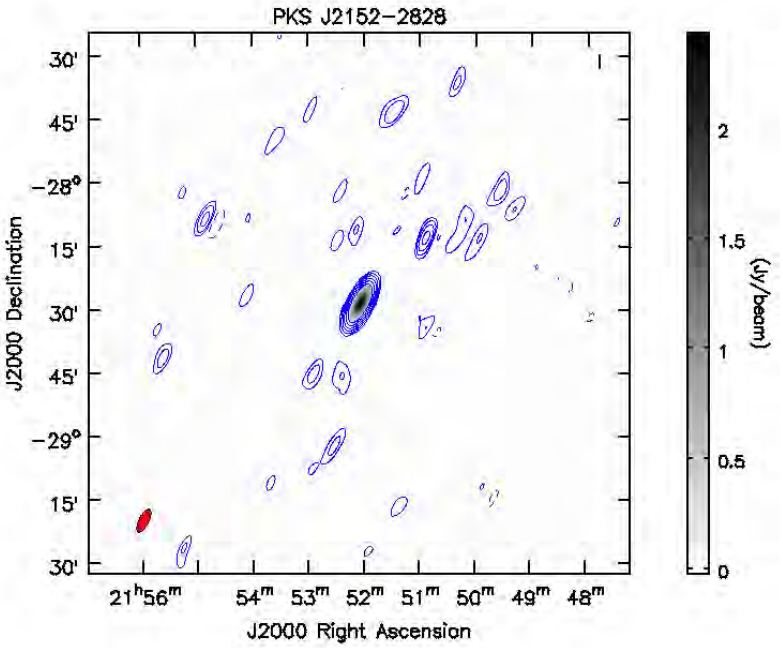

FIGURE 4.63: KAT-7 1.83 GHz radio image of PKS J2152-2828. Contours are drawn at [-1, 1, 2, 4, 8, 16, 32]× 9.60 mJy/beam; where the image has a noise of 3.30 mJy/beam and peak brightness of 2.44 Jy/beam. The synthesised beam is $5.90' \times 2.28'$ and shown in the left bottom with a red filled ellipse.

- **PKS J2206-1835**

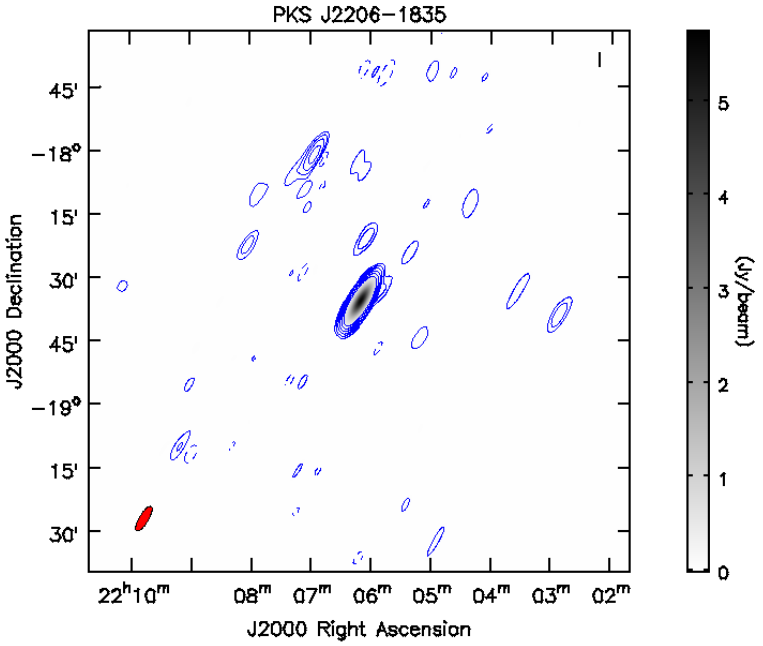

FIGURE 4.64: KAT-7 1.83 GHz radio image of PKS J2206-1835. Contours are drawn at [-1, 1, 2, 4, 8, 16, 32]× 11.10 mJy/beam; where the image has a noise of 3.67 mJy/beam and peak brightness of 5.75 Jy/beam. The synthesised beam is $6.69' \times 2.13'$ and shown in the left bottom with a red filled ellipse.

- **PKS J2219-2756**

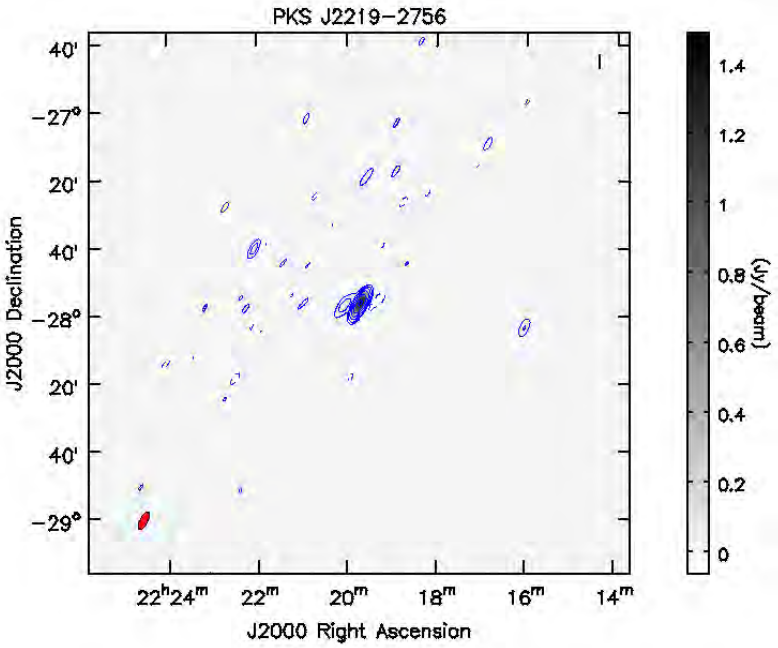

FIGURE 4.65: KAT-7 1.83 GHz radio image of PKS J2219-2756. Contours are drawn at × 4.20 mJy/beam; where the image has a noise of 1.40 mJy/beam and peak brightness of 1.49 Jy/beam. The synthesised beam is $5.88' \times 2.17'$ and shown in the left bottom with a red filled ellipse.

Chapter 5

Conclusions And Future Work

Conclusion

In this thesis we have taken the first steps towards identifying good flux-density calibrators for the prototype radio telescope KAT-7 and verified the capability of the KAT-7 array to track extragalactic sources with very good accuracy. The systematic error due to bootstrapping accuracy for KAT-7 was found to be about $\sim 5\%$ of the measured flux density. The calibrators we have found can be used for future science with the KAT-7 telescope by providing standards for use in the data reduction procedures. For this purpose, we recommend the good flux density calibrator candidates we identified; namely the 18 sources that had values less than 0.05 in their Variability Index (`VI`) and Modulation Index (`MI`) and all the sources in the field had less than 10% of the peak flux density of the calibrator candidate ; see Table 4.2 and 4.3). One source (PKS J0837-1951), which showed low variability and hence appeared to be a good flux-density calibrator candidate (class A), was deemed to be not a good flux-density calibrator candidate because a strong confusing source (NVSS J083639-201658) was found within its primary beam. More generally, these sources may be useful flux density calibrator candidates for interferometry arrays with short spacings.

On the other hand, five sources were identified as being variable source and hence inappropriate as flux density calibrators because they had `VI` or `MI` values greater than 0.09 (see Table 4.2 and 4.3). Other studies of these sources (see Section 2.4) supported this conclusion that these sources are significantly variable. 16 sources, which we included them under class B and class C, should be examined and studied further.

In addition we used another measure of variability, the de-biased modulation index $\mathtt{M}_d$, defined by Chen et al. [76]. We determined whether the observed variation in flux

density could be due only measurement errors by simulating a large number of constant sources with the observed error bars and observing cadence and asking what fraction of the simulations had larger de-biased modulation indices larger than the observed value.

Future Work

During the due course of this research work, we have recognized some research points we recommend be incorporated in future work:

- Only the flux variabilities of the sources at a single frequency (1.83 GHz) have been studied in this thesis. However, it is very important to examine the flux variabilities at different frequencies with sufficient data so as to obtain a complete picture. In addition to this, polarization characteristics of the sources have to be studied in order to fully declare their suitability as calibrators [80] and understand their emission properties.

- We identified good flux calibrator candidates by statistically analyse their temporal flux variabilities. We note that the flux variability can either be intrinsic or extrinsic, or a combination of both phenomenons (refer Section 1.3.7). We recommend for future study which of the phenomenons contribute to the flux variability in each source.

- The southern sky lacks suitable flux calibrator sources. Based on the method used in this thesis, further observations can be performed in order to fill the southern sky with enough calibrator sources. This is particularly vital during the commissioning phase of radio telescope arrays around the southern hemisphere.

  In this thesis, the flux densities and positions of the sources were extracted from their "CLEAN" images (Section 3.3) by Gaussian fitting. Determining parameters in this way can lead to biased estimations for the following reasons [16, 81].

  1. During the process of deconvolution, inaccurate cleaning may occur. As a consequence, we will get biased images that give us incorrect results of the desired parameters.
  2. Errors that are confined in the u-v plane will be dispersed throughout the entire image while Fourier transformed. In this case, errors corresponding to different pixels in an image will be correlated while measurements at different points in the u-v plane are uncorrelated. As a result, quantitative analysis and error estimations derived from the image may give unreliable results .

3. In case of sparse u-v coverage, an image will have extensive sidelobes. In such cases, identifying the desired source will be so uneasy and ambiguous that estimating the parameters from the image will be problematic.
4. Images of a source produced by visibility data observed at different times can show changes when compared each other. In such circumstance, it is challenging to specifically determine whether the differences are associated with real changes, or owing to the u-v sampling and image parameters.

Because of the above reasons, analysing the visibility data directly in the u-v domain is preferable so as to accurately determine the desired parameters. In order to give possible solutions to the listed problems, an alternative approaches can be implemented. Bayesian interference techniques are a promising method for future work as they can be applied directly in the visibility domain and take advantage of the rapidly increasing computational power available through Moore's Law.

Bibliography

[1] Kraus, J. D. *Radio Astronomy* (Cygnus-Quasar Books, 1984).

[2] Morison, I. *Introduction To Astronomy And Cosmology* (Wiley, 2008).

[3] Akhmanw, C. & Khokblov, R. Karl Jansky: His Career At Bell Telephone Laboratories. *Phys. Rev* **1**, 1350 (1959).

[4] Burke, B. F. & Francis Graham-Smith, S. *An Introduction To Radio Astronomy* (Cambridge University Press, 2002).

[5] Reber, G. A Play Entitled The Beginning Of Radio Astronomy. *Journal Of The Royal Astronomical Society Of Canada* **82**, 93 (1988).

[6] Miller, D. Basics Of Radio Astronomy For The Goldstone-Apple Valley Radio Telescope, 1997. *Retrieved April* **12** (2010).

[7] Zeilik, M. & Gregory, S. A. *Introductory Astronomy And Astrophysics* (Brooks/Cole Publishing, 1998).

[8] Wilson, T. T. L., Rohlfs, K. & Hüttemeister, S. *Tools Of Radio Astronomy* (Springer, 2009).

[9] Jewell, P. R. & Prestage, R. M. The Green Bank Telescope. In *Proc. of SPIE Vol*, vol. 5489, 313 (2004).

[10] Napier, P. *et al.* The Very Long Baseline Array. In *IEEE Proceedings*, vol. 82, 658–672 (1994).

[11] Thompson, A. R., Moran, J. M. & Swenson Jr, G. W. *Interferometry And Synthesis In Radio Astronomy* (Wiley-Vch, 2008).

[12] Haniff, C. An Introduction To The Theory of Interferometry (2006).

[13] Cornwell, T. J., Golap, K. & Bhatnagar, S. The noncoplanar baselines effect in radio interferometry: The w-projection algorithm. *Selected Topics in Signal Processing, IEEE Journal of* **2**, 647–657 (2008).

[14] Clark, B. C. Coherence In Radio Astronomy. In *Synthesis Imaging in Radio Astronomy*, vol. 6, 1 (1989).

[15] Briggs, D., Schwab, F. & Sramek, R. Synthesis Imaging In Radio Astronomy II. In *Proc. ASP Conf. Ser. Vol. 180*, 127 (Astron. Soc. Pac., 1999).

[16] GB Taylor, R. P. & Carilli, C. Synthesis Imaging In Radio Astronomy II, a Collection of Lectures On Synthesis Imaging In Radio Astronomy. *San Francisco, CA: ASP* **171** (1999).

[17] Perley, R. A. & Butler, B. J. An Accurate Flux Density Scale From 1 to 50 GHz. *astro-ph* (2012).

[18] Baars, J., Genzel, R., Pauliny-Toth, I. & Witzel, A. The Absolute Spectrum of CAS: An Accurate Flux Density Scale And a Set of Secondary Calibrators. *Astronomy and Astrophysics* **61**, 99–106 (1977).

[19] Alloin, D. Physics Of Active Galactic Nuclei At All Scales. In *Physics of Active Galactic Nuclei at all Scales*, vol. 693 (2006).

[20] Murdin, P. Encyclopedia Of Astronomy And Astrophysics (2001).

[21] Perley, R., Dreher, J. & Cowan, J. The Jet And Filaments In Cygnus A. *The Astrophysical Journal* **285**, L35–L38 (1984).

[22] Emonts, B. *Nearby Radio Galaxies: The Interplay Of Gas, Star Formation And Active Nucleus* (University Library Groningen][Host], 2006).

[23] Huege, T. & Falcke, H. Principles Of Synchrotron Emission: In An Astrophysical Context. *The Role of VLBI in Astrophysics, Astrometry and Geodesy* 13–27 (2005).

[24] Karttunen, H., Kröger, P. & Oja, H. *Fundamental Astronomy* (Springer Verlag, 2007).

[25] Fanaroff, B. & Riley, J. The morphology of extragalactic radio sources of high and low luminosity. *Monthly Notices of the Royal Astronomical Society* **167**, 31P–36P (1974).

[26] Saripalli, L. Understanding the fanaroff–riley radio galaxy classification. *The Astronomical Journal* **144**, 85 (2012).

[27] Schneider, P. *Extragalactic Astronomy And Cosmology: An Introduction* (Springer Verlag, 2006).

[28] Plank Collaboration. Planck 2013 Results. I. Overview Of Products And Scientific Results. *astro-ph* (2013).

[29] Carter, S. J. B. *Long-Term Remote Single-Dish Observations Of Blazar Radio Variability.* Ph.D. thesis, University of Tasmania (2008).

[30] Krawczynski, H. & Treister, E. Active Galactic Nuclei-the Physics of Individual Sources And The Cosmic History Of Formation And Evolution. *astro-ph* (2013).

[31] Kiepenheuer, K. Cosmic Rays As The Source of General Galactic Radio Emission. *Physical Review* **79**, 738 (1950).

[32] Peterson, B. M. *An Introduction To Active Galactic Nuclei* (Cambridge University Press, 1997).

[33] O'Dea, C. P. & Baum, S. A. Constraints On Radio Source Evolution From The Compact Steep Spectrum And GHz Peaked Spectrum Radio Sources. *The Astronomical Journal* **113**, 148–161 (1997).

[34] Ulrich, M.-H., Maraschi, L. & Urry, C. M. Variability Of Active Galactic Nuclei. *Annual Review of Astronomy and Astrophysics* **35**, 445–502 (1997).

[35] Heeschen, D., Krichbaum, T., Schalinski, C. & Witzel, A. Rapid Variability Of Extragalactic Radio Sources. *The Astronomical Journal* **94**, 1493–1507 (1987).

[36] Koay, J. *et al.* Interstellar Scattering As A Cosmological Probe. In *General Assembly and Scientific Symposium, 2011 XXXth URSI*, 1–4 (IEEE, 2011).

[37] Bernhart, S. *Flux Density and VLBI Measurements Of The IDV Source 0917+624.* Ph.D. thesis, Universitäts-und Landesbibliothek Bonn (2010).

[38] Blandford, R. D. *Pulsars As Physics Laboratories*, vol. 341 (Oxford University Press, 1993).

[39] Walker, M. A. Interstellar Scintillation Of Compact Extragalactic Radio Sources. *Monthly Notices Of The Royal Astronomical Society* **294**, 307–311 (1998).

[40] KAT-7 Commissioning Team. Specfications of The KAT-7 Telescope (2012). http://public.ska.ac.za/kat-7.

[41] Condon *et al.* The NRAO VLA Sky Survey (1998).

[42] Reynolds, J. A Revised Flux Scale For The AT Compact Array. *ATNF Internal* (1994).

[43] Sault, R. ATCA Flux Density Scale At 12 mm (2003).

[44] ATCA Calibrator Database V3. Flux Density Time Series Plots (2012). http://www.narrabri.atnf.csiro.au/calibrators.

[45] Peng, B., Kraus, A., Krichbaum, T., Witzel, A. *et al.* Long-Term Monitoring Of Selected Radio Sources. *Astronomy and Astrophysics Supplement Series* **145**, 1–10 (2000).

[46] Tyulbashev, S. & Chernikov, P. Physical Conditions In Steep-Spectrum Radio Sources. *Astronomy Reports* **44**, 286–297 (2000).

[47] Kedziora-Chudczer, L., Jauncey, D., Wieringa, M., Reynolds, J. & Tzioumis, A. Four Southern Intraday Variable Radio Sources. In *Astronomical Society Of The Pacfic Conference Series*, vol. 144, 271–272 (Astronomical Society Of The Pacfic, 1998).

[48] di Serego-Alighieri, S., Danziger, I., Morganti, R. & Tadhunter, C. New Identifications And Redshifts For Southern 2-Jy Radio Sources. *Monthly Notices of the Royal Astronomical Society* **269**, 998 (1994).

[49] Labiano, A. *et al.* GPS Radio Sources: New Optical Observations And An Updated Master List. *astro-ph* (2006).

[50] Healey, S. E. *et al.* Crates: An All-Sky Survey Of Flat-Spectrum Radio Sources. *The Astrophysical Journal Supplement Series* **171**, 61 (2007).

[51] Tadhunter, C. *et al.* The Origin Of The UV Excess In Powerful Radio Galaxies: Spectroscopy And Polarimetry Of A Complete Sample Of Intermediate-Redshift Rradio Galaxies. *Monthly Notices of the Royal Astronomical Society* **330**, 977–996 (2002).

[52] Morganti, R. *et al.* The Radio Structures Of Southern 2 Jy Radio Sources: New ATCA And VLA Radio Images. *astro-ph* (1999).

[53] Edwards, P. & Tingay, S. New Candidate GHz Peaked Spectrum And Compact Steep Spectrum Sources. *astro-ph* (2004).

[54] Tingay, S. J. *et al.* ATCA Monitoring Observations of 202 Compact Radio Sources in Support of The VSOP AGN Survey. *Publications of the Astronomical Society of Japan* **55**, 351–384 (2003).

[55] Tadhunter, C., Morganti, R., di Serego-Alighieri, S., Fosbury, R. & Danziger, I. Optical Spectroscopy Of a Complete Sample Of Southern 2-Jy Radio Sources. *Monthly Notices of the Royal Astronomical Society* **263**, 999 (1993).

[56] Dallacasa, D., Fanti, C., Fanti, R., Schilizzi, R. & Spencer, R. A Sample Of Small Size Compact Steep-Spectrum Radio Sources. 1: VLBI Images At 18 cm. *Astronomy and Astrophysics* **295**, 27–42 (1995).

[57] Liu, X., Cui, L., Luo, W.-F., Shi, W.-Z. & Song, H.-G. VLBI Observations Of Nineteen GHz-Peaked-Spectrum Radio Sources At 1.6 GHz. *astro-ph* (2007).

[58] Zirbel, E. L. & Baum, S. A. The Ultraviolet Continuum Emission Of Radio Galaxies. i: Description of Sources From The Hubble Space Telescope Archives. *The Astrophysical Journal Supplement Series* **114**, 177 (1998).

[59] Tornikoski, M., Jussila, I., Johansson, P., Lainela, M. & Valtaoja, E. Radio Spectra And Variability Of Gigahertz-Peaked Spectrum Radio Sources And Candidates. *The Astronomical Journal* **121**, 1306 (2001).

[60] Morganti, R. *et al.* The Radio Structures Of Southern 2-Jy Radio Sources: New ATCA and VLA Radio Images. *astro-ph* (1999).

[61] Fomalont, E. *et al.* The VSOP 5 GHz Continuum Survey: The Prelaunch VLBA Observations. *The Astrophysical Journal Supplement Series* **131**, 95 (2000).

[62] Scott, W. *et al.* The VSOP 5 GHz Active Galactic Nucleus Survey. III. Imaging Results For The First 102 Sources. *The Astrophysical Journal Supplement Series* **155**, 33 (2004).

[63] Shen, Z.-Q. *et al.* A 5 GHz Southern Hemisphere VLBI Survey Of Compact Radio Sources. II. *The Astronomical Journal* **115**, 1357 (1998).

[64] Dallacasa, D., Bondi, M., Alef, W. & Mantovani, F. European VLBI Network Dual Frequency Observations Of CSS-GPS Candidates. *Astronomy and Astrophysics Supplement Series* **129**, 219–236 (1998).

[65] Jorstad, S. G. *et al.* Multiepoch Very Long Baseline Array Observations Of EGRET-Detected Quasars And BL Lacertae Objects: Superluminal Motion Of Gamma-Ray Bright Blazars. *The Astrophysical Journal Supplement Series* **134**, 181 (2001).

[66] Mantovani, F. *et al.* Observations At Arcsecond Resolution Of Steep-Spectrum Sources Which Vary At Low Frequencies. *Monthly Notices of the Royal Astronomical Society* **257**, 353–367 (1992).

[67] Falomo, R., Scarpa, R. & Bersanelli, M. Optical Opectrophotometry Of Blazars. *The Astrophysical Journal Supplement Series* **93**, 125–143 (1994).

[68] Morganti, R. *et al.* HI Absorption In Radio Galaxies: Effect Of Orientation or Interstellar Medium? *Monthly Notices of the Royal Astronomical Society* **323**, 331–342 (2001).

[69] Miller-Jones, J. *Relativistic Radio Jets In Our Galaxy.* Ph.D. thesis, University of Oxford (2004).

[70] Reynolds, J. A Revised Flux Scale For The AT Compact Array. *CSIRO, ATNF Technical Memo* **39**, 040 (1994).

[71] Perley, R. & Taylor, G. VLA Calibration Manual: Socorro, (NRAO) (2003).

[72] Winn, J. N., Patnaik, A. R. & Wrobel, J. Interferometric Phase Calibration Sources In The Declination Range 0 to–30. *The Astrophysical Journal Supplement Series* **145**, 83 (2003).

[73] Högbom, J. Aperture Synthesis With a Non-Regular Distribution Of Interferometer Baselines. *Astronomy and Astrophysics Supplement Series* **15**, 417 (1974).

[74] Napier, P. J. The Primary Antenna Elements. In *Synthesis Imaging in Radio Astronomy*, vol. 6, 39 (1989).

[75] Mauch, T. *et al.* Sumss: A wide-field Radio Imaging Survey Of The Southern Sky–II. The Source Satalogue. *Monthly Notices of the Royal Astronomical Society* **342**, 1117–1130 (2003).

[76] Chen, X. *et al.* Long-term variability of extragalactic radio sources in the planck early release compact source catalogue. *astro-ph* (2013).

[77] Bignall, H. E. *Radio Variability And Interstellar Scintillation Of Blazars.* Ph.D. thesis, University of Adelaide (2003).

[78] Trott, C. *et al.* A Survey For Transients And Variables With The Murchison Widefield Array 32-tile Prototype at 154 mhz (2013).

[79] Cimò, G. *et al. Multi-Frequency Analysis of Intraday Variable Radio Sources.* Ph.D. thesis, Universitäts-und Landesbibliothek Bonn (2003).

[80] Perley, R. & Butler, B. Integrated Polarization Properties Of 3C48, 3C138, 3C147, and 3C286. *The Astrophysical Journal Supplement Series* **206**, 16 (2013).

[81] Trott, C. M., Wayth, R. B., Macquart, J.-P. R. & Tingay, S. J. Source Detection In Interferometric Visibility Data. I. Fundamental Estimation Limits. *The Astrophysical Journal* **731**, 81 (2011).